Transient Thermo-Mechanical Response and Failure in Selected Turbine Cooling Geometries



Alexander C. F. Bebb
St. Peter's College
University of Oxford

A thesis submitted for the degree of
Doctor of Philosophy
Trinity 2024

For Anna,
and all the inspiration you've lent me

Acknowledgements

I owe a tremendous amount to Professor Peter Ireland and Dr. Christos Skamniotis for their support and guidance throughout this journey. Peter, you are a fantastic mentor, and I am honoured to have studied under you. You truly pulled me out of the depths of the COVID-19 pandemic and fostered an environment where this project could grow and flourish. Christos, your support and instruction on modelling has been invaluable to this work. Your research paved the way for me, and you always showed sincere patience as I struggled to learn various concepts. To Professor Simon Gill and Professor Matthew McGilvray, reviewing the entirety of a 250 page work is no small task. I am grateful for the time and care you dedicated to ensuring that this work was to standard, and for your insight and recommendations presented during my viva. Thank you, all.

Zachary Jackson, you have made fantastic contributions to the design of ELSA and its procedures. Your readiness to share your experience streamlined much of this work. Assistance in monitoring the rig during near-countless hours of testing is greatly appreciated. You are a terrific engineer and a wonderful colleague. Dave O'Dell and Duncan Blake, thank you for your design input and for putting up with ridiculous machining requests. I am sure Duncan is happy that he will never have to cut another of my plenum. Hal Surtel, thank you for all your efforts in assembling my monstrosity. You are a beacon of joy at Osney, and I will miss the occasional chat on the lab floor. To Craig Parsons and Roger Robinson, thank you for putting up with my endless requests for hard drives. Thank you to Rolls Royce PLC and, specifically, Dr. Janendra Telisinghe for all the funding and research support.

Anna, I am forever grateful for your love and support. You continue to be my motivation each day. No matter how challenging this degree has been, you were with me. Thank you for the countless times you put up with my early rises and late nights, my breakdowns, and my manic reaction to my brief successes. I am so excited for what is to come. Of course, it takes a village and my family is no exception. An enormous thank you to my family for believing in me and supporting me through the last 26 years: Mum, Dad, Charlotte, Brock, Manny, Bernadette, Kai, Mikalyn, Harriet, Millie, and all my wonderful extended relatives.

A special thank you is reserved for my grandparents, Danda and Boppa. You have cemented your firm belief in education in me and provided endless support throughout the years. I hope you look at this with pride.

Michael van de Noort, Manuela Sisti, Matthew Stokes, Jack Slater, Matthew Courtis, and Alex Murray thank you for your friendship. Our coffee chats and lunch breaks have made the monotony bearable, and your sounding board has proven invaluable. I will miss our usual whinging about the current state of affairs, lab or otherwise. You will always have a seat at my table, wherever that may be.

I would be remiss if I did not acknowledge James Innes Ker, Rev. Christopher Rimmer, Kaitie Dennis, Pat Dawson, Professor Leanne Hodson, and the boys in the boat: Felix Drinkall, Tassilo von Mueller, Jean-Phillipe Dufour, Freddie Orpin, Tom Sharrock, James Forward, and everyone else at OUBC and SPCBC, thank you. Branching out from this degree has kept me sane, for the most part. You have been incredibly supportive, and I will miss you all dearly. Although the victories were few, the wealth of experience is vast. I look back on our time with nothing but joy.

Thank you to the Cornell Crew for your support and friendship. I want to thank Mac Manion, Ben Hawley, Michael Grady, Michael Gates, Finn Putnam, Tommy Brittingham, Christopher Wilkins, James Aimer, Matt Tomaszewski, Andrew Greubel, and Todd Kennett. Professor Charles Williamson, thank you for putting your faith in a lowly undergrad who desperately wanted to work in your lab. Greg Szybka, thank you for instilling a desire to push my limits. Mr. Tweedle, I probably owe you the most. From the beginning, you took a keen interest in fostering my love of studying. Without the lessons learnt during your office hours, I would not have been able to experience all that I have.

There are countless others who deserve to be mentioned and there is so little space to do so. I will forever be grateful to those named and unnamed for their contribution to this work, however small. One last time: thank you.

Abstract

Decarbonising the aviation industry is imperative, as CO_2 accumulates in our atmosphere. Reducing the specific fuel consumption of gas turbine engines is achievable by increasing the turbine entry temperature (TET). A reduction in TET promises reduced emissions and lower costs to operators and consumers. Increasing engine temperatures requires more efficient cooling systems to ensure adequate safety and component life. A double-walled effusion-cooled system promises improved performance. It harmonises several existing technologies to produce favourable aerothermal performance. A growing wealth of literature is focused on the mechanical performance of such a system. Prior analytical and computational modelling of the thermal and stress fields requires confirmation and calibration of experimental results. This work aims to establish a new standardised experimental methodology to assess the aerothermal and mechanical performance of these new systems.

An engine-representative flat-plate test section, or coupon, was designed and modelled alongside a test rig, the Effusion Life and Stress Addition (ELSA). The coupon was designed to promote failure at the film hole wedge, the region created near the film holes' intersection with the hot-walls' exterior. This was achieved by removing pedestals from the non-test region and reducing kinematic constraints and the local stress field. Further stress mitigation was achieved by scaling the outermost pedestals and associated fillets, which was shown to reduce local stress by 41%. ELSA employed a combination of vertical-cavity surface-emitting lasers and a compound parabolic concentrator to supply engine-representative heat fluxes of up to 7.4 $\frac{\mathrm{W}}{\mathrm{mm}^2}$, and laboratory-temperature cooling air of up to 200 standard litres per minute to achieve engine-representative thermal gradients. Coupons obtained a maximum measured temperature of 1050 °C with thermal differences of up to 365 °C. The surrounding rig remained below 75 °C at all measured locations. The control settings did not exceed 50% of the available laser power, indicating that higher temperatures and thermal ramp rates are possible.

Engine-representative metal temperatures and distributions were evaluated for Inconel 625 and CMSX-4 coupons. The predicted crack initiation location for circular holes was

confirmed at film hole wedges for most components. The results showed a negligible dependence on the thermal gradient, normal to the coupon, in determining crack initiation. Instead, a dependence on the peak temperature was displayed. Experiments with varying normal thermal differences for the same maximum temperature show little to no effect on the number of cycles to crack initiation. An increased maximum temperature with an identical thermal gradient led to rapid buckling failure in less than 30 cycles. Furthermore, elliptical holes outperformed circular holes for identical internal geometries. This was with respect to both aerothermal and thermo-mechanical performance. In the ELSA test facility, elliptical holes with identical cross-sectional areas required an increase in laser power and a decrease in coolant to achieve identical thermal distributions. Elliptical holes endured three times more cycles than circular holes before developing cracks. Finally, the single-crystal CMSX-4 coupon was shown to survive eight times longer than a 3D-printed Inconel 625 component for an identical geometry and thermal field.

A numerical model was developed to extract the specific elastic stress state from a transient simulation of the thermal cycling profiles. It estimated an elastic nominal stress state, membrane stresses far from features, as a boundary-value problem. The boundaries were approximated on the basis of known thermal data of the quasi-steady hold region of the testing. The results of the finite elements showed reasonable agreement with the experimental values. A sub-domain approach was used to model the stresses at a critical point: the film-hole exterior wedge. Elasto-plastic models were used to estimate the total strain range. The results were compared to an established empirical Manson-Coffin relation to estimate the number of cycles to crack initiation. All models underestimated the fatigue life of CMSX-4 relative to the observed experimental values. An alternate estimate for the fatigue life, based on crystal plasticity, was then applied. The new estimated fatigue lives straddled the experimental results. A Molski-Glinka model offered a conservative estimate, while a constant-strain approach overestimated fatigue life.

Contents

Acknowledgements **i**

Abstract **iii**

List of Figures **ix**

List of Tables **xviii**

Nomenclature **xx**

1 Introduction **1**

1.1 The Brayton Cycle 1

1.2 Advancements in Turbine Cooling 4

1.2.1 Internal Cooling 6

1.2.2 External Cooling 7

1.2.3 Thermal Barrier Coatings 10

1.3 Double-Wall Effusion-Cooling 10

1.4 Project Motivation 13

1.5 Achievements 14

2 Review of Literature **16**

2.1 Common Failures in Turbine Blades 16

2.2 Stresses in a Double-Wall Effusion-Cooled Geometries 18

2.3 Life Prediction Methods 22

2.3.1 Low-Cycle Fatigue in Double-Wall Systems 23

2.4 Single-Crystal Super-Alloys 27

2.5 Energy Supply Methods 30

2.6 Compound Parabolic Concentrators 31

2.7 Summary 33

3 Design of a Double-Wall Effusion-Cooled Test Section **35**

3.1 Requirements and Considerations 35

3.2 Geometries and Accompanying Tests 37

3.2.1 Tensile Adapted 38

3.2.2 Concentric Cylinder 39

3.2.3 Flat Plate 40

3.3 Selection of Preferred Geometry 41

3.3.1 Domain and Boundary Conditions 41

3.3.2 Mesh 43

3.3.3 Results 44

3.4 Initial Selection 47

3.5 Mechanical Optimisation of a Preferred Geometry 48

3.5.1 Domain and Boundary Conditions 49

3.5.2 Results 50

3.6 Final Selection 52

3.6.1 Materials and Manufacturing 54

4 Thermal Stresses in a Representative Coupon Domain **55**

4.1 Derivation of a New Nominal Stress Model 55

4.1.1 Domain and Boundary Conditions 56

4.1.2 Thermal Cases 57

4.1.3 Governing Equations 59

4.1.4 Nominal Stresses 64

4.2 Finite Element Analysis 66

4.2.1 Domain and Boundary Conditions 67

4.2.2 Mesh 68

4.2.3 Results 68

4.3 Discussion of Thermal Cases and Impact on Stresses 71

5 Design of a Thermo-Mechanical Fatigue Facility **74**

5.1 Existing Infrastructure: Oxford Laser Heating Facility 74

5.2 Design Requirements and Considerations 77

5.3 Effusion Lifespan and Stress Addition (ELSA) 79
5.3.1 Modules 79
5.3.2 Instrumentation and Metering 85
5.3.3 LabView Control System 88
5.4 Coupon Coolant Air Supply 88
5.4.1 Minimising Conductive Losses 89
5.4.2 Coolant Supply Sizing 91
5.5 Coupon Energy Supply 92
5.5.1 Modified CPC Equations 92
5.5.2 Selection of Concentrator Configuration 94
5.5.3 VCSEL Bracket and Exhaust Management 100
5.6 Water Cooling System 106
5.7 Component Finite Element Analysis 108
5.7.1 Domains and Boundary Conditions 109
5.7.2 Meshes 113
5.7.3 Results and Discussion 114

6 ELSA Commissioning and Component Troubleshooting 117
6.1 Water Cooling System 117
6.2 Reflecting Surfaces 119
6.2.1 Surface Finish 119
6.2.2 Pulse Testing 121
6.2.3 Pulse Testing Finite Element Analysis 128
6.3 Hold Testing 134
6.4 IN625-C-I1 136
6.5 Addressing Coupon Overheating 138
6.5.1 Domain and Boundary Conditions 138
6.5.2 Mesh and Models 140
6.5.3 Results and Discussion 141
6.6 IN625-C-I2 145
6.6.1 Thermal Distribution 145
6.6.2 Initial Failure 146

6.7 Summary 148

7 Testing of DWEC Coupons **150**

7.1 Thermal Distribution Testing 150

7.1.1 Experimental Method 151

7.1.2 Results and Discussion 151

7.2 Thermo-Mechanical Fatigue Testing 156

7.2.1 Experimental Method 156

7.2.2 Results 158

7.3 Summary 174

8 Computational Analysis of Experimental Conditions **176**

8.1 Finite Element Analysis 176

8.1.1 Domains and Boundary Conditions 176

8.1.2 Mesh and Formulation 178

8.1.3 Results and Discussion 181

8.2 Elastic-Plastic Modelling 184

8.2.1 Strain Range Estimation 185

8.2.2 Results 187

8.3 Discussion 189

8.3.1 Perturbation Analysis 191

9 Conclusion **193**

9.1 Future Work 197

References **200**

Appendix I: Derivation of DWEC Coupon Equations **212**

Appendix II: Selected Material Properties **215**

Appendix III: Manufacturing **218**

Appendix IV: Strain Range MATLAB Script **223**

List of Figures

1.1 *(a) a diagram of the Brayton Cycle showing gas flow in red, work and heat flow in blue, and the shaft connection in black (b) a temperature-entropy plot comparing the actual and ideal cases of the Brayton Cycle* 2

1.2 *(a) cycle efficiency as a function of pressure ratio for selected temperature ratios (b) cycle efficiency as a function of per cent coolant flow rate for a constant pressure ratio and selected temperature ratios* 3

1.3 *evolution of turbine entry temperature for Rolls-Royce PLC engines, reproduced from [131]* 4

1.4 *diagrams depicting various methods for (a) internal blade cooling (b) external blade cooling, reproduced from [47]* 6

1.5 *cross section of film cooling with relevant values and features identified, reproduced from [76]* 8

1.6 *film effectiveness for various levels of wall porosity at constant dimensionless mass flow, reproduced from [30]* 9

1.7 *theoretical cooling effectiveness for various methods of cooling, reproduced from [74]* 11

1.8 *example of a double-wall effusion-cooled blade segment, reproduced from [76]* 12

1.9 *overall effectiveness of various double-wall effusion-cooled geometries against coolant mass flow, reproduced from [76]* 13

2.1 *damage to first stage turbine blades cause by excessive thermal loading and corrosion, reproduced from [11]* 17

2.2 *left: stress results for a double-wall effusion-cooled system, reproduced from [76]; right: identification of stress region (red) that was unaffected by pinned corners to the left* 18

2.3 *domain used in the derivation of stress relations showing thermal and mechanical boundaries, reproduced from [36]* 19

2.4 *representative stress state for a double-wall geometry under thermal loading showing large compressive stresses at the stream-wise extents of the inclined film holes, reproduced from [103]* 21
2.5 *example core temperature and mass flow for a typical civilian flight cycle* . . 22
2.6 *stress-strain curves for a double-wall system modelled using a constant energy approach for the case where the stress range exceeds the maximum temperature-dependent yield strength, reproduced from [101]* 25
2.7 *comparison of selected models and approaches to estimating crack formation in double-wall effusion-cooled systems, reproduced from [101]* 26
2.8 *scanning electron microscope imaging of CMSX-4 showing γ' precipitates, reproduced from [39]* 27
2.9 *relative Youngs' Modulus variation with crystallographic orientation, displaying a large anisotropy between the $< 001 >$ and $< 111 >$ directions, reproduced from [99]* 28
2.10 *vertical-cavity surface-emitting laser components and architecture at various length scales, reproduced from [127]* 30
2.11 compound parabolic concentrator shape and key features 31
2.12 *transmission curves for various polygonal compound parabolic concentrators for acceptance angles of (a) 5 degrees (b) 30 degrees, reproduced from [29]* . 33

3.1 *renderings of (a) tensile-adapted test article (b) side-fed variant* 38
3.2 *renderings of (a) concentric-cylinder test article (b) flattened variant* 39
3.3 *renderings of (a) flat plate test article (b) floating flat plate test article* . . . 40
3.4 *(a) double-wall effusion-cooled geometry used in the mesh-independence study with a cut-away on the hot-wall to show internal pedestal geometry (b) coarse surface-mesh showing refinement around fillets* 42
3.5 *tracked values versus mesh size for (a) body size refinement (b) face size refinement* 43
3.6 *thermal field for the central double-wall effusion-cooled region used across all test articles* 44
3.7 *nominal stress distribution for both planar dimensions in each test article* . 45

3.8 *maximum absolute principal stress distribution on the hot-wall of (a) TA (b) CF (c) FP (d) FFP* 46
3.9 *maximum absolute principal stresses on the interior of the hot-wall and pedestals of (a) TA (b) CF (c) FP (d) FFP* 46
3.10 *exterior pedestal fillet stresses in the optimised geometry, displaying regions of elevated maximum absolute principal stress on the external pedestal fillets* 49
3.11 *global average of both x- and z-direction nominal stress distribution for each refinement step* 50
3.12 *maximum absolute principal stress concentration factors, relative to the extracted nominal stress on the nearest wall, for each refinement step, displaying a sharp spike as fillets interact at large pedestal radii* 51
3.13 *a render of the final coupon design for the case of cylindrical holes* 53
3.14 *a render of the final coupon design for the case of elliptical holes* 53

4.1 *2D coupon-representative domain* 56
4.2 *simplified thermal profiles for a linear superposition of (a) the simplified thermal boundary with a uniform step from* $\mathrm{T_i}$ *to* $\mathrm{T_c}$ *(b) the simplified loss condition in zone 1 and a uniform step from* $\mathrm{T_i}$ *to* $\mathrm{T_c}$ 57
4.3 *zone 1 free body diagram* 59
4.4 *zone 2 free body diagram* 60
4.5 *zone 3 free body diagram* 61
4.6 *an example of the geometry used for the mesh study of (a) the 2D domain (b) the 3D domain, showing the fixed wall in light blue, the zone 1-zone 2 boundary in dark blue, the zone-2 zone-3 boundary on orange, and the symmetry condition in yellow* 66
4.7 *mesh study results for selected lines or planes, respectively, at various heights through each wall thickness for (a) the 2D domain (b) the 3D domain* . . . 67
4.8 *nominal stresses present for the realistic thermal case on a 2D geometry as a function of (a)* $\hat{\mathrm{t}}_\mathrm{b}$ *(b)* $\hat{\mathrm{H}}$ *(c)* $\hat{\mathrm{L}}_2$ *(d)* $\hat{\mathrm{L}}_3$ 69
4.9 *nominal stresses present for the realistic thermal distribution on a 3D geometry as a function of (a)* $\hat{\mathrm{t}}_\mathrm{b}$ *(b)* $\hat{\mathrm{H}}$ *(c)* $\hat{\mathrm{L}}_2$ *(d)* $\hat{\mathrm{L}}_3$ 70

4.10 *comparisons of (a) the nominal stresses as calculated by the analytical model to the FEA of the selected coupon from the previous chapter (b) the relative contribution of the loss temperature (c) the relative contribution of the initial temperature* 72

5.1 *existing Oxford Laser Heating Facility schematic diagram showing systems integration: blue is the cooling water out, red is the cooling water return, green is the 6.89 bar dry air supply, black is the data transfer connections, and orange is the laser interlock system, recreated from Jackson [63, 64]* 75

5.2 *cross-section of the Effusion Lifespan and Stress Addition showing the layout of assembled components* 79

5.3 *render of the coupon cooling air supply in the absence of fasteners, with components labelled* 80

5.4 *render of the coupon energy supply in the absence of fasteners, with components labelled* 83

5.5 *locations and identification of water cooling channels in machined components, from left to right: vertical-cavity surface-emitting laser bracket, compound parabolic concentrator half, coolant plenum* 84

5.6 *schematic of the Effusion Lifespan and Stress Addition-specific supply lines and the integration to the Oxford Laser Heating Facility with blue as the cooling water out, red as the cooling water return, green as the 6.89 bar dry air supply, and black as the data transfer connections* 84

5.7 *render and identification of the Effusion Lifespan and Stress Addition systems, shown in representative colours of various materials, integrated in to the existing Oxford Laser Heating Facility, shown in dark blue* 86

5.8 *(a) geometry used to evaluate the plenum stiffness showing various second moment of areas used (b) normalised stiffness versus normalised cross-sectional area showing a near 10% reduction in area for a 0.5% reduction in stiffness over the range of geometries studied* 89

5.9 *normalised plenum end-temperatures versus overall plenum length* 91

5.10 *reflecting surface profiles and focal points for (a) comparison between a normal compound parabolic concentrator and a modified compound parabolic concentrator for the same θ_{acc} (b) comparison between the modified compound parabolic concentrators investigated* 93

5.11 *vertical-cavity surface-emitting laser array configurations used in the ray tracing analysis for (a) the two 4.8 kW arrays (b) the four 2.4 kW arrays, with the solid lines representing the extent of the emitting surfaces, while the dashed lines denote the size of the through-hole in the VCSEL bracket, sized to accommodate a beam half angle of 10 degrees [89]* 95

5.12 *vertical-cavity surface-emitting laser angular distribution [88], in black, and comparison to uniform distribution approximations for the same total emitted power, with root mean square difference values included to show the relative accuracy of each approximation, compared to the true distribution* 96

5.13 *results of the independence study showing convergence to a ray-independent solution, done by increasing the number of modelled rays and tracking their effect on (a) the maximum heat flux (b) the per cent error* 96

5.14 *illumination distributions for $\theta_{\text{acc}} = 15$ degrees showing (a) 0 mm target spacing (b) 0 mm target spacing with VCSEL bracket (c) 1 mm target spacing (d) 1 mm target spacing with VCSEL bracket* 97

5.15 *comparison of assembly for a 1 mm target spacing, defined as the exit aperture from target plane separation for (a) optical efficiency (b) peak flux (c) mean flux and error bars of one standard deviation* 98

5.16 *illumination distributions for both VCSEL configurations and all acceptance angles at a 1 mm target spacing for a constant total power and aperture size* 99

5.17 *cross-section of the VCSEL bracket showing the internal geometry for half of a channel of the positive pressure exhaust management system, with the location of outlet A identified with the hatch, as this feature is not present on the positive pressure configuration* 102

5.18 *a mesh representative of that used for the fluid domain analysis (a) isometric view showing the inflation layer (b) along the y-direction showing the refinement around the hot gas inlets* 103

5.19 *tracked values versus mesh size for (a) face refinement (b) body refinement* 104
5.20 *full-domain streamline originating from the hot gas inlet for (a) negative pressure CPC (b) positive pressure CPC* 105
5.21 *predictions of volumetric flow rate versus pressure ratio for the water cooling loops across the range of available pressure settings showing the minimal variation between the single- and double-pass configurations* 108
5.22 *illumination distributions for the realistic case (a) VCSEL bracket (b) CPC front (c) coupon, taken from results output by LightTools* 112
5.23 *a mesh representative of that used for the solid domain analysis (a) compound parabolic concentrator solid domain, in blue, showing integration with fluid domain, in yellow, grey, and red (b) coupon coolant air assembly with the plenum in blue, the gaskets in red, the window in green, and the window bracket in beige* 113
5.24 *tracked values versus mesh size for (a) CPC solid (b) plenum assembly* . . . 114
5.25 *thermal field for the VCSEL bracket and CPC assembly* 115
5.26 *thermal field of the plenum* 115

6.1 *(a) raw data for the water cooling system tests, with red shades identifying the sampling windows to average-out oscillations in flow measurement (b) comparison of the true network to the low order network model* 118
6.2 *(a) Alicona measurement set-up for one half of the compound parabolic concentrator, showing the approximate location of a sample taken at the exit aperture and the visual quality of the reflecting surfaces. (b) Alicona data with a sampling path shown in red and the vertical gradient identifying the curvature present on the reflecting surface* 120
6.3 *roughness data sampled at three paths for the compound parabolic concentrator* 120
6.4 *alternate calibration run testing set-up showing (a) calibration plate installed on ELSA with associated cooling connections (b) calibration plate* 122
6.5 *comparison of roughness with different surface finishes for alternate calibration run-2 and alternate calibration run-4* 123
6.6 *post-testing plates showing visual change for (a) alternate calibration run-2 (b) alternate calibration run-4* 125

6.7 *plastic deformation of the calibration plate following testing* 125
6.8 *(a) measured temperatures from cyclic testing for alternate calibration run-4 (b) corresponding surface emissivity as calculated through equation (6.1)* . . 126
6.9 *calculated emissivity versus pyrometer (true) temperature for (a) alternate calibration run-2 (b) alternate calibration run-3 (c) alternate calibration run-4* 127
6.10 *alternate calibration run transient-thermal mesh-independence results for tracked values of (a) temperature (b) maximum heat flux (c) mean heat flux* 129
6.11 *illumination at various CPC-target spacings* 130
6.12 *inconel 625 absorbance versus temperature from alternate calibration run testing* 131
6.13 *comparison of maximum temperatures of low-order transient model and alternate calibration run testing for (a) alternate calibration run-2 (b) alternate calibration run-4* 132
6.14 *comparison of thermal distributions achieved through finite element analysis and experiments* 133
6.15 *(a) full experimental set-up of the Effusion Lifespan and Stress Addition with the plenum and all coolant and supply lines installed (b) representative positioning of the measurement region pyrometer 1, over the centre of the coupon* 134
6.16 *long-hold test temperatures in (a) coupon pyrometer readings (b) plenum thermocouples (c) water cooling loop return flow* 135
6.17 *cyclic-hold test temperatures in (a) coupon pyrometer readings (b) plenum thermocouples (c) water cooling loop return flow* 136
6.18 *imaging of IN625-C-I1 in (a) visible spectrum (b) emissivity-corrected infrared spectrum* 137
6.19 *impingement hole configurations of (a) V0 (b) V1 (c) V2 (d) V3 (e) V4 (f) V5, showing existing impingement holes in red and proposed holes in green.* 139
6.20 *components of the conjugate mesh showing (a) solid domain (b) fluid domain (c) integration of solid and fluid domains with refinements around fillets* . . 139
6.21 *mesh-independence results for the conjugate model showing (a) total mass flow rate (b) area-average convective HTC (c) mass-average solid temperature* 141
6.22 *hot side thermal distributions for (a) V0 (b) V1 (c) V2 (d) V3 (e) V4 (f) V5* 142

6.23 *thermal distributions for the V5 design (a) hot side (b) cold side* 143
6.24 *flow vector field sampled for an x-z plane (a) pedestal mid-height (b) hot-wall adjacent* 144
6.25 *flow vector field sampled for an x-y plane (a) 2 rows of film holes (b) 3 rows of film holes* 144
6.26 *cold-wall of IN625-C-I2 post-machining showing the difference in 3D-printed and machined impingement hole profiles.* 146
6.27 *imaging of IN625-C-I2 in (a) visible spectrum (b) emissivity-corrected infrared spectrum* 146
6.28 *(a) IN625-C-I2 glowing hot following vertical-cavity surface-emitting laser pulse (b) ray tracing illuminance distribution* 147
6.29 *IN625-C-I2 post cycling exhibiting large cracks originating from the central film holes, where the local temperature was greatest* 148

7.1 *Aremco 840-CM applied to the surface of (a) IN625-C-T1 (b) IN625-E-T1* . 151
7.2 *emissivity versus temperature for (a) IN625-C-T1 (b) IN625-E-T1* 152
7.3 *effect of vertical-cavity surface-emitting laser power and coolant flow rate for IN625-C-T1 (a)* $\mathrm{T_{max}}$ *(b)* $\Delta\mathrm{T_{normal}}$ 153
7.4 *effect of vertical-cavity surface-emitting laser power and coolant flow rate for IN625-E-T1 (a)* $\mathrm{T_{max}}$ *(b)* $\Delta\mathrm{T_{normal}}$ 154
7.5 *distress of Aremco 840-CM coating following testing for (a) IN625-C-T1 (b) IN625-E-T1* 155
7.6 *pyrometer and thermocouple measurement locations with thermal gradient definitions* 157
7.7 *IN625-C-T2 testing profiles of (a) vertical-cavity surface-emitting laser power (b) coolant flow rate (c) coolant temperature (d)* $\mathrm{T_{max}}$ *(e)* $\Delta\mathrm{T_{normal}}$ 160
7.8 *progression of cycling fatigue on the exterior surface of IN625-C-T2* 161
7.9 *IN625-E-T2 testing profiles of (a) vertical-cavity surface-emitting laser power (b) coolant flow rate (c) coolant temperature (d)* $\mathrm{T_{max}}$ *(e)* $\Delta\mathrm{T_{normal}}$ *(f)* $\Delta\mathrm{T_{planar}}$ 162
7.10 *progression of cycling fatigue on the exterior surface of IN625-E-T2* 163
7.11 *IN625-C-T3 testing profiles of (a) (a) vertical-cavity surface-emitting laser power (b) coolant flow rate (c) coolant temperature (d)* $\mathrm{T_{max}}$ *(e)* $\Delta\mathrm{T_{normal}}$. 164

7.12 *progression of cycling fatigue on the exterior surface of IN625-C-T3* 165
7.13 *IN625-E-T3 testing profiles of (a) vertical-cavity surface-emitting laser power (b) coolant flow rate (c) coolant temperature (d)* T_{max} *(e)* ΔT_{normal} *(f)* ΔT_{planar} 166
7.14 *progression of cycling fatigue on the exterior surface of IN625-E-T3* 167
7.15 *IN625-C-T4 testing profiles of (a) vertical-cavity surface-emitting laser power (b) coolant flow rate (c) coolant temperature (d)* T_{max} *(e)* ΔT_{normal} 168
7.16 *progression of cycling fatigue on the exterior surface of IN625-C-T4* 169
7.17 *IN625-E-T4 testing profiles of (a) vertical-cavity surface-emitting laser power (b) coolant flow rate (c) coolant temperature (d)* T_{max} *(e)* ΔT_{normal} *(f)* ΔT_{planar} 170
7.18 *progression of cycling fatigue on the exterior surface of IN625-E-T4* 171
7.19 *CMSX-4-T1 testing profiles of (a) vertical-cavity surface-emitting laser power (b) coolant flow rate (c) coolant temperature (d)* T_{max} *(e)* ΔT_{normal} *(f)* ΔT_{planar} 172
7.20 *progression of cycling fatigue on the exterior surface of CMSX-4-T1* 173

8.1 *(a) global modelling utilised (b) close up of central region featuring mesh refinement (c) sub-modelling unit domain* 179
8.2 *mesh-independence results for (a) global mesh refinement (b) unit body refinement (c) fillet refinement* 180
8.3 *comparison of finite element analysis to testing data for IN625-E-T2 (a)* T_{max} *(b)* ΔT_{normal} *(c)* ΔT_{planar} 182
8.4 *comparison of finite element analysis to testing data for IN625-E-T4 (a)* T_{max} *(b)* ΔT_{normal} *(c)* ΔT_{planar} 182
8.5 *comparison of finite element analysis to testing data for CMSX-4-T1 (a)* T_{max} *(b)* ΔT_{normal} *(c)* ΔT_{planar} 183
8.6 *(a) Cauchy component stresses in the unit coordinate system over the modelled cycle (b) maximum principal stresses for the aforementioned Cauchy stress state* 184
8.7 *IN625-C-T2 hysteresis curves for various plastic formulations* 188
8.8 *CMSX-4-T1 hysteresis curves for various plastic formulations* 188

9.1 *motion amplification locations and displacements during hold testing* 198

List of Tables

3.1 *selected dimensions for the double-wall effusion-cooled region of the proposed test articles* 37

3.2 *root mean square difference of each test section nominal stress relative to the theoretical model [36, 102]* 45

3.3 *comparison of global and central test region stresses across proposed test articles* 47

3.4 *stresses on the exterior pedestal fillets and dimensionless areas between pedestals for varied fillet radii and pedestal diameters* 51

4.1 *elastic and thermal strain components for the analytical model* 63

5.1 *relevant technical data of available Oxford Laser Heating Facility vertical-cavity surface-emitting lasers, reproduced from [89]* 82

5.2 *material properties used in the low-order thermal resistance model of the plenum assembly* 90

5.3 *heat flow rates across conjugate walls for both exhaust management system configurations* 105

5.4 *geometries and loss coefficients used in the network analysis to assess the performance of the Effusion Lifespan and Stress Addition water cooling loops* 107

5.5 *predicted flow rates and heat transfer coefficients for water cooling channels* 109

5.6 *material properties used in finite element analysis of Effusion Lifespan and Stress Addition coupon coolant air supply components* 110

5.7 *number of cycles to failure in Effusion Lifespan and Stress Addition components as estimated through finite element analysis and S-N data for simple monotonic cyclic loading with a magnitude of* $\sigma_{\max}$ 116

6.1 *surface roughness values for major reflecting surfaces* 121

6.2 *alternate calibration run pulse testing duration and corresponding vertical-cavity surface-emitting laser power settings* 123

6.3 *average surface roughness for each alternate calibration run plate* 124
6.4 *linear fit coefficients for the emissivity of conditioned plates at each plate roughness* 128
6.5 *relevant temperature values for coupon redesign variants* 142

7.1 *coupon target temperatures for the quasi-steady region of thermo-mechanical fatigue cycling* 156
7.2 *coupon masses before and after testing, accurate to ± 0.03 g* 175

8.1 *total test average values for the quasi-steady hold region during fatigue testing* 177
8.2 *absorbance coefficients used in finite element analysis of transient cycling* . 178
8.3 *characteristic time values for the coupon geometry and selected materials* . 181
8.4 *strain range and number of cycles to crack initiation as predicted by Neuber-type methods and the Scholz-Manson-Coffin relationship [95]* 189
8.5 *strain range and number of cycles to crack initiation as predicted by Neuber-type methods and the Skamniotis relation [104] for CMSX-4* 189
8.6 *uncertainty calculations for the CMSX-4 coupon under T2 conditions* 192

Nomenclature

General

η	Efficiency
m	Mass
$\dot{q}$	Power
T	Temperature
t	Time
U	Uncertainty
Φ	Dimensionless Temperature

Fluid Mechanics

α_T	Turbulent Thermal Diffusivity
ϵ_o	Effectiveness
h	Heat Transfer Coefficient
P	Pressure
Q	Energy
v	Velocity
V	Volume
W	Work

Subscripts

aw	Adiabatic Wall
c	Convection
c,e	Coolant Exit
c,i	Coolant Inlet
comp	Compressor
cycle	Total Cycle
f	Film
m	Metal
net	Difference
turb	Turbine
∞	Main Stream

Solid Mechanics

A	Area
D	Diameter
E	Energy
ϵ	Strain
G	Geometric Parameter
H	Channel Height
I	Bending Moment of Inertia
κ	Curvature
L	Length
M	Moment
N	Normal Force
N_f	Number of Cycles to Failure
P	Point
ρ	Radius
S	Peak Stress Magnitude
σ	Stress
t	Wall Thickness
V	Shear Force

Subscripts

a	Hot-Wall

b	Cold-Wall
c	Cold Value
cr	Creep
e	Elastic
eq	Equivalent
f	Failure
fe	Fictitious Elastic
h	Hot Value
i	Initial Value
l	Loss
p	Plastic
pd	Pedestal
pf	Pedestal Fillet
tr	True Value
1	Maximum Principal
2	Median Principal
3	Minimum Principal

Radiation and Optics

a	Characteristic Length
α	Absorption
C	Concentration Ratio
d	Distance
ϵ	Emissivity
h	Height
θ	Angle
I	Intensity
K_{err}	Scattering Efficiency
n_r	Average Number of Reflections
ρ	Surface Efficiency
σ_{sb}	Stefan-Boltzmann Constant
t	General Parameter
ψ	Angle

Subscripts

acc	Acceptance
cpc	CPC Value
ex	CPC Outlet Value
h	Height
in	CPC Inlet Value
ir	Infrared Camera
mod	Modified CPC Value
opt	Optical Value
p	Pyrometer
w	Width

Material Properties

α	Coefficient of Thermal Expansion
C_p	Specific Heat Capacity
E	Youngs' Modulus
G	Shear Modulus
γ	Ratio of Specific Heats
k	Thermal Conductivity
ν	Poissons' Ratio
Q	Activation Energy
R	Gas Constant
ρ	Density
σ_{y0}	Yield Stress, Room Temperature
$\sigma_{yT_{max}}$	Yield Stress, Max Temperature

Acronyms

ACR	Alternate Calibration Run
CFD	Computational Fluid Dynamics
CPC	Compound Parabolic Concentrator
CT	Computed Tomography

DAQ	Data Acquisition
DSLR	Digital Single-Lens Reflex
DWEC	Double-Wall Effusion-Cooled
ELSA	Effusion Lifespan and Stress Addition
FEA	Finite Element Analysis
FHW	Film Hole Wedge
HCF	High-Cycle Fatigue
HTC	Heat Transfer Coefficient
LCF	Low-Cycle Fatigue
NGV	Nozzle Guide Vane
OLAHF	Oxford Laser Heating Facility
RMSD	Root Mean Square Difference
SCF	Stress Concentration Factor
SLPM	Standard Litres Per Minute
TBC	Thermal Barrier Coating
VCSEL	Vertical-Cavity Surface-Emitting Laser

Introduction

Demands for reducing humanitys' impact on our planet continue to increase. Each revelation of how profound our influence is on the world further highlights the immediate need to address our collective emissions. This approach is increasingly prevalent in future planning. The airline industry accounts for almost 2.5% of global CO_2 emissions [92], just over 1.04 billion tonnes of CO_2 for 2018. In response, the International Air Transport Association (IATA), representing some 290 airlines, adopted a resolution to address the industrys' emissions. The IATA calls upon aviation industry stakeholders to develop alternative and sustainable fuels, reform air navigation routes to address inefficiencies, and produce new airframes and propulsion units [60]. A cost-effective way to achieve the latter demand is through the improvement of high-pressure turbine blade cooling systems.

1.1 The Brayton Cycle

Modern large-scale aviation is heavily reliant on the Brayton cycle. It is used to power turboprop, turbojet, turboshaft, and turbofan engines. In its idealised form, it is comprised of three stages shown in Figure 1.1:

1-2s: Isentropic compression of the gas

2s-3: Isobaric heat addition

3-4s: Isentropic expansion of the gas

The dotted lines in Figure 1.1 refer to the idealised case described above. The solid lines refer to a realistic case in which entropy is generated during compression and expansion of the gas. The compressor heats the gas, and the turbine does not recover all the thermal energy. The isentropic efficiencies may be defined as:

$$\eta_{\text{comp}} = \frac{\mathrm{T_{2s}} - \mathrm{T_1}}{\mathrm{T_2} - \mathrm{T_1}} \qquad \eta_{\text{turb}} = \frac{\mathrm{T_3} - \mathrm{T_4}}{\mathrm{T_3} - \mathrm{T_{4s}}} \tag{1.1}$$

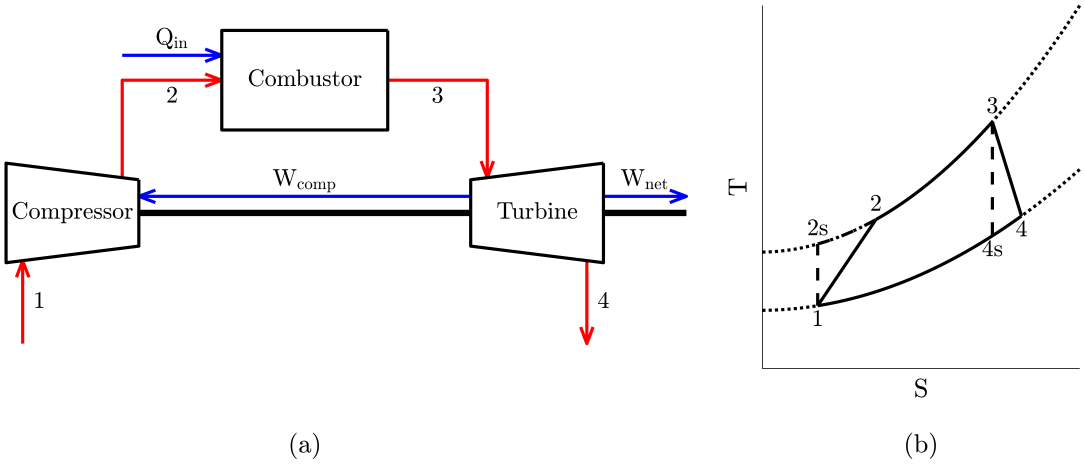


Figure 1.1: *(a) a diagram of the Brayton Cycle showing gas flow in red, work and heat flow in blue, and the shaft connection in black (b) a temperature-entropy plot comparing the actual and ideal cases of the Brayton Cycle*

The work of the compressor and the turbine is defined using isentropic flow relations in combination with the above efficiencies and the ideal gas law [75]. It is useful to define the pressure ratio as $\mathrm{PR} = \frac{\mathrm{P_2}}{\mathrm{P_1}} = \frac{\mathrm{P_3}}{\mathrm{P_1}}$.

$$\mathrm{W_{comp}} = \frac{\mathrm{P_{2s}V_{2s}} - \mathrm{P_1V_1}}{\eta_{\mathrm{comp}}\,(\gamma - 1)} = \frac{\mathrm{mR}\gamma}{\eta_{\mathrm{comp}}}\frac{\mathrm{T_{2s}} - T_1}{\gamma - 1} = \frac{\mathrm{mR}\gamma\mathrm{T_1}}{\eta_{\mathrm{comp}}}\left(\frac{(\mathrm{PR})^{\frac{\gamma-1}{\gamma}} - 1}{\gamma - 1}\right) \tag{1.2}$$

$$\mathrm{W_{turb}} = \eta_{\mathrm{turb}}\frac{\mathrm{P_3V_3} - \mathrm{P_{4s}V_{4s}}}{\gamma - 1} = \eta_{\mathrm{turb}}\mathrm{mR}\gamma\frac{\mathrm{T_3} - \mathrm{T_{4s}}}{\gamma - 1} = \frac{\eta_{\mathrm{turb}}\mathrm{mR}\gamma\mathrm{T_3}}{\gamma - 1}\left(1 - \frac{1}{(\mathrm{PR})^{\frac{\gamma-1}{\gamma}}}\right) \tag{1.3}$$

The net work is then calculated as the difference between the turbine work output and the work required to run the compressor:

$$\mathrm{W_{net}} = \mathrm{W_{turb}} - \mathrm{W_{comp}} = \frac{\mathrm{mR}\gamma\mathrm{T_1}}{\gamma - 1}\left(\eta_{\mathrm{turb}}\frac{\mathrm{T_3}}{\mathrm{T_1}}\left(1 - \frac{1}{(\mathrm{PR})^{\frac{\gamma-1}{\gamma}}}\right) - \frac{(\mathrm{PR})^{\frac{\gamma-1}{\gamma}} - 1}{\eta_{\mathrm{comp}}}\right) \tag{1.4}$$

The cycle efficiency can be obtained by dividing the net work output by the thermal

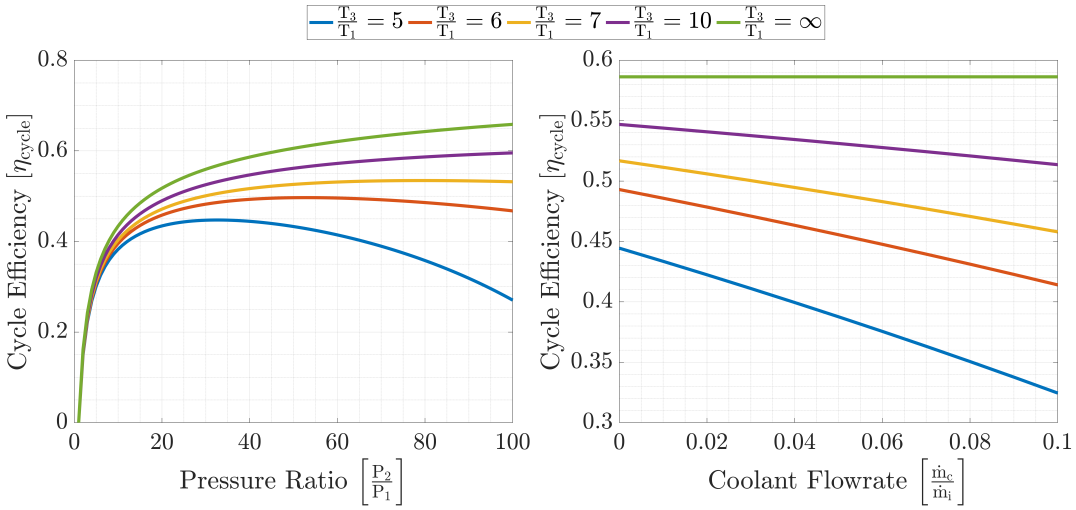


Figure 1.2: *(a) cycle efficiency as a function of pressure ratio for selected temperature ratios (b) cycle efficiency as a function of per cent coolant flow rate for a constant pressure ratio and selected temperature ratios*

energy added by the combustor between points 2 through 3:

$$\begin{aligned}\eta_{cycle} = \frac{W_{net}}{Q_{in}} &= \frac{\frac{mR\gamma T_1}{\gamma-1}\left(\eta_{turb}\frac{T_3}{T_1}\left(1-\frac{1}{(PR)^{\frac{\gamma-1}{\gamma}}}\right)-\frac{(PR)^{\frac{\gamma-1}{\gamma}}-1}{\eta_{comp}}\right)}{mC_p\left(T_3-T_2\right)} \\ &= \frac{\eta_{turb}\frac{T_3}{T_1}\left(1-\frac{1}{(PR)^{\frac{\gamma-1}{\gamma}}}\right)-\frac{(PR)^{\frac{\gamma-1}{\gamma}}-1}{\eta_{comp}}}{\frac{T_3}{T_1}-\frac{(PR)^{\frac{\gamma-1}{\gamma}}-1}{\eta_{comp}}-1}\end{aligned} \tag{1.5}$$

An illustration of Equation (1.5) is provided in Figure 1.2. Various pressure ratios are presented for four realistic temperature ratios in addition to the limit as $\frac{T_3}{T_1} \to \infty$. The isentropic efficiencies of the compressor and turbine were set equal to 0.9. The ratio of specific heat capacities was set at 1.4, which is in line with standard air. For reference, a modern gas turbine operates at a pressure ratio of approximately 40 and a temperature ratio of 6 [107]. The reported cycle efficiency illustrates the profound effect of the pressure and temperature ratios. Figure 1.2 (a) clearly shows that the total cycle efficiency can be increased by increasing both. An alternate approach was taken to understand the cycle efficiency for an engine-standard pressure ratio, reported above, as the per cent coolant flow by mass increases. In line with a true engine, coolant air was modelled as being siphoned off the compressor stage and bypassing the combustor. The analysis assumes that no energy

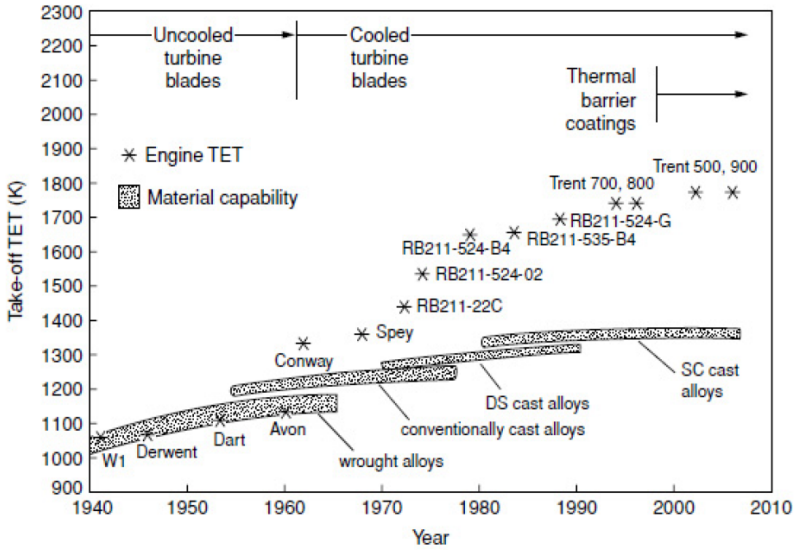


Figure 1.3: *evolution of turbine entry temperature for Rolls-Royce PLC engines, reproduced from [131]*

was recovered from this air. The mass term in Equation (1.5) was divided in to $\dot{m}_{\text{comp}}$ and $\dot{m}_{\text{turb}}$ to model this siphoning effect. Figure 1.2 (b) shows that the coolant flow rate directly affects the efficiency of the cycle, with reduced impacts at greater temperature ratios. Therefore, the increase in cycle efficiency is to be achieved through the increase in TET and a decrease in the cooling air requirements.

1.2 Advancements in Turbine Cooling

The historical progression of the turbine entry temperature (TET) is shown in Figure 1.3. It is immediately apparent that the thermal demand on modern turbine components far exceeds the current material capabilities. For the Trent 500 and 900 engines, the TET is near 1800 K, 30% greater than the melting point of most single-crystal (SC) cast alloys. Early generation engines, between 1940 and 1960, were able to rely solely on available wrought alloys due to the low TET requirements. The development of cooling technologies enabled modern engines to achieve far greater TETs without melting. The temperature of the mainstream flow was approximately 30% greater than the melting temperature of these blades. Explicitly, modern engines will not function without thermal intervention.

Blade cooling technologies rely on an abundant coolant medium: air. Traditionally, air is siphoned from the latter stages of the compressor and bypasses the combustor before

being supplied to the blades [50]. Some engines require per cent cooling airflow near 25-30% [32]. Due to non-isentropic compression and expansion, this cooling air is at 1000 K when it reaches the turbine [32, 107]. The subsequent flow pathways were commonly grouped in to two categories: internal cooling and external cooling. Internal cooling describes a class of methods that use geometries within the blade to increase conduction through the blade material itself or convection to a coolant medium that remains within the blade structure [6, 42, 47, 50]. It is a reactive method as it removes thermal energy that has already convected in to the blade. External cooling utilises the features on the blade surface to remove excess thermal energy. The common goal among external cooling designs is the establishment of a cooling film layer [7, 30, 47, 50, 67]. This is a proactive method as the cooler film prevents convection between the blade surface and the hot mainstream flow [33, 47]. Each technique is ranked according to several key metrics which define system efficiencies. Relative increases in these efficiencies result in higher TET capacities for the associated method.

The most general metric is the overall effectiveness, ϵ_{o}, presented in Equation (1.6) [47]:

$$\epsilon_{\mathrm{o}} = \frac{\mathrm{T}_{\infty} - \mathrm{T}_{\mathrm{m}}}{\mathrm{T}_{\infty} - \mathrm{T}_{\mathrm{c,i}}} \tag{1.6}$$

T_{∞} is the mainstream temperature at the stage inlet, T_{m} is the bulk metal temperature, which is assumed to be uniform, and $\mathrm{T}_{\mathrm{c,i}}$ is the coolant inlet temperature. A value of zero indicates that there is no cooling. A value of unity represents perfect cooling in which the bulk temperature of the blade is equal to the coolant inlet temperature. The overall effectiveness of such systems is a function of the efficiencies of the cooling system. The two most relevant are the convective and film efficiencies.

Convective efficiency is often used to describe heat exchangers. It quantifies the performance of internal cooling by relating the change in coolant temperature as it flows through the system to the bulk metal temperature [47].

$$\eta_{\mathrm{c}} = \frac{\mathrm{T}_{\mathrm{c,e}} - \mathrm{T}_{\mathrm{c,i}}}{\mathrm{T}_{\mathrm{m}} - \mathrm{T}_{\mathrm{c,i}}}; \tag{1.7}$$

Where $\mathrm{T}_{\mathrm{c,e}}$ is the temperature of the coolant as it exits the blade, $\mathrm{T}_{\mathrm{c,i}}$ is the coolant inlet temperature, and T_{m} is the bulk metal temperature. A value of zero indicates there is no internal transfer of heat. Perfect internal cooling is represented by a value of unity. In

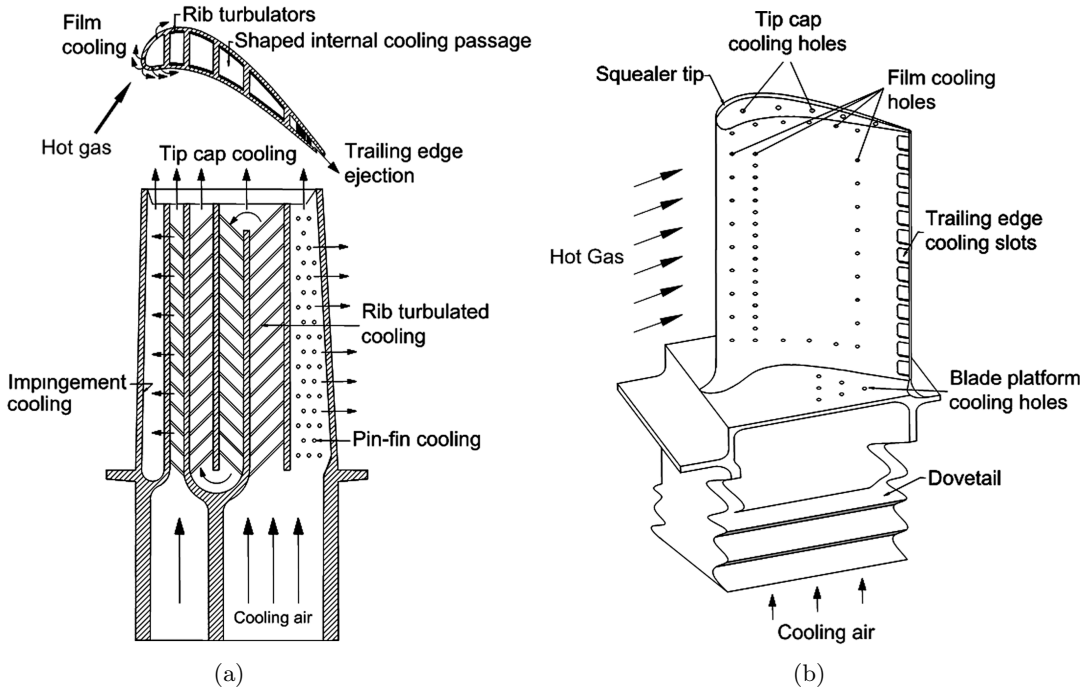


Figure 1.4: *diagrams depicting various methods for (a) internal blade cooling (b) external blade cooling, reproduced from [47]*

this case, the fluid exits the blade at the equilibrium temperature.

External cooling is best quantified using the adiabatic film effectiveness, η_{f}. It is defined as [76]:

$$\eta_{\mathrm{f}} = \frac{\mathrm{T}_{\infty} - \mathrm{T}_{\mathrm{aw}}}{\mathrm{T}_{\infty} - \mathrm{T}_{\mathrm{c,e}}} \tag{1.8}$$

T_{∞} is the mainstream temperature, T_{aw} is the adiabatic wall temperature, and $\mathrm{T}_{\mathrm{c,e}}$ is the coolant temperature as it exits the blade to create the film. A value of unity exists when the adiabatic wall temperature is equal to the coolant temperature. A value of zero indicates the absence of a film.

1.2.1 Internal Cooling

The early generations of turbine blades relied exclusively on internal cooling, as this was adequate for a relatively low TET. Holland gives an example of a convection system for early radial cooling, which enabled the blades to survive nearly 5000 hours of service [50]. Moving through time in Figure 1.3, the demand for increased TET drove the advancement of this original approach. The RB211 HP blade made use of a multi-pass system [50]. The illustration in Figure 1.4 (a) shows a multi-pass system with various features to improve

convective efficiency.

One such feature is rib-turbulators [6, 42, 47]. These are small, roughly rectangular features that create sharp undulations in the lining of internal channels. Most are no larger than 5-10% of the hydraulic diameter of the channel [47]. Turbulated passages increase both the channel friction factor and heat transfer [6], the latter by roughly 125% in certain cases [6]. They do so by promoting turbulent mixing of the channel boundary layer to reduce the film temperature. Similar results are achieved through pin-fins [42, 47]. These protrude from the channel walls, occasionally bridging the span of the channel. They increase turbulent flow and offer alternate conductive pathways [47]. Each feature improves the convective efficiency of the blade.

Impingement cooling is extensively featured in modern vanes. Coolant air is exhausted through a small hole, or series of small holes, and strikes the inner wall of the aerofoil [43, 47, 59, 94]. Typically, two parallel plates are used to achieve this. The plate with holes is known as the orifice plate and the other is the impingement plate. Normally incident jets are characterised by a central stagnation region surrounded by a disk of coolant that accelerates outward. This stagnation point is associated with high local Nusselt numbers [43, 59]. Goldstein and Behbahani show that for low normalised plate spacings, $\frac{L}{D} < 6$, there is a 55-60% reduction in Nusselt number at a distance of 5D, or hole diameters, from the stagnation point [43]. With lower plate spacing, re-circulation impacting the impinging jet gives rise to additional, smaller peaks in Nusselt numbers around 2.4D away from the stagnation point [94]. Impingement is an effective method of internal cooling, but arrays of impingement holes are required to effectively and uniformly cool large regions. A high-density array decreases the local Nusselt numbers for a high density of impingement holes [59]. The highest heat transfer rate of enclosed systems is dominated by the convection between the coolant and the impingement plate, or aerofoil [42]. The average Nusselt numbers on the orifice plate, in which the holes were bored, are roughly 20-25% of the impingement plate [42].

1.2.2 External Cooling

Figure 1.4 (b) presents common external features in modern blades. These are used to establish a film on the exterior of the blade surface. Figure 1.5 provides relevant features

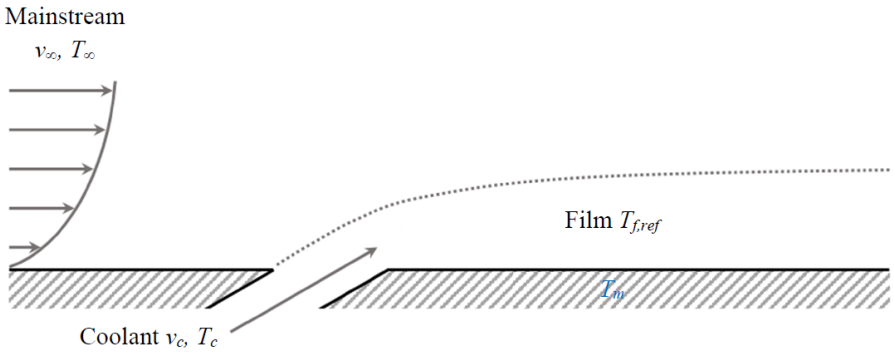


Figure 1.5: *cross section of film cooling with relevant values and features identified, reproduced from [76]*

for film cooling from a discrete coolant injection location. For systems incorporating both internal and external cooling methods, the film temperature, $T_{f,ref}$, is sensitive to the convective efficiency of the internal system [67]. The design of the external system requires balancing the total coverage of the blade exterior while minimising the mass of cooling air required [7]. Work is needed to pump the cooling air, and the aerodynamic losses incurred by injecting a low-speed fluid in to a high-speed flow must be carefully balanced with the increase in cooling efficiency. As a result, advances in cooling are characterised by an increase in convective efficiency and cooling effectiveness while simultaneously reducing the proportion of core flow siphoned off as coolant supply. To this end, various features from hole diffusers, asymmetrical holes, inclined holes, and increased porosity [7, 30, 67] have been investigated. Hole shape and inclination are used to assist in distributing the coolant flow and prevent film detachment at high blowing ratios [67]. High levels of inclination minimise the coolant requirements and improve the effectiveness of the film [67]. The size of the hole has an influence on the overall effectiveness as it changes the porosity of the outer skin for the same hole centre spacing. Increasing the diameter of the hole, or porosity, from 1.18 mm to 2.16 mm for a constant blowing ratio increases the efficiency of the film from 0.54 to 0.63 [7]. This is attributed to the decrease in the cooling exit velocity v_c in Figure 1.5.

In addition to hole size, the density of holes is used to increase porosity [30]. Goldstein [43] proposed an empirical correlation to quantify the effectiveness of the film of each discrete hole. This was modified by Murray [76] and is presented in Equation (1.9).

$$\eta_f\left(x,z\right) = \frac{Mv_\infty D}{8\alpha_t\left(x/D + x_{decay}\right)} \exp\left(-\frac{z}{c_1}\right)^{c_2} \tag{1.9}$$

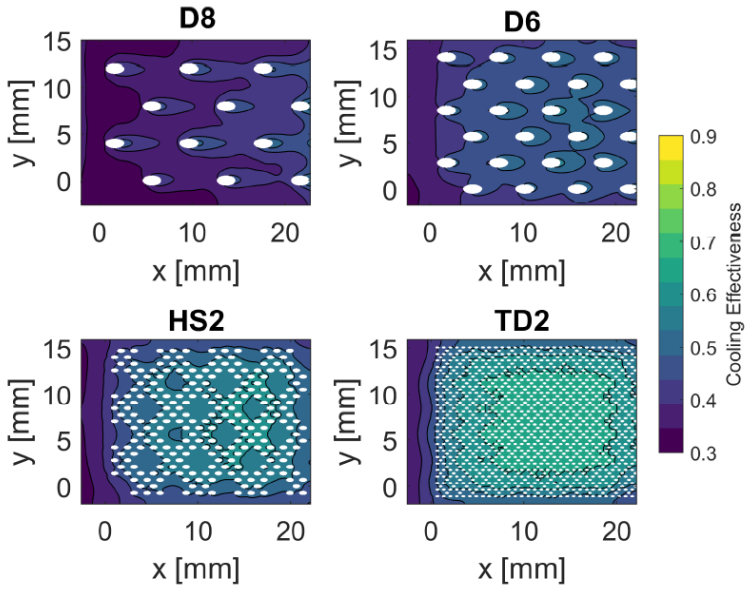


Figure 1.6: *film effectiveness for various levels of wall porosity at constant dimensionless mass flow, reproduced from [30]*

Where x is the stream-wise coordinate and z is span-wise. The turbulent thermal diffusivity, α_t, and x_{decay} were fit to the experimental data [30, 76]. The values for c_1 and c_2 are functions of the blowing ratio, M, and position. This equation is combined with an equation quantifying the interaction between individual films using a superposition method proposed by Sellers [97]:

$$\eta_f(x,z) = 1 - \prod_{j=1}^{n} (1 - \eta_{f,j}(x,z)) \tag{1.10}$$

Together, Equations (1.9) and (1.10) enable a complete computation of the film for any number of holes. As is apparent from Equation (1.9), there is maximum effectiveness at the hole, which decreases in both the stream-wise and span-wise directions. Increasing the porosity through the addition of small holes in the span-wise direction evens out the distribution by reducing the penalty incurred by the z-term. The superposition of holes in the stream-wise direction reduces the efficiency penalty caused by x_{decay}. The effect of this can be seen in Figure 1.6, in which increasing porosity through increasing hole density results in increased uniformity in the developed film and a higher span-wise average film effectiveness [30]. The reduction in 'hot streaks', regions of minimal to no film effectiveness, was severely reduced between HS2 and TD2.

The use of a discrete hole array is called effusion cooling. Continuing to increase the hole density while maintaining porosity tends towards a design in which the blade surface

has an infinite number of infinitely small holes. This is desirable as it increases the mean film effectiveness [7, 30]. The theoretical limit is termed transpiration cooling, defined as the point at which the solid and coolant fluid have reached the same temperature. To this end, Courtis defined a transpiration factor, TF [30]. T_w is the wall temperature, T_f is the film temperature, T_∞ is the mainstream temperature, and $T_{c,i}$ is the coolant temperature at the film hole. The ideal value for the TF is 0, as this indicates that the film and wall temperatures are equal.

$$TF = \frac{T_w - T_f}{T_\infty - T_{c,i}} \tag{1.11}$$

The achievement of true transpiration is not possible due to physical and manufacturing constraints. In lieu of this, modern blades aim to operate in the quasi-transpiration realm. This is defined as an effusion-cooled system with a sufficiently low TF. The TF for Courtis' pieces ranges from 0.36 for the E1 to 0.09 for the T2 as a function of the coolant flow rate [30]. The T2 features a minimum value of 0.035 [30]. Courtis considered this to be sufficiently low to be classified as quasi-transpiration [30].

1.2.3 Thermal Barrier Coatings

Figure 1.3 also illustrates the impressive capabilities of ceramics. Ceramic material, usually containing zirconium, is used as a thermal barrier coating (TBC) [33, 86]. TBCs are applied to the metal blade structure by applying a metallic bond coating at a thickness of 100-400 μm [33, 86]. The brittle ceramic is supported by the underlying structure. The high thermal tolerance and low thermal conductivity of TBCs make them an excellent choice to protect the metal from melting and oxidation [11, 33, 86]. In combination with the aforementioned cooling methods, a TBC enables a TET in excess of 1700 °C with bond temperatures below 1150 °C [33]. TBCs also offer a physical boundary against corrosion.

1.3 Double-Wall Effusion-Cooling

Figure 1.7 presents an approximate comparison of the overall effectiveness of individual and combination blade cooling methods. Blades that use both internal and external cooling methods allow the highest TET [47] at a similar cooling airflow. Increasing the flow rate without altering the design results in a minimal increase in overall effectiveness, with a

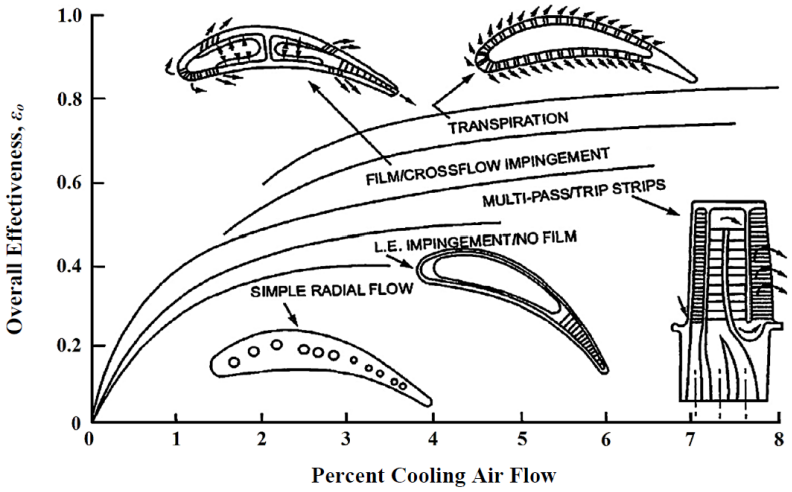


Figure 1.7: *theoretical cooling effectiveness for various methods of cooling, reproduced from [74]*

significant decrease in total cycle efficiency due to siphoning and later injection of coolant back in to the mainstream. The injection of cool, low-speed air in the turbine absorbs energy that would otherwise be recovered by the spinning blades. It was concluded that increased performance is best achieved with improvements in the implementation of cooling methods rather than the increase in the coolant flow. For these reasons, the double-wall effusion-cooled (DWEC) geometry shows promise.

The DWEC geometry is presented in Figure 1.8 for a mock blade segment. Key features are identified. The parallel or concentric walls, depending on the local curvature, are joined by pedestals. The impingement holes are located on the interior wall, and the film holes are located on the exterior wall. Coolant air first supplies impingement cooling to the interior surface of the external wall. The coolant circulates between the walls before exiting to create a film on the exterior surface. The pedestals act as pin-fins, churning the flow. They provide a conductive pathway between the walls and additional surface area for internal convection. The array of film holes on the exterior establishes a high film effectiveness and even coverage.

Extensive study in to the aero-thermal performance of the double-wall system for use in turbine cooling has been conducted [30, 37, 76, 79, 126]. Elstrop [37] and Murray [76] investigated predominantly flat plate geometries with internal configurations similar to Figure 1.8. Elstrop developed a low-order thermal model that relates various geometric parameters to a 1D heat transfer through the system [37]. Elstrop found that the geometry with an increased internal wetted area was most favourable for cooling [37]. The increase in

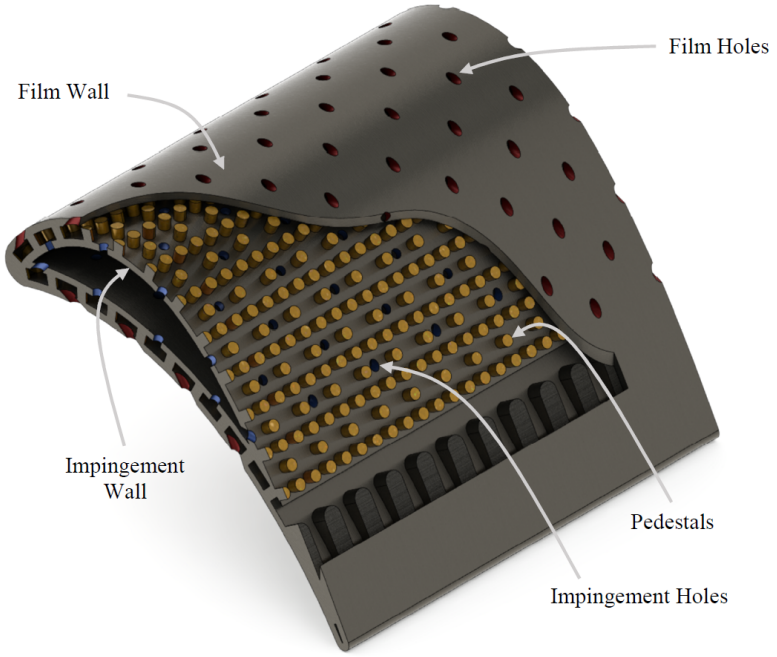


Figure 1.8: *example of a double-wall effusion-cooled blade segment, reproduced from [76]*

pedestal cross-sectional area for the 4S and Cross designs produced the greatest increase in wetted area [37]. Murray expanded on the original thermal model to develop a conjugate model for aerothermal performance. The conjugate model exhibited reasonable adherence to experimental results, although it was found that the Goldstein equation with a Sellers' superposition overestimates film performance in multiple-row effusion cooling geometries [76]. A corrected Goldstein equation was developed and is provided; see Equation (1.9).

Murrays' experimental work showed a high overall effectiveness [76] for the DWEC system, reported for several geometries in Figure 1.9. Murray also investigated how the overall efficiency varied with the internal geometry. Increasing the diameters of the film holes showed a marked improvement in the range studied [76]. An increase in pedestal diameter decreased overall effectiveness, although changes in pedestal height exhibited negligible influence, $< 1\%$.

Courtis, Ngetich, and Wambersie [30, 79, 126] studied methods to increase film effectiveness. Ngetich tested multi-row effusion geometries in a blade-representative geometry using diamond and circular pedestals. It was observed that large pressure gradients between the pressure and suction side of the blade result in significantly different blowing ratios between the two sides [79]. The result was a higher film effectiveness on the suction side. The suction

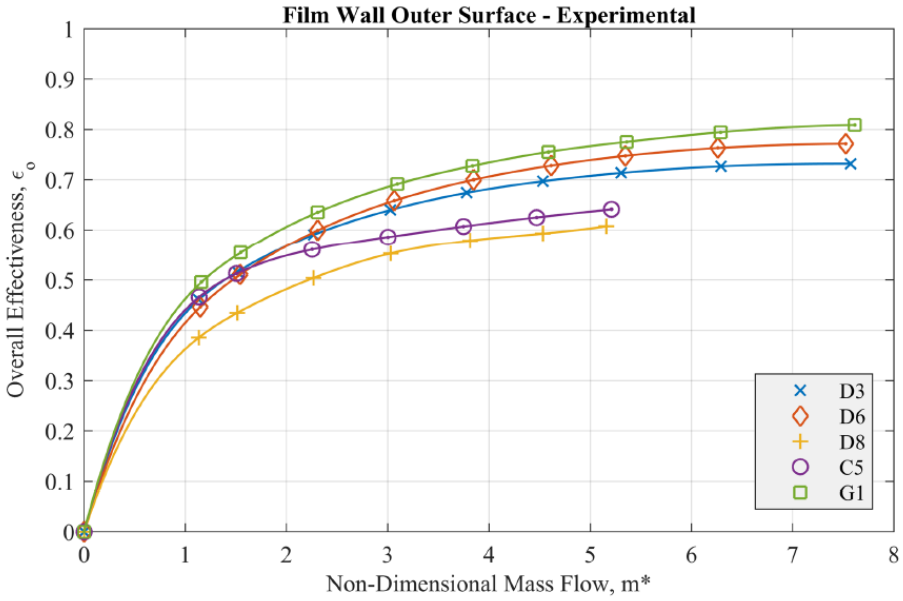


Figure 1.9: *overall effectiveness of various double-wall effusion-cooled geometries against coolant mass flow, reproduced from [76]*

side was also observed to have a higher film effectiveness than the pressure side for the same flow rate. At low mass flow rates, roughly 0.5-1.3%, more porous designs failed to produce a film [79]. At these extremes, the mainstream flow was ingested in to the DWEC system [79]. Ingestion proves challenging, as it leads to rapid overheating of nearby regions [11]. This problem was corrected with Wambersies' use of internal spars, which minimise migration and prevent ingestion [126]. Wambersie also developed modifications to the hot-wall by creating highly porous panels to achieve a 95% film effectiveness in some tests [126]. The effect is similar to the results shown in Figure 1.6 [30].

1.4 Project Motivation

There is a growing wealth of literature about the steady aerothermal and thermo-mechanical performance of DWEC geometries; however, a significant gap exists in the transient regime. Cyclic thermo-mechanical loading at engine temperatures presents a unique design challenge. Operational engine components should be able to withstand 2000-5000 hours of service [50, 93, 107], depending on the engine specifications. A detailed understanding of specific fatigue behaviour is imperative to ensure operational and safety targets are met.

Several studies on the origin of static stresses in DWEC geometries are readily available

[36, 37, 76, 100, 102, 103]. All indicate that the major stresses present in the system are attributed to a mismatch in thermal expansion between the internal and external walls, driven by a large thermal gradient. Local stresses around holes, pedestals, and fillets are determined using stress concentration factors (SCFs). This has been expanded further for transience and an-isotropy in selected blade materials [101, 104, 105, 106]. Preliminary results indicate that both the maximum temperature and the thermal gradient limit the lifespan. An increase in the former reduces the resistance of the material to plastic behaviour. An increase in the latter increases the stress state in the component.

There has been a considerable reliance on analytical and computational modelling for current results. While the quality of finite element solvers continues to increase, calibration of plastic and fatigue models to experimental results is required. The primary motivation of this work is to evaluate existing models and confirm or recommend changes based on adherence to physical experiments. The secondary motivation is to improve the overall design process. Modern design techniques involve substantial quantities of 'silo-ing', where various groups focus on a specific aspect of the blade: aero, thermal, or mechanical. This results in reduced communication. Errors identified by one group may propagate down the line, resulting in a significant waste of invested time and capital. This project aims to provide a methodology for rapid prototyping that bridges the silo gap and hopefully improves the design efficiency.

1.5 Achievements

The specific achievements of the work are set out below:

1. Design of a novel test article to ensure an engine-representative thermal loading was possible for transient ramping and quasi-steady holds. This was followed by an optimisation of the selected article to ensure that an exaggerated yet realistic stress distribution was generated and that failure did not occur outside the test region.

2. Development of an analytical model to explain the origin of stresses in the DWEC geometry. This was done to develop an understanding of how various geometric and thermal parameters affect failure.

3. Design and commissioning of an experimental facility to enable controlled thermal

cycling using select components from the existing Oxford Laser Heating Facility at the University of Oxfords' Thermofluids Institute.

4. Experimental evaluation of the effects of thermal cycling on developed double-wall effusion-cooled geometries, which examined a range of thermal loading conditions across different materials and geometries to establish a baseline for comparison of merit.

5. Development of a numerical modelling technique to determine appropriate finite element and elasto-plastic approaches for stress and lifespan prediction in relation to experimental results.

Review of Literature

The importance of TET in advancing the efficiency of the Brayton cycle has inspired a vast quantity of research. Established methods of turbine blade cooling were combined and optimised to construct a double-wall effusion-cooled (DWEC) geometry. This chapter presents and discusses the existing literature relevant to this work. This is done to add depth and context to the various approaches taken. An overview of common blade failures illustrates the relevance of low-cycle fatigue and the driving forces behind it. This leads to various analytical and numerical methods for estimating the stresses and life spans of engine components. A discussion of the nature of single-crystal alloys, a class of materials commonly used in turbine blade applications, is included. The chapter concludes with an overview of the literature relevant to the test platform, the design of which is set out in Chapter 5.

2.1 Common Failures in Turbine Blades

The general perception of exceptionally high reliability in aerospace components is, in part, attributed to strict regulations around the inspection of component wear [11, 26]. Routine exposure to large-amplitude mechanical and thermal loads severely limits the useful life of the component. First-stage nozzle guide vanes (NGVs) and turbine blades are among the most commonly replaced components in in-service engines [26]. Pertinent to this work is the multitude of failure methods in NGVs and turbine blades caused by these harsh thermal and mechanical conditions.

Foreign object damage is relatively rare in the turbine stage. The vast majority of the material ingested by the engine is ground in the fan and compressor stages prior to incineration in the combustor [11, 26]. Volcanic ash is an exception, as fine carbon particles are highly abrasive to components and prone to deposition on various surfaces [26]. Both phenomena threaten the aerothermal performance and effectiveness of cooling



Figure 2.1: *damage to first stage turbine blades cause by excessive thermal loading and corrosion, reproduced from [11]*

systems. For effusion cooling, the multitude of small holes is worrisome, as small patches of deposited material may cause a complete collapse of the cooling infrastructure. In addition to deposition, corrosion wear from sulphides and oxidation of the metal blade structure are extremely common [11, 26]. An example of corrosion leading to overheating and failure is provided in Figure 2.1. Rapid changes in thermal conditions also damage components. Thermal shock can result in cracked and detached TBCs [26]. Detached material may strike later-stage components, causing foreign object damage.

During long flights, high temperatures and large centrifugal forces in rotating components lead to creep damage. Most failures are avoided through routine inspection of the tip-clearance and overall blade length [26]; however, locally accumulated creep around micro-features may go unnoticed until failure. Modern blades use single-crystal super-alloys. This class of material offers substantial creep resistance in blades due to the mixture of various precipitates within a larger metallic structure [2, 35]. High heat fluxes through these materials can result in localised melting that redistributes precipitates [66]. This coarsens the matrix and reduces both the yield strength and the creep resistance of the blade [66].

Cycling failure is one of the most important considerations when evaluating blade performance. It is divided in to high-cycle fatigue (HCF) and low-cycle fatigue (LCF). HCF

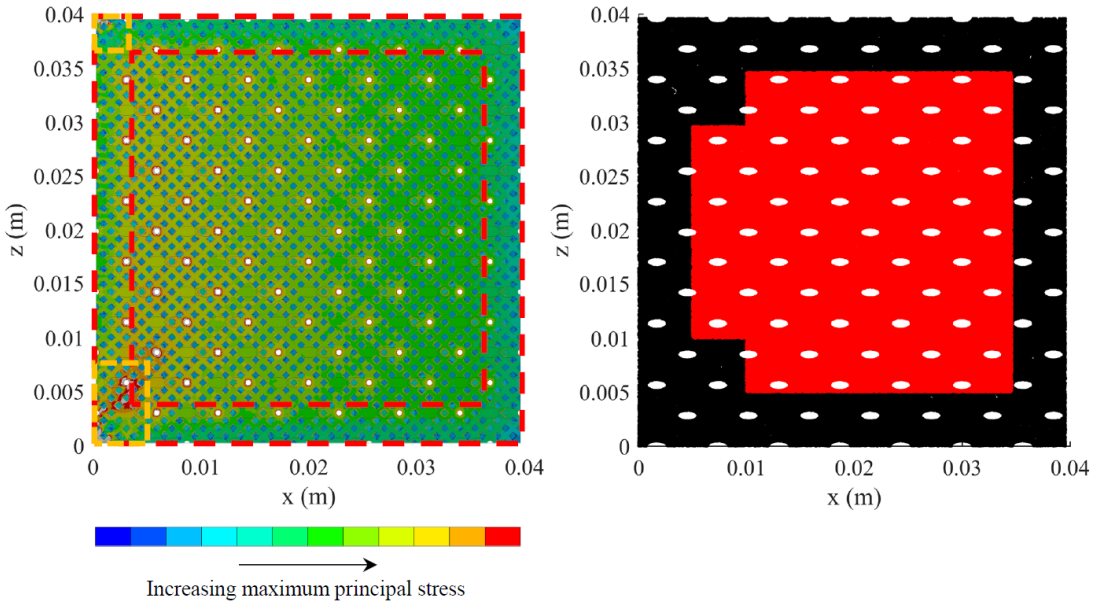


Figure 2.2: *left: stress results for a double-wall effusion-cooled system, reproduced from [76]; right: identification of stress region (red) that was unaffected by pinned corners to the left*

is most likely to occur due to rotational or aerodynamic instabilities or acoustic resonance within the blade [11, 26]. These are often dealt with by utilising an odd number of blades to reduce the harmonics of the disk [26]. Of importance for this work is LCF, which tends to impose a limit on the life of the components [26]. LCF is dominated by the flight cycle. A simple flight cycle consists of a combination of thermal and mechanical loads for start-up, hold, take-off, cruise, descent, landing, hold, and shut-down [10, 34]. The harshest loading occurs during take-off and landing with reverse thrust, when the engine is at full throttle [10, 34]. Cycling between the extremes of take-off and shut-down creates an accumulation of plastic wear, resulting in failure if left unchecked [26].

2.2 Stresses in a Double-Wall Effusion-Cooled Geometries

Evaluating LCF in components necessitates an understanding of the driving forces behind the stresses. Elstrop and Murray [37, 76] investigated the effects of simplified thermal distributions. Elstrop noted that stresses in the DWEC system are dominated by thermal expansion of the exterior wall [37]. They developed a heated strip structure based on Timoshenkos' general theory of bending a bi-metallic strip [37, 115]. Stresses arise due to the expansion demanded by the hot exterior skin and the resistance provided by the

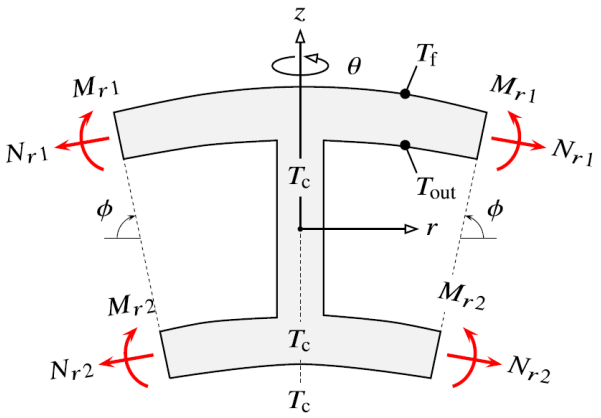


Figure 2.3: *domain used in the derivation of stress relations showing thermal and mechanical boundaries, reproduced from [36]*

cooler interior skin. It was noted that increased pedestal diameters resulted in lower system stresses as they carried additional force [37]. Murray applied the conjugate thermal field to a similar domain. An increase in pedestal height was reported to decrease the average von Mises stress, although the thermal difference between the walls was greater [76]. This trend was offset by high porosity in one geometry with a short pedestal height. Increasing the size of the film hole decreases the mean global stress, and increasing the size of the impingement hole leads to an increase [76]. This was thought to be due to the increase in film coverage and coolant flow rate, respectively. The latter generated a higher thermal gradient. In both works, the stress field within the DWEC system showed insensitivity to mechanical constraints at a distance greater than 2 'units' [37, 76]. The unit was defined as the smallest repeating block of the DWEC system. An example is provided in Figure 2.4.

A full analytical stress theory was devised by Elmukashfi [36] and Skamniotis [100, 101, 102, 103, 105] using the domain in Figure 2.3. The approach modelled nominal membrane stresses, defined as the stresses in each skin in the absence of additional features. Additional features include holes, pedestals, and fillets. Consistent with Elstrop and Murray, stresses were modelled as being directly proportional to the thermal gradient normal to the component. The pedestals were replaced with a kinematic constraint in which the interior surfaces of both walls were coupled. In the case of a flat plate, these must deform together and exhibit equal curvature. This was referred to as the periodicity constraint [36, 102]. It was idealised over a 2D domain derived from classical beam theory [81, 115]. It was extrapolated to 3D

with a scaling factor of $(1-\nu)$, assuming the stress state was equibiaxial.

The requirement for the periodicity constraint is that the walls must rotate by the same amount for small strains:

$$\kappa_{\mathrm{a}} = \kappa_{\mathrm{b}} = \kappa \tag{2.1}$$

Where κ denotes the curvatures of the exterior and interior walls, subscripts a and b, respectively. The membrane strains are also constrained such that:

$$\epsilon_{\mathrm{a}} = \epsilon_{\mathrm{b}} + \kappa \check{\mathrm{H}} \tag{2.2}$$

ϵ is the total membrane strains encountered in the centre lines of the walls, and $\check{H}$ is the distance between the centre lines, defined as $\check{\mathrm{H}} = \mathrm{H} + (\mathrm{t_a} + \mathrm{t_b})/2$ for wall thicknesses $\mathrm{t_a}$ and $\mathrm{t_b}$. Axial forces and bending moments must be in equilibrium and are governed by:

$$\mathrm{N_a} + \mathrm{N_b} = 0 \tag{2.3}$$

$$\mathrm{M_a} + \mathrm{M_b} + \mathrm{N_a}\check{\mathrm{H}} = 0 \tag{2.4}$$

Curvatures and strains were decomposed in to elastic and thermal contributions, resulting in a 4 x 4 system of equations to solve for each force and moment in the system. Rearranging the solution allows for the extraction of the geometric function, $\hat{\mathrm{G}}$.

$$\hat{\mathrm{G}} = \frac{\hat{\mathrm{t}}_{\mathrm{b}}^3 + \hat{\mathrm{t}}_{\mathrm{b}}^2 + 12\left(\hat{\mathrm{H}} + \frac{\hat{\mathrm{t}}_{\mathrm{b}}}{2} + \frac{1}{2}\right)^2 - 6\left(\hat{\mathrm{H}} + \frac{\hat{\mathrm{t}}_{\mathrm{b}}}{2} + \frac{1}{2}\right)}{\hat{\mathrm{t}}_{\mathrm{b}}^3 + \hat{\mathrm{t}}_{\mathrm{b}}^2 + 12\left(\hat{\mathrm{H}} + \frac{\hat{\mathrm{t}}_{\mathrm{b}}}{2} + \frac{1}{2}\right)^2 + \hat{\mathrm{t}}_{\mathrm{b}}^{-1} + 1} \tag{2.5}$$

Where each value is normalised by $\mathrm{t_a}$, the thickness of the external wall. The components for axial forces and moments were given by:

$$\begin{aligned}
\hat{\mathrm{G}}_{\acute{\mathrm{N}}_{\mathrm{a}}} &= \frac{1}{12}\frac{\hat{\mathrm{G}} + \hat{\mathrm{t}}_{\mathrm{b}}^3\left(\hat{\mathrm{G}} - 1\right)}{\hat{\mathrm{H}} + \frac{\hat{\mathrm{t}}_{\mathrm{b}}}{2} + \frac{1}{2}} \\
\hat{\mathrm{G}}_{\acute{\mathrm{M}}_{\mathrm{a}}} &= -\frac{1}{2}\hat{\mathrm{G}} \\
\hat{\mathrm{G}}_{\acute{\mathrm{N}}_{\mathrm{b}}} &= -\frac{\hat{\mathrm{G}}_{\acute{\mathrm{N}}_{\mathrm{a}}}}{\hat{\mathrm{t}}_{\mathrm{b}}} \\
\hat{\mathrm{G}}_{\acute{\mathrm{M}}_{\mathrm{b}}} &= \hat{\mathrm{t}}_{\mathrm{b}}\left(\frac{1}{2} + \hat{\mathrm{G}}_{\acute{\mathrm{M}}_{\mathrm{a}}}\right)
\end{aligned} \tag{2.6}$$

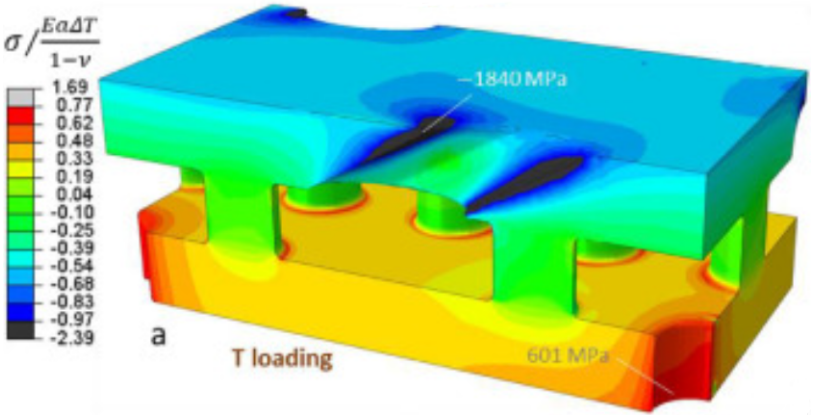


Figure 2.4: *representative stress state for a double-wall geometry under thermal loading showing large compressive stresses at the stream-wise extents of the inclined film holes, reproduced from [103]*

From classical beam theory, the nominal stress state is expressed using the superposition of the axial forces and moment contributions [81, 115]:

$$\sigma = \left(\hat{G}_{\acute{N}_i} + \bar{y}\hat{G}_{\acute{M}_i}\right) E\alpha\Delta T \tag{2.7}$$

Where i denotes which wall is being assessed, $\bar{y}$ is the dimensionless position in the wall, E is the Youngs' Modulus, α is the coefficient of thermal expansion, and ΔT is the thermal gradient through the exterior wall. This nominal stress field is scaled by a stress concentration factor (SCF) distribution to obtain the entire stress field. These SCF values were found numerically [100, 102, 103] and may be a function of both geometry and thermo-mechanical loading.

Analysis of the derived equations showed that a decrease in normalised interior wall thickness, $\hat{t}_b$, decreased the nominal stresses in the system [102]. This was most pronounced at low values of $\hat{H}$ for both the plane stress and axisymmetric cases [102]. Initial FEA investigations focused on the fillet between the pedestal and the exterior wall [100, 102]. The stresses were highest in this region in the absence of film holes. A decrease in t_b matched the model results for the nominal field as well as for the pedestal fillet stresses [100]. Similar trends were observed for $\hat{H}$. The increase in pedestal spacing was found to decrease the nominal stress field while increasing the SCF of the pedestal fillet [100].

Later analyses using realistic unit geometries were performed by Courtis [31] and Skamniotis [103]. A combination of thermal and mechanical loading was applied to the unit block.

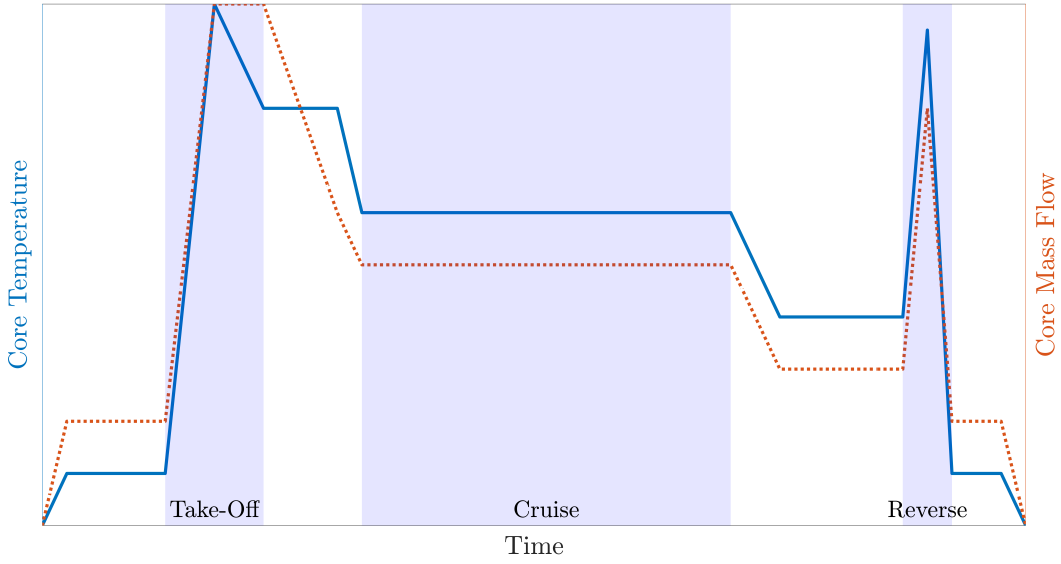


Figure 2.5: *example core temperature and mass flow for a typical civilian flight cycle*

It was concluded that LCF due to thermal and centrifugal loading stresses in cooling holes is of primary concern [31, 103]. The results for the case of pure thermal loading are presented in Figure 2.4. The magnitude of the fluid pressures was ignored due to the insignificant contribution [103]. Film holes were suggested to be critical for fatigue, as is evident in Figure 2.4. The presence of higher temperatures produced regions with unfavourable material properties. High-inclination holes built in to effusion cooling systems generated large SCFs [31, 103]. For purely thermal loading on a 60-degree inclined film hole, the SCF in the external acute wedge-vertex of the film hole was 4.57, roughly 2.54 times the pedestal fillet [103]. The SCF for the internal wedge-vertex was actually more significant, at 5.78; however, lower nominal stresses result in a reduced stress state [103].

2.3 Life Prediction Methods

Accurate prediction of component lifespan is crucial before a design enters service. Predicting LCF in turbine components is approached on a flight-cycle basis [6, 10, 34]. An example is provided in Figure 2.5. The flight profile may be simplified to two transient regimes for the heat-up and cool-down, which book-end a long quasi-steady hold [101] during the early design phase. This differs for military cycles, where ramp rates may be much higher

and cycles are more complex and mission-specific [34]. The actual stress states are often complex; however, they are often simplified and modelled as 1D in critical regions using the maximum principal stress [10, 101]. This enables comparison with uni-axial creep and fatigue data, assuming that $|\sigma_{\mathrm{p}}|_{\max} >> |\sigma_{\mathrm{p}}|_{\mathrm{med}}, |\sigma_{\mathrm{p}}|_{\min}$. The maximum principal stress is used to estimate the maximum principal normal strain range. This strain range enables estimation of the component life span based on available 1D experimental test data.

Cunha proposed a different formulation, using the stress and strain data to calculate the maximum shear stress for a critical point [34]. The thermal ratchet mechanism [22, 23] was applied to estimate the local strain. The fatigue life was then assessed by analysing each mission stage separately, using a Larson-Miller parameter for the corrected strain range. The number of overall cycles was calculated using a Miners' fraction rule to sum the creep and fatigue damage linearly [34]. A study was performed on a NASA Energy Efficient Engine blade [34, 114]. The results of Cunhas' method were in agreement with the original blade design life requirements [34, 114].

2.3.1 Low-Cycle Fatigue in Double-Wall Systems

Skamniotis [101] presented a similar method to estimate the number of cycles to crack initiation for a DWEC component for alternate boundary conditions to those described above. Differing from the initial derivation, a zero-total curvature constraint was used to constrain the system. This assumed that the DWEC system resists any thermal curvature with a fictitious reaction moment on the external wall [101]. The result was a system of equations that govern the thermo-elastic solution:

$$\begin{aligned} \kappa_{\mathrm{a}} = \kappa_{\mathrm{a,e}} + \kappa_{\mathrm{a,T}} \rightarrow \frac{\mathrm{M_a}}{\mathrm{EI_a}} + \frac{\alpha \Delta \mathrm{T}}{\mathrm{t_a}} = 0 \\ \bar{\epsilon}_{\mathrm{a}} = \bar{\epsilon}_{\mathrm{b}} \rightarrow \frac{\mathrm{N_a}}{\mathrm{Et_a}} + \frac{\alpha \Delta \mathrm{T}}{2} = \frac{\mathrm{N_b}}{\mathrm{Et_b}} \\ \mathrm{N_a} + \mathrm{N_b} = 0 \end{aligned} \tag{2.8}$$

This produced a stress field different from that described in Equations (2.5-2.7). The stress field on the exterior wall was exaggerated due to the extra imposed constraints. With no moment modelled for the internal wall, the stress field was governed only by the tensile force imposed by the expansion in the exterior wall. This model was extended to

include creep in the hot layer. With the reduced temperature, creep in the internal wall was neglected. To satisfy continuity, the creep was governed by [101]:

$$\begin{aligned} \int_{-\frac{t_a}{2}}^{\frac{t_a}{2}} d\sigma y dy - dM_a = 0 \\ \int_{-\frac{t_b}{2}}^{\frac{t_b}{2}} d\sigma dy - dN_a = 0 \end{aligned} \tag{2.9}$$

These equations were combined with the constituent strain relations from classical beam theory [81, 115] to relate the elasto-plastic stresses and strains in the walls.

Component life was estimated through the strain range $\Delta\epsilon$, a similar approach to Arvanitis and Cunha [10, 34]. Both constant strain and constant energy approaches were used to calculate the strain range. The constant strain approach assumed that the total strain in the absence of plasticity remains the same in the presence of plasticity [101]. The strain range was, therefore, governed by:

$$\Delta\epsilon = \frac{S}{E}; \tag{2.10}$$

Where S is the peak compressive stress magnitude, and E is the Youngs' Modulus. This is only valid when the elastic follow-up factor, Z [28], is at unity. Therefore, an alternate equation is offered that relates the plastic strain on heat-up, $\epsilon_{p,heatup}$, to the creep strain, ϵ_{cr}, and stress relaxation [101].

$$\Delta\epsilon = \epsilon_{p,heatup} + |\epsilon_{cr}| + \frac{|\sigma_3| + \sigma_{y0}}{E} \tag{2.11}$$

Where σ_3 is the stress state at the end of the creep dwell, and σ_{y0} is the yield stress at room temperature. The value is case-dependent, with 3 cases defined for various stress states. They are [101]:

1. The stress range, S, is below the room-temperature yield strength. This causes compressive plastic strain on initial cycles, with residual stresses gradually increasing due to the accumulation of strain. This ends when residual stress is constant, and the compressive stress is zero. This is known as elastic shake-down.

2. The stress range is between the room-temperature yield strength and the maximum

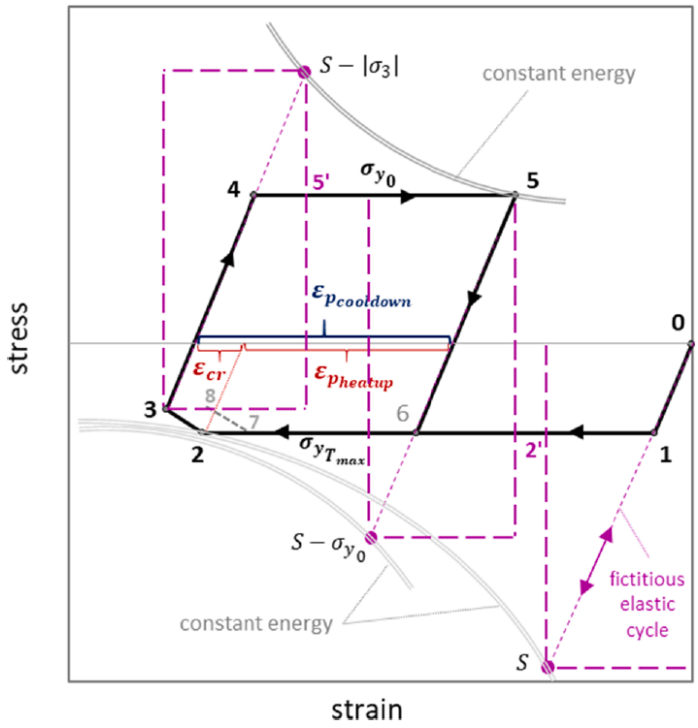


Figure 2.6: *stress-strain curves for a double-wall system modelled using a constant energy approach for the case where the stress range exceeds the maximum temperature-dependent yield strength, reproduced from [101]*

temperature-dependent yield strength, causing the accumulation of residual stresses to exceed the yield on cool-down. At a certain point, the creep strain equals the plastic strain at low temperatures. This is known as plastic shake-down.

3. The stress range exceeds the maximum temperature-dependent yield strength, causing plastic strain during the first heat-up and cool-down.

Skamniotis also considered the constant energy approach for a more conservative estimate of cycles to rupture [101]. The Neuber rule [78], which considers that the sum of the fictitious elastic strain and the complementary strain energy density, $\mathrm{E_{e_N}} = \frac{\mathrm{S}^2}{\mathrm{E}}$, is conserved. The Molski-Glinka approach [73] differs in that only the true strain energy density, $\mathrm{E_{e_G}} = \frac{\mathrm{S}^2}{2\mathrm{E}}$, is conserved. Equations were given to calculate the strain states that form the loop presented in Figure 2.6. The strain range was calculated using a simple trapezoidal heating, hold, and cooling cycle. The total strain range was given as [101]:

$$\Delta\epsilon = \frac{\mathrm{S}^2}{\mathrm{E}\left(\sigma_{\mathrm{y0}} + \sigma_{\mathrm{yT_{max}}}\right)} + |\epsilon_{\mathrm{cr}}| + |\epsilon_{e23}| \quad \text{(i)} \quad \text{Neuber} \tag{2.12}$$

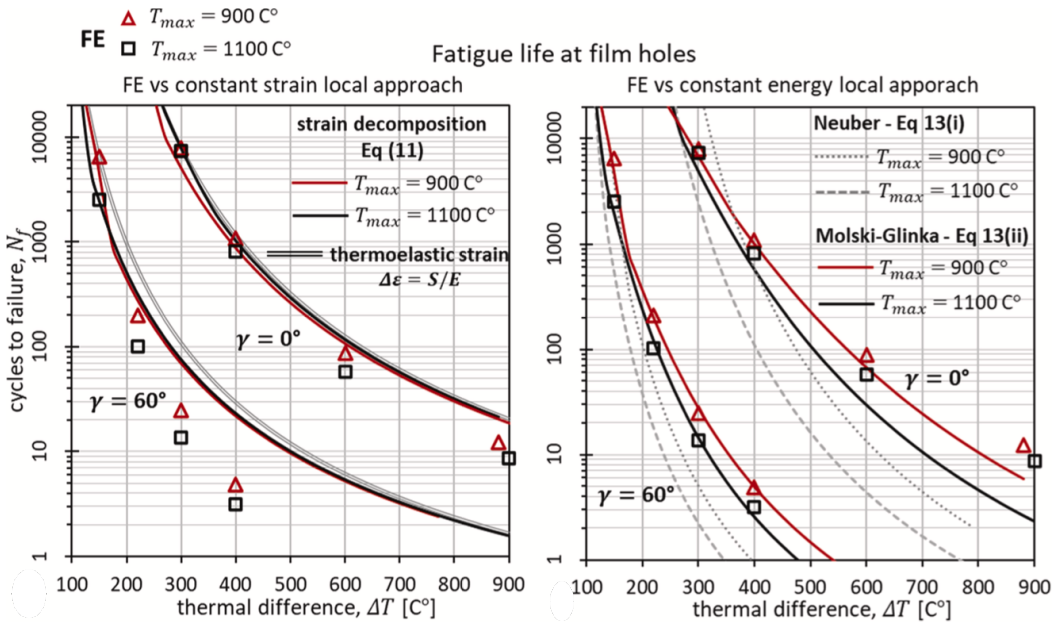


Figure 2.7: *comparison of selected models and approaches to estimating crack formation in double-wall effusion-cooled systems, reproduced from [101]*

$$\Delta\epsilon = \frac{\mathrm{S}^2 + (\sigma_{\mathrm{y0}} + |\sigma_3|)^2}{2\mathrm{E}\left(\sigma_{\mathrm{y0}} + \sigma_{\mathrm{yT_{max}}}\right)} + |\epsilon_{\mathrm{cr}}| + |\epsilon_{e23}| \quad \text{(ii)} \quad \mathrm{Molski-Glinka} \tag{2.13}$$

The fatigue life was estimated through a combined Basquins' and Manson-Coffin law, modified by Scholz to include dependence on temperature [12, 95, 101]. The number of cycles to crack initiation was determined through:

$$\Delta\epsilon = \mathrm{A}_1\left[\tau\left(\mathrm{C} + \log \mathrm{N_f}\right)\right]^{\mathrm{B}_1} + \mathrm{A}_2\left[\tau\left(\mathrm{C} + \log \mathrm{N_f}\right)\right]^{\mathrm{B}_2} \tag{2.14}$$

Where $\mathrm{A_i}$, $\mathrm{B_i}$ and C are material-specific constants and $\mathrm{N_f}$ is the number of cycles. τ is defined as: $\tau = \frac{\mathrm{T}+273}{1000}$ [95]. Skamniotis made the approximation that τ may be defined using the mean temperature, and the fatigue curve is independent within the ranges studied [101].

Several cycles were evaluated through FEA [101]. Simulated stress and strain data show adherence to all approaches, with certain strain range formulations better approximating each case test case. For the case of 60-degree inclined holes, the constant energy approaches align well. The Neuber method captured the cycle for the 150 °C difference, while the Molski-Glinka method captured the cycle for the 400 °C difference. A further comparison of approaches shows that the Molski-Glinka method accurately estimated fatigue life when

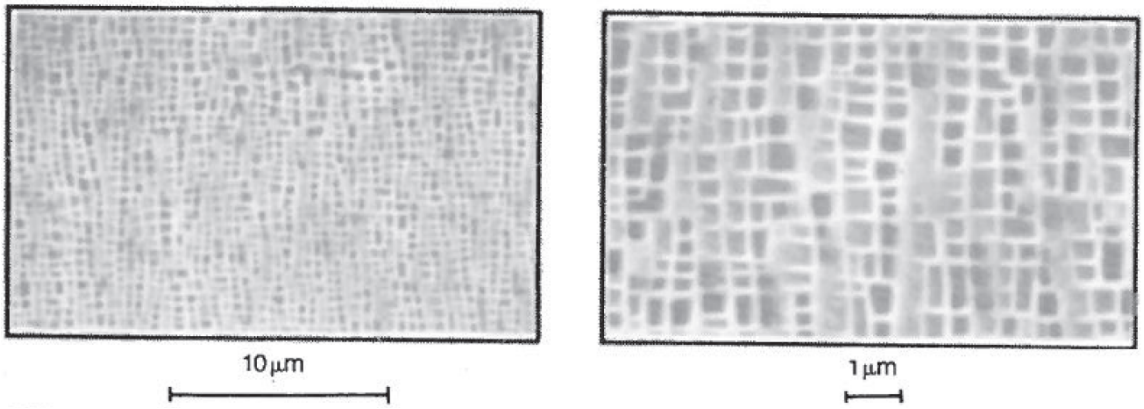


Figure 2.8: *scanning electron microscope imaging of CMSX-4 showing γ' precipitates, reproduced from [39]*

comparing the analytical system with FEA [101]. The results are presented in Figure 2.7. More broadly, a high film inclination limits the maximum thermal gradient through the component, and Skamniotis' opinion is that the use of such a high inclination should be done sparingly to prevent premature failure [101].

2.4 Single-Crystal Super-Alloys

The constituent materials are an important consideration when assessing the life-limiting aspects of any system. A history of increasing thermal and mechanical performance of NGV and turbine blades through the advancement of materials is presented in Figure 1.3. Modern blades utilise a class of materials referred to as 'super-alloys' [33, 39, 40, 66]. These are defined as metallic alloys that are capable of high mechanical performance near their melting point, where other materials exhibit a sharp drop. One such material is CMSX-4, commonly used in the hot sections of the engine [33, 39, 40, 66]. This is a nickel-based alloy that consists of an atomic matrix of nickel, called the γ-phase, with metallic precipitates throughout, referred to as the γ'-phase [33, 39]. SEM imaging is presented in Figure 2.8. It shows the square structure of the γ'-phase. CMSX-4 has a γ'-phase volume content in excess of 65% [21]. These precipitates are adverse to molecular dislocations and provide increased creep resistance at elevated temperatures[39]. In addition, tungsten and cobalt are added to increase corrosion resistance and strength, respectively [39]. CMSX-4 offers low corrosion penetration, high stress-rupture properties at temperatures in excess of 950 °C, and is resistant to 'freckle' formation [40]. Freckling occurs when the crystal grain is

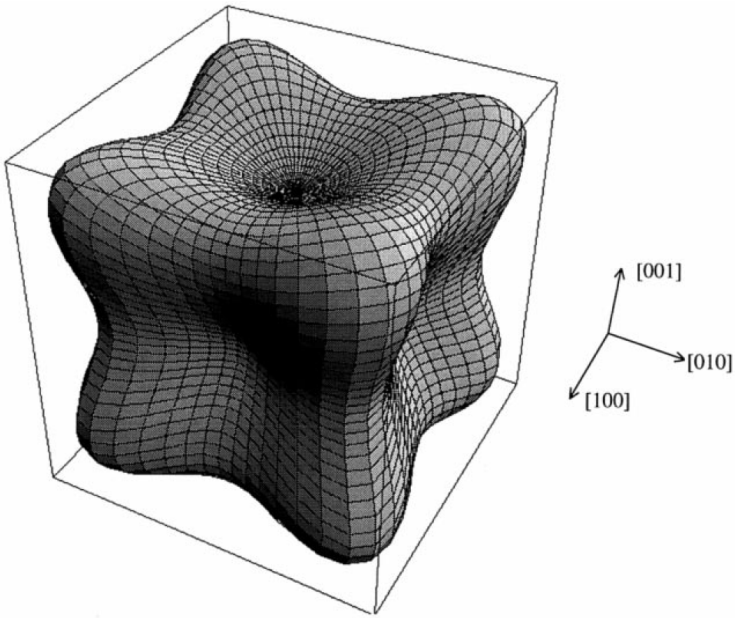


Figure 2.9: *relative Youngs' Modulus variation with crystallographic orientation, displaying a large anisotropy between the* $< 001 >$ *and* $< 111 >$ *directions, reproduced from [99]*

distorted at the metal-mould boundary during casting.

The strongest super-alloys are those cast as single-crystals. These are grown in a mould. Careful extraction from a furnace allows the material to solidify slowly. The crystal grows from one end, usually from a seed crystal or a pigs-tail device, which orients the crystal in the correct direction. CMSX-4 is a second-generation single-crystal super-alloy [39, 61]. It has a primary, $< 001 >$, and two secondary, $< 010 >$ and $< 100 >$, directions [99]. Single-crystals are inherently anisotropic. CMSX-4 has an anisotropy factor of 2.85 [99]. This means that the ratio between the minimum Youngs' Modulus, in the $< 001 >$ direction, and the maximum Youngs' Modulus, in the $< 111 >$ direction, is nearly three. A representation of this is provided in Figure 2.9. This anisotropy necessitates the use of Hills' modification to the von Mises criterion when evaluating yield [35]:

$$f^2(\sigma) = F(\sigma_{22} - \sigma_{33}) + G(\sigma_{33} - \sigma_{11}) + H(\sigma_{11} - \sigma_{22}) + 2L\sigma_{23} + 2M\sigma_{31} + 2N\sigma_{12} \quad (2.15)$$

Where σ_{ij} denotes the normal and shear stress state. F, G, H, L, M, and N were defined as cyclic permutations of the following equations. Dye et al. defined R_{ii} and R_{ij} as 2.45 and

4.24, respectively, for CMSX-4 [35].

$$F = \frac{1}{2}\left(\frac{1}{R_{22}^2} + \frac{1}{R_{33}^2} + \frac{1}{R_{11}^2}\right) \tag{2.16}$$

$$L = \frac{3}{2R_{23}^2} \tag{2.17}$$

The thermal properties are favourable, with the diffusivity showing a primary dependence on temperature, regardless of treatment and manufacture [2]. It has a high melting point with a solidus temperature at 1336 °C and a liquidus temperature of 1397 °C [2]. The spectral emissivity of CMSX-4 is also beneficial to this work as it is relatively high. High emissivity, given Kirchoffs' law of radiation, lends to a high rate of absorption of incoming light, since the two are equivalent at equilibrium. At 650 °C, the emissivity is approximately 0.85 [3]. This decays to a minimum value of approximately 0.8 at 875 °C and remains constant to 1050 °C. Cyclic and static fatigue tests in the principal and secondary directions showed that the lifespan increased significantly for the principal direction above 950 °C [21]. Furthermore, below 950 ° C, a Larson-Miller parameter of 20 did not offer the best adherence [95]. Instead, the fit was best achieved using a Larson-Miller parameter of 14.07 [21]. A full accounting of material properties is provided in Appendix II.

Single-crystals optimised for flight have the primary direction aligned with the blade span, as this direction has the highest creep resistance [39]. The two secondary directions often have a random orientation in a plane perpendicular to the primary direction. Skamniotis [105] determined that the orientation of the secondary direction plays an integral role in determining the location and magnitude of peak stresses in a DWEC system. Each crystallographic direction has a different elastic Modulus and creep behaviour. As such, the location also dictated the magnitude of local stresses and the type of plastic-creep slip activity [105]. The orientation of the secondary directions is often not determined, given the historical impression that they are not particularly important. Skamniotis showed that the assumption of using the $< 001 >$ direction to determine fatigue characteristics is not adequate [105]. The maximum stress can increase by up to 81% based on the orientation of the secondary directions [105]. This is of primary concern around the film hole wedge, as the crystallographic direction may differ locally as the crystal curves around features.

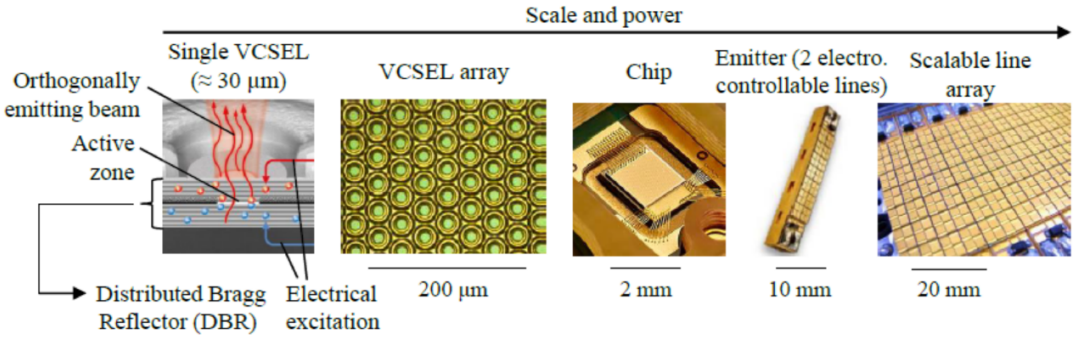


Figure 2.10: *vertical-cavity surface-emitting laser components and architecture at various length scales, reproduced from [127]*

2.5 Energy Supply Methods

Achieving consistent and reliable thermal conditions is crucial to thermo-mechanical fatigue (TMF) testing. The use of lasers as a thermal energy source offers improved performance in comparison to traditional alternatives. The applications for ion beams [44, 45, 69, 90], hot gases [70], resistance heaters [48, 72, 98] and laser radiation [68, 91, 127, 128, 129] have been well studied. The latter offers compatibility with a broad range of materials and predictable and easily tunable power settings [64]. Crucially, it enables the use of an open cooling loop for tested components.

The optimal configuration for large-area supply is vertical-cavity surface-emitting lasers (VCSELs). These are relatively small emitters that are capable of being densely packed in to arrays. An example of the system architecture of a VCSEL array is presented in Figure 2.10. VCSEL arrays offer 12 or 24 controllable zones for the 2.4 kW and 4.8 kW models, respectively, adding the benefit of spatial control [89]. Together, VCSELs are the clear choice for a heat flux facility.

For modelling purposes and at large distances, the distribution of a single VCSEL may be extended to the entire emitting surface and scaled to the fractional power output [88]. The angular distribution of a singular VCSEL is governed by:

$$\mathrm{I}(\psi) = 1892\frac{\mathrm{W}}{\mathrm{sr}}\left[\mathrm{e}^{-\left(\frac{\psi}{4.345^\circ}\right)^2} - 0.9532\mathrm{e}^{-\left(\frac{\psi}{4.000^\circ}\right)^2}\right] \tag{2.18}$$

Where ψ is the angle from normal, and the coefficients were determined experimentally [88].

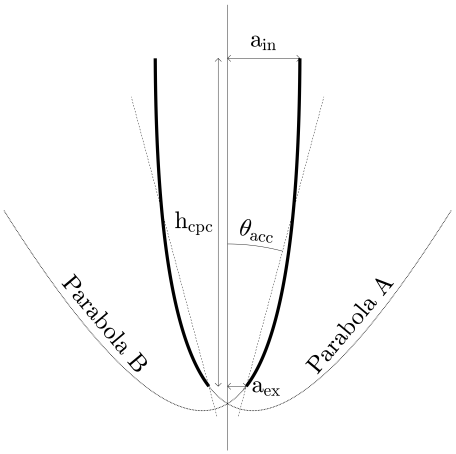


Figure 2.11: compound parabolic concentrator shape and key features

2.6 Compound Parabolic Concentrators

Heat flux analysis in gas-turbine applications requires a capacity of up to 5 $\frac{W}{mm^2}$ [96]. This requirement is only increased for VCSELs when the fractional absorption of incident light decreases from unity. A reliable method to increase incident power is a compound parabolic concentrator (CPC). A CPC is a non-imaging optical device that utilises truncated parabolic surfaces to reflect and focus incoming rays in the exit aperture [29, 41, 71, 96]. They are commonly employed in solar applications to focus and increase the incident power of the sun [41, 96]. Alternatives, such as conical or triangular concentrators, may be used; however, the highest theoretical efficiency is attained by the CPC [130]. The defining characteristic of a CPC is the geometric parameter, C: the concentration ratio.

$$C = \frac{a_{in}}{a_{ex}} = \frac{1}{\sin\theta_{acc}} \tag{2.19}$$

Where a_{in} is the characteristic-length of the inlet aperture, a_{ex} is the characteristic-length of the exit aperture, and θ_{acc} is the acceptance angle. An example is provided in Figure 2.11. θ_{acc} is defined as the threshold at which an incoming beam is likely to be rejected due to the CPCs' inability to focus it to the exit aperture [29, 41, 96, 130]. It is defined this way as, while it is theoretically possible for all light to pass through at or below the acceptance

angle, scatter due to material properties and surface defects must be taken in to account [29]. The shape of a 2D section of the reflecting surface is defined by [96]:

$$\begin{cases} x_{cpc} = a_{ex}\frac{1-\cos(t_{cpc}+2\theta_{acc})+2\sin(t_{cpc}+\theta_{acc})}{\cos(t_{cpc})-1} \\ y_{cpc} = a_{ex}\cos\left(t_{cpc}+\theta_{acc}\right)\frac{1+\sin(\theta_{acc})}{\sin^2\left(\frac{t_{cpc}}{2}\right)} \end{cases} \quad \text{and} \quad \frac{3\pi}{2}-\theta_{acc} \leq t_{cpc} < 2\left(\pi-\theta_{acc}\right) \quad (2.20)$$

Where t_{cpc} is a parameter defined to simplify and constrain the curve of the reflecting surface during the derivation of the curve equations. Doing so simplifies the trigonometric terms generated through the rotation of a parabolic surface using a standard 2D rotation matrix. The design of a traditional CPC requires only the desired exit aperture dimension and acceptance angle. The constraint placed on the inlet dimension by Equation (2.19) is reflected in the curve equations.

The theoretical efficiency for the CPC is commonly derived for the axisymmetric case [41, 130]. Equation (2.20) is revolved around the neutral axis. The manufacture of this shape is undoubtedly a challenge. Most applications opt for a trough or polygonal cross-section due to the feasibility of manufacturing and the application requirements [29, 41, 96, 130]. Cooper [29] categorised the efficiencies for a uniform diffuse light source at the inlet for a range of polygonal cross sections. Cooper found that the optical efficiency, η_{opt}, is a function of the acceptance efficiency, η_{acc}, the effect of scattering due to surface imperfections, K_{err}, and the reflectance of the optical surface, ρ [29].

$$\eta_{opt} = \eta_{acc}K_{err}\left(\rho\right)^{n_r} \quad (2.21)$$

Where n_r is the average number of reflections of a transmitted ray. Each of the terms in Equation (2.21) was determined by fitting to the experimental data. Cooper found that higher-order polygons display higher efficiency, with the limit of $n_{polygon} \to \infty$ equal to the axisymmetric case [29]. The exception was for the square CPC at acceptance angles less than 15 degrees. This is due to a combination of increased acceptance efficiency and reduced scattering relative to other more complex shapes. The observed transmission results are presented in Figure 2.12.

Altering the parametric equation for the reflecting surface was also shown to increase the acceptance and optical efficiencies of CPCs [71]. Altering the profile by a variable offset

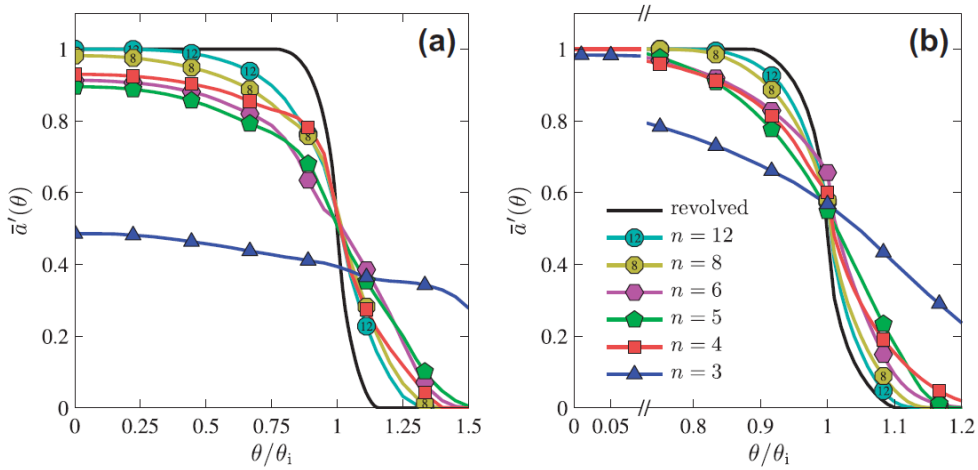


Figure 2.12: *transmission curves for various polygonal compound parabolic concentrators for acceptance angles of (a) 5 degrees (b) 30 degrees, reproduced from [29]*

perturbation, spline increased the optical efficiency of an axisymmetric CPC by over 2%. The optimal shape of the CPC was observed to be highly case-dependent, and the nature of the incident light plays an important role in determining the optimal shape [71]. A similar result was shown by Schwartz, in which the final output flux was highly variable as a function of the light source and overall shape [96].

2.7 Summary

Blade damage caused by chemical and thermal wear is typical [11, 26], with LCF driven by thermal cycling limiting the service life of many hot-section components. Theoretical approaches to studying and quantifying stresses in these systems are numerous [31, 36, 37, 76, 100, 101, 102, 103, 104, 105, 106]. The stresses in a DWEC system are driven by the thermal gradients imposed between the walls [36, 37, 102]. The exterior wall expands and is resisted by the cooler interior wall. The elevated temperatures and high SCF present near the film holes result in the greatest compressive stress magnitudes [31, 101, 103, 104] and lowest creep resistance. These represent the life-limiting areas of the DWEC system due to the accumulation of elastic and plastic strain [101].

Both the DWEC geometry and the single-crystal material are intricate, adding a degree of complexity to the analysis. The anisotropic nature of CMSX-4 alters the properties of the material depending on the crystallographic orientation [99, 104]. This creates regions of

complex interactions with intricate 3D geometry features. Modelling and estimating the life span in such situations is possible [10, 34, 66, 101, 106]; however, physical experimentation is required to validate and calibrate existing models. This is primarily due to the lack of data on local multiaxial creep. Existing modelling has relied on uni-axial creep-fatigue data [101], which does not fully capture the stress state nor slip systems present in the γ and γ'-phases.

The VCSEL is a clear choice to supply a thermal load to components [64]. They offer increased spatial control, high temperatures and heat fluxes, and do not require specific materials or conditions in which to operate [64]. To complement the VCSEL system, CPCs are to be used to direct and concentrate the laser power to achieve sufficient heat flux values at the outlet aperture. A square polygonal CPC exhibits high efficiency at low acceptance angles [29]. Altering the parametric equation for the shape of the reflecting surface may also improve the efficiency of the system [71].

Design of a Double-Wall Effusion-Cooled Test Section

The design of a test article for thermo-mechanical fatigue (TMF) testing was achieved through a balance of several competing criteria. Feasibility of manufacture, the degree to which the thermal and stress fields at steady-state were engine-representative, compatibility with instrumentation, and the experimental procedure were all considered. Numerous designs were conceived and evaluated, each presenting various degrees of feasibility across all design points. This chapter presents the four designs that best satisfied the initial requirements: the Tensile Adapted (TA), Concentric Flat (CF), Flat Plate (FP), and Floating Flat Plate (FFP) articles. Of these, the FFP was selected as the preferred geometry due to its representative thermal and stress state [102]. Following this, a mechanical field optimisation study was conducted to reduce stresses outside of the central test section. This was done to ensure that the failure occurred on the exterior surface of the article in a region easily observed during thermal cycling. This chapter concludes with a discussion of the final design, associated variants, and the selection of materials and manufacturing processes.

3.1 Requirements and Considerations

1. **The maximum test article dimensions were constrained to a cylinder no larger than 100 mm in diameter and no more than 200 mm in length.** Test articles were to be produced through casting or additive manufacturing. Both methods limited the maximum size; however, the constraints placed on the final design by the available casting furnace were the most extreme.

2. **The centre of the article was to be flat as to enable compatibility with vertical-cavity surface-emitting laser (VCSEL) arrays.** They offer better

performance than electron-beam devices across a far greater range of materials [44, 45, 64, 69]. VCSEL arrays also do not impact the exhaust gas flow, unlike an acetylene flame or an equivalent [64, 70]. Utilising a light source for heating presents a unique problem: the angular dependence on absorption. Utilising a flat target surface mitigates this. This ensured the heat flux and, therefore, the temperature of the external wall were as even as possible.

3. **The test article and surrounding facility were to be capable of routine disassembly and reassembly for high-resolution imaging of the test article during testing.** The detection of experimentally generated cracks was central to this work. Removal after a set number of cycles for either digital single-lens reflex or computed tomography images was necessary to both detect crack initiation and track crack growth rates and patterns.

4. **Both sides of the test article were to contain either a groove for an embedded thermocouple or have an unobstructed line-of-sight for non-contact temperature measurements.** The thermal distribution normal to the test article exterior was prioritised as the result of the flat plate work conducted by Skamniotis [100, 101, 102, 103, 105]. He showed that the nominal stresses are proportional to the total thermal difference between the temperature at the outer surface of the outer wall and the outer surface of the inner wall. This result may be scaled by stress concentrations to obtain the local distribution around holes, pedestals, and fillets. Monitoring of the temperatures on the hot- and cold-walls was paramount to ensure the correct stress field was achieved during testing. It also enabled comparative finite element analysis (FEA). Direct comparison between the stress fields of both the test article and the infinite flat plate was also preferred.

5. **The steady-state thermal and stress fields in the central test section should independently capture features around critical locations, as identified in prior work.** The truncation of the domain risked imposing strict displacement or rigid boundary constraints, altering the stresses present [37, 115]. It was necessary to consider using novel features to ensure the stress fields are reproducible and uniform, with a dependence on the maximum temperature and the thermal gradient through the

hot-wall. Some deviation was acceptable as the root and tip of a blade will constrain the displacement, resulting in an actual blade stress field that differs from the flat plate [102].

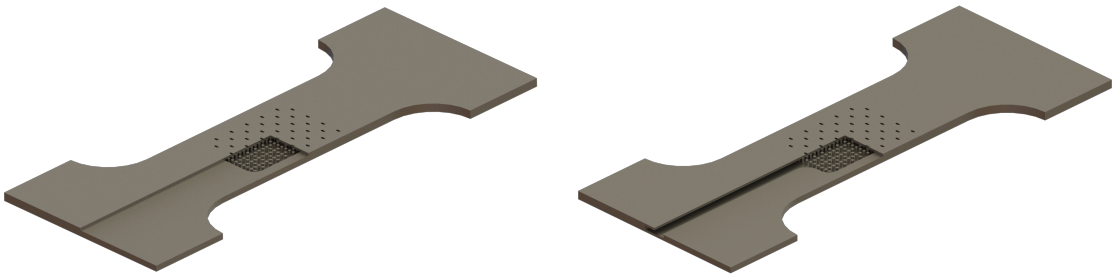
6. **Internal feature selection was to be chosen such that the chance of developing a detectable crack within 200 cycles is maximised** It was not feasible to test each sample for the few thousand hours required to reach failure in modern blades at engine conditions [11, 32, 93]. There were two options to decrease the time to failure: exaggerate the thermal field and select internal features to maximise stress concentrations.

Dimension	Value	Unit
t_a	1.00	mm
$\hat{t}_b$	1.00	-
$\hat{H}$	1.50	-
$\hat{L}$	1.00	-
$\hat{D}$	1.00	-
$\hat{\rho}_{pd}$	0.10	-
$\hat{\rho}_h$	0.05	-
θ_{fh}	60	deg

Table 3.1: *selected dimensions for the double-wall effusion-cooled region of the proposed test articles*

3.2 Geometries and Accompanying Tests

The internal geometry of the test article was selected to promote rapid failure at the intersection of the film hole and the exterior of the hot-wall, referred to as the film hole wedge (FHW). The values reported in Table 3.1 are normalised by the thickness of the outer skin, t_a. A 60-degree inclined hole produces a stress concentration factor of 4.5 [103], nearly 2.5 times that of a transverse hole. The remainder of the dimensions were selected to ensure that failure will occur on the hot-wall of an infinite plate [103]. It was found that 60 degrees is an upper limit on the inclination of the holes for this geometry. The fillets surrounding the projected ellipse, caused by the intersection of the film hole and the inner surface of the hot-wall, began to overlap with the neighbouring pedestal fillets. As a result, the local



(a) (b)

Figure 3.1: *renderings of (a) tensile-adapted test article (b) side-fed variant*

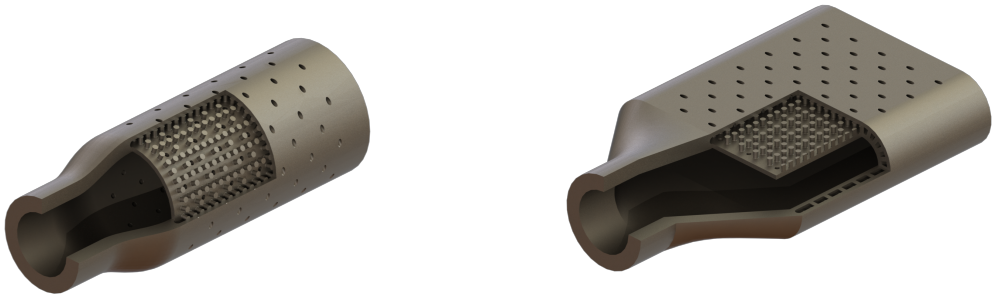
stress state exceeded that in the FHW. This internal geometry was consistent across the following proposed test articles.

3.2.1 Tensile Adapted

The test articles in Figure 3.1 mimic a shape commonly used by tension test specimens [16] and measure 200 mm x 80 mm x 3.5 mm, which is why it is named 'Tensile Adapted'. The test article was to be placed in hinged grips to minimise the boundary constraint. The primary benefit of this design would be the ability to add combined thermal and mechanical loading for blade-representative testing. The TA article features a flat central test section compatible with VCSEL arrays.

Most of the design requirements were met by the TA article in Figure 3.1 (a). The challenge arose with the thermal field. Achieving the correct thermal distribution requires that the coolant air enters through the impingement holes, circulates, and is exhausted through the film holes [76]. The TA article would require either a built-in coolant plenum or individual coolant feeds to each hole. The former renders the design a triple-walled system, altering the stress field. The latter requires an unnecessary degree of complexity due to the small feed lines and attachment points, which required threading. The interactions between threaded components would be challenging to model, resulting in concern about the accuracy of the predictions.

The proposed solution, shown in Figure 3.1 (b), was to remove the impingement holes. Coolant was to be fed through the side of the test article, allowing it to circulate and exhaust. A large jet of coolant would impinge on the rear side to further increase the cooling capacity.



(a) (b)

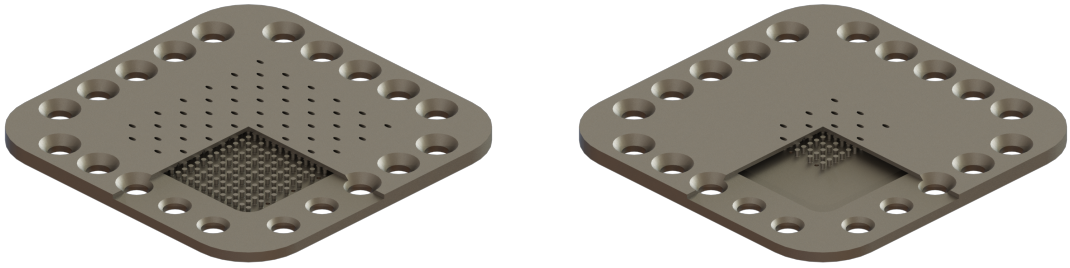
Figure 3.2: *renderings of (a) concentric-cylinder test article (b) flattened variant*

This design did not take advantage of the impingement cooling provided on the internal surface of the hot-wall.

3.2.2 Concentric Cylinder

Supplying coolant to one-sided, or open, test articles is a challenge. A closed 3D shape, such as a blade, confines the fluid without requiring additional features. The Concentric Cylinder (CC) article, pictured in Figure 3.2 (a), would have made use of this with a simplified cylindrical geometry, measuring 78.5 mm x 29 mm x 29 mm. The constant stream-wise curvature and relatively long span would allow for a theoretical comparison with the hoop constraint proposed by Skamniotis [100, 102]. The CC article would exhibit analogous root- and tip-effects with the threaded mounting and end-cap constraining deformation. With no flat side, energy was to be supplied using an induction coil [98].

There were two significant concerns about the design: the removal of the mould and support material from manufacturing and the accessibility to measurement devices. The former required the CC article to be manufactured as two pieces before being joined. The film and impingement holes were not sufficient for material removal, and larger channels had to be provided. Having a joint between the central test region and a constraining body was a cause for concern as this would create a weakened region that may fail prematurely. The joined region would be subject to significant shear and moment-driven normal stresses [102, 103]. With no line-of-sight, a pyrometer was to be swapped with a thermocouple for the cold-wall measurement. Correctly placing and adhering to the device would be challenging,



(a) (b)

Figure 3.3: *renderings of (a) flat plate test article (b) floating flat plate test article*

having to be done through the threaded mounting. A feed-through in the supply line was required to connect to a data acquisition (DAQ) system.

A variant with two parallel flat sections was proposed to better capture the stresses present in a flat plate. The CF article in Figure 3.2 (b) has the same benefits as the CC article. It measures 83.5 mm x 52.25 mm x 16.25 mm and is also compatible with a VCSEL energy source. As the effects of the surroundings are minimised within 2-3 rows of pedestals [76], the central test section exhibits flat-plate behaviour. This allows for a direct comparison to the theory and the alternate proposed test articles.

3.2.3 Flat Plate

Closed test articles provide a set of unique challenges with respect to measurements. Embedding measurement devices within the geometry inhibits efficient rapid prototyping, as a multitude of cables and couplings increases the potential for faults and delay. Multiple loading and cooling systems increase the opportunities for failure and add an unnecessary degree of freedom for fine-tuning. The FP test article was designed with simplicity in mind. It would be mounted to a coolant plenum via a flange-type connection, identified by the large holes around the exterior in Figure 3.3 (a). It was 85 mm x 85 mm x 3.5 mm and was compatible with a VCSEL.

The primary concern was the mechanical constraint placed on the system by mounting it to a plenum. Modelling the boundary as rigid was estimated to add a uniform compressive

shift to the central region stresses as the thermal expansion would be resisted. The effects of rigid boundary conditions are known to decrease significantly within two rows of pedestals [76]. The two phenomena were thought to establish a representative stress field in the centre with exaggerated compressive stresses on the exterior of the hot-wall.

An alternate design, shown in Figure 3.3 (b), featured the same base geometry as the FP article. The FFP sought to improve the stress field by minimising the mechanical constraints imposed by the boundary through the addition of a 'floating' region. It was hypothesised that the decoupled deformation allowed the floating region to mitigate the effects of uneven heating on the hot-wall, creating regions of high stresses outside of the central test region. A compressive shift was still predicted; however, it was thought to be reduced relative to the FP article.

3.3 Selection of Preferred Geometry

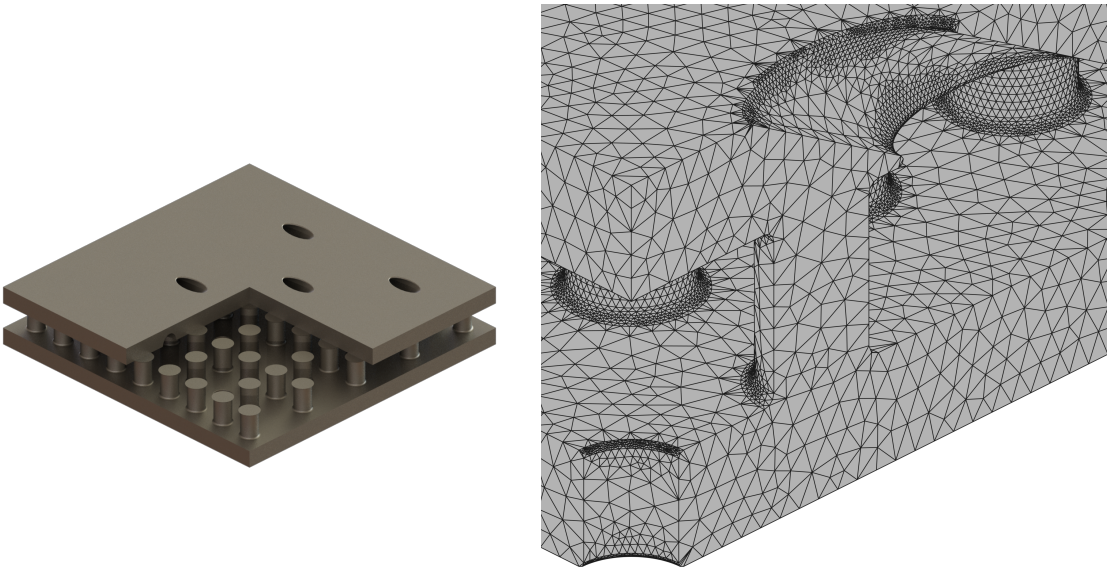
A numerical evaluation of the TA, CF, FP, and FFP geometries was conducted in Ansys Mechanical[1]. The aim was to determine mechanical performance as a function of the test article, controlling for thermal loading. All features - holes, pedestals, and fillets - were included. The maximum absolute principal stresses, $\max\left(|\sigma_1|, |\sigma_2|, |\sigma_3|\right)$, were used to identify areas prone to plastic deformation and crack initiation [20, 115].

3.3.1 Domain and Boundary Conditions

The geometries in Figures 3.1-3.3 were used as the domains. The central test region is sectioned as a separate body for later analysis. It was stitched to the peripheral geometry using Ansys DesignModeler[2] was used to share the topology for meshing and solution.

The thermal boundary conditions and material properties were kept consistent with Skamniotis [102]. A surface temperature of 727 °C was imposed on the outer surface of the hot-wall. Both the interior surfaces and the exterior of the cold-wall were set at 27 °C. These were both defined in a 32 mm x 32 mm square, chosen to represent an approximate size of the VCSEL-heated region following beam concentration. A full explanation of the choice of dimensions is offered in Chapter 5. The initial temperature of the system was 27

[1] Ansys®Academic Research Mechanical, Release 19.2
[2] Ansys®Academic Research DesignModeler, Release 19.2



(a) (b)

Figure 3.4: *(a) double-wall effusion-cooled geometry used in the mesh-independence study with a cut-away on the hot-wall to show internal pedestal geometry (b) coarse surface-mesh showing refinement around fillets*

°C. Values for CMSX-4 at 527 °C were used: E = 120 GPa, $\nu = 0.3$, $\alpha = 1.2 \times 10^{-5}$ $\frac{1}{°C}$, and k = 14 $\frac{W}{m°C}$ [102]. The full crystallographic orientation of CMSX-4 in final test specimens was unknown due to a lack of control during manufacture. For this reason, this analysis assumed elastic isotropy throughout the domain.

The mechanical boundary conditions differ according to the test article; however, a consistent orientation and coordinate convention was used. x was defined as the stream-wise direction, aligned with the film hole inclination and pointed downstream. y was defined as normal to the hot-wall and was pointed away from the test article. z followed the right-hand rule and was in the span-wise direction. This convention is consistent throughout this work. The TA article was first constrained by setting a remote boundary condition on the two faces farthest from each other along its length (opposite z-normal faces). These faces were fixed in all three axial dimensions. Another remote displacement condition was applied, allowing for free x-rotation and constraining the remaining degrees of freedom. The CF article was rigidly constrained on the threaded face. The FP and FFP articles were rigidly constrained on the vertical (y-direction parallel) and chamfer faces of the large mounting holes.

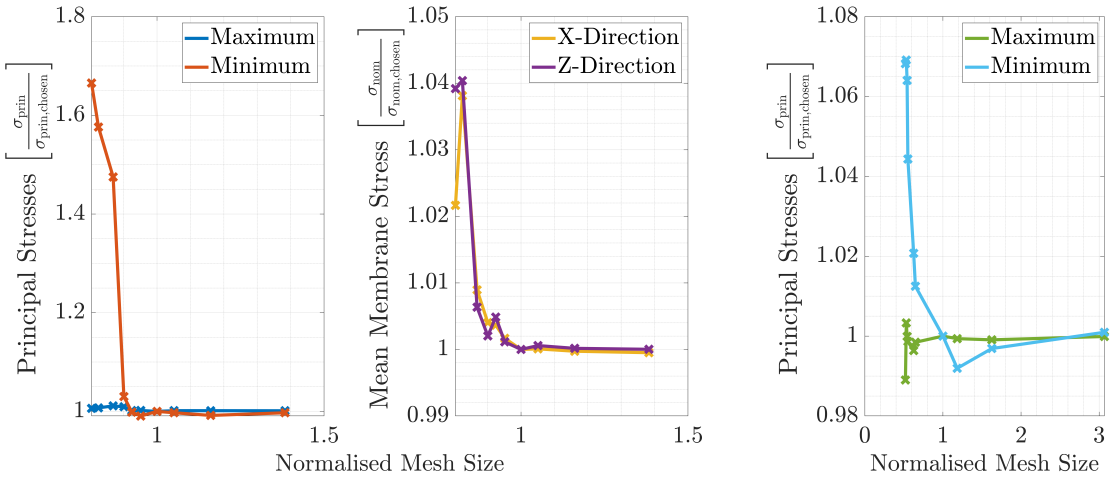


Figure 3.5: *tracked values versus mesh size for (a) body size refinement (b) face size refinement*

3.3.2 Mesh

A mesh-independence study was conducted on a representative geometry, pictured in Figure 3.4. It is the same 16 mm x 16 mm section used in the 'test region', using the internal geometry in Table 3.1. A thin - 7.5% total width - boundary was added to each skin on the x- and z-normal faces to remove local conflicts between multiple boundary conditions with shared vertices. The thermal boundary conditions and material properties were identical to those of the test articles. The mechanical boundary conditions were set to emulate an infinite flat plate [36, 102] using constraint equations. The total rotation and normal deflection to the extent of the geometry were constrained so that both quantities were equal in both walls. It is shown, in Figure 3.7, that these were sufficient to match the infinite flat plate to within 3%.

The mesh was initially refined through body sizing until a mesh-independent solution was found. The face sizing of all fillets was then reduced. The absolute maximum principal stress and the directional membrane stress are reported in Figure 3.5. The results are normalised by the value of the selected mesh. The final mesh was chosen to balance grid-independence and computational demands.

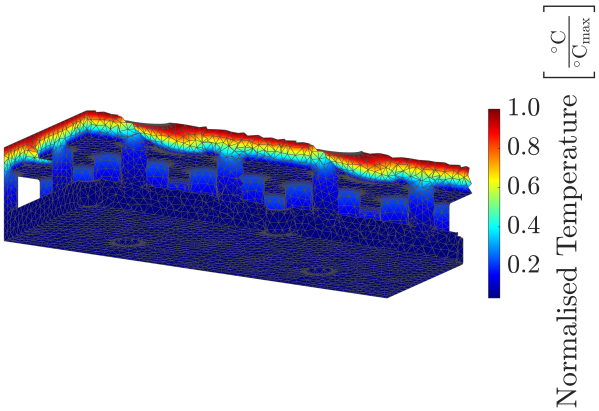


Figure 3.6: *thermal field for the central double-wall effusion-cooled region used across all test articles*

3.3.3 Results

The thermal field for the central region is shown in Figure 3.6. It was consistent across all test articles. The results are normalised using $\phi = \frac{T-T_c}{T_h-T_c}$.

The nominal stress fields were extracted by sampling the x- and z-direction stresses along various paths, normal to the outer surface of the hot-wall. Separate paths were used to minimise the effect of various features and obtain quasi-far-field values for the hot- and cold-walls. The hot-wall paths were placed above the impingement holes, and the cold-wall paths were placed below the film holes. The results shown in Figure 3.7 are the average values in all paths in both the stream-wise and span-wise directions. The stresses are normalised by $E\alpha\Delta T$ and presented alongside the theoretical nominal stress for an infinite flat plate under identical thermal loading with an equibiaxial stress state [36, 102]. The TA article best represents the infinite flat plate. The decreased gradient of stress through the hot-wall in the span-wise direction indicates a reduced moment contribution in the same direction as the degree of freedom of the hinge. This leads to a 21% reduction in the outer surface of the hot-wall compared to the infinite plate. The CF article has the next-closest hot-wall stresses yet exhibits tensile cold-wall stresses. Both effects were considered to be due to the quasi-hoop effect caused by the closed geometry [103]. The difference between the stream-wise and span-wise peak stresses follows the same trend as the TA article, suggesting a reduced moment contribution. The FP and FFP articles have nearly identical nominal stress fields. They exhibit a net compressive shift of 0.4 on the hot-wall, consistent with an unheated mounting ring resisting expansion. The cold-wall carries nominal stresses similar

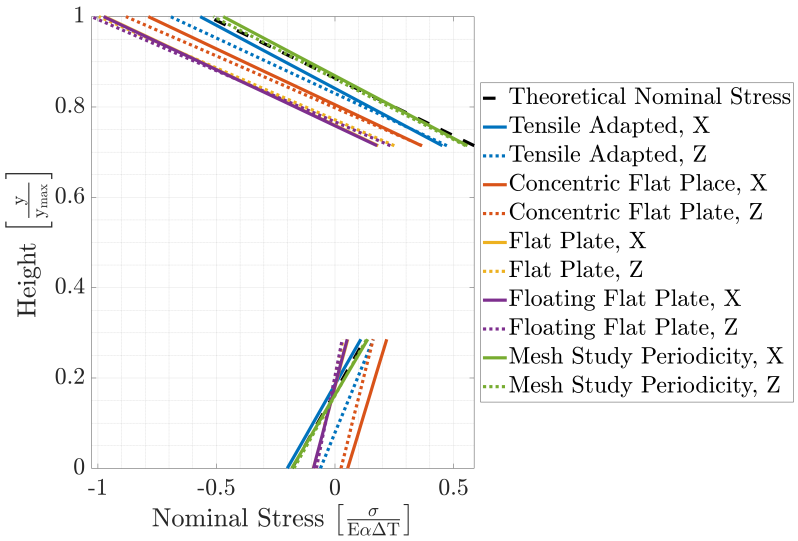


Figure 3.7: *nominal stress distribution for both planar dimensions in each test article*

to those in the theoretical case, but with a significantly reduced moment contribution.

Article	TA	CF	FP	FFP
X-Error	0.0069	0.0498	0.0859	0.0868
Z-Error	0.0314	0.0683	0.0907	0.0968

Table 3.2: *root mean square difference of each test section nominal stress relative to the theoretical model [36, 102]*

Table 3.2 is provided to present the root mean square difference (RMSD) between the nominal fields and the theoretical flat plate at each sample point. A smaller number represents better adherence to flat plate predictions. The minimum value for the TA article reflects a superior adherence compared to other proposed articles. A 355% difference from the stream-wise and span-wise directions for the TA is consistent with the qualitative trend identified in Figure 3.7.

Figures 3.8 and 3.9 show the maximum absolute principal stress on the outer surface of the hot-wall and the internal surfaces of the central test region, respectively. The TA article has the lowest maximum absolute principal stresses, with the global value exceeding the test value by 36%. This global value exists adjacent to the thermal boundary condition imposed on the pedestal fillet where it meets the hot-wall. This is consistent, with differing

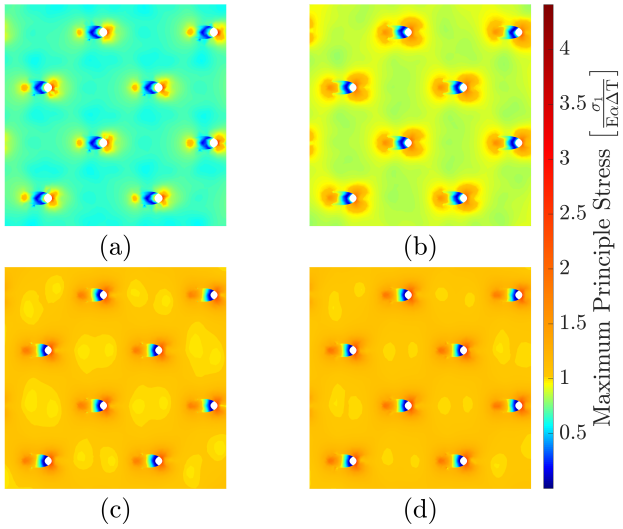


Figure 3.8: *maximum absolute principal stress distribution on the hot-wall of (a) TA (b) CF (c) FP (d) FFP*

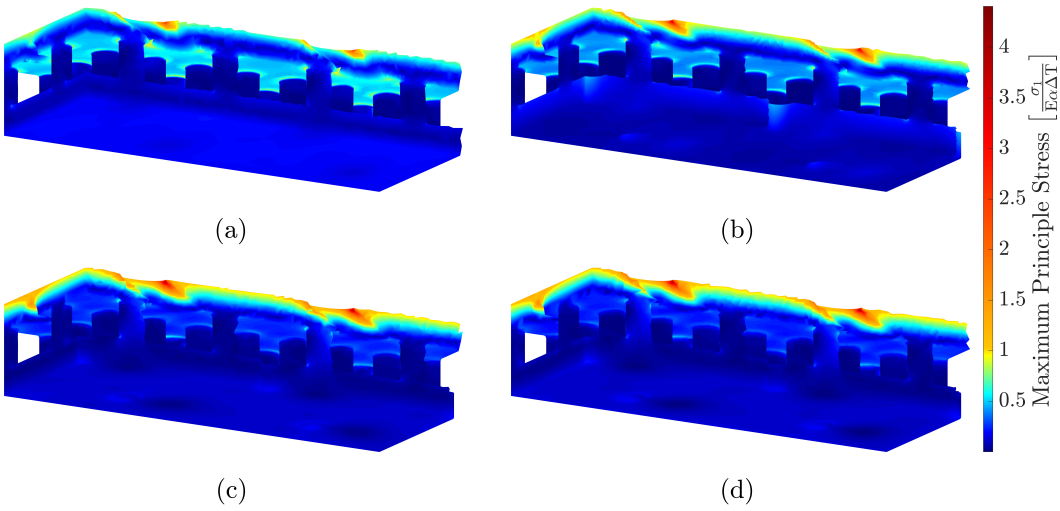


Figure 3.9: *maximum absolute principal stresses on the interior of the hot-wall and pedestals of (a) TA (b) CF (c) FP (d) FFP*

Article	$\lvert\sigma_{1,\text{global,max}}\rvert$	$\lvert\sigma_{1,\text{test,max}}\rvert$	R
TA	3.6052	2.6553	1.3577
CF	3.7943	3.4790	1.0907
FP	4.4572	4.0052	1.1129
FFP	4.2333	4.2333	1.0000

Table 3.3: *comparison of global and central test region stresses across proposed test articles*

magnitudes, in all CF and FP articles, with an overshoot of roughly 9% and 10%. The FFP article is different due to the removal of pedestals, which eliminates a potential weakness. The maximum absolute principal stress for the FFP article is clearly visible on the FHW.

Table 3.3 contains the maximum values for both the maximum absolute principal stresses. 'Global' is defined as the value for the entire test article. 'Test' is defined as the value for the central test region. The 'R' column presents the ratio of global to central test region stress. A value of unity indicates that the maximum value is located within the central test region. A value above unity represents a per cent over-stress.

3.4 Initial Selection

The selection of the preferred test article was achieved through the comparison of the stresses present in each proposed geometry. The thermal field was not considered because it was constant in each article. Geometry and assembly considerations were also neglected as each article possesses identical internal geometry and satisfies geometric limits imposed by the casting furnace.

With respect to the nominal stress distribution, presented in Figure 3.7 and Table 3.2, the TA article ranks first. It best approximates the nominal distribution and possesses the lowest RMSD. The remaining articles have greater RMSD values but still contain a negative gradient through the hot-wall.

The results of Figures 3.8-3.9 are summarised in Table 3.3. In the order in which the articles are presented, there is a clear increase in the maximum absolute principal stress in the central test region, up to 51% in the FP and 60% in the FFP. The magnitude of the stress is believed to increase proportionally with the constraints imposed by the specific

mounting method. The maximum absolute principal stress increases in the film hole on the stream-wise sides and decreases on the span-wise sides. The CF article features an increased maximum absolute principal stress in the impingement holes, consistent with the hoop constraint [100, 102].

For a test article to be deemed acceptable, the maximum absolute principal stresses must be located in the central test region. The FFP was proposed as it is believed that the removal of the constraining effects of the pedestals will reduce elevated stresses outside the desired area. The findings support this theory. The global maximum for the TA, CF, and FP articles occurs adjacent to the imposed thermal boundary on one of the interior pedestal fillets. The FFP performs best with an R-value of unity, the absolute maximum stress occurring on the exterior of the film holes on the FHW. Crack initiation occurring on the exterior surface of the component is preferable for the detection of initiation and observation of growth due to a clear line of sight. The FFP article is accessible for measurements and features a more favourable stress field than the alternatives. The compressive shift in the stress field due to the rigid boundary is considered beneficial as the gradient of the nominal stress is blade-representative. The exaggerated stress state accelerates failure and minimises the time required for testing.

3.5 Mechanical Optimisation of a Preferred Geometry

The FFP article was found to carry a maximum absolute principal stress on the outer-most pedestal fillets in excess of 27% of the central test region. An illustration of the maximum absolute principal stresses is shown in Figure 3.10. Murray and Elstrop found that local stresses in double-wall effusion-cooled (DWEC) systems may be dealt with using local scaling [37, 76] and that small changes have a negligible impact on global thermal and stress fields. A study was performed in Mechanical to investigate the effect of local pedestal diameter and fillet radii on mitigating elevated absolute maximum stresses. This was done to minimise the chance of premature failure outside of the FHW. This work supports prior findings, as increasing the outer-most pedestal diameters and fillet radii was shown to reduce the local stresses, provided neighbouring pedestal fillets do not interact.

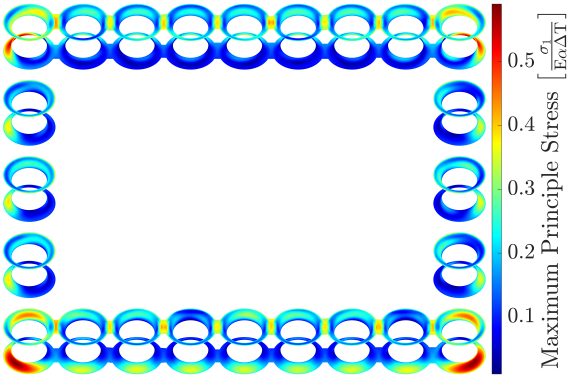


Figure 3.10: *exterior pedestal fillet stresses in the optimised geometry, displaying regions of elevated maximum absolute principal stress on the external pedestal fillets*

3.5.1 Domain and Boundary Conditions

The geometry in Figure 3.3 (b) was used as the domain. The pedestal fillet radius was first studied, ranging from $\hat{\rho} = 0.1$ to $\hat{\rho} = 0.4$. The pedestal diameter was then increased from $\hat{\mathrm{D}} = 1.0$ to $\hat{\mathrm{D}} = 1.5$. The coordinate system was consistent with the previous analysis. A further refined mesh, roughly 120% larger than the previous FFP domain, was used to increase grid-independence. The increased mesh density on the fillet faces better resolved the local distributions.

The thermal boundary conditions and material properties were kept consistent with Skamniotis [102]. A surface temperature of 727 °C was imposed on the outer surface of the hot-wall. Both the interior surfaces and the exterior of the cold-wall were set at 27 °C. These were both defined in a 32 mm x 32 mm square, central to the test section and including the separate 16 mm x 16 mm central test region. The initial temperature of the system was 27 °C. Values for CMSX-4 at 527 °C were used: E = 120 GPa, $\nu = 0.3$, $\alpha = 1.2 \times 10^{-5}$ $\frac{1}{°\mathrm{C}}$, and $k = 14$ $\frac{\mathrm{W}}{\mathrm{m°C}}$ [102]. The full crystallographic orientation of CMSX-4 in the final test specimens was unknown due to a lack of control during manufacture. For this reason, this analysis assumed elastic isotropy throughout the domain.

The mechanical boundary condition for the FFP optimisation was consistent with the original rigid constraint placed on the vertical and chamfer faces of the large mounting holes.

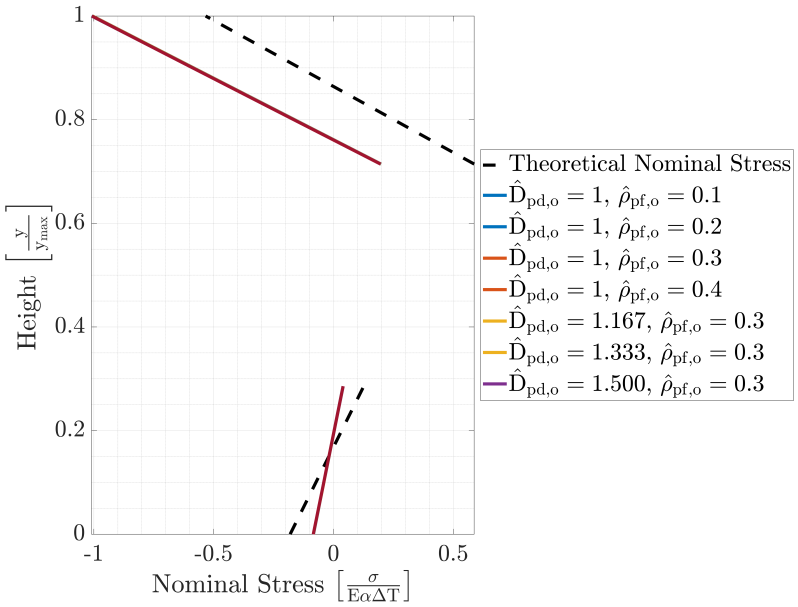


Figure 3.11: *global average of both x- and z-direction nominal stress distribution for each refinement step*

3.5.2 Results

Figure 3.11 presents the mean nominal stresses in each of the optimisation cases. The nominal stress field was extracted by sampling the directional stresses along various paths, normal to the outer surface of the hot-wall. The paths were selected and sampled in a manner identical to that in the selection study.

Table 3.4 reports the maximum absolute principal stress fields for the entire test article and the fillet. $\hat{A}_{min}$ is the dimensionless cross-sectional area between neighbouring outer-most pedestals. This value was critical in assessing a cut-off for feature scaling due to structural requirements during manufacturing. An over-reduction in this value may create a weak spot that results in the failure of the mould during casting. Alternatively, the removal of mould material post-casting may be impossible. Both render the test article useless. It was estimated that an $\hat{A}_{min}$ of 0.6-0.7 should serve as a cut-off.

Figure 3.12 combines the data from Figure 3.11 and Table 3.4. Following the method used by Skamniotis [100, 101, 103], the stress concentration factor (SCF) in the hole was calculated using the nominal stress on the internal surface of the cold-wall, taken from the paths sampled.

$\hat{\rho}_{\mathrm{pd,ext}}$	$\hat{\mathrm{D}}_{\mathrm{pd,ext}}$	$\lvert\sigma\rvert_{\mathrm{global,max}}$	$\lvert\sigma\rvert_{\mathrm{fillet,max}}$	$\hat{\mathrm{A}}_{\mathrm{min}}$
0.1	1.000	4.5007	1.2307	1.4686
0.2	1.000	4.5265	0.8954	1.3743
0.3	1.000	4.5658	0.7303	1.2173
0.4	1.000	4.6017	0.6298	0.9973
0.3	1.000	4.5658	0.7303	1.2173
0.3	1.127	4.5898	0.6471	1.0268
0.3	1.333	4.6300	0.5905	0.7178
0.3	1.500	4.6679	1.3184	0.4673

Table 3.4: *stresses on the exterior pedestal fillets and dimensionless areas between pedestals for varied fillet radii and pedestal diameters*

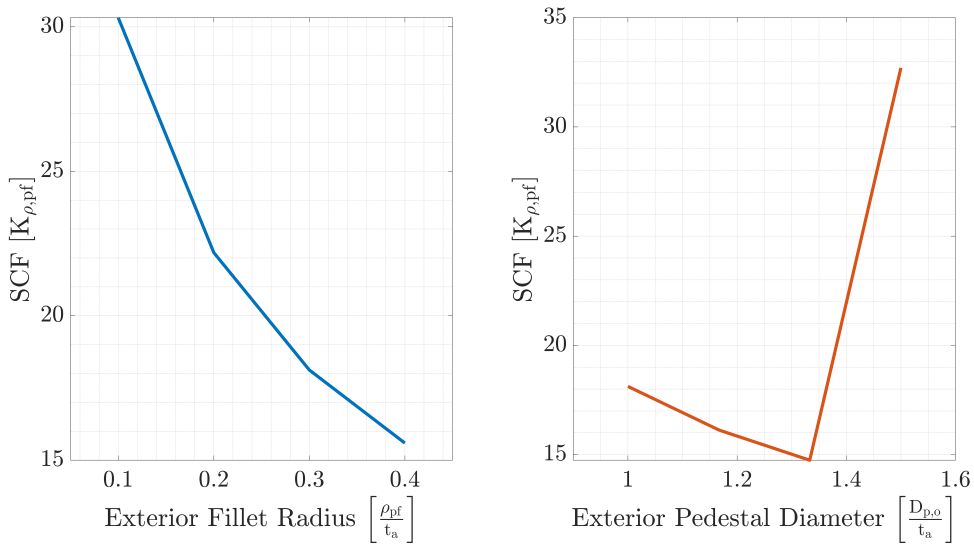


Figure 3.12: *maximum absolute principal stress concentration factors, relative to the extracted nominal stress on the nearest wall, for each refinement step, displaying a sharp spike as fillets interact at large pedestal radii*

3.6 Final Selection

In Figure 3.11, the nominal distributions are nearly identical and appear to overlap. Therefore, it was concluded that the scaling of the external pedestals did not produce a measurable global effect for the nominal stresses. The hot-wall retains a blade-representative gradient and a compressive shift of approximately 0.4 normalised units.

From both Table 3.4 and Figure 3.12, it is shown that an increase in the radius of the fillet or the diameter of the pedestal decreases the maximum absolute principal stress located in the fillet. Each successive increase exhibits a diminishing marginal return. The increase from $\hat{\rho}_{\text{pd,ext}} = 0.3$ to $\hat{\rho}_{\text{pd,ext}} = 0.4$ shows only a reduction of 14%, compared to the reduction of 27% between $\hat{\rho}_{\text{pd,ext}} = 0.1$ and $\hat{\rho}_{\text{pd,ext}} = 0.2$. The reduced return prompted the selection of $\hat{\rho}_{\text{pd,ext}} = 0.3$ before investigating the diameter. It is clear from the $\hat{\rho}_{\text{pd,ext}} = 0.3$, $\hat{\text{D}}_{\text{pd,ext}} = 1.5$ case that there is an upper limit to the effectiveness of stress reduction through feature enlargement. The size of the fillet and the diameter of the pedestal result in an overlap of neighbouring fillets, which increases the local stresses as the pedestal geometries interact.

The design of the FFP article is further improved by an optimisation that reduced the maximum absolute principal stress on the pedestal fillets by 41%. As the stress on the pedestal fillet decreased with increasing pedestal dimensions, the global stress, located at the FHW, increased by 3%. This was attributed to an increase in the effective stiffness. Given the effective reduction in stresses and an $\hat{\text{A}}_{\text{min}} > 0.7$, the optimal parameters were $\hat{\rho}_{\text{pd,ext}} = 0.3$ and $\hat{\text{D}}_{\text{pd,ext}} = 1.333$. For the remainder of this work, the optimised FFP article will be referred to as the 'coupon'.

Figures 3.13 and 3.14 present the two coupons evaluated in this work. The impingement holes are coloured blue, the pedestals orange, and the film holes red. The scaling of the outer-most pedestals and fillets can be seen. Included in the rendering are holes for material removal. The plugs were to be brazed after printing or casting. The only difference between the two designs was the film holes. The internal geometries were identical. Figure 3.13 featured cylindrical holes, which create an elliptical cross-section when viewed normal to the exterior surface. Figure 3.14 featured elliptical holes, oriented and scaled such that they create circular cross-sections when viewed normal to the exterior surface. The ellipses

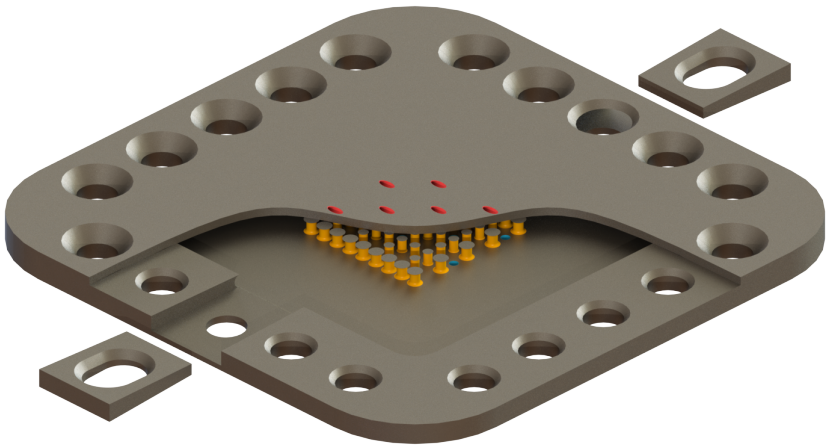


Figure 3.13: *a render of the final coupon design for the case of cylindrical holes*

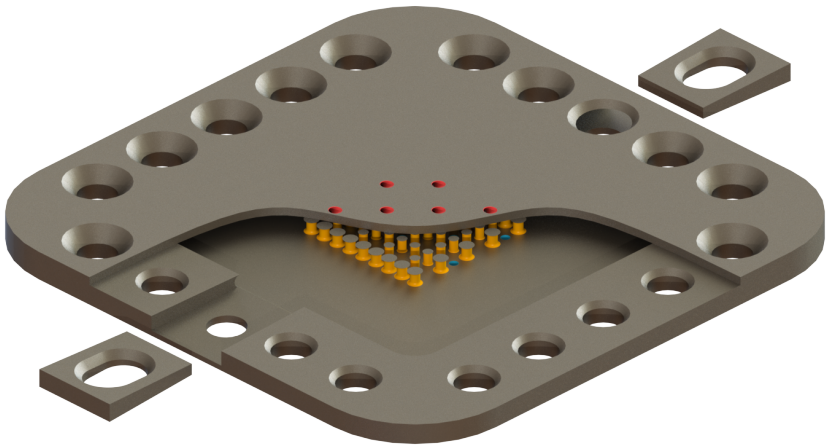


Figure 3.14: *a render of the final coupon design for the case of elliptical holes*

were scaled so that they had the same cross-sectional area perpendicular to the flow. It was hypothesised that the elliptical holes would have an inherently lower SCF, resulting in reduced stress and longer component life under identical thermal conditions.

3.6.1 Materials and Manufacturing

The two materials chosen for testing were single-crystal CMSX-4 and Inconel 625. CMSX-4 was selected as the material of choice for some commercial engine components. The drawback of single-crystal CMSX-4 is that it must be cast to ensure the correct orientation of the γ and γ' matrix. Casting comes with unique challenges. Inconel 625 was selected due to its reduced cost and ability to be manufactured through 3D printing processes. This renders it far more reliable for rapid prototyping, where novel features may not be possible through current casting techniques.

The two concerns with the casting were whether small internal features may be appropriately resolved and whether the mould or support material can be safely and reliably removed from the finished cast. The former was supported by an internal study using a 'Rainbow Plate' to determine the minimum dimensions of a pedestal that can be reliably cast. The minimum achievable scaling was 120% of full scale. The coupons rendered in Figures 3.13 and 3.14 have an internal geometry scaled by this 120% while keeping the macro x- and z-dimensions the same. This increased the maximum absolute principal stresses in the film holes by 7%, but did not change the distribution noticeably. The removal of all mould or support material is a priority to ensure that coolant flow, heat transfer, and deformation occur as predicted. The film and impingement holes were deemed too small to ensure that this was achieved, so two channels were cut on the span-wise sides of the coupons. The plugs were brazed in to these holes to prevent coolant air from venting out of the sides.

Thermal Stresses in a Representative Coupon Domain

The selected coupon from Chapter 3 features a quasi-rigid boundary which significantly differs from the prior modelling of infinite domains [36, 100, 102]. The addition of kinematic constraints renders a nominal stress state that differs from that of the infinite flat plate. To understand the origin of stresses in the coupon, a new set of equations was derived to describe the nominal stress state. This chapter aims to provide context for the driving factors that influence the stress field in the selected coupon and to develop an approach for future analytical modelling. Equations governing the stress field were proposed and evaluated over a selection of thermal loads. The model was then validated through finite element analysis (FEA). A comparison between nominal coupon stresses and the model showed that the model underestimates the contribution of the moment in the inner wall and underestimates the nominal stress on the exterior of the outer wall by 3.2%. In addition, a parametric study that varied the thermal field indicated that the stress state is sensitive to the temperature difference between the mounting and the centre of the coupon. For the coupon geometry, this contribution is 57 times greater than the temperature difference between the hot- and cold-walls.

4.1 Derivation of a New Nominal Stress Model

A similar approach to Elmukashfi [36] and Skamniotis [102] was implemented in the derivation of a new model. The coupon was simplified by removing all internal features: impingement and film holes, pedestals, and associated fillets. These were found to have negligible effects on far-field stresses for pedestal spacing greater than twice the thickness of the outer wall [36]. The stresses in these features may be found later using a stress concentration factor to

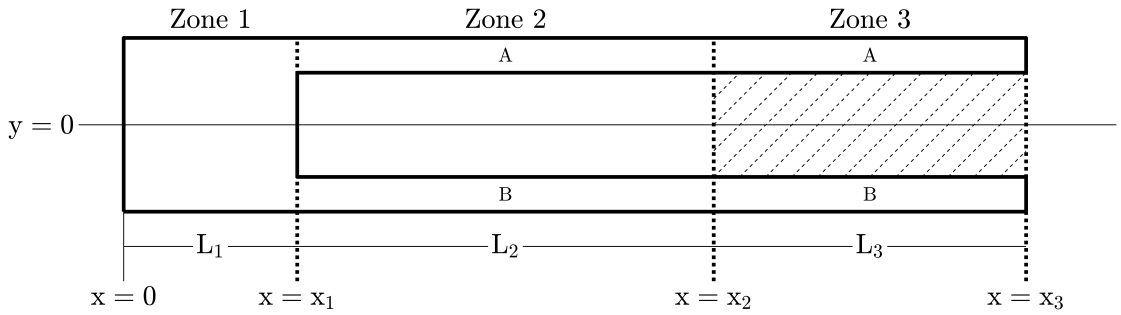


Figure 4.1: *2D coupon-representative domain*

scale the nominal field [100, 102, 103]. Two thermal boundary conditions were developed to capture both: a first-order approximation of the boundary conditions present in the previous chapters' studies and a nearly identical field with the addition of a reduced temperature near the mounting holes. The latter was thought to be representative of the result of conduction from the coupon to the mounting fixture. The domain was assessed along the centre-line of each zones' wall or walls, as applicable. The forces and moments had to satisfy equilibrium across all boundaries. The y-deformation was neglected for this analysis, and the rationale behind this is explained in Appendix I.

4.1.1 Domain and Boundary Conditions

Figure 4.1 shows the idealised domain used for this analysis. A 2D slice of the coupon in Figures 3.13 and 3.14 was taken along the x-y plane. The domain was reduced through a symmetry condition at the mid-point, $x = x_3$ and subdivided in to three distinct 'zones', each with unique mechanical and thermal boundaries. The wall receiving vertical-cavity surface-emitting laser (VCSEL) energy is defined as the hot-wall, 'wall A', and the other is the cold-wall, 'wall B'. Each of the zones is defined using the length, L_i, where $i = 1, 2, 3$. The thicknesses of wall A and wall B are defined as t_a and t_b, respectively. H is the height of the pedestals. The zones are described below:

1. **The mounting ring** stretches from $x = 0$ to $x = x_1$. It is modelled as a beam with a zero-total curvature condition. The boundary condition at $x = 0$ is rigid, and at $x = x_1$ is coupled to each wall in zone 2.

2. **The decoupled region** exists between $x = x_1$ and $x = x_2$. There is no mechanical coupling between the skins due to the lack of pedestals. Each wall is free to deform

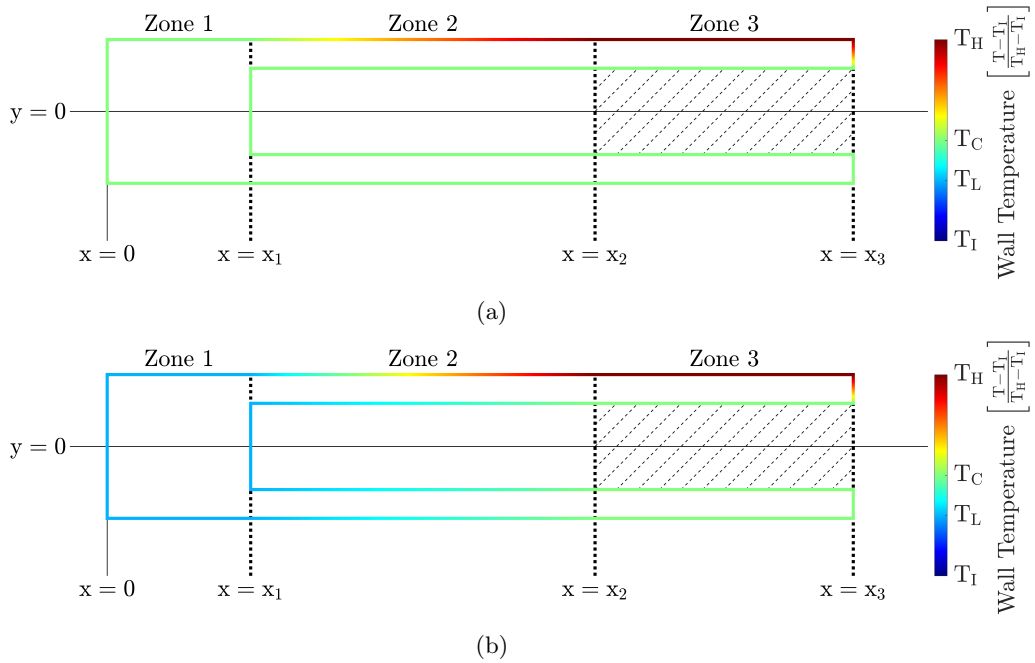


Figure 4.2: *simplified thermal profiles for a linear superposition of (a) the simplified thermal boundary with a uniform step from* T_i *to* T_c *(b) the simplified loss condition in zone 1 and a uniform step from* T_i *to* T_c

within the limits imposed by the adherence to continuity at the coupled boundaries of zones 1 and 3 at $x = x_1$ and $x = x_2$, respectively.

3. **The central test region** is between $x = x_2$ and $x = x_3$. The mechanical deformation of each skin is constrained by a zero-total curvature condition. The boundary at $x = x_2$ is coupled to each wall in zone 2, and $x = x_3$ is the symmetry plane.

4.1.2 Thermal Cases

The two thermal boundary conditions were constructed using two of three component boundary conditions. Formulating these separately was possible by assuming that the stress field is linearly elastic, allowing the individual stress fields to be linearly superimposed [115]. It also allowed for the later comparison of the relative magnitudes of the stress fields as various thermal components were scaled.

Figure 4.2 provides an illustration of the two boundary conditions. There are four crucial temperature values: T_h, T_c, T_i, and T_l. T_h is the mean temperature on the outer surface of the hot-wall in zone 3. It was the result of heat from the main-stream flow, which was replaced by the VCSEL for testing. T_c is the temperature achieved on the internal

surface of the hot-wall and the entire cold-wall in zone 3. This modelled the combination of impingement and turbulent coolant air, which removes energy from the system. In reality, T_c varied across these surfaces; however, variations are neglected, as Elmukashfi [36] found that the stresses caused by higher order approximations of the thermal field have a less than 10% effect on the stress state. T_i is the initial temperature of the coupon before a uniform step to T_c. T_l is the temperature of zone 1, defined to model the conductive loss through the plenum. The temperatures were constrained such that $T_i < T_l < T_c < T_h$.

4.1.2.1 Ideal Thermal Case

The ideal thermal case was defined as the combination of the simplified thermal boundary and a uniform step. It was considered ideal because there was no loss through the mounting fixture. The outer surface of the hot-wall in zone 3 was set to T_h, while the remaining surfaces in zone 3 were set to T_c. The boundary at $x = x_1$ was set to T_c. A steady-state solution of these boundaries concluded that zone 1 and the cold-walls of zones 2 and 3 remained at T_c. Wall A of zone 3 featured a thermal field that varies in y, from T_c to T_h. Wall A of zone 2 varied from the mean wall temperature of wall A, $\frac{T_h+T_c}{2}$, in zone 3 at $x = x_2$ to T_c at $x = x_1$.

$$\begin{gathered} T_1(x,y) = T_c \\ T_{2,a}(x,y) = \frac{T_h - T_c}{2(x_2 - x_1)}(x - x_1) + T_c \quad \text{and} \quad T_{2,b}(x,y) = T_c \\ T_{3,a}(x,y) = \frac{T_h - T_c}{t_a}\left(y - \frac{H}{2}\right) + T_c \quad \text{and} \quad T_{3,b}(x,y) = T_c \end{gathered} \tag{4.1}$$

4.1.2.2 Realistic Thermal Case

The realistic thermal case was defined as the combination of a simplified thermal boundary in zone 3, a uniform step from T_i to T_c, and a loss temperature for zone 1. The outer surface of the hot-wall in zone 3 was set to T_h, while the remaining surfaces in zone 3 were set to T_c. This differs in that the boundary at $x = x_1$ was set to T_l. The first-order solution concluded that zone 1 remained at T_l, and both walls in zone 2 varied with x, from T_l to

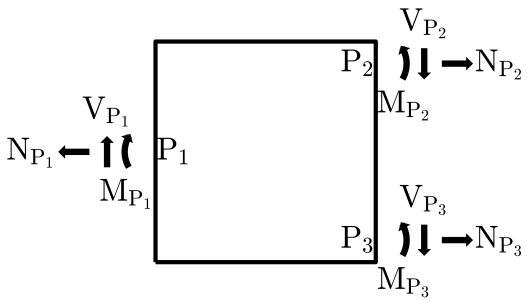


Figure 4.3: *zone 1 free body diagram*

$\frac{T_h+T_c}{2}$ in wall A or T_c in wall B.

$$
\begin{gathered}
T_1(x,y) = T_l \\
T_{2,a}(x,y) = \frac{T_h + T_c - 2T_l}{2(x_2 - x_1)}(x - x_1) + T_l \quad \text{and} \quad T_{2,b}(x,y) = \frac{T_c - T_l}{(x_2 - x_1)}(x - x_1) + T_l \\
T_{3,a}(x,y) = \frac{T_h - T_c}{t_a}\left(y - \frac{H}{2}\right) + T_c \quad \text{and} \quad T_{3,b}(x,y) = T_c
\end{gathered}
\tag{4.2}
$$

4.1.3 Governing Equations

The forces at the points laid out below are defined as: $F_{point} = F(x = x_{point})$. Deformation normal to the coupon was neglected due to the assumption that $(H + t_a + t_b) << (L_1 + L_2 + L_3)$ and the results of Appendix I.

4.1.3.1 Zone 1 Equilibrium

Figure 4.3 shows the external component forces and moments in zone 1. The point P_1 represents the rigid boundary where the coupon is mounted. The points P_2 and P_3 represent the forces and moments at the interface between zones 1 and 2 on wall A and wall B, respectively. The sums of the forces are:

$$
\Sigma F_{Z1,x} = N_{P_2} + N_{P_3} - N_{P_1} = 0 \quad \text{and} \quad \Sigma F_{Z1,y} = V_{P_1} - V_{P_2} - V_{P_3} = 0 \tag{4.3}
$$

The sum of the moments about P_1 is taken as:

$$
\begin{aligned}
\Sigma M_{P_1} = M_{P_2} + M_{P_3} - M_{P_1} - \left(\frac{H}{2} + \frac{t_a}{2}\right) N_{P_2} \\
+ \left(\frac{H}{2} + \frac{t_b}{2}\right) N_{P_3} - L_1 V_{P_2} - L_1 V_{P_3} = 0
\end{aligned}
\tag{4.4}
$$

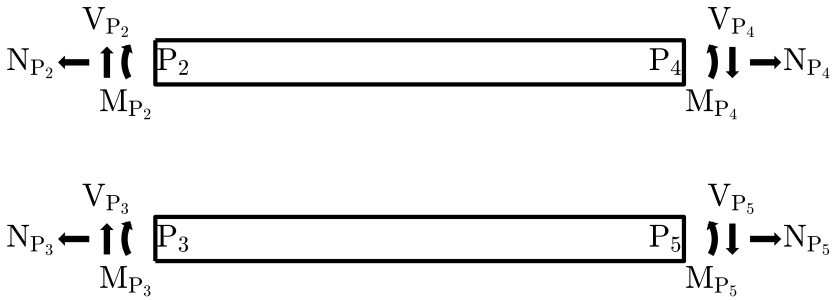


Figure 4.4: *zone 2 free body diagram*

It was concluded that the x- and y-force components through this zone are not functions of x. For the remainder of this analysis, alternate subscripts are used for simplicity:

$$N_1(x) = N_{P_1} = N_1 \quad \text{and} \quad V_1(x) = V_{P_1} = V_1 \tag{4.5}$$

4.1.3.2 Zone 2 Equilibrium

Figure 4.4 shows the external component forces and moments in zone 2. The points P_2 and P_3 were the same as defined above. The points P_4 and P_5 represent the forces and moments at the interface between zones 2 and 3 on wall A and wall B, respectively. As the skins are not coupled, they were analysed separately. The sums of the forces in wall A are:

$$\Sigma F_{Z2,a,x} = N_{P_4} - N_{P_2} = 0 \quad \text{and} \quad \Sigma F_{Z2,a,y} = V_{P_2} - V_{P_4} = 0 \tag{4.6}$$

The sum of the moments in the outer skin about P_2 was taken as:

$$\Sigma M_{P_2} = M_{P_4} - M_{P_2} - L_2 V_{P_4} = 0 \tag{4.7}$$

The sum of the forces in the x and y-directions in wall B are:

$$\Sigma F_{Z2,b,x} = N_{P_5} - N_{P_3} = 0 \quad \text{and} \quad \Sigma F_{Z2,b,y} = V_{P_3} - V_{P_5} = 0 \tag{4.8}$$

The sum of the moments in the inner skin about P_3 was taken as:

$$\Sigma M_{P_3} = M_{P_5} - M_{P_3} - L_2 V_{P_5} = 0 \tag{4.9}$$

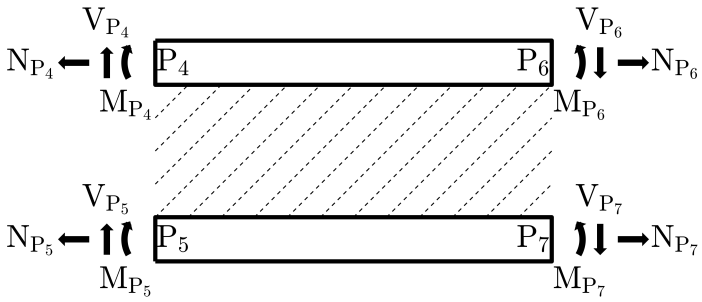


Figure 4.5: *zone 3 free body diagram*

It was concluded that x- and y-force components through this zone were not functions of x. For the remainder of this analysis, alternate subscripts are used for simplicity:

$$N_{2,a}(x) = N_{P_2} = N_{P_4} = N_{2,a} \quad \text{and} \quad V_{2,a}(x) = V_{P_2} = V_{P_4} = V_{2,a} \tag{4.10}$$

$$N_{2,b}(x) = N_{P_3} = N_{P_5} = N_{2,b} \quad \text{and} \quad V_{2,b}(x) = V_{P_3} = V_{P_5} = V_{2,b} \tag{4.11}$$

4.1.3.3 Zone 3 Equilibrium

Figure 4.5 shows the external component forces and moments in zone 3. The points P_4 and P_5 were the same as defined above. The points P_6 and P_7 represent the reaction forces in the symmetry plane for wall A and wall B, respectively. The sums of the forces are:

$$\begin{aligned} \Sigma F_{Z3,x} &= N_{P_6} + N_{P_7} - N_{P_4} - N_{P_5} = 0 \quad \text{and} \\ \Sigma F_{Z3,y} &= V_{P_4} + V_{P_5} - V_{P_6} - V_{P_7} = 0 \end{aligned} \tag{4.12}$$

The sum of the moments about P_5 were taken as:

$$\begin{aligned} \Sigma M_{P_5} =& M_{P_6} + M_{P_7} - M_{P_4} - M_{P_5} + \left(H + \frac{t_a}{2} + \frac{t_b}{2}\right) N_{P_4} \\ &- \left(H + \frac{t_a}{2} + \frac{t_b}{2}\right) N_{P_6} - L_3 V_{P_6} - L_3 V_{P_7} \end{aligned} \tag{4.13}$$

The complete complementary derivation provided in Appendix I shows that the normal forces in zone 3 are constant throughout the domain. For the remainder of this analysis, alternate subscripts are used for simplicity:

$$N_{3,a}(x) = N_{P_6} = N_{3,a} \quad \text{and} \quad V_{3,a}(x) = V_{P_7} = V_{3,a} \tag{4.14}$$

$$N_{3,b}(x) = N_{P_7} = N_{3,b} \quad \text{and} \quad V_{3,b}(x) = V_{P_7} = V_{3,b} \tag{4.15}$$

4.1.3.4 Strain Relations

The combination of the rigid boundary at x = 0 and the symmetry condition applied at $x = x_3$ constrained the coupon to exhibit zero-total strain. Zero-total curvature was assumed for zones 1 and 3 due to the self-constraint imposed by the relative moment of inertia and the coupling provided by the pedestals. This was a reasonable assumption for this case, according to Skamniotis [101]. The total change in the length of the half-coupon is given:

$$\Delta L_{tot} = \Delta L_1 + \Delta L_2 + \Delta L_3 \tag{4.16}$$

Similarly, the total strains of zones 2 and 3 were constrained. The pedestals were not modelled to carry stress, yet the walls in zone 3 were required to deform together. Therefore, the local displacement in walls A and B at the same x-location must be equivalent. Integrating this over the entire zone, the total change in length of this region must be the same. Zone 2 does not have pedestal coupling, although the total change in the length of wall A and wall B must also be equal as the zero-total curvature restricts any rotation at $x = x_1$, and continuity must be satisfied at $x = x_1$ and $x = x_2$. These are both given as:

$$\Delta L_{2,a} = \Delta L_{2,b} \tag{4.17}$$

$$\Delta L_{3,a} = \Delta L_{3,b} \tag{4.18}$$

Based on the assumption of linear elasticity, the strains of each zone and wall may be decomposed in to component elastic and thermal contributions using $\epsilon_e(x) = \frac{N(x)}{E(x)t(x)}$ and $\epsilon_t(x) = \alpha(x)\Delta T(x)$, respectively. E is the Youngs' Modulus and α is the coefficient of thermal expansion. T(x) is the thermal profile along the centre line of each wall. Therefore:

$$\epsilon(x) = \epsilon_e(x) + \epsilon_t(x) = \frac{N(x)}{E(x)t(x)} + \alpha(x)\Delta T(x) \tag{4.19}$$

Integrating the strain across each section yields the total change in length, given by:

$$\Delta L_i = \int_{x_{i-1}}^{x_i} \epsilon_{i,e}(x)dx + \int_{x_{i-1}}^{x_i} \epsilon_{i,t}(x)dx \tag{4.20}$$

Elastic	Thermal
$\epsilon_{1,e}(x) = \frac{1}{E(H+t_a+t_b)}N_1$	$\epsilon_{1,t}(x) = \alpha\Delta T_1(x)$
$\epsilon_{2,a,e}(x) = \frac{1}{Et_a}N_{2,a}$	$\epsilon_{2,a,t}(x) = \alpha\Delta T_{2,a}(x)$
$\epsilon_{2,b,e}(x) = \frac{1}{Et_b}N_{2,b}$	$\epsilon_{2,b,t}(x) = \alpha\Delta T_{2,b}(x)$
$\epsilon_{3,a,e}(x) = \frac{1}{Et_a}N_{3,a}$	$\epsilon_{3,a,t}(x) = \alpha\Delta T_{3,a}(x)$
$\epsilon_{3,b,e}(x) = \frac{1}{Et_b}N_{3,b}$	$\epsilon_{3,b,t}(x) = \alpha\Delta T_{3,b}(x)$

Table 4.1: *elastic and thermal strain components for the analytical model*

Table 4.1 presents the strain components for each zone and wall, as they vary in x. The force components, N_i, were constant. Similarly, the Youngs' Modulus, pedestal height, and skin thicknesses were assumed constant over the entire domain. The contributions of thermal strain were left in the general form as each function varies in each thermal case.

4.1.3.5 Bending Relations

The complete set of equations defined from the free-body diagrams included both the shear and the moment terms. Appendix I provides proof that the moments in zones 1 and 2 and the shear force over the entire domain are negligible for the selected thermal fields. It also concludes that the moments in zone 3 are constant throughout the region. The moments in zone 3 are derived from the zero-curvature constraint:

$$\kappa_{3,a} = \kappa_{3,b} = 0 \tag{4.21}$$

Similarly to normal strain, the curvature contributions were decomposed to the elastic and thermal contributions, using $\kappa_e(x) = \frac{M(x)}{E(x)I(x)}$ and $\kappa_t(x) = -\alpha\frac{\delta}{\delta y}T(x,y)$, respectively. I is the bending moment of inertia, and ΔT_y is the thermal gradient normal to the wall.

$$\kappa(x) = \kappa_e(x) + \kappa_t(x) = \frac{M(x)}{E(x)I(x)} - \alpha\frac{\delta}{\delta y}T(x,y) \tag{4.22}$$

The curvature equations for both skins across both thermal distributions have identical thermal contributions.

$$\kappa_{3,a} = \frac{1}{EI_a} M_{3,a} - \alpha \frac{T_h - T_c}{t_a} \quad \text{where} \quad I_a = \frac{t_a^3}{12} \tag{4.23}$$

$$\kappa_{3,b} = \frac{1}{EI_b} M_{3,b} - 0 \quad \text{where} \quad I_b = \frac{t_b^3}{12} \tag{4.24}$$

Solving equations (4.23) and (4.24) for the moments, using equation (4.21):

$$M_{3,a} = \frac{t_a^2}{12} E\alpha(T_h - T_c) \quad \text{and} \quad M_{3,b} = 0; \tag{4.25}$$

4.1.4 Nominal Stresses

There are seven unknowns, and therefore, seven equations are required to define a unique solution. There are two equilibrium relations that related the sum of the normal forces at $x = x_1$ and $x = x_2$. There are three strain equations that govern the deformation of each of the three zones. There are two curvature equations that defined the moments in the inner and outer skins. This derivation isolated the thermal terms in unique vectors, allowing for the decoupled solution. The solution matrix is a property of the domain and is therefore consistent throughout.

Substituting equations (4.10) to (4.11) in to equation (4.3), equilibrium at the $x = x_1$ boundary is:

$$0 = N_1 - N_{2,a} - N_{2,b} \tag{4.26}$$

Substituting equations (4.10) to (4.11) and (4.14) to (4.15) in to equation (4.12), equilibrium at the $x = x_2$ boundary is:

$$0 = N_{2,a} + N_{2,b} - N_{3,a} - N_{3,b} \tag{4.27}$$

The strain equations required that the equations set out in Table 4.1 were substituted in to equation (4.20), and the elastic components were evaluated. These equations were substituted in to equations (4.16) and then further in to (4.18). Collecting the thermal

terms on the left:

$$-\mathrm{E}\alpha\int_0^{\mathrm{x}_1}\Delta\mathrm{T}_1(\mathrm{x})\mathrm{dx}-\mathrm{E}\alpha\int_{\mathrm{x}_1}^{\mathrm{x}_2}\Delta\mathrm{T}_{2,\mathrm{b}}(\mathrm{x})\mathrm{dx}-\mathrm{E}\alpha\int_{\mathrm{x}_2}^{\mathrm{x}_3}\Delta\mathrm{T}_{3,\mathrm{b}}(\mathrm{x})\mathrm{dx} = \frac{\mathrm{L}_1}{(\mathrm{H}+\mathrm{t_a}+\mathrm{t_b})}\mathrm{N}_1+\frac{\mathrm{L}_2}{\mathrm{t_b}}\mathrm{N}_{2,\mathrm{b}}+\frac{\mathrm{L}_3}{\mathrm{t_b}}\mathrm{N}_{3,\mathrm{b}} \tag{4.28}$$

$$\frac{\mathrm{E}}{\mathrm{L}_2}\alpha\int_{\mathrm{x}_1}^{\mathrm{x}_2}\left(\Delta\mathrm{T}_{2,\mathrm{a}}(\mathrm{x})-\Delta\mathrm{T}_{2,\mathrm{b}}(\mathrm{x})\right)\mathrm{dx} = \frac{1}{\mathrm{t_b}}\mathrm{N}_{2,\mathrm{b}}-\frac{1}{\mathrm{t_a}}\mathrm{N}_{2,\mathrm{a}} \tag{4.29}$$

$$\frac{\mathrm{E}}{\mathrm{L}_3}\alpha\int_{\mathrm{x}_2}^{\mathrm{x}_3}\left(\Delta\mathrm{T}_{3,\mathrm{a}}(\mathrm{x})-\Delta\mathrm{T}_{3,\mathrm{b}}(\mathrm{x})\right)\mathrm{dx} = \frac{1}{\mathrm{t_b}}\mathrm{N}_{3,\mathrm{b}}-\frac{1}{\mathrm{t_a}}\mathrm{N}_{3,\mathrm{a}} \tag{4.30}$$

The thermal components of equations (4.28) to (4.30) were evaluated and combined with equations (4.25) to (4.27). The system of equations is defined below.

$$\overbrace{\begin{bmatrix}0\\0\\0\\ \mathrm{E}\alpha\left(\frac{\mathrm{T_h}-\mathrm{T_c}}{2}\right)\\ \frac{\mathrm{t_a}^2}{12}\mathrm{E}\alpha(\mathrm{T_h}-\mathrm{T_c})\\0\end{bmatrix}}^{\text{Ideal Case}}\quad\overbrace{\begin{bmatrix}0\\0\\-\mathrm{E}\alpha(\mathrm{T_c}-\mathrm{T_i})(\mathrm{L}_1+\mathrm{L}_2+\mathrm{L}_3)\\0\\0\\0\\0\end{bmatrix}}^{\text{Uniform Step}}\quad\overbrace{\begin{bmatrix}0\\0\\-\mathrm{E}\alpha(\mathrm{T_l}-\mathrm{T_c})\left(\mathrm{L}_1+\frac{1}{2}\mathrm{L}_2\right)\\ \mathrm{E}\alpha\left(\frac{\mathrm{T_h}-\mathrm{T_c}}{4}\right)\\ \mathrm{E}\alpha\left(\frac{\mathrm{T_h}-\mathrm{T_c}}{2}\right)\\ \frac{\mathrm{t_a}^2}{12}\mathrm{E}\alpha(\mathrm{T_h}-\mathrm{T_c})\\0\end{bmatrix}}^{\text{Realistic Case}}$$

$$=\begin{bmatrix}1&-1&-1&0&0&0&0\\0&1&1&-1&-1&0&0\\ \frac{\mathrm{L}_1}{\mathrm{H}+\mathrm{t_a}+\mathrm{t_b}}&0&\frac{\mathrm{L}_2}{\mathrm{t_b}}&0&\frac{\mathrm{L}_3}{\mathrm{t_b}}&0&0\\0&-\frac{1}{\mathrm{t_a}}&\frac{1}{\mathrm{t_b}}&0&0&0&0\\0&0&0&-\frac{1}{\mathrm{t_a}}&\frac{1}{\mathrm{t_b}}&0&0\\0&0&0&0&0&1&0\\0&0&0&0&0&0&1\end{bmatrix}\begin{bmatrix}\mathrm{N}_1\\\mathrm{N}_{2,\mathrm{a}}\\\mathrm{N}_{2,\mathrm{b}}\\\mathrm{N}_{3,\mathrm{a}}\\\mathrm{N}_{3,\mathrm{b}}\\\mathrm{M}_{3,\mathrm{a}}\\\mathrm{M}_{3,\mathrm{b}}\end{bmatrix}\begin{matrix}(4.26)\\(4.27)\\(4.28)\\(4.29)\\(4.30)\\(4.25)\\(4.25)\end{matrix}$$

A MATLAB[1] script was written to invert the solution matrix and multiply the correct thermal case vector to obtain the corresponding force and moment components. As required, thermal cases 1 or 3 were combined with case 2. These components were used to calculate the stresses present in the system. The stresses were given by the following equation and were normalised by $\mathrm{E}\alpha(\mathrm{T_h}-\mathrm{T_c})$.

$$\sigma_\mathrm{i} = \frac{\mathrm{M_i}}{\mathrm{EI_i}}\bar{\mathrm{y}}+\frac{\mathrm{N_i}}{\mathrm{Et_i}} \tag{4.31}$$

[1]The MathWorks, Inc (2021). *MATLAB version: 9.10 (R2021a)* https://www.mathworks.com

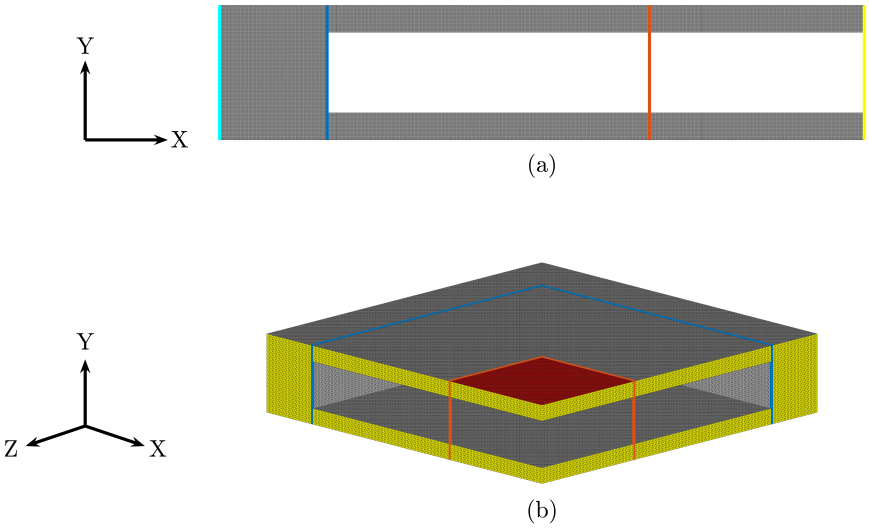


Figure 4.6: *an example of the geometry used for the mesh study of (a) the 2D domain (b) the 3D domain, showing the fixed wall in light blue, the zone 1-zone 2 boundary in dark blue, the zone-2 zone-3 boundary on orange, and the symmetry condition in yellow*

$\bar{y}$ is the normalised y-position through the wall thickness, such that $\bar{y} = 0$ is the centre-line, and the range is from [-1,1].

Two extremes were evaluated with the model: a Youngs' Modulus of 0 in zones 1 and 2 and a Youngs' Modulus of ∞ with a α of 0. The former produced a stress state nearly identical to an unconstrained DWEC system with a zero-total curvature condition [105]. The latter produced a stress state similar to that of a fully constrained zone 3.

4.2 Finite Element Analysis

To verify the validity of the derived model, an FEA study was performed in Mechanical[2]. Both a simplified 2D and 3D geometry were investigated over a range of wall thicknesses, pedestal heights, and zone lengths. FEA nominal stresses show apparent adherence to model predictions, validating the approach for the 2D case. The 3D case is also considered validated; however, the model over-predicted the nominal stresses in wall A of zone 2 by up to 14%. The stresses of the analytical model were scaled by dividing by $(1 - \nu)$, assuming an equibiaxial stress state [115], for comparison with the 3D case.

[2] Ansys®Academic Research Mechanical, Release 21.2

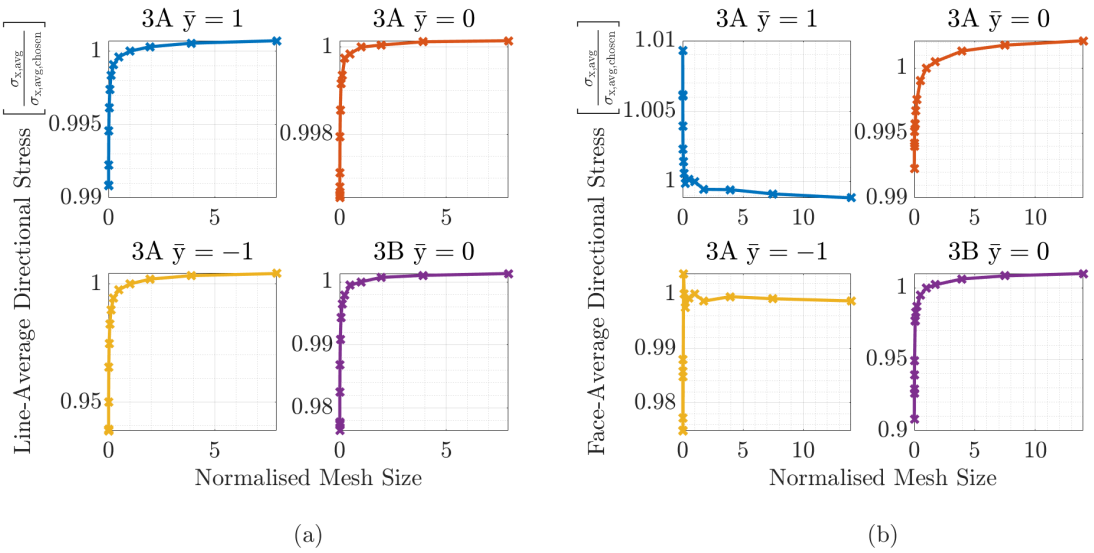


Figure 4.7: *mesh study results for selected lines or planes, respectively, at various heights through each wall thickness for (a) the 2D domain (b) the 3D domain*

4.2.1 Domain and Boundary Conditions

Two domains were used and are shown in Figure 4.6. The domains were generated in DesignModeler[3], and dimensions were parametrised for analysis. The investigated geometric parameters are: L_1, L_2, L_3, t_a, t_b, and H. Shared topology was used to ensure that contact modelling between zones was not required.

The values chosen for each of the defined model temperatures were consistent across each geometric analysis. They are: $T_h = 727$ °C, $T_c = 327$ °C, $T_i = 27$ °C, and $T_l = 127$ °C. Both previously described thermal fields were implemented identically to the model. Values for CMSX-4 at 527 °C were used: E = 120 GPa, $\nu = 0.3$, $\alpha = 1.2 \times 10^{-5}$ $\frac{1}{°C}$, and $k = 14$ $\frac{W}{m°C}$ [102]. Consistent with the analytical equations, the boundary at $x = 0$ was modelled as rigid, and the boundary at $x = x_3$ was assigned as mirror-symmetric. The equivalent strain in zone 3 was modelled using a coupled remote point on the zone 2-3 boundary normal displacement at $x = x_2$. The zero-total curvature was modelled by setting the rotation to rigid in both wall bodies. The wall spacing was maintained through a coupled y-displacement on the interior surfaces of zone 3. These remote points were adapted for the 3D domain by applying them in both x- and y-directions.

[3] Ansys®Academic Research DesignModeler, Release 21.2

4.2.2 Mesh

A structured mesh was used in the absence of curved features. A mesh-independence study was performed in a domain with coupon-representative geometry: $L_1 = 12$ mm, $L_2 = 36$ mm, $L_3 = 16$ mm, $t_a = 1$ mm, $t_b = 1$ mm, and $H = 3$ mm. The ideal thermal case and mechanical boundaries consistent with the above description were used. The mesh was refined through body sizing until a mesh-independent solution was found. The average stresses at each $\bar{y}$ for the entire zone were extracted. Figure 4.7 reports the nominal stress in four locations. Wall A was sampled at $\bar{y} = -1$, 0 and 1, and wall B was sampled at $\bar{y} = 0$. The stress values and the relative size of the mesh are normalised by the chosen mesh. Figure 4.6 shows both meshes used. The body sizing was consistent with what is shown in the figure, while the geometry was altered accordingly.

4.2.3 Results

The nominal stress values were extracted from several locations in both geometries. For the 2D case, stresses were sampled along lines defined at $\bar{y} = -1$, 0 and 1 in both walls of zones 2 and 3. For the 3D case, stresses were sampled at the same $\bar{y}$ locations but on surfaces parallel to the exterior of the coupon. These extracted values were averaged to obtain the mean nominal stresses, reported normalised using $E\alpha\Delta T$. Two sets of 3D case values were assessed, the x- and z-components. These were found to differ, in all locations, by less than 2%. The stress field was confirmed to be equibiaxial, and only the x-components are reported in the following figures. Equation (4.25) predicts that the moment distribution only varies with t_a. Due to this, the stresses at $\bar{y} = -1$ and 1 exhibit identical trends as for $\bar{y} = 0$, for the same T_h, T_c, and t_a. For the results presented, T_h, T_c, and t_a are kept constant and only $\bar{y} = 0$ is reported, except in wall A of zone 3. The geometry values presented are normalised by the thickness of wall A, such that $\hat{g} = \frac{g}{t_a}$ for any geometric parameter, g.

Figure 4.8 presents the comparison between the model and FEA for the realistic thermal case. The accuracy is identical to the ideal thermal case; however, the relative magnitude of the stress field in the realistic case has decreased on average by 14%. This is due to the decrease in the mean temperature of both walls in zone 2, which results in a lower thermal expansion. As can be seen in the graphs, the maximum magnitude of the nominal stress is found at $\bar{y} = 1$ in wall A of zone 3. Across all walls, an increase in $\hat{t}_b$ is associated with a

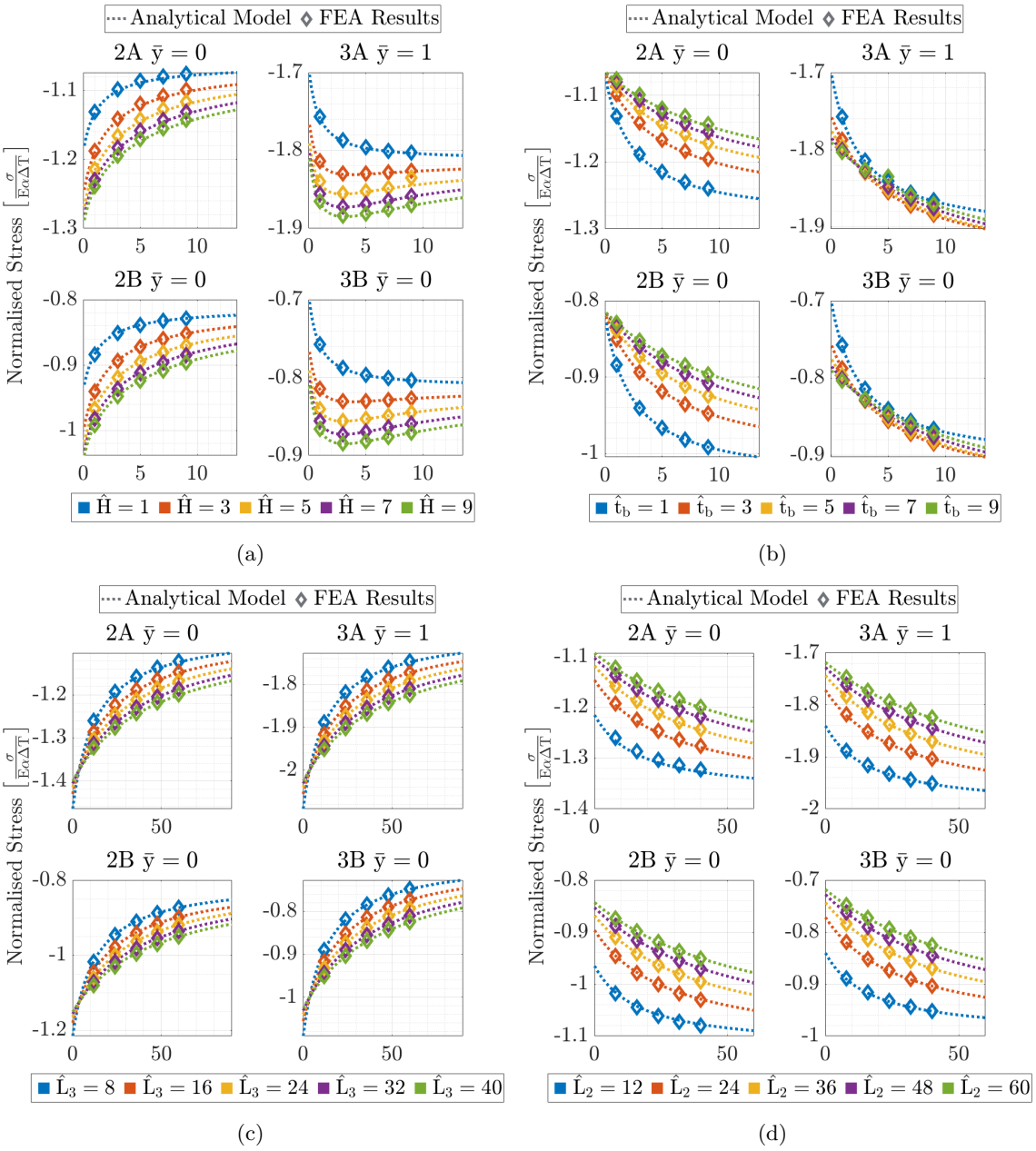


Figure 4.8: *nominal stresses present for the realistic thermal case on a 2D geometry as a function of (a)* $\hat{t}_b$ *(b)* $\hat{H}$ *(c)* $\hat{L}_2$ *(d)* $\hat{L}_3$

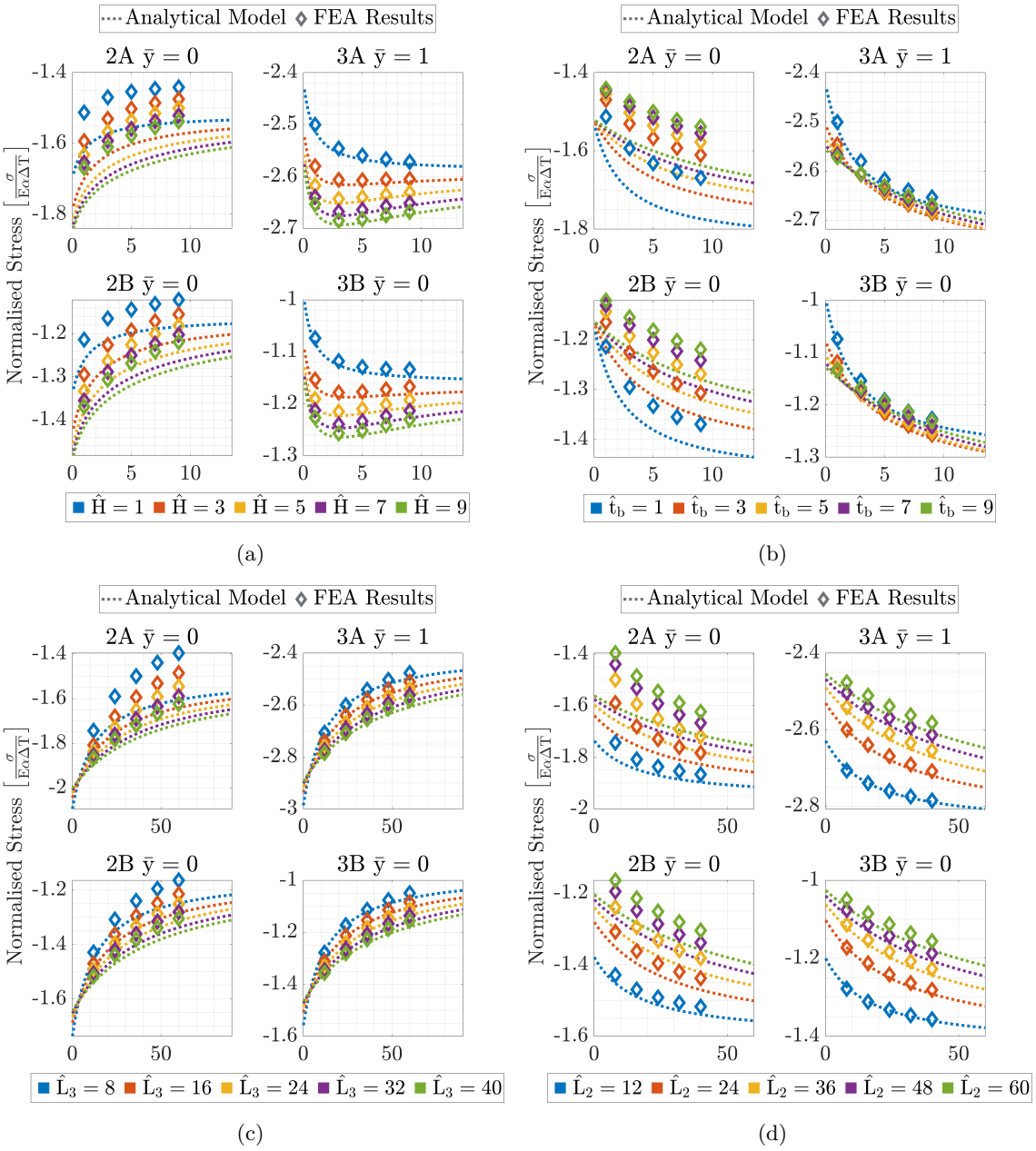


Figure 4.9: *nominal stresses present for the realistic thermal distribution on a 3D geometry as a function of (a)* $\hat{t}_b$ *(b)* $\hat{H}$ *(c)* $\hat{L}_2$ *(d)* $\hat{L}_3$

decrease in the nominal stress magnitude in zone 2 and an increase in zone 3. The increase in $\hat{H}$ results in a global increase in the nominal stress magnitudes for all regions. This is attributed to the increase in the constraint imposed by a thicker zone 1. As $\hat{L}_2$ and $\hat{L}_3$ increase, the nominal stresses decrease and increase, respectively. For $\hat{L}_2$, the increase in size results in a more significant portion of the domain that exhibits a lower mean temperature. This effect holds for an increase $\hat{L}_3$, where a more significant portion of the domain exhibits a higher mean temperature. The minimisation of boundary constraints can be achieved through an increase in $\hat{t}_b$ and $\hat{L}_2$, and a decrease in $\hat{H}$ and $\hat{L}_3$.

Figure 4.9 presents the same data as Figure 4.8, except that the FEA results are from the 3D domain. As the thermal distribution is the same as in the 2D case, the trends observed in the analytical model are identical to those in the previous paragraph. Consistent across all four sub-figures, the model over-predicts the stress field in the 3D domain. This is most noticeable in zone 2, where the model differs by up to 18% in smaller geometric parameters. This decrease, when comparing the FEA with the model, can be explained by the addition of 3D heat flow, which is not considered in the derivation of a 2D model. $\hat{L}_2$ is defined along the x- and z- directions. As such, there exist regions where this $\hat{L}_2$ does not capture the full length of the thermal distribution. In Figure 4.6 (b), the distance from the top-most corner of zone 2 to the top-most corner of zone 3 is longer. Additionally, conduction will occur in both the x- and z-directions. The net result is similar to the increase in $\hat{L}_2$ for the 2D case, in which the mean expansion experienced by the entire component is decreased. The difference in prediction in zone 3 is considered acceptable, as it is less than 4%, on average.

4.3 Discussion of Thermal Cases and Impact on Stresses

For the 2D geometry, the model predicts the nominal stress to be within 3.1% across all walls and zones. For the 3D geometry, this is greater at 8.3%, on average. The model underestimates the magnitude of the nominal stresses across all geometries. It was concluded that the FEA reported in the previous section validated the analytical model to predict the nominal stresses in the selected coupon for the 2D and 3D geometries, since the discrepancy is below 10%.

Following on, a comparison to the selected coupon is performed and reported in Figure 4.10 (a). The analytical model was calibrated for the domain. The values used are: $\hat{L}_1 = 3.95$,

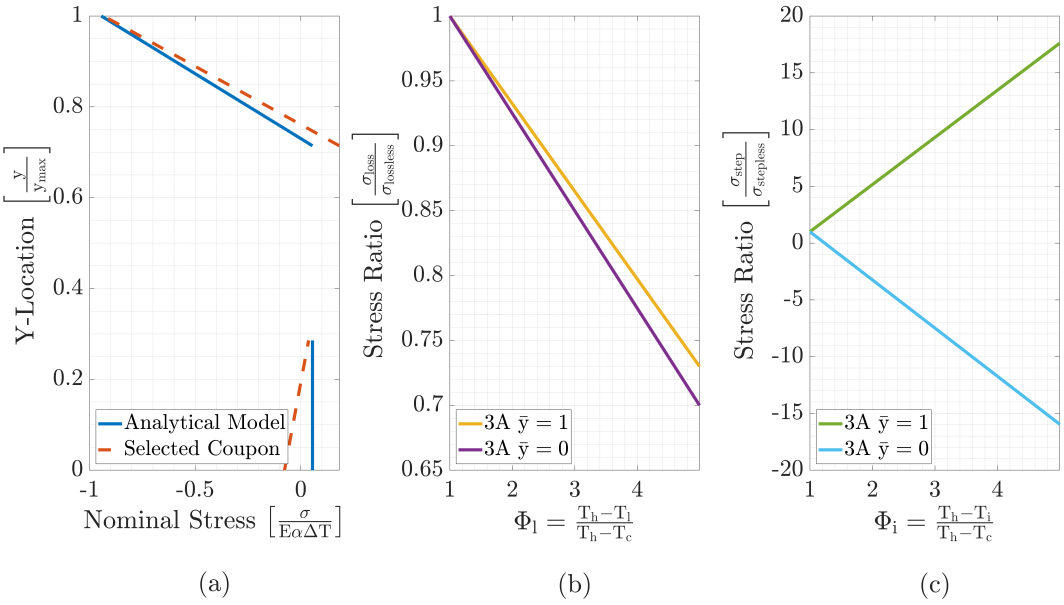


Figure 4.10: *comparisons of (a) the nominal stresses as calculated by the analytical model to the FEA of the selected coupon from the previous chapter (b) the relative contribution of the loss temperature (c) the relative contribution of the initial temperature*

$\hat{L}_2 = 15$, $\hat{L}_3 = 16.67$, $\hat{t}_b = 1$, and $\hat{H} = 1.5$. As expected, the model only shows a tensile shift in wall B, as it models the moment on the inner skin as zero. This differs from the true nominal field in the coupon; however, it is considered inconsequential because the stresses and temperatures present in wall A will promote failure long before failure in wall B. The magnitude of the nominal stresses in the inner skin is only 9.4% that of the outer skin at its maximum. The model also underestimates the moment on the outer skin by approximately 17%. The end result is that the peak nominal stress on the outer surface of wall A, as predicted by the model, is 3.2% less than the FEA result. The remainder of the stresses in wall A were over-predicted. This is considered beneficial because overshoot in model prediction will result in conservative estimates for component life.

The motivation behind the derivation of the low-order model was the determination of what underlying factors influence the nominal stresses in the novel coupon geometry. The previous section presented and discussed geometric factors. The decoupled formulation of the temperature fields enables a comparison of the relative contributions of both conductive loss and the initial temperature. The stress values for 3A $\bar{y} = 0$ and 1 were calculated using the coupon-identical values: $\hat{L}_1 = 3.95$, $\hat{L}_2 = 15$, $\hat{L}_3 = 16.67$, $\hat{t}_b = 1$, and $\hat{H} = 1.5$. An

engine-representative T_h = 1000 °C and T_c = 800 °C were chosen. For the investigation in to T_l, T_i = 25 °C and T_l = [1,T_c] °C. For the investigation in to T_i, T_l = 400 °C and T_i = [1,T_c] °C.

To quantify the relative share, a stress ratio, SR, and a temperature ratio, Φ, were defined. The stress ratio is taken as the fraction of the stress with a feature investigated to the stress without the feature. For T_l, this was calculated by dividing the stresses for the realistic thermal case by the stresses for the ideal thermal case. For T_i, this was calculated by dividing the stresses for the realistic thermal case by the stresses for only a uniform step. The temperature ratio is taken as the difference from T_h, normalised by the thermal gradient in wall A of zone 3, $(T_h - T_c)$. A Φ of 1 represents $T_l = T_c$. The increase in Φ corresponds to a decrease in the magnitude of T_l or T_i and the increase in its effect on the system.

$$\Phi_{l,i} = \frac{T_h - T_{l,i}}{T_h - T_c} \tag{4.32}$$

Figures 4.10 (b) and (c) present the results of both comparisons, which show that the increase in the magnitude of both Φ values had a significant effect on the system. The stresses in wall A decreased by 30% in the range of T_l investigated and increased by 1750% in the range of T_i investigated. A coupon experiencing loss will have a lower stress field than the lossless alternative due to a lower mean temperature in zones 1 and 2; however, the magnitude of this effect is significantly smaller than that of the initial temperature step. The decrease in T_i is the dominant effect for this configuration, 57 times that of T_l. This is due to the more significant component of compressive stress carried by the coupon as it attempts to expand more in a confined space. The comparison highlights that this initial step must be considered as it will produce the majority of stresses in the coupon. This differs significantly from prior work, which has previously attributed stress magnitudes to the thermal gradient in wall A. Although the remainder of this work continues to be normalised by this temperature gradient, $(T_h - T_c)$, the results from this section show that other factors must be considered for the design of a constrained geometry.

Design of a Thermo-Mechanical Fatigue Facility

A modified facility was proposed and constructed to facilitate thermo-mechanical fatigue testing. The Effusion Lifespan and Stress Addition (ELSA) was designed to interface with the existing Oxford LAser Heating Facility (OLAHF) [63, 64], as the latter provided established wider-system architecture. ELSA utilises four vertical-cavity surface-emitting lasers (VCSELs) and coolant air to drive high heat flux and thermal gradients through coupons. These VCSELs feed in to a compound parabolic concentrator (CPC) to focus and concentrate VCSEL power [41, 96, 130], allowing for engine-representative heat fluxes and beyond. It was constructed with the goal of providing flexible cycling, influencing the design of its physical components and control program. In combination with a water cooling loop, the control program also introduces safety measures to ensure that there is minimal damage to the rig and the coupon in the event of a malfunction. This chapter lays out specifics about OLAHF and ELSA before covering the architecture of the design process. The design and selection of CPCs for use with VCSELs were studied and presented. In addition, a discussion of selected instrumentation for experimental and process measurements is included. This chapter concludes with a conjugate CFD-FEA analysis, performed to assess and tune the thermal and mechanical performance of the designed components to prevent failure during testing.

5.1 Existing Infrastructure: Oxford Laser Heating Facility

The entirety of the following section is devoted to covering the work done by Zachary Jackson [63, 64] to design and install the existing OLAHF system. Figure 5.1 shows the existing OLAHF architecture. It features a water cooling loop, 6.89 bar filtered and dried air supply,

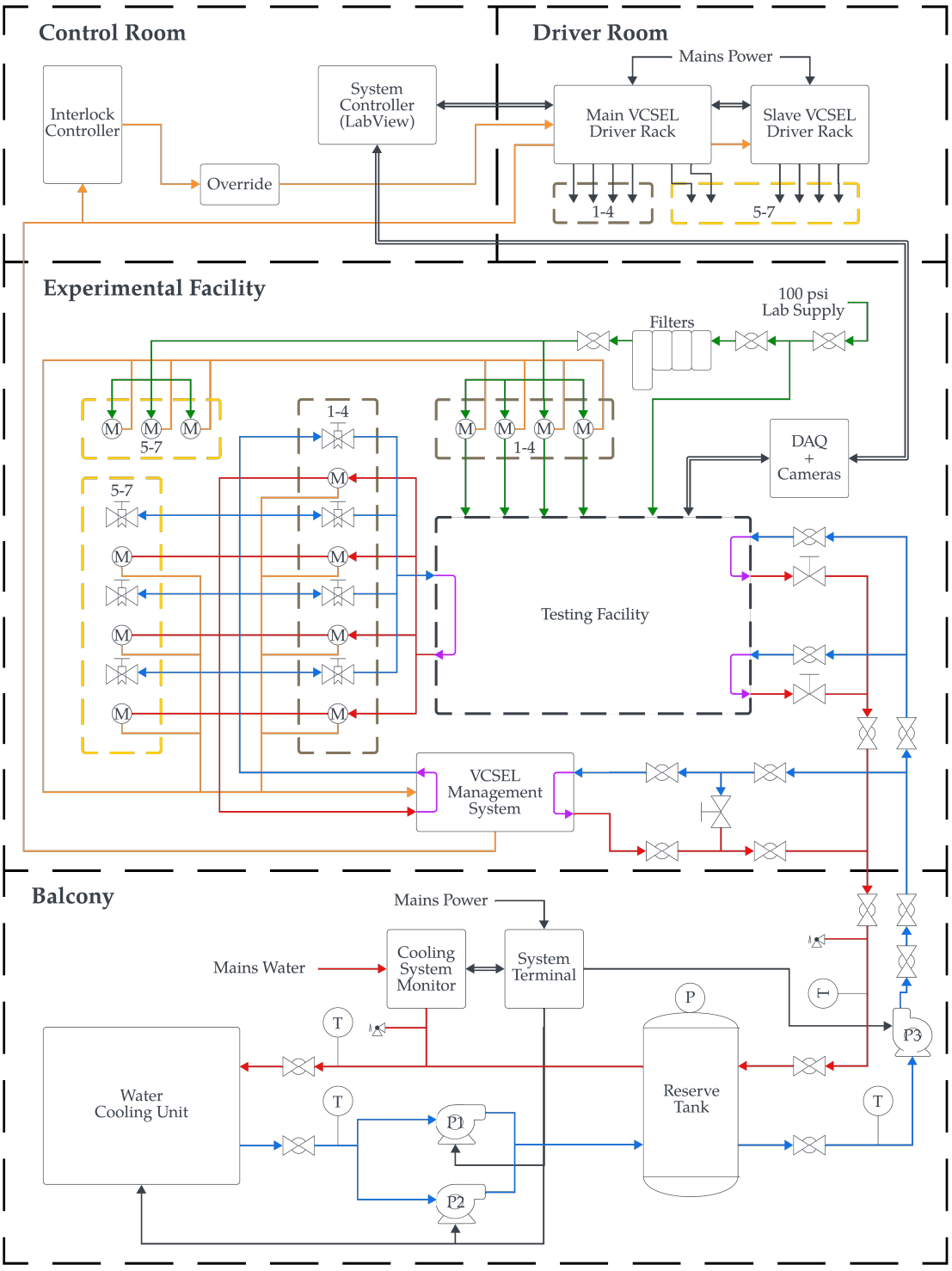


Figure 5.1: *existing Oxford Laser Heating Facility schematic diagram showing systems integration: blue is the cooling water out, red is the cooling water return, green is the 6.89 bar dry air supply, black is the data transfer connections, and orange is the laser interlock system, recreated from Jackson [63, 64]*

and fully integrated laser control, management, and interlock systems [63, 64].

A Dynaciat LGN condenser[1] provides up to 25 kW of cooling capacity to the water cooling loop. The water coolant temperature is set to the minimum temperature, 6 °C. Pumps 1 and 2 correspond to Grundfos MAGNA1 D twin-head pumps[2], which maintain the system pressure at 1.7 bar. Pump 3 corresponds to a Grundfos TPE3[3], providing up to 25 m of head at 120 LPM, depending on user preferences. The system is monitored through a Mikrofill 3[4], which maintains water levels within the system and monitors the pressures of the system and the performance of the pump, reporting faults to the system terminal on the balcony. The water cooling system is plumbed to include a VCSEL cooling loop and two auxiliary loops for additional cooling when needed. A bypass valve prevents dead-heading of the pump system when the auxiliary cooling loops are not in use. The VCSEL water cooling is isolated from the main cooling flow through a Trumpf PPC108-50 VCSEL Management System[5], as it was filled with deionised water to protect the VCSEL arrays. It features an integrated heat exchanger and thermal monitoring equipment to maintain the VCSELs at 20 °C, in addition to an internal pump to provide system pressure. The flow rate to each VCSEL is set manually with needle valves, and the flow rates were monitored using SV4200 vortex flow meters[6]. [63, 64]

Cooling air is drawn from the main laboratory supply, provided at 6.89 bar. One branch passes airflow through the 3 Festo MS-Series[7] filters and a Festo MS-Series[8] dryer. The flow is divided in to seven lines, one per each VCSEL module. This is metered using a SMC digital flow switch[9], each set to 0.7 SLPM for an adequate VCSEL purge air supply. The other branch is fed directly to the Testing Facility, as required. [63, 64]

Both the VCSEL cooling water and purge air flow rates are reported to the Trumpf PPC108-50 unit, which is passed to the interlock system. The VCSEL units are disabled if flow rates drop below a predefined value, signifying either a blockage or cable disconnection [87]. Furthermore, the system will disarm if the VCSEL temperatures exceed a threshold

[1]Carrier, (2020). *Dynaciat Sales Brochure* https://www.ciat.com/en/eu
[2]Grundfos inc. (2020). *Technical Data - MAGNA 1 Circulator Pumps* https://www..grundfos.com/uk
[3]Grundfos inc. (2020). *Data Booklet - In-Line Circulator Pumps* https://www.grundfos.com/uk
[4]Turner, S. (2020). *Mikrofill 3 Pressurisation Booklet* https://www.mikrofill.com
[5]Trumpf (2020). *PPC108-50 VCSEL Management System* https://www.trumpf.com/en_GB
[6]IFM-Electronic, (2020). *SV4200 Vortex Flow Meter With Display* https://www.ifm.com/gb/en
[7]Festo. (2020). *Filters, MS Series* https://www.festo.com
[8]Festo. (2020). *Dryers, MS Series* https://www.festo.com
[9]SMC. (2020) *2-Colour Display Digital Flow Switch* https:/www.smc.eu/en-gb

or the water level drops substantially [87]. The VCSELs are controlled using the Trumpf PPU109-72 (main) and PPU109-48 (slave) driver racks, with a total of ten PPD007-12 drivers[10] to set VCSEL power and monitor feedback. This is tied in to the interlock system, which disarms in the event of a power surge or set point error. [63, 64]

The OLAHF facility can function with up to seven VCSELs, four supplying 2.4 kW each and three supplying 4.8 kW each [63, 64]. It is designed to be controlled through LabView, which is capable of interfacing with the VCSEL system and National Instruments DAQ. In addition, connections are in place for IR cameras, pyrometers, and digital monitoring devices. [63, 64]

5.2 Design Requirements and Considerations

1. **The components that make up ELSA, excluding supply lines, must not exceed 1.20 m x 1.20 m x 0.95 m.** These are the dimensions of the 1.20 m x 1.20 m optical table and 0.95 m of clear space above, provided by OLAHF [63, 64].

2. **The coolant air supply to the coupon must be capable of sustaining a mass flow rate of at least 2 $\frac{g}{sec}$, with a maximum of at least 4 $\frac{g}{sec}$.** A low-order thermal-fluid model from van de Noort [80] was utilised to estimate the required coolant flow for the DWEC system. The time step and conditions were tuned for laminar flow with inlet conditions estimated from the Murray [76] relations for the C6 geometry. An inlet gauge pressure of 200-400 kPa and an outlet gauge pressure of 0 kPa were used. The inlet temperature was set to 27 °C, and the film equations were replaced with VCSEL flux boundaries. Properties for air at the mean pressure and 250 °C were used. The solid domain was modelled using the conductivity for CMSX-4 at 527 °C, k = $14\frac{W}{m°C}$ [102]. A series of scaled powers were supplied uniformly to the outer surface, and the flow rate was adjusted to achieve an engine-representative gradient [42, 76, 79]. The maximum temperature predicted was 1014 °C, with a thermal difference of 203 °C at a coolant flow rate of 1.8 $\frac{g}{sec}$.

3. **The coupon mounting and coolant air supply must be compatible with the selected coupon and designed to thermally isolate the coupon within reason.**

[10] Philips-Photonics (2017). *VCSEL Driver Rack PPD007/8-xx Reference and Installation Manual* https://www.trumpf.com/en_GB

Heat loss to the mounting from the coupon will require offsetting through VCSEL power. Minimising this ensures the thermal field is more even and obtainable during steady-state. Additionally, the effective stiffness of the plenum must be maximised to constrain the coupon with a rigid boundary; however, the design must incorporate features that distribute stresses and ensure the plenum does not suffer premature failure.

4. **At steady-state, the maximum heat flux supplied to the coupon centre must be at least 5 $\frac{W}{mm^2}$ and up to 7.5 $\frac{W}{mm^2}$, at full power.** 5 $\frac{W}{mm^2}$ [96] was required, with an optimal value 50% greater,to ensure that Inconel 625 [108] and CMSX-4 [3] attain engine-representative temperatures. This maximum value was to be centred on the coupon with a low relative standard deviation to achieve a near-uniform temperature.

5. **Energy is to be supplied to a 35 mm x 35 mm area, and the flux distribution must be within 1 SD of the maximum in the centre 20 mm x 20 mm.** The total area and requirement for the even distribution were chosen to ensure that 4-5 film holes were exposed to engine-representative temperatures. This enabled the study of growth patterns in the area following initial crack formation.

6. **All components must be compatible with testing and measurement requirements**. For the coupon mounting and coolant air supply, imaging of the coupon surface was critical for crack detection. Ease of removal was included in the design approach to minimise the required time for testing. Similarly, measurement of the normal thermal gradient was required to maintain consistent cycling conditions. For the energy supply, a clear view of the exterior of the coupon was required for IR, digital imaging, and pyrometer measurements. The latter was of primary importance in tracking the maximum temperature throughout testing.

7. **Thermally sensitive components must be protected from VCSEL radiation and hot gases.** A build-up of thermal energy will occur in components connected to the coupon or exposed to VCSEL radiation. While natural convection and radiation do occur, the use of auxiliary water cooling loops may be necessary to ensure components do not creep or melt. This prevents large temperatures and thermal gradients in the assembly, allowing the system to survive at least 10000 cycles.

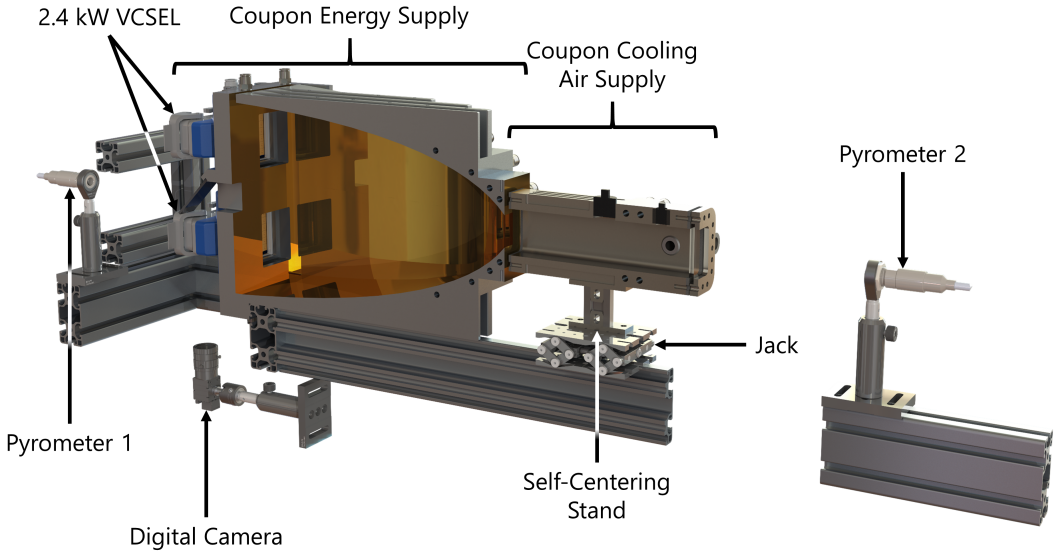


Figure 5.2: *cross-section of the Effusion Lifespan and Stress Addition showing the layout of assembled components*

5.3 Effusion Lifespan and Stress Addition (ELSA)

The requirements set out above led to a series of investigations that narrowed down the final design of ELSA, presented in Figure 5.2. This section presents the final design, giving a thorough account of various modules and constituent components and the motivations behind including them. ELSA is broken down in to modules, the large sub-assemblies that provide structure and supply the rig, instrumentation, and control system. The subsequent sections cover the various steps and studies taken to overcome design challenges and meet design requirements.

5.3.1 Modules

ELSA is mounted horizontally to fit the available space, as the VCSEL array power cables feature a considerable bend radius, adding 400 mm to the length of the pictured assembly. The assembly in Figure 5.2 measures 1190 mm long, 430 mm wide, and 700 mm tall. There are two main modules: the coupon coolant air supply and the coupon energy supply. Both feature integrated water cooling systems to prevent creep and melting in ELSA components.

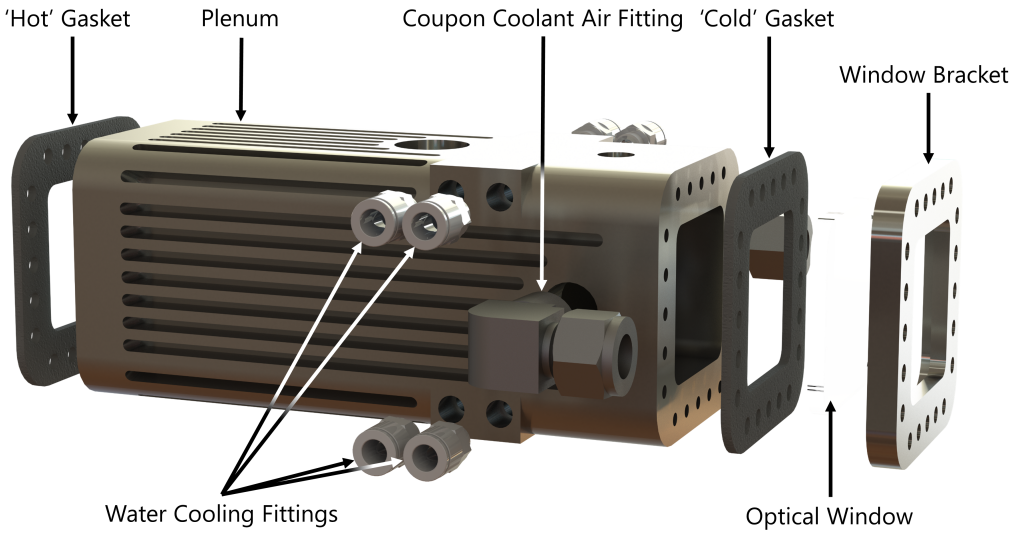


Figure 5.3: *render of the coupon cooling air supply in the absence of fasteners, with components labelled*

5.3.1.1 Coupon Coolant Air Supply

The application of laser power alone is not compatible with long-duration testing, as cooling of the test section is imperative to drive thermal gradients responsible for thermal stresses [100, 101, 102, 103]. The use of air as coolant is commonplace in jet engines, although it is at much higher pressures and temperatures [93, 107] than the laboratory air available. The coupon coolant air assembly was designed to provide both mounting and 6.89 bar lab-temperature air to the coupon. This offered a unique opportunity to exaggerate the thermal gradient through a lower coolant temperature.

The components of the assembly were CNC milled in-house from 304 steel due to its high continuous operating temperature of 925 °C [62]. A flange connection for the coupon was considered; however, a thick plenum wall decreases stresses and increases stiffness. A 17.5 mm thick wall was used throughout the length. The internal sizing of the plenum is identical to the coupon, with a 50 mm x 50 mm cross-section and corner fillets of 5 mm. The exterior sizing matches the coupon, as well, at 85 mm x 85 mm with 15 mm corner fillets. As there are no reflecting surfaces, it did not require additional surface finishing. Two Milam PSS gaskets, provided by Klinger [11], were used to seal both ends. The gaskets are capable

[11] Klinger Holdings (2022). https://www.klinger-international.com/en

of continuous operation at 900 °C and have a thermal conductivity of 0.5 $\frac{\text{W}}{\text{m°C}}$ [65]. One interfaces with the coupon, and the other seals against a sapphire window, provided by UQG Optics[12]. This enables the transmission of IR light for pyrometer measurements of the cold side of the coupon as sapphire has a high transmission rate of approximately 89% between 1.45-1.75 μm [122]. Sapphire glass also has high tensile and compressive strengths: 0.27 GPa and 2.00 GPa, respectively [122]. The window was affixed to the 'cold' side of the plenum using a steel bracket. The coolant supply was connected to the plenum using Swagelok[13] Elbows, connected to a $\frac{1}{2}$" Swagelok FM Series Hose. These components allow operating pressures in excess of 60 bar at temperatures up to 450 °C [110, 111]. The location of the fitting was not expected to exceed 50 °C during normal operation as they are opposite the coupon with respect to the water cooling channels (see Figure 5.3); however, the components were selected to ensure that there was no rapid failure should there be a fault in the water cooling system. The grooves were milled on the side of the plenum to retain mechanical stiffness and decrease the cross-sectional area for heat flow, minimising conductive loss. The assembly was mounted to a rail using a post with a vertical slot. A tapered piece was affixed to the bottom of the plenum so that it self-centres when placed in the vertical slot. This design did not require the use of a fastener, as the weight of the assembly maintained its position in the vertical slot. The height of the coupon coolant air assembly was controlled using a small jack. This allowed the base of the post to be fixed in place and adjusted so that the CPC-coupon alignment and spacing were able to be tuned while also allowing for quick connection and disconnection for imaging.

5.3.1.2 Coupon Energy Supply

To achieve thermal loading, four 2.4 kW VCSELs were used to supply IR light to the coupon, for a total of 9.6 kW. The technical data for the 2.4 kW and 4.8 kW VCSELs, reproduced from [89], are presented in Table 5.1. As per the Table, the nominal heat flux values for the 2.4 kW array are insufficient to achieve the design requirements of the systems. The power intensity is below the 5 $\frac{\text{W}}{\text{mm}^2}$ minimum; however, the spatial variance is low. A CPC is a convenient and efficient [29, 41, 71, 130] method of increasing the power intensity of a source. A beneficial side effect was that the CPC is capable of directing energy to the

[12]UQG ltd. (2022). https://www.uqgoptics.com
[13]Swagelok Company (2021) https://www.swagelok.com/en

Module Specification		PPM412-12-980	PPM412-24-980
Dimensions L x W x H	[mm]	107.5 x 87 x 77	159.7 x 87 x 77
Nominal Optical Power	[kW]	2.4	4.8
Controllable Zones	[-]	12	24
Emission Area L x W	[mm]	40 x 52	40 x 104
Power Intensity	$[\frac{W}{mm^2}]$	1.15 (at aperture)	
Wavelength	[nm]	980 ± 20	
Beam Half Angle	[deg]	10 (95% power)	

Table 5.1: *relevant technical data of available Oxford Laser Heating Facility vertical-cavity surface-emitting lasers, reproduced from [89]*

required 35 mm x 35 mm target area.

A previous attempt to machine a CPC [96] resulted in significant warping during manufacturing due to the use of multiple thin sections, which inhibited final performance as the reflecting surfaces deviated from the ideal CPC curve. Given this, the CPC was machined from two blocks of aluminium. They were CNC milled before various surfaces, coloured gold in Figure 5.2, were hand-polished to a maximum surface roughness of 200 nm. These polished surfaces were then plated with 50 nm Ni-Cr and 0.4 μm gold by Teer Coatings[14]. The combination of low surface roughness and IR reflectance of gold resulted in a surface that reflected more than 95% [64] of the VCSEL power.

The reflection of light off the target surface back in to the CPC was a concern, as this light may strike the VCSEL. The thermal load introduced was deemed unacceptable for the arrays as a result of their cost. The standard VCSEL cooling system was thought to be unable to handle any additional energy in to the VCSEL system. The polished gold surface present on the VCSEL bracket, affixed to the inlet of the CPC, reflected rays that were both rejected by the CPC and reflected off the target. The physical barrier provided by the reflecting surface protected the VCSELs from this rejected or reflected light. The VCSEL bracket features several cut-outs for VCSEL radiation to pass through, in addition to a viewport. A cold mirror was mounted at 45 degrees to the mounting bracket on the exterior of this viewport. It allows IR light through while reflecting visible light. This enabled the digital camera and the IR pyrometer to share line-of-sight through the small hole at the top of the VCSEL bracket. It also ensured that the digital camera receives minimal thermal

[14]Teer Coatings ltd. (2021) https://www.teercoatings.co.uk

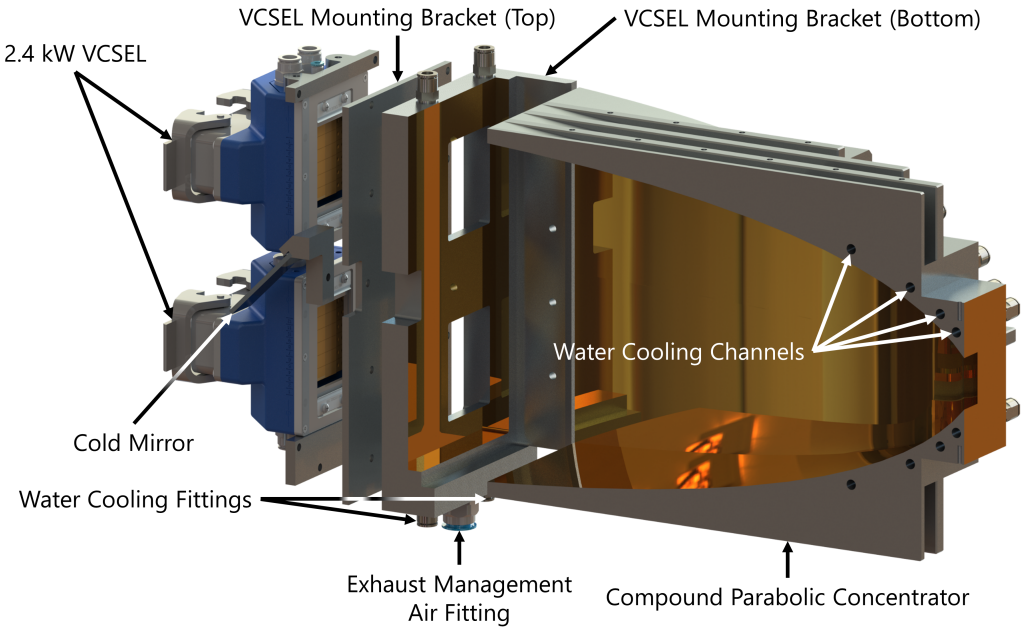


Figure 5.4: *render of the coupon energy supply in the absence of fasteners, with components labelled*

radiation, preventing damage to the electronics through overheating. Two large channels were milled in to the VCSEL bracket and run vertically inside the assembly. These provided a large volume of cooling air to protect the VCSELs from exhaust gas from the coupon, which otherwise enters the CPC and contacts the outer surface of the arrays. These were supplied through the labs' 6.89 bar line, running parallel to the coupon coolant air and VCSEL purge air lines. Together, this air supply and associated channels are referred to as the exhaust management system.

5.3.1.3 Water Cooling

IR light incident on the coupon, CPC, and VCSEL bracket introduces a risk of overheating. Aluminium exhibits creep behaviour above 250 °C [132]. To address this, the plenum, CPC, and VCSEL bracket all feature channels for cooling water supplied by the auxiliary loops in the existing OLAHF architecture [63, 64]. 7 mm diameter horizontal channels were drilled through the width of the plenum and the CPC to allow cooling water to flow through the components. Similarly, 7 mm diameter channels were drilled vertically in to the VCSEL bracket. There are two halves of the CPC, each with the four channels labelled in Figure 5.5, for a total of 16 water cooling channels for the whole rig.

A schematic showing the connections between the various systems is presented in Figure

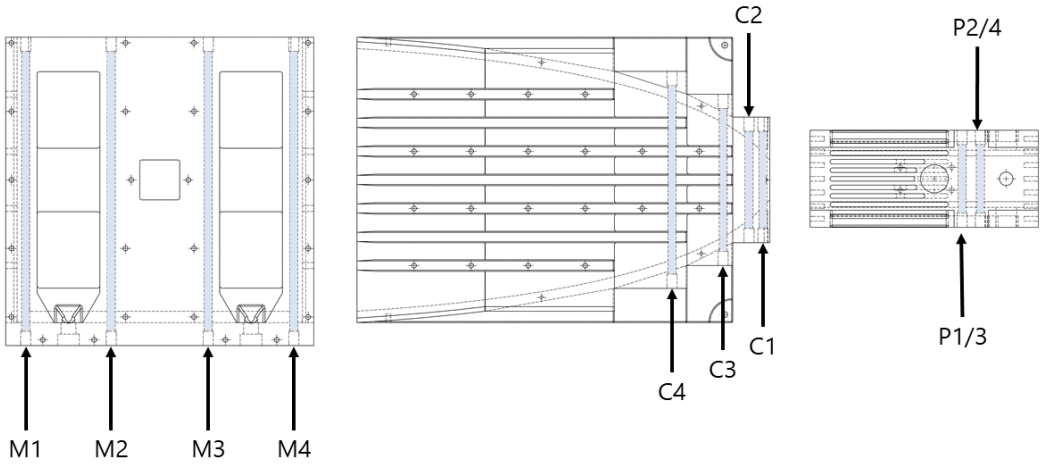


Figure 5.5: *locations and identification of water cooling channels in machined components, from left to right: vertical-cavity surface-emitting laser bracket, compound parabolic concentrator half, coolant plenum*

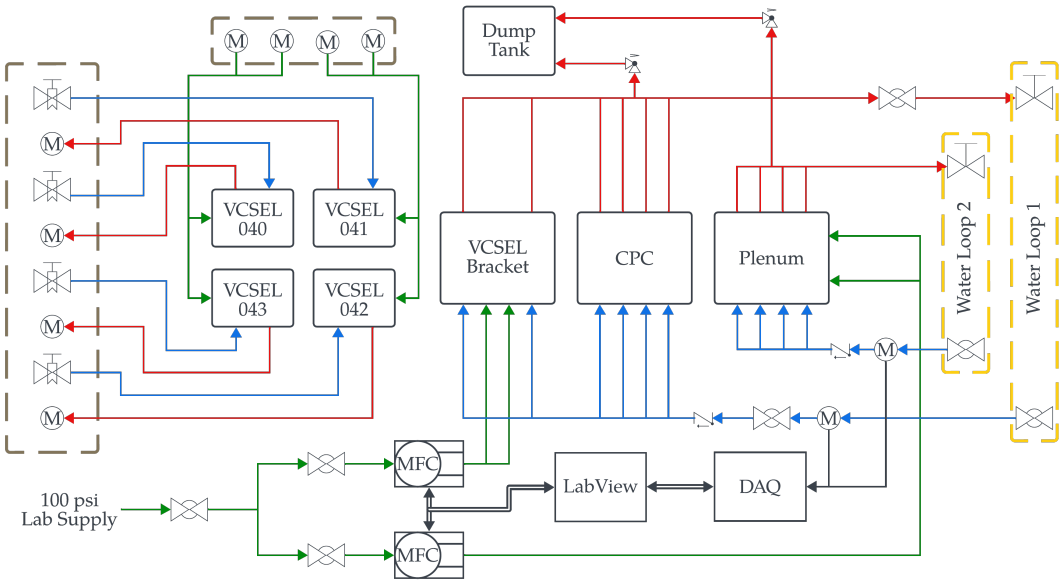


Figure 5.6: *schematic of the Effusion Lifespan and Stress Addition-specific supply lines and the integration to the Oxford Laser Heating Facility with blue as the cooling water out, red as the cooling water return, green as the 6.89 bar dry air supply, and black as the data transfer connections*

5.6. It shows the multiple line divisions and connections to the designed components. Dashed lines denote those features or fittings that integrate with the existing facility.

5.3.2 Instrumentation and Metering

The properties of the coolant air were measured using the Alicat MC-Series[15] controllers. A 200 SLPM variant was used for the coupon coolant air to provide the required 4 $\frac{g}{sec}$, while a 1000 SLPM variant was used for the exhaust management system to ensure adequate capacity to protect the VCSEL arrays. The flow temperature and volumetric flow in LPM and SLPM were recorded, as well as the air temperature at each sampling interval. The flow temperature was accurate to ±0.75 °C, while the pressure was accurate to within ±0.8% of reading plus ±0.2% of full-scale [5].

The thermal measurements of the coupon were provided by two Optris[16] CTratio 2M pyrometers. They provide emissivity-independent temperature measurements between 400 and 1500 °C [83]. The recorded value is the maximum temperature measured within a narrow beam with a thermal resolution of 0.1 °C and an accuracy of ±(0.5% + 2 °C) [83]. As the fraction of transmitted light is more significant than 0.85 for both the cold mirror [118] and the sapphire window [122], the emissivity-independent pyrometers did not require signal amplification [83]. Optris PI 640i infrared cameras [84, 85] were used to complement the narrow beam of the pyrometer. These provide spatial thermal measurements between -20 and 1500 °C at an accuracy of ±2% between 8-14 μm. The final images were calibrated for the surface emissivity of the coupon using the true temperature, reported by the emissivity-independent pyrometer [83]. The final coupon measurement was used to monitor the mounting ring temperature. A type K thermocouple was sandwiched between the coupon and the hot gasket. This provided measurements for later use in post-testing FEA to calibrate a model for conductive loss through the plenum.

Two mass flow meters, one for each water cooling loop, were used. The Omega FLMW[17] devices are shown at the bottom right of Figure 5.7. Two models were used: a 37 LPM unit for Loop 1 and a 19 LPM unit for Loop 2. These provide monitoring of the coolant flow rate within ±2% of the full scale. They were connected to the LabView control program

[15] Alicat Scientific inc (2021). https://www.alicat.com
[16] Optris ltd. (2020) www.optris.com/en
[17] Omega Sensing Solutions plc. (2020) *Economical In-Line Liquid Flow Meters* https://www.omega.co.uk

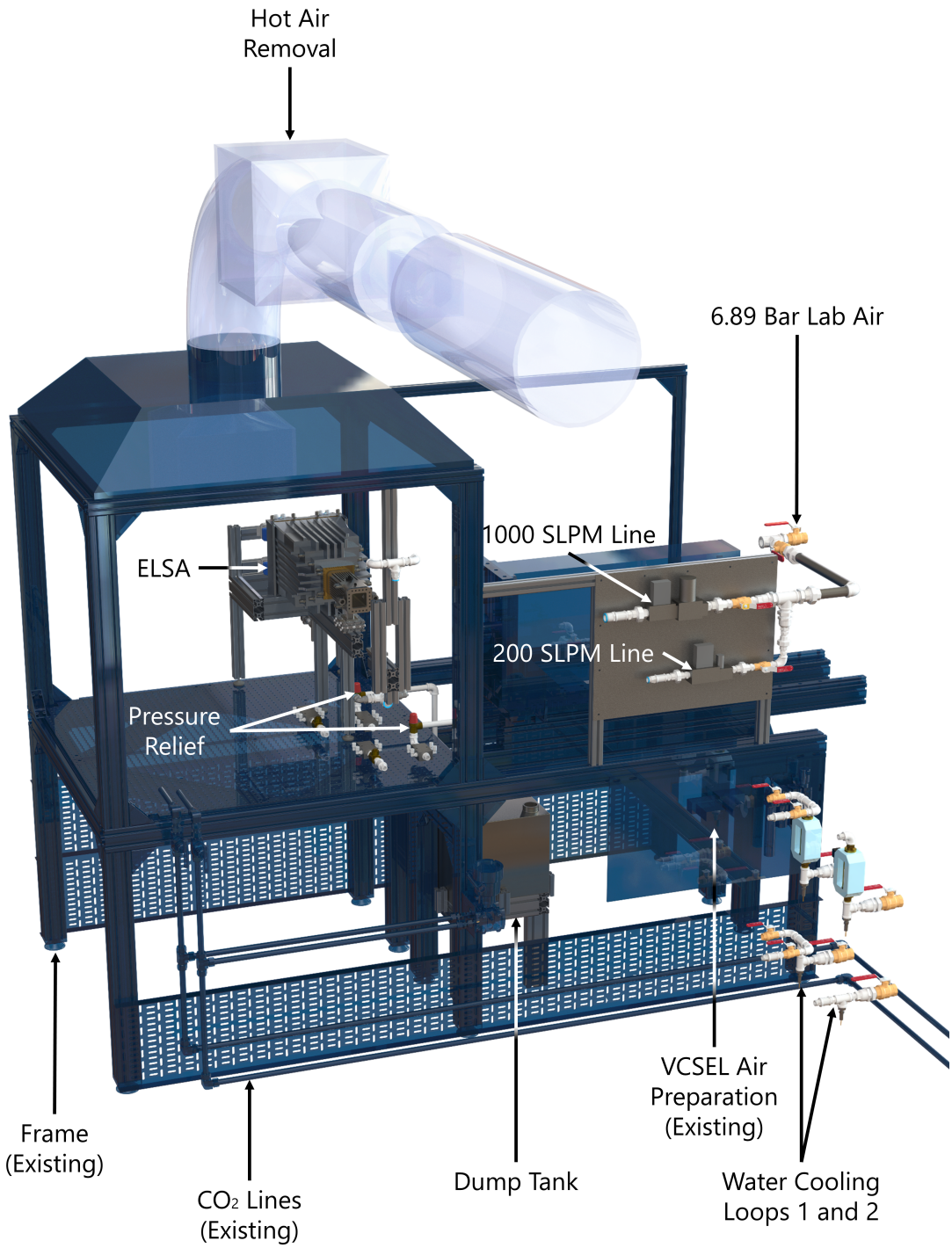


Figure 5.7: *render and identification of the Effusion Lifespan and Stress Addition systems, shown in representative colours of various materials, integrated in to the existing Oxford Laser Heating Facility, shown in dark blue*

and disarmed the system in the event of a blockage or fitting rupture, corresponding to a significant decrease or increase in flow rate, respectively.

Two Lucid Phoenix cameras were used for rig monitoring purposes. One viewed the hot surface of the coupon through the cold mirror. The other is not pictured and viewed the rig as a whole from the side. Type T thermocouples were placed in areas of maximum temperatures, as determined by finite element analysis (FEA). One was placed next to each of the four plenum coolant channels. Four were embedded in 3 mm diameter holes, bored to within 2 mm of the CPC reflecting surfaces at the exit aperture. Two additional thermocouples were placed on the top surface of the CPC adjacent to the water channels C3 and C4, identified in Figure 5.5. The aforementioned thermocouples were set to alarm above 100 °C. Four final thermocouples, one each, were placed on the VCSEL arrays and alarm over 40 °C.

The detection and measurement of cracks was performed by digital imaging of the exterior surface, as the predicted mode of failure was tensile rupture during shut-down following an accumulation of plastic deformation during start-up and hold. These cracks were hypothesised to be easy to detect as they would remain open after being cooled to room temperature. A Canon[18] EOS 850D body was used with an EF 100 mm f/2.8L Macro Lens. This provides a high degree of resolution (4000 px x 6000 px), with a minimum focus distance of 300 mm [24, 25]. A frame was constructed with two consistent and rigid camera mounting points. One captures the entire test region of the coupon and the other captures each hole in greater detail. Multiple close-up images of each coupon were taken at each imaging stage. A MATLAB[19] script was written to stitch the close-up images together and re-balance the colour profile for the overlap region to get a full, high-resolution image of the coupon surface. Measurements for feature size and development were performed using a simple trigonometric pixel-distance conversion:

$$P_s = \tan\left(\frac{AOV_H}{2}\right)\frac{d}{P_w} \tag{5.1}$$

Where P_s is the size of the pixel in metres, AOV_H is the angle of view in the horizontal direction, d is the distance from the lens to the object in metres and P_w is the half-width of

[18] Canon Camera Co. inc. (2021) https://www.canon.co.uk
[19] The MathWorks, inc (2021), *MATLAB version: 21.1 (R2021a)*, https://www.mathworks.com

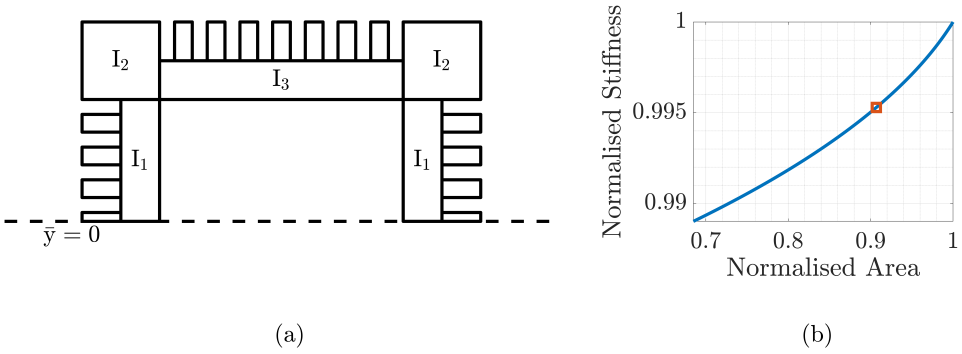
the image, in pixels. Using the properties of the camera and lens, the angle of view was 19.8 degrees, the pixel width was 6000 px, and the distance between the receiver and the object was 0.21 m ±0.005 m, for close-up, or 0.24 m ±0.005 m for wide view. This corresponds to a pixel distance of 6.11×10^{-6} $\frac{\text{m}}{\text{px}}$ $\pm$ 1.45×10^{-7} $\frac{\text{m}}{\text{px}}$ and 6.89×10^{-6} $\frac{\text{m}}{\text{px}}$ $\pm$ 1.45×10^{-7} $\frac{\text{m}}{\text{px}}$, respectively. Aberrations did not need to be considered due to the use of a macro lens [24].

5.3.3 LabView Control System

A control system was developed with the help of AMH Test Systems[20]. The set-up was based on the existing OLAHF code [63, 64]. The profiles for VCSEL power and both the 200 SLPM and 1000 SLPM coolant air lines were interpreted from CSV files and treated as step functions. Additional flexibility in logging was included by specifying the desired recording frequency between various cycle times. This reduced the data collected, as the frequency may be high for thermal ramping and reduced for holds. Feedback and active monitoring of both the experimental and process parameters was displayed live. Warnings and alarms were defined for appropriate ranges, with critical thermal measurements set to trigger shut-down on alarm. A complementary MATLAB life script reported peak temperatures and thermal gradients for each cycle. This was done to help the operator determine various trends over the course of many cycles, allowing the adjustment of the power and coolant air supplies to maintain the appropriate thermal conditions.

5.4 Coupon Coolant Air Supply

There were two challenges in designing the coupon coolant air supply: mitigating the conduction from the coupon to the plenum and preventing choking in the air supply lines. The former was solved by reducing the cross-sectional area and extending the length of the plenum. This increased the thermal resistance of the component and reduced the heat conducted away from the coupon. The latter was solved through a compressible flow analysis to ensure that the flow remained below a Mach number of 0.5.



(a) (b)

Figure 5.8: *(a) geometry used to evaluate the plenum stiffness showing various second moment of areas used (b) normalised stiffness versus normalised cross-sectional area showing a near 10% reduction in area for a 0.5% reduction in stiffness over the range of geometries studied*

5.4.1 Minimising Conductive Losses

The removal of material to reduce the cross-section of the plenum was thought to reduce the second moment of area of the plenum. This was to be avoided, as a quasi-rigid boundary for the coupon was considered beneficial due to the elevated stress state and earlier predicted failure. To assess the feasibility of the reduction of area, an analysis was performed relating the second moment of area of a half-section of plenum about the neutral axis in the centre for an idealised domain. The geometry is shown in Figure 5.8 (a). The dimensions were identical to those of the plenum, and the neutral axis was labelled at y = 0. The second moment of area was calculated for each individual section and translated from the neutral axis using: $I_i = I_{i,s} + A_i d_i^2$, where d is the distance between the body and the global neutral axes. The grooves were 3.5 mm wide and vary in depth from $\hat{t}$ =[0,1], where $\hat{t}$ was the normalised distance through the skin. It was hypothesised that this groove approach would leave enough material far enough from the neutral axis as to maintain a high second moment of area.

Figure 5.8 (b) presents the relative change in area with respect to the effective stiffness. Both were normalised by their maximum value, corresponding to $\hat{t} = 0$. While $\hat{t} = 1$ results in a plenum that does not have functioning walls to contain the flow, it was shown that over the entire range of $\hat{t}$, a decrease in the cross-sectional surface area of 32% corresponds to a decrease in stiffness of only 1.1%. To ensure that the walls were capable of containing fluid, a minimum wall thickness of 7.5 mm was used. This corresponds to a $\hat{t}$ of 0.57, and was

[20] AMH Test Systems ltd. (2023) http://amhtestsystems.co.uk

marked in Figure 5.8 (b). The area was reduced by approximately 9.5%, while the stiffness decreased only by 0.5%.

Pathway	A $[m^2]$	L [m]	k $[\frac{W}{m°C}]$	h $[\frac{W}{m^2°C}]$
Gasket	4.078 E-3	3 E-3	0.5	-
Plenum	3.115 E-3	[1 E-3,2 E-1]	32	-
Channel	2.638 E-3	-	-	3513

Table 5.2: *material properties used in the low-order thermal resistance model of the plenum assembly*

The increase in the length of the plenum enables the water cooling channels to be further from the coupon; however, this increased distance risks having cooling channel wall temperatures in excess of the boiling point of water. Therefore, a low-order thermal resistance model was used to assess the benefits of this approach. Figure 5.3 was reduced to four points in a linearly connected system: the coupon side of the hot gasket, the hot gasket-plenum interface, the cooling channel walls and the cold water. This relates to two conduction pathways and one convection pathway. The geometric values are shown in Table 5.2. Thermal conductivity values were taken from Klinger [65] for the 3 mm thick gasket and The American Institute of Iron and Steel [62] for the plenum. The convective heat transfer coefficient was calculated using a Dittus-Boelter correlation for a 7 mm diameter channel carrying 2.5 LPM water. The length of the plenum varied and the temperatures at each node were studied. The coupon temperature was set to 1000 °C, and the water temperature was set to 6 °C at 2 bar gauge.

Figure 5.9 presents the normalised thermal data from the model for the range of lengths studied. The temperatures were normalised by the design maxima, set to 500 °C for the hot gasket-plenum interface and 50 °C for the channel walls. Both values were selected to provide a thermal safety factor of at least 1.5 from creep [62] and boiling [58]. The length of the plenum is normalised by the value selected for ELSA. Increasing the length of the plenum increases the thermal resistance. Less heat was removed from the hot gasket-plenum interface, and the temperature of the node increased. This reduction in heat flow decreases the temperature of the wall of the coolant channel, reducing the risk of boiling. The region where both curves were below y = 1 is considered acceptable. The optimal point was chosen

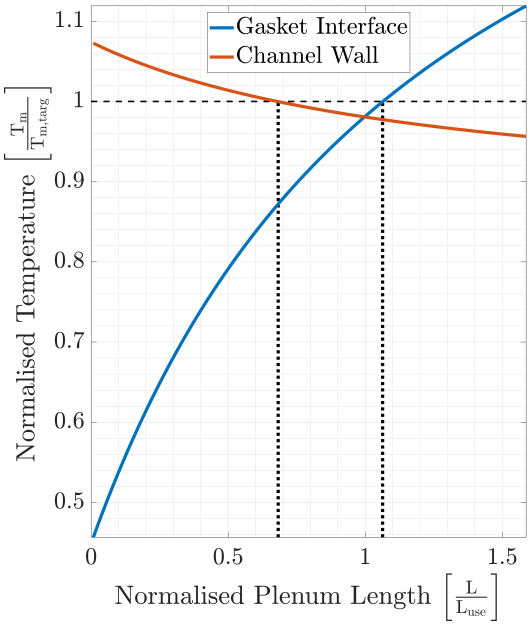


Figure 5.9: *normalised plenum end-temperatures versus overall plenum length*

as the intersection of both curves as it represents the geometry for which both temperatures undershoot the design maximum by the same per cent margin.

5.4.2 Coolant Supply Sizing

The performance of both the coupon coolant air supply and exhaust management system would be reduced if any of the 6.89 bar air supply lines were undersized. Based on design requirements, a 200 SLPM line and a 1000 SLPM line were required, allowing 4.3 $\frac{g}{sec}$ and 21.5 $\frac{g}{sec}$ of metered coolant flow.

The coolant air was piped using both galvanised steel and flexible nylon tubing. The flexible tubing has a uniform diameter for each line. The pipe diameters were selected using isentropic flow equations at a range of flow pressures for each flow rate. A maximum Mach number cut-off of 0.5 was chosen to ensure an adequate speed margin to avoid choking. Pipe diameters of 25.4 mm were selected for the upstream feeds, 19.1 mm for the 1000 SLPM line, and 12.7 mm for the 200 SLPM line. A 22 mm diameter tube supplied the 1000 SLPM flow to a manifold, which split in to two lines, one for each channel in the VCSEL bracket. The manifold was attached to the VCSEL bracket using 16 mm diameter tubes. The 200 SLPM line was fed using 16 mm diameter tubes. Taking in to account the 7 SLPM required

for the VCSEL array purge air, the maximum Mach number was below 0.39 at standard sea level pressure for the maximum flow rate in each section of the lines. The system was rated at 10 bar and 90 °C, well over the 6.89 bar inlet pressure.

5.5 Coupon Energy Supply

As was the case with the coupon coolant air supply, there were two significant obstacles to the design of the coupon energy supply. The design of a CPC that would feature a large enough inlet aperture for the selected VCSEL configuration was not possible given Equation (2.20) for a standard CPC. A new formulation for the reflecting surfaces was required to enable a CPC with the correct inlet and outlet sizing and an acceptance angle that would accommodate the beam divergence of the VCSELs. The second hurdle was the protection of the VCSELs from both IR radiation and hot gas from the coupon. The VCSEL bracket solved both of these problems through its reflecting surface and exhaust management system.

5.5.1 Modified CPC Equations

For a given a_{in} and θ_{acc}, a_{ex} is defined by Equation (2.19). Using Equation (2.19), it was concluded that the maximum inlet dimensions for the specified outlet dimensions and a $\theta_{acc} > 10$ degrees were 201.56 mm x 201.56 mm. This was not acceptable for this application, as a 240 mm x 240 mm inlet aperture was required to ensure that the VCSELs and optical viewing ports had sufficient space.

Increasing the acceptance angle decreases these dimensions. In contrast, lowering the acceptance angle was not possible as the half-angle of the beam of the supplied VCSELs [89] is 10 degrees. Instead, a novel approach for the formulation of a CPC was derived. The alteration of the reflecting surfaces is not new, having been undertaken by Metcalf [71]. Whereas Metcalf [71] added undulations to the surface with the aim of increasing efficiency, the approach taken in this work breaks the constraint: that the focus of 'Parabola A' must exist at the outlet on 'Parabola B', and vice-versa. Removing the focal point from this location increased the number of rejected rays, decreasing efficiency; however, analysis shows that this was a reasonable trade-off to ensure compatibility with this set-up. Additional features were also used to minimise this additional incurred loss. Figure 5.10 (a) shows a comparison of the same CPC with a reformulated case, with focal points marked.

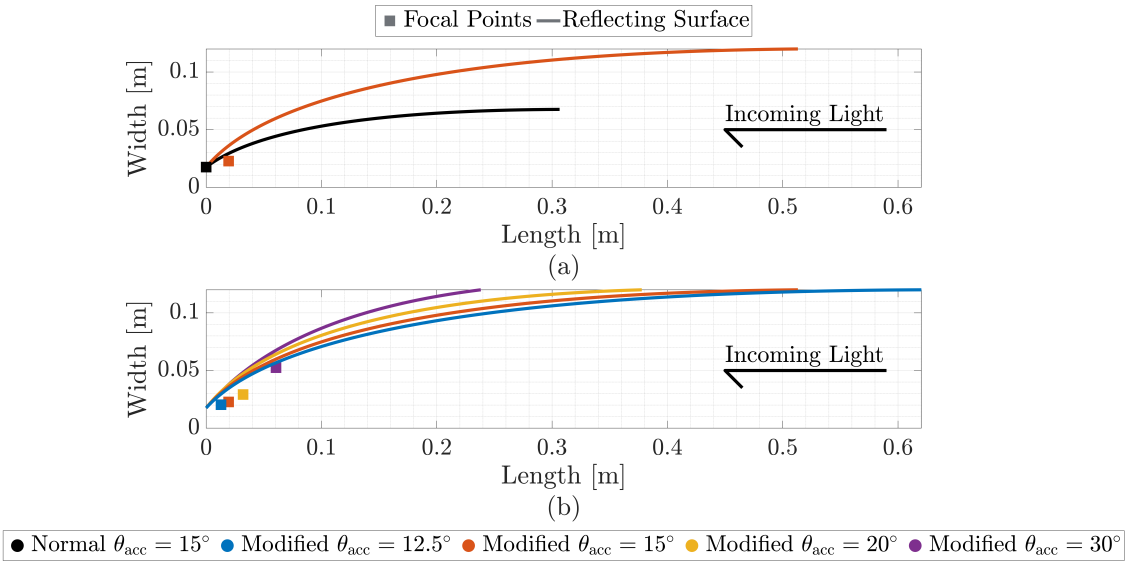


Figure 5.10: *reflecting surface profiles and focal points for (a) comparison between a normal compound parabolic concentrator and a modified compound parabolic concentrator for the same* θ_{acc} *(b) comparison between the modified compound parabolic concentrators investigated*

The equation for the modified CPC reflecting surface is defined as a parabola of the form $y = ax^2 + b$, which is rotated about the origin by θ_{acc}. Through the novel approach, a new CPC height, h_{cpc}, and offset from the origin, δh_{cpc}, are defined using:

$$h_{cpc} = \frac{a_{in} + a_{ex}}{\tan \theta_{acc}} \quad \text{and} \quad \delta h_{cpc} = \frac{a_{ex}}{\tan \theta_{acc}} \tag{5.2}$$

Two points are defined as $(a_{in}, h_{cpc} + \delta h_{cpc})$ and $(a_{ex}, \delta h_{cpc})$, which denote the inlet and outlet of the CPC, respectively, along the reflecting surface. These points are transformed through a rotation by $-\theta_{acc}$. A parabola in the form $y = ax^2 + b$ is then defined as:

$$\begin{aligned} a &= \frac{-2\, a_{in} \sin(\theta_{acc})^2 + a_{ex} + a_{in}}{4\, a_{in}\, (2\, a_{ex} + a_{in}) \left(\sin(\theta_{acc}) - \sin(\theta_{acc})^3\right)} \\ b &= \frac{a_{ex} \left(-{a_{ex}}^2 + \cos(2\,\theta_{acc})\; a_{ex}\, a_{in} + \cos(2\,\theta_{acc})\; {a_{in}}^2\right)}{a_{in}\, \sin(\theta_{acc})\, (2\, a_{ex} + a_{in})} \end{aligned} \tag{5.3}$$

This curve is rotated and offset by δh, so that the origin of the coordinate system is moved to the centre of the outlet. The coordinates of the modified reflecting surfaces are

given as:

$$\begin{cases} x_{mod} = t_{mod} \sin\theta_{acc} - \left(at_{mod}^2 + b\right)\cos\left(\theta_{acc}\right) \\ y_{mod} = t_{mod} \cos\theta_{acc} - \left(at_{mod}^2 + b\right)\sin\left(\theta_{acc}\right) \end{cases} \tag{5.4}$$

$$\text{and} \quad 2a_{ex}\cos\left(\theta_{acc}\right) \leq t_{mod} \leq 2\left(a_{ex} + a_{in}\right)\cos\left(\theta_{acc}\right)$$

Figure 5.10 (b) compares the profiles and focal points in a range of θ_{acc}. As the θ_{acc} is increased, the focal point shifts up and away from the exit aperture. This was predicted to decrease the efficiency of large θ_{acc} concentrators.

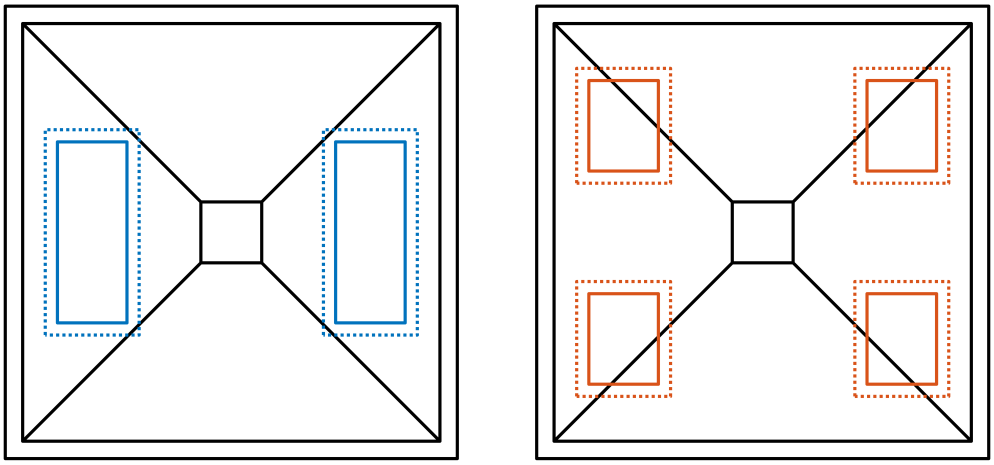
5.5.2 Selection of Concentrator Configuration

Following the derivation of these equations, the modified CPC was investigated using ray-tracing, performed in LightTools[21], to determine the best configuration of the CPC, VCSEL bracket, and VCSELs. The available system architecture for OLAHF [64] dictates the use of a combination of 2.4 kW or 4.8 kW VCSELs as a heat source. It was decided to use either two 4.8 kW arrays or four 2.4 kW arrays to supply 9.6 kW of power. This section refers to these as the 4.8 kW and 2.4 kW configurations, respectively.

5.5.2.1 Domain and Boundary Conditions

Four CPC profiles, shown in Figure 5.10 (b), were investigated. A minimum θ_{acc} of 12.5 degrees was chosen to increase the tolerance for VCSEL misalignment and other manufacturing defects from CNC milling [1]. A range of acceptance angles were studied to investigate the effects of altering the CPC shape using modified equations. Previous work indicated a dependence on the alignment of the VCSEL [96]. Two configurations of VCSELs were studied, shown in Figure 5.11 (a). The dashed lines show the extent of through-holes modelled in the VCSEL bracket, offset by 7.5 mm from the sides of the VCSEL emitting surfaces to account for the beam half-angle. For ray tracing, the VCSEL bracket was represented by a flat surface that covers the rear of the CPC, where the VCSELs are fitted. Simulations were run for each case with and without the VCSEL bracket. In an effort to reduce the overall height of the CPC, a 'short' version was investigated for the cases $\theta_{acc} = 12.5$ degrees and $\theta_{acc} = 15$ degrees. The reflecting surfaces were defined by the same x and y as in Equation (5.4); however, t_{mod} was limited such that the inlet aperture was 230

[21] Synopsis inc. (2022) *LightTools(64) 2022.03 SR1* https://www.synopsis.com



(a) (b)

Figure 5.11: *vertical-cavity surface-emitting laser array configurations used in the ray tracing analysis for (a) the two 4.8 kW arrays (b) the four 2.4 kW arrays, with the solid lines representing the extent of the emitting surfaces, while the dashed lines denote the size of the through-hole in the VCSEL bracket, sized to accommodate a beam half angle of 10 degrees [89]*

mm x 230 mm. The internal faces of the CPC and the internal face of the VCSEL bracket were set as reflecting surfaces. Each of the reflecting surfaces was modelled as perfectly reflective.

The VCSELs were modelled using rectangular surface sources set to the dimensions in Table 5.1. Each was set to its maximum radiometric power. The beam distribution of each individual VCSEL was not modelled. Instead, a beam half-angle of 7 degrees was used for an even distribution. An approximation of Equation (2.18) was made by comparing even distributions across a range of angles and intensities. These were set such that the total power was identical to the VCSEL when integrated over the distribution. These were compared with the VCSEL distribution by root mean square difference (RMSD). The results and comparison are presented in Figure 5.12. As labelled, the 7- and 8-degree approximations have the lowest RMSD from the VCSEL distribution. The 7-degree distribution was selected because it was within 6% of 8 degrees, the minimum, and captured the highest values in the centre.

The rays from the exit aperture of a CPC diverge at angles up to 89 degrees [96, 130], requiring that the test section be placed close to the exit aperture. The receivers were placed

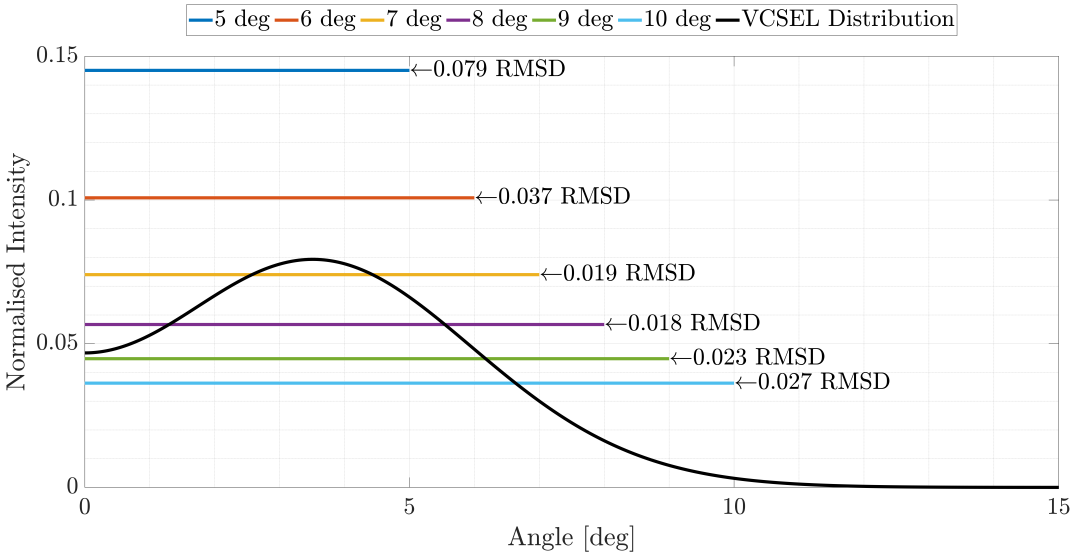
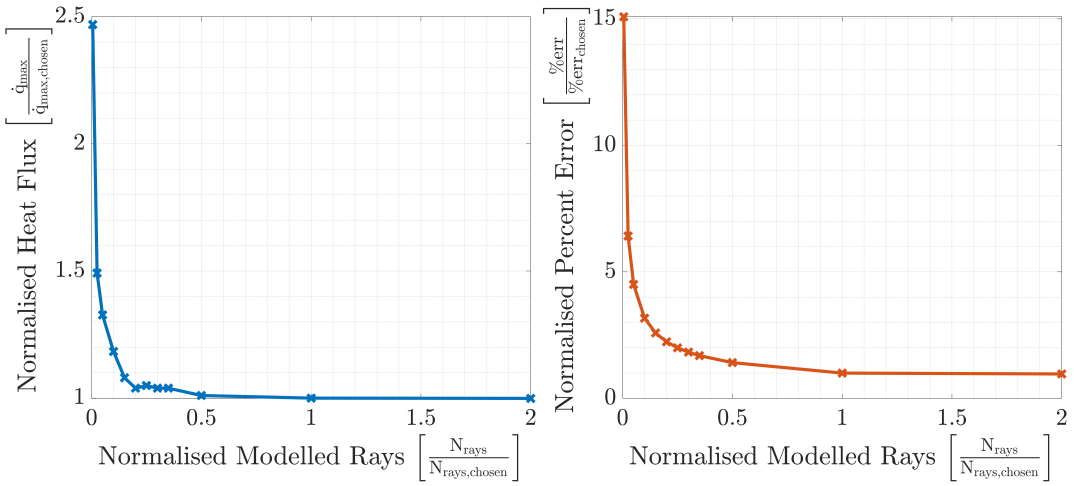


Figure 5.12: *vertical-cavity surface-emitting laser angular distribution [88], in black, and comparison to uniform distribution approximations for the same total emitted power, with root mean square difference values included to show the relative accuracy of each approximation, compared to the true distribution*



(a) (b)

Figure 5.13: *results of the independence study showing convergence to a ray-independent solution, done by increasing the number of modelled rays and tracking their effect on (a) the maximum heat flux (b) the per cent error*

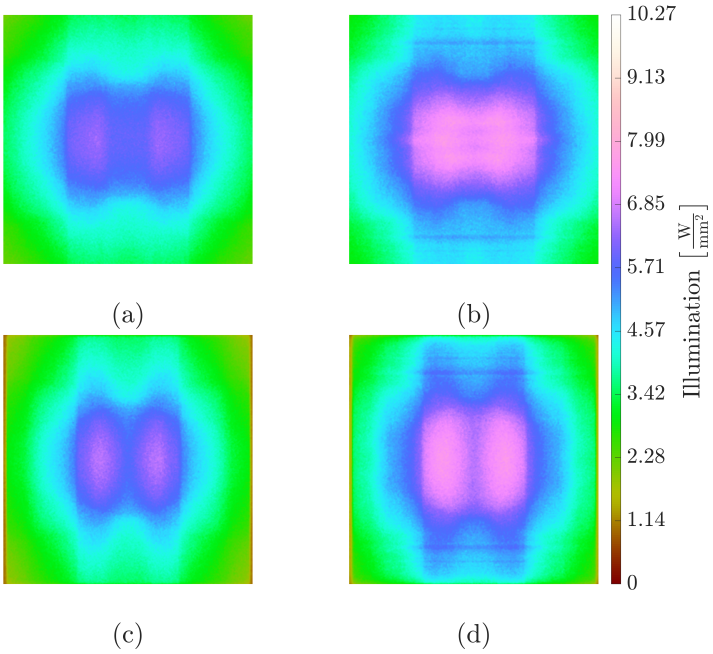


Figure 5.14: *illumination distributions for* $\theta_{\text{acc}} = 15$ *degrees showing (a) 0 mm target spacing (b) 0 mm target spacing with VCSEL bracket (c) 1 mm target spacing (d) 1 mm target spacing with VCSEL bracket*

at 0 and 1 mm from the exit aperture to compare the effect of increasing the spacing. A mesh size of 0.1 mm was chosen and an error-reduction study was performed by increasing the number of incident light rays until a stable solution was reached. The results of this are shown in Figure 5.13.

5.5.2.2 Results and Discussion

Figure 5.14 presents the four cases of incident flux on a target surface for a CPC with an acceptance angle of 15 degrees. The presence of a highly reflective surface on the VCSEL bracket greatly increases the optical efficiency of the CPC. The mean increase was 98.4% in all variants studied, with a maximum of 657% and a minimum of 9.36%. None of the geometries investigated saw a decrease in efficiency with the inclusion of the additional reflecting surface. The rejected rays are reflected back and have an extra chance to contribute to coupon heating.

Figure 5.15 (a) presents the optical efficiencies of each CPC for both the absence and addition of the VCSEL bracket surfaces in the range of acceptance angles studied, keeping the dimensions of the inlet and outlet apertures constant. Optical efficiency is defined as the ratio of energy out to the ratio of energy in, $\eta_{\text{opt,LT}} = \frac{\dot{q}_{\text{out}}}{\dot{q}_{\text{in}}}$. The black dotted line

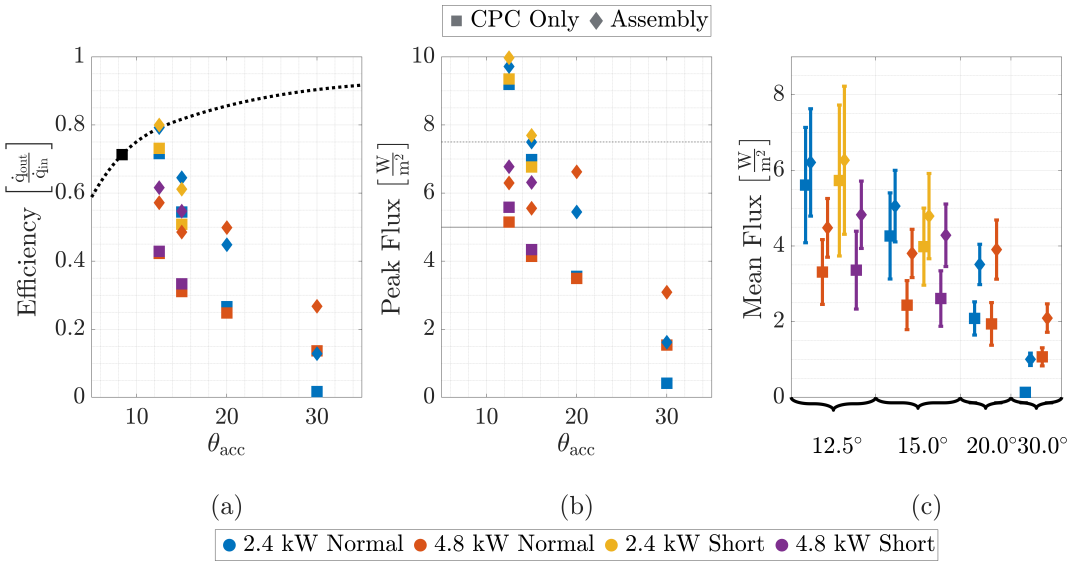


Figure 5.15: *comparison of assembly for a 1 mm target spacing, defined as the exit aperture from target plane separation for (a) optical efficiency (b) peak flux (c) mean flux and error bars of one standard deviation*

represents the theoretical η_{opt} for a standard-profile square-aperture CPC [29] with a fixed outlet aperture of 35 mm x 35 mm. The theoretical calculations model a surface reflectance of $\rho = 1$ and a mean surface roughness of 0.57 degrees, representative of a polished surface. The black square is the optical efficiency of a square-polygonal CPC with inlet dimensions of 240 mm x 240 mm, corresponding to a θ_{acc} of 8.39 degrees [29]. There was a clear trend for decreasing efficiency with increasing acceptance angle for identical inlet and outlet aperture sizes. It was consistent with the migration of the focal point away from the exit aperture shown in Figure 5.10 (b). This increases the number of rays that are rejected, especially for the cases without the VCSEL bracket. For the case of the 2.4 kW arrays and a θ_{acc} of 30 degrees, $\eta_{opt,LT}$ was 0.017. This penalty is minimised with decreasing acceptance angles. The trend intercepts the theoretical line near $\theta_{acc} = 8.39$ degrees, where the shape of the CPC from both formulations was the same, and the focal point lies in the exit aperture. For $\theta_{acc} = 12.5$ and 15 degrees, the short CPC was investigated to reduce the overall length of the CPC. Truncating the CPC to the height required to have an inlet aperture of 230 mm x 230 mm reduces the overall length by 30% for both cases. Doing so increases the efficiency of $\theta_{acc} = 12.5$ for both the 2.4 and 4.8 kW configurations. The efficiency increases for $\theta_{acc} = 15$ with a 4.8 kW configuration and decreases for the 2.4 kW case by 5.3%. Despite being supplied with identical power, the relative spacing of the arrays increases efficiency.

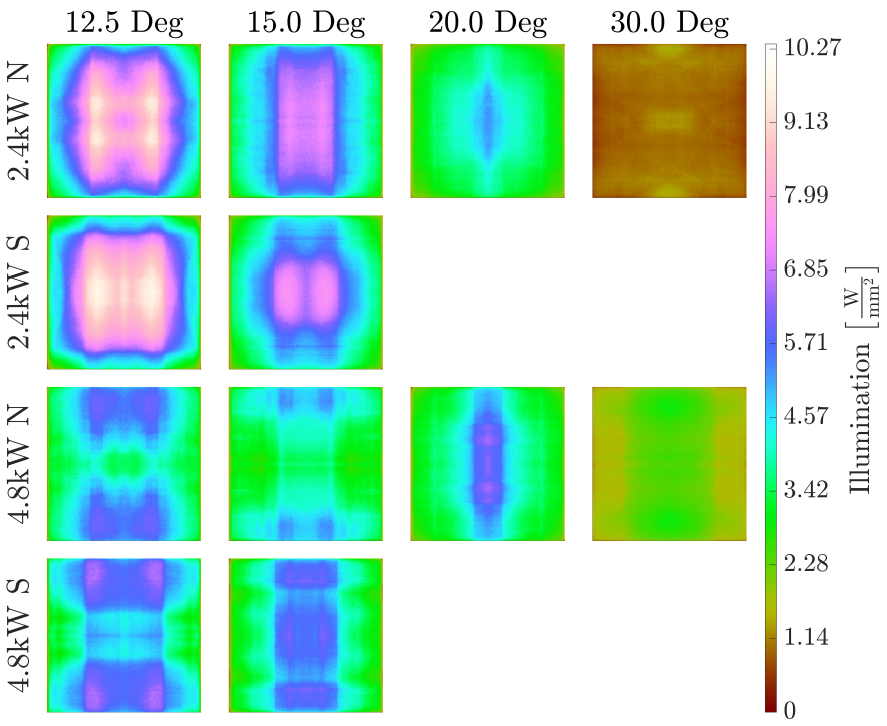


Figure 5.16: *illumination distributions for both VCSEL configurations and all acceptance angles at a 1 mm target spacing for a constant total power and aperture size*

Similar trends were observed for the peak and mean flux, reported in Figure 5.15 (b) and (c). The peak flux decreases with increasing θ_{acc}. A solid line representing the 5 $\frac{\text{W}}{\text{mm}^2}$ cut-off and a dashed line representing the 7.5 $\frac{\text{W}}{\text{mm}^2}$ target are provided. The high acceptance angle cases do not concentrate enough of the incident power to generate a sufficiently high heat flux. The 2.4 kW array configuration for the low acceptance angle CPCs provides the highest peak flux, with minimal improvements for the short cases in the presence of the VCSEL bracket. Bars are added to Figure 5.15 (c) with a length of 1 standard deviation. The addition of the VCSEL bracket decreases the standard deviation for $\theta_{\text{acc}} = 12.5$ and 15 degrees. Increasing the acceptance angle decreases the standard deviation.

The irradiance profiles for a 1 mm target spacing for all the studied configurations are presented in Figure 5.16. The 20- and 30-degree CPCs reject a large portion of the power and fail to provide sufficient power to the target. This is most pronounced with the 2.4 kW configuration with $\theta_{\text{acc}} = 30$. The 2.4 kW configuration outperforms the 4.8 kW configuration across all small acceptance angles studied. The exception is the 4.8 kW arrays and a θ_{acc} of 30 degrees. This was thought to be determined by the locations of the emitting

surfaces in Figure 5.11, in which the 2.4 kW arrays overlap the sharp corners of the CPC more than the 4.8 kW arrays. The results of Cooper [29] and Jackson [64] indicate that these corner regions act as light funnels, creating peak temperature distributions toward the corners of the exit aperture for uniform inlet light. The relative maximum flux is centred and greater for the discreet sources used. The 2.4 kW Short has a more symmetrically square distribution in the centre. The $\theta_{\text{acc}} = 12.5$ degree, in particular, features a large and comparatively uniform distribution throughout the target.

The selection of the final CPC design and configuration with VCSELs was based on the results laid out in this subsection. The CPC was defined using alternate equations for the formulation of the parabolic reflecting surfaces. The removal of the 'focal point' constraint allows for tailored inlet and outlet sizing at a minor expense of optical efficiency. A comparison of the distributions shows a clear choice in the 2.4 kW configuration, since the peak flux was central to the target plate and the distributions were relatively symmetric. The configuration selected for ELSA was the 2.4 kW Short configuration, $\theta_{\text{acc}} = 15$ degrees. It was differentiated from other low θ_{acc} CPCs due to the central nature of the peak flux. The remaining three options feature fluxes greater than $5\frac{\text{W}}{\text{mm}^2}$ near the periphery, which was thought to risk overheating away from the cooled central region.

5.5.3 VCSEL Bracket and Exhaust Management

Following the selection of the CPC design, a study of the construction of the VCSEL bracket was performed. In order to protect the VCSEL arrays from the hot coupon exhaust, two methods were proposed: a solid boundary and convective cooling. The solid boundary consists of a window fixed to the VCSEL bracket to prevent the hot gas from reaching the VCSEL array of the CPC. An issue with this method is the absorption of IR radiation by the window. Even a 5% absorption of the VCSEL power was thought to cause failure due to melting or thermal stresses. A range of IR-compatible windows was considered, ranging from barium fluoride to zinc sulphide [116, 117, 119, 120, 121, 123, 124, 125]. Several were discounted because of the inability to transmit sufficient power at 980 nm. To assess the remaining four, a 2D steady heat transfer solver was developed. An eight-cell by eleven-cell domain was used to represent a 55 mm x 67 mm optical window. Linear 1D conduction equations were used to model heat transfer to immediately adjacent cells. The boundaries

were fixed at a temperature of 75 °C to approximate the metal temperature of the VCSEL bracket during the testing. The VCSEL power supplied to the window was assumed to be uniform throughout the area and was scaled by a fractional absorbance coefficient. A range of thermal conductivities and absorbance coefficients of the glass were studied. For the range of k_{glass} studied, 0.03-11.2 $\frac{W}{m°C}$, an absorbance of only 1% of incident light results in a peak temperature in excess of 845 °C. This is well above the estimated creep temperature for most glasses with melting temperatures in the range of 1200-1400 °C. The optical window design was abandoned.

Convective cooling is achieved by routing additional cool air to the VCSEL bracket through the supply fitting, identified in Figure 5.17. This was diverted from the labs' 6.89 bar supply. Two channels can be seen orientated in the vertical direction of Figure 5.5 and link the VCSEL emitting cut-outs in the VCSEL bracket. The aim was to form a protective film of lab-temperature air on the exterior of the VCSELs to prevent hot exhaust from making contact. Additionally, it was hypothesised that this air will mix turbulently with the exhaust inside the CPC, decreasing the bulk fluid temperature. Two variations were proposed and investigated using Fluent[22]. The first variation features both outlets A and B, and the second variation only features outlet B. The former is referred to as the 'negative pressure' VCSEL bracket due to the high-velocity primary coolant flow creating a low-pressure region at the top of the CPC. The latter is referred to as the 'positive pressure' VCSEL bracket, as the flow is pumped directly in to the CPC, increasing the pressure.

5.5.3.1 Domain and Boundary Conditions

The domain was constructed by combining the channel geometry in Figure 5.17 with the selected CPC. The volume was extracted and used as the domain. The hot exhaust gas from the coupon was modelled using five ellipses on the CPC exit aperture, defined as the projection from the coupon film holes. The VCSEL bracket did not include the fitting for simplicity. Instead, the channel was truncated at the CPC boundary, leaving a small rectangular face for the coolant inlet. Outlets A and B, as well as the viewport, were set as outlets. An additional outlet condition was established for the 1 mm gap modelled at the CPC exit aperture to capture the influence of the CPC-coupon spacing. Due to the quasi-

[22] Ansys®Academic Research Fluent, Release 21.2

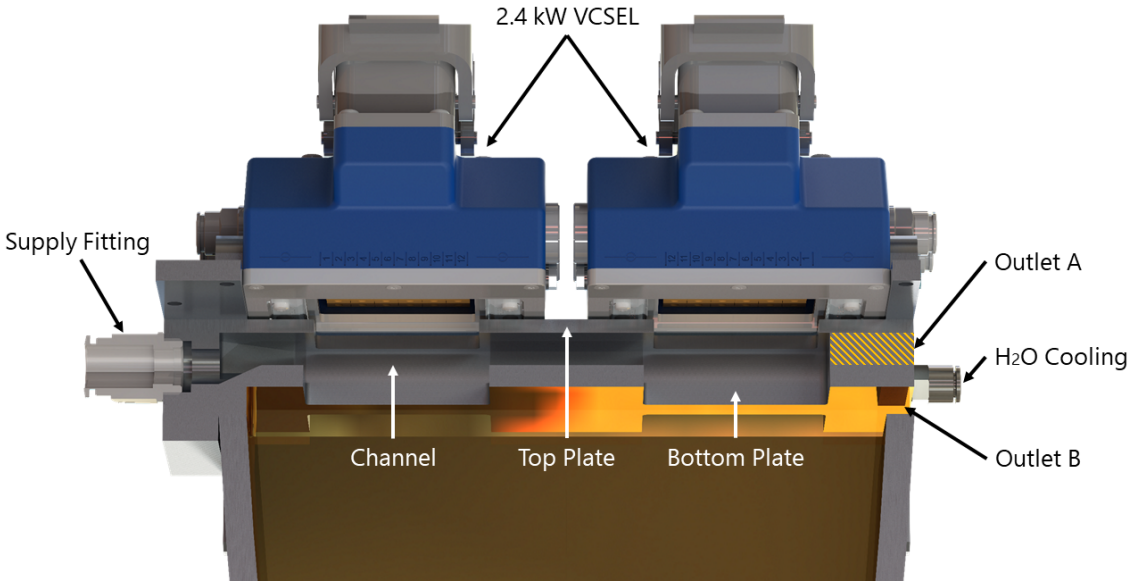


Figure 5.17: *cross-section of the VCSEL bracket showing the internal geometry for half of a channel of the positive pressure exhaust management system, with the location of outlet A identified with the hatch, as this feature is not present on the positive pressure configuration*

symmetry of the domain with turbulence, half the volume was used, and a symmetry plane was placed along the xy plane to improve solution times and mesh refinement capabilities.

The coupon exhaust flow conditions were derived from van de Noorts' [80] model and Murrays' [76] flat-plate data for the C6 geometry. 2 $\frac{g}{sec}$ [80] was selected, corresponding to a convective efficiency η_{conv}, of 0.47 [76]. For a metal target temperature of 1000 °C, the flow will exhaust the coupon at no more than 500 °C.

These values were chosen to exceed the expected values required for testing by at least 10% to minimise risk should the estimates be overly conservative. The exhaust management flow was defined using a ratio of the mass flow rate to the coupon supply. It was set to 5 to ensure that no hot gas was in contact with the VCSEL arrays. The static pressures of each outlet were set at 1 atmosphere. The walls of the CPC and the VCSEL bracket were set to 75 °C, an estimate for the bulk temperature of the CPC during the testing.

The density of the fluid was determined using the ideal gas law. All other material properties for both the fluid and the aluminium walls were kept at default [8]. In this investigation, gravity and buoyant forces were ignored.

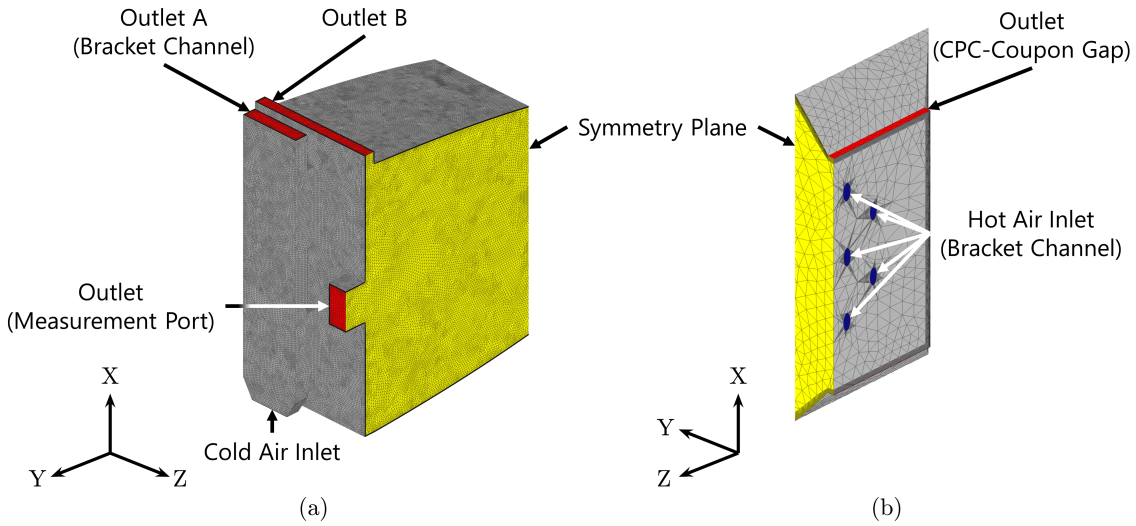
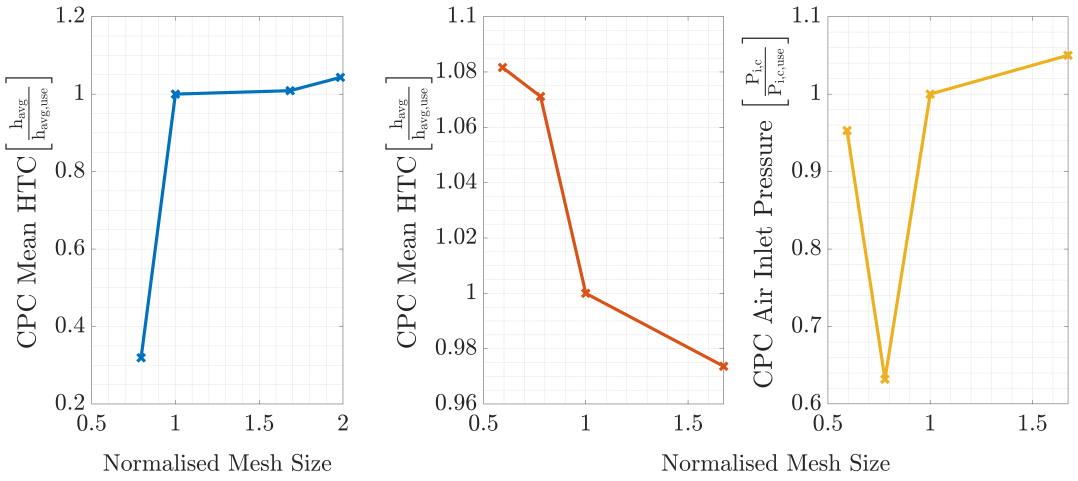


Figure 5.18: *a mesh representative of that used for the fluid domain analysis (a) isometric view showing the inflation layer (b) along the y-direction showing the refinement around the hot gas inlets*

5.5.3.2 Mesh and Models

Figure 5.18 shows the mesh used for the CPC fluid domain. The coupon exhaust holes can be seen in the high-density ellipses in (b). An inflation layer was defined along each wall, with 15 layers and a total thickness of 0.12 mm. Local mesh refinement was used during the solution to ensure that y+ remains at or below unity. A mesh-independence study was performed by first reducing the face sizing and then the body sizing. The total convection heat transfer and surface-average heat transfer coefficients were tracked for both reductions. Body size and pressure on mass flow inlets were tracked. The results are presented in Figure 5.19 (a) and (b), respectively.

Several models and solution settings were used. Both standard and realisable k-ϵ and both standard and SST k-ω RANS formulations were investigated as possible turbulence models. k-ω SST with a production limiter offered the best energy balance for the converged solution. The energy equations were used because of the compressive flow and thermal boundary. A coupled scheme was used with a distance-based Rhie-Chow [8] flux type. A second-order discretisation scheme was used for all parameters. A pseudo-transient formulation was used with a conservative length scale method, as this improved convergence and reduced



(a) (b)

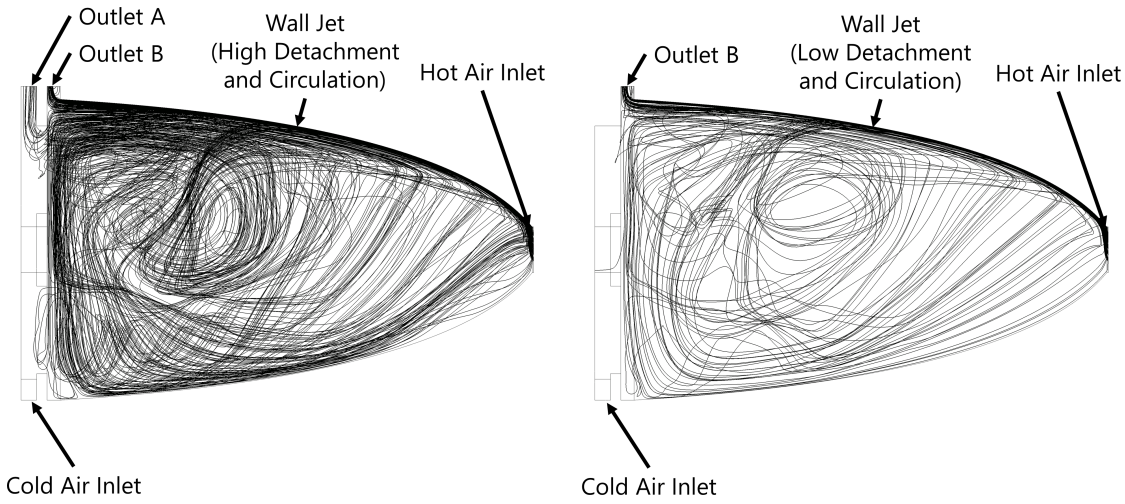
Figure 5.19: *tracked values versus mesh size for (a) face refinement (b) body refinement*

imbalances. The solution was run until the residuals were stable and both the mass and energy imbalances were less than 1%.

5.5.3.3 Results and Discussion

The streamlines for the fluid from the coupon are presented in Figure 5.20. These were generated using identical seed points. The exhaust gas is shown to contact the upper wall and form a wall jet along the top surface for both designs, fanning out as the CPC cross section increases towards the CPC inlet. In the negative case, the flow tends to detach more from the wall and circulate inside the cavity. This was driven by the coolant flow, generating a low pressure region in the channel and drawing the coupon exhaust away from outlet B. In the case of the positive CPC, the exhaust management flow was directed in to the cavity. There was still circulation, yet the majority of the exhaust flow exits through outlet B without circulating.

The bulk fluid temperatures and convective heat transfer rates are presented in Table 5.3. The convective heat transfer rates are reported separately for the CPC and the VCSEL bracket. A positive heat flow indicates that the fluid received energy from the walls. The thermal data align with the trends observed for the streamlines: for the negative VCSEL bracket, the exhaust entrapment increases the bulk temperature of the fluid. This was further reflected in the negative heat flow in the CPC, in which the structure would experience an



(a) (b)

Figure 5.20: *full-domain streamline originating from the hot gas inlet for (a) negative pressure CPC (b) positive pressure CPC*

increase in the bulk temperature from the initial guess of 75 °C. The results show that the channel flow provides some cooling to the VCSEL bracket, with the positive configuration providing a 16% higher cooling capacity.

Design	T_{bulk}	$\dot{q}_{CPC}$	$\dot{q}_{Bracket}$
Negative	59 °C	-59.7 W	66.6 W
Positive	51 °C	7.70 W	77.4 W

Table 5.3: *heat flow rates across conjugate walls for both exhaust management system configurations*

For the negative VCSEL bracket, most of the flow exits through outlet A. For the positive VCSEL bracket, the majority exits through B. For both configurations, the net mass flow through the CPC-coupon gap outlet was less than 1% of the total inlet flow. Any potential conductive cooling effects on the hot surface of the coupon were assumed to be negligible as a result. The positive VCSEL bracket was selected as the best design moving forward. It satisfies the design requirement for isolating the VCSEL arrays from the hot exhaust gas for a coolant-to-exhaust ratio of 5. It also offers increased cooling performance in the channel and decreases the bulk fluid temperature in the CPC cavity, reducing the thermal load.

5.6 Water Cooling System

The TPE3 pump is capable of supplying up to 120 LPM [46]; however, not all of this flow is available for use in the auxiliary channels. Trumpf recommends that no more than 60 LPM of water should be utilised for ELSA components, leaving at least 60 LPM for the VCSEL Management System [87]. The absence of available metering systems in the existing water cooling infrastructure for the two auxiliary loops is therefore concerning. Overdrawing cooling water for the auxiliary loops will lead to VCSEL overheating, resulting in rig shut-down or component damage.

To evaluate the flow through the proposed flow networks, a MATLAB script was developed. The PI&D diagrams in Figures 5.1 and 5.6 were evaluated. Geometric parameters and estimated loss coefficients were used to determine head loss through a flow path using a Fanning friction factor combined with inertial loss coefficients. The script finds a solution using an iterative approach from Brkic [15]. Mass flow rates were first estimated and evaluated for each section of the cooling loop. The flow in each section was then updated to conserve mass through the system and to match pressure drops in parallel paths. Table 5.4 presents the loss coefficients and geometries used. Variations in the loss coefficient with the Reynolds number were neglected. The locations of each channel are marked in Figure 5.5. 1-4 were the VCSEL bracket channels. 1-2 were the CPC short channels, C3 was the CPC mid-length channel, and C4 was the CPC long channel. It should be noted that Figure 5.5 only shows one-half of the CPC. The halves were stacked one on top of the other to form a rectangular CPC. The geometry and cooling channels were referred to using 'top' or 'bottom' to differentiate. P1/3 and P2/4 were 4 channels in the plenum, pictured in Figure 5.3. Two configurations of cooling were considered: single- and double-pass. The single-pass configuration utilises ten channels: M2-3, Top-C1-3, Bottom-C1, and P1-4. Each of the ten feed lines directs water to pass through the component once. The double-pass arrangement, however, utilises all the available channels. It forms two loops in the VCSEL bracket: M2 to M1, and M3 to M4. There are four loops in the CPC: Top-C1 to Bottom-C3, Top-C2 to Bottom-C4, Bottom-C1 to Bottom-C2, and Top-C3 to Top-C4. The plenum remains single-pass in this case; however, the water supplied to the VCSEL bracket and the CPC flows through each component twice before returning to the chiller.

Fitting	K [−]	D_h [mm]	L_o [mm]	T_{max} [°C]	P_{max} [bar]	Cite
G$\frac{1}{2}$-12 mm Push-In	0.5	9	32	150	20	[27, 38]
R$\frac{1}{8}$-8 mm Push-In (Straight)	0.5	5	25	150	30	[27, 38]
R$\frac{1}{8}$-8 mm Push-In (Elbow)	3	5	38	150	30	[27, 38]
12 mm OD Tubing	2.5	9	3250	100	50	[27]
8 mm OD Tubing	0.5	6	-	250	56	[27]
90 degree Turn	2	-	-	-	-	[27]
G$\frac{1}{2}$-G$\frac{1}{4}$ Manifold	10	9	180	150	20	[27]
$1\frac{1}{2}$"-$\frac{1}{2}$" Nipple	1.2	8	50.5	300	50	[27]
$\frac{1}{2}$"-$\frac{1}{4}$" Nipple	0.8	8	30.5	300	50	[27]
$\frac{1}{2}$"-$\frac{1}{4}$" Reducer	1.1	8	26.5	300	50	[27]
$1\frac{1}{2}$" Tee	1.5	32	100	300	50	[27]
$\frac{1}{2}$" Tee	2.9	12	75	300	50	[27]
VCSEL Bracket Channel	0.5	7	270	105	10	
CPC Channel (Long)	0.5	7	190	105	10	
CPC Channel (Mid)	0.5	7	150	105	10	
CPC Channel (Short)	0.5	7	110	105	10	
Plenum Channel	0.5	7	85	105	10	
$1\frac{1}{2}$" Ball Valve	5	32	105	300	50	[27]
$1\frac{1}{2}$" Gate Valve	2	32	105	300	50	[27]
$\frac{1}{2}$" Ball Valve	4	15	85	300	50	[27]
$\frac{1}{2}$" Check Valve	7	15	85	185	10.5	[4, 27]
$\frac{1}{2}$" Relief Valve	4.2	15	55	110	3.5	[27, 77]

Table 5.4: *geometries and loss coefficients used in the network analysis to assess the performance of the Effusion Lifespan and Stress Addition water cooling loops*

Local and global coolant flow rates were assessed for both designs using an inlet gauge pressure of 3 to 5 bar. This is the rated range for the OLAHF cooling system. An outlet pressure of 1.7 bar was used. This was maintained by the Mikrofill 3. The majority of the pipe network was supplied using galvanised pipes, so a surface roughness of 1.5 E-6 was used. Properties for water were evaluated at 10 °C and 4 bar gauge. The results for volumetric flow rate are presented in Figure 5.21. Both configurations perform similarly with 10 LPM per loop. This is due to the dominant contribution of existing OLAHF components.

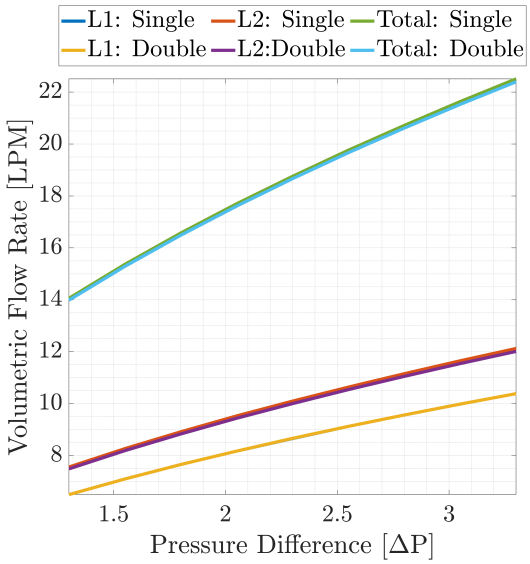


Figure 5.21: *predictions of volumetric flow rate versus pressure ratio for the water cooling loops across the range of available pressure settings showing the minimal variation between the single- and double-pass configurations*

The double-pass configuration was selected as it will not exceed the limits imposed by the VCSEL management system [87] and increases the available cooling area by 74%. The total flow results of the estimates for each of the mass flow rates through each loop for an inlet pressure of 3 bar gauge are presented in Table 5.5. The Dittus-Boelter correlation was used to estimate the average channel HTCs.

A pressure relief system was required to protect components and operators in the event of channel blockage or pump failure. It was configured as a boiler [14, 49]. The required diameter was estimated for the case of abnormal external heat input as defined by ISO 4126-10:2010 [17, 18, 19]. DN15, rated at 6 bar and 150 °C with relief at 3.5 bar, gauge [77] was selected. The valve was connected to an open-top 50 L steel dump dank via $\frac{1}{2}$" galvanised steel tubing and fittings. Figure 5.7 shows the location and set-up of the water cooling system and the relief valves and the dump tank. The 6.89 bar air supply and the location of the remaining components are shown. Flexible tubing connections are omitted for the sake of clarity.

5.7 Component Finite Element Analysis

A finite element analysis of thermal and mechanical fields was performed to evaluate and adjust the component design. This was divided in to two separate analyses: the coupon

Channels	$\dot{V}$ [LPM]	Re_D [−]	h $\left[\frac{W}{m^{2\circ}C}\right]$
P1	1.92	5800	3830
P2	1.32	4000	2850
P3	1.32	4000	3830
P4	1.92	5800	2850
TC1-BC3	1.26	3900	2790
TC2-BC4	1.20	3700	2670
BC1-BC2	1.26	3900	2790
TC3-TC4	1.20	3700	2670
M2-M1	1.26	3800	2730
M3-M4	1.26	3800	2730

Table 5.5: *predicted flow rates and heat transfer coefficients for water cooling channels*

coolant air supply and the coupon energy supply. The plenum analysis was conducted using Mechanical[23]. The CPC-VCSEL bracket assembly uses a conjugate thermal-fluid solver in Fluent. The thermal field was fed in to Mechanical for the structural analysis.

5.7.1 Domains and Boundary Conditions

The coupon energy supply domain expands on the quasi-steady analysis used to determine the exhaust management configuration: the fluid domain was identical, and a full solid domain was added. The exterior shape differs from a CPC as the material was machined from the original block to create the fins that run the length of the component, visible in Figure 5.23. These provide structural support and increase the external surface area by 217% to enhance convective cooling. The thermal effect of these features was excluded from this model. Channels M1, M2, and half of each of the remaining channels were included. The CPC and VCSEL bracket were assigned to be aluminium: E = 69 GPa, $\nu = 0.33$, $\alpha = 2.28 \times 10^{-5}\ \frac{1}{^\circ C}$, and k = 155.3 $\frac{W}{m^\circ K}$. The material properties of the air were consistent with the exhaust management system study.

The fluid-solid interfaces for the coupon energy supply were coupled using shared topology in DesignModeler[24]. Each of the cooling channels was defined using a convective boundary

[23] Ansys®Academic Research Mechanical, Release 21.2
[24] Ansys®Academic Research DesignModeler, Release 21.2

with convection coefficients from Table 5.5 and a bulk fluid temperature of 10 °C, which was confirmed as a representative laboratory utility water temperature. VCSEL boundary conditions were extracted from ray tracing. An explanation of this approach and the distributions are provided below. The mechanical boundary was established by constraining the bottom of the CPC to a plane to represent the mounting frame. A point on the bottom face was assigned as fixed to pin the domain in place. The xy-plane was used as a symmetry condition. The interior pressure of the cooling channel was set to 7.5 bar, 150% of the maximum rated pressure, in the model.

The coupon coolant air supply domain modelled each feature in Figure 5.3 with the addition of a solid plate instead of a coupon. Inconel 718 bolts were used to connect the coupon to the plenum and were modelled as un-threaded rods. Inconel 718 was chosen due to its high melting temperature of 1260 °C and a high yield strength of 689 MPa at 850 °C [109]. All component interactions were modelled using contact sets, configured to allow for separation if required. The material properties of the test plate were set to those of Inconel 625, Milam PSS was used for the gaskets, the plenum and window bracket were structural steel and the window was sapphire. A summary of the properties is provided in Table 5.6.

Material	Cite	E [GPa]	ν [−]	α $[\frac{1}{°C}]$	k $[\frac{W}{m°C}]$	σ_y [MPa]
Inconel 625	[108]	200	0.294	1.4 E-5	16	414
Inconel 718	[109]	200	0.294	1.3 E-5	11.4	1034
Milam PSS	[65]	20	0.35	1.0 E-7	0.5	100
Sapphire Glass	[122]	400	0.29	7.0 E-6	40	275
Steel	[9]	200	0.3	1.2 E-5	60.5	250

Table 5.6: *material properties used in finite element analysis of Effusion Lifespan and Stress Addition coupon coolant air supply components*

For the coupon coolant air supply, a 35 mm x 35 mm section was cut out of both the 'hot' and 'cold' faces of the test plate. The hot side was set to 1300 °C, and the cold side was set to 1150 °C. Each of the four coolant channels was cooled using the convective coefficients of Table 5.5 with a bulk fluid temperature of 10 °C. The internal faces of the coolant supply assembly were assigned a fluid pressure of 7.5 bar, approximately 110% of the pressure available from the 6.89 bar supply line. The water cooling channels were set at 7.5 bar to

model 150% of the maximum rated pressure. The four threaded mounting holes on the underside of the plenum were rigidly fixed. 200 N of bolt pre-tensioning was supplied to the Inconel 718 bolts used to mount the test plate and to the rear steel bolts used to mount the window bracket.

For both domains, all components had an initial temperature of 27 °C and gravity was ignored.

5.7.1.1 Rejected Ray Tracing

Previous unpublished work by Zachary Jackson observed considerable overheating of the VCSEL arrays due to low target surface absorbance. The presence of the VCSEL bracket protects the array casing from these reflected rays, and embedded water cooling loops protect the aluminium and steel components. The effect of these reflected rays was included in the FEA. The 15-degree short CPC and VCSEL bracket form the basis of the domain. A flat surface was added around the exit aperture of the CPC, measuring 150 mm x 150 mm, to model the actual geometry of the CPC. This is referred to as the 'front' surface. A mesh size of 0.1 mm x 0.1 mm was used on the coupon and front surfaces. The mesh size on the VCSEL bracket was reduced to 0.2 mm x 0.2 mm due to memory constraints. The emitting surfaces were modelled identically to the previous CPC investigation, and the same number of rays was used to ensure that the flux values and errors were consistent.

Two cases were modelled: the 'realistic' case and the 'worst' case. Both modelled each of the relevant surfaces as simple mirrors. The realistic case assumed that the reflectance of the surface was 95% [64]. The worst case assumed that the reflectance was 90% [64]. The absorbance of the coupon was governed by the emissivity of Inconel 625. The powdered form was measured to have a reflectance of 0.35 [13]. The slight polishing of the 3D-printed surface was estimated to increase this to 0.4, which is used for the realistic-case, while the worst-case estimate was 0.5.

The results for the realistic case are presented in Figure 5.22. Each is presented in the same orientation, consistent with the coordinates used in Chapter 3. The stream-wise direction is vertical, and the span-wise is horizontal. The effect of the domain change on the illumination of the target is minimal, and the distribution and peak flux value are within 1% of those reported in Figure 5.15. The rays are inclined in the span-wise direction, leading

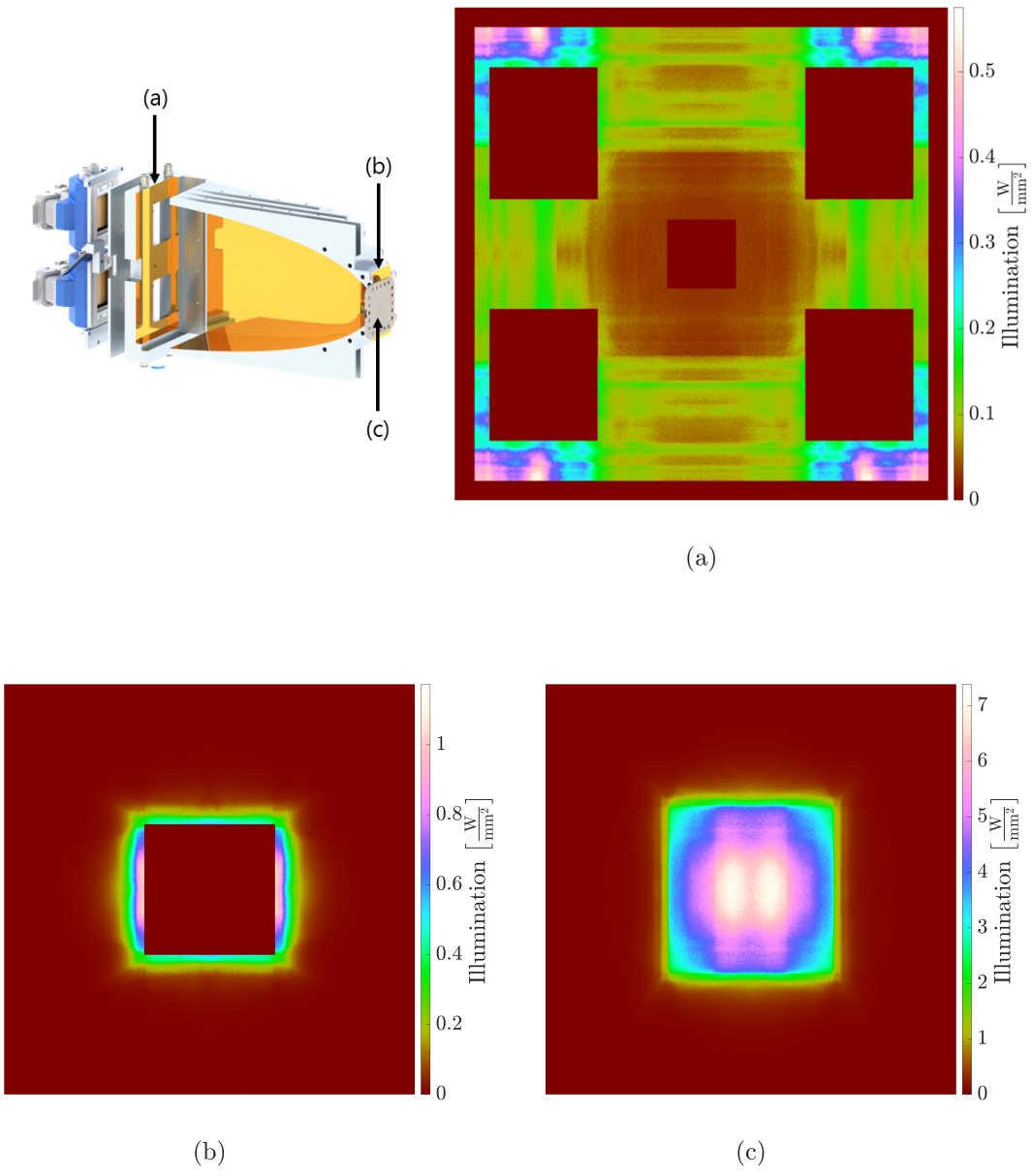


Figure 5.22: *illumination distributions for the realistic case (a) VCSEL bracket (b) CPC front (c) coupon, taken from results output by LightTools*

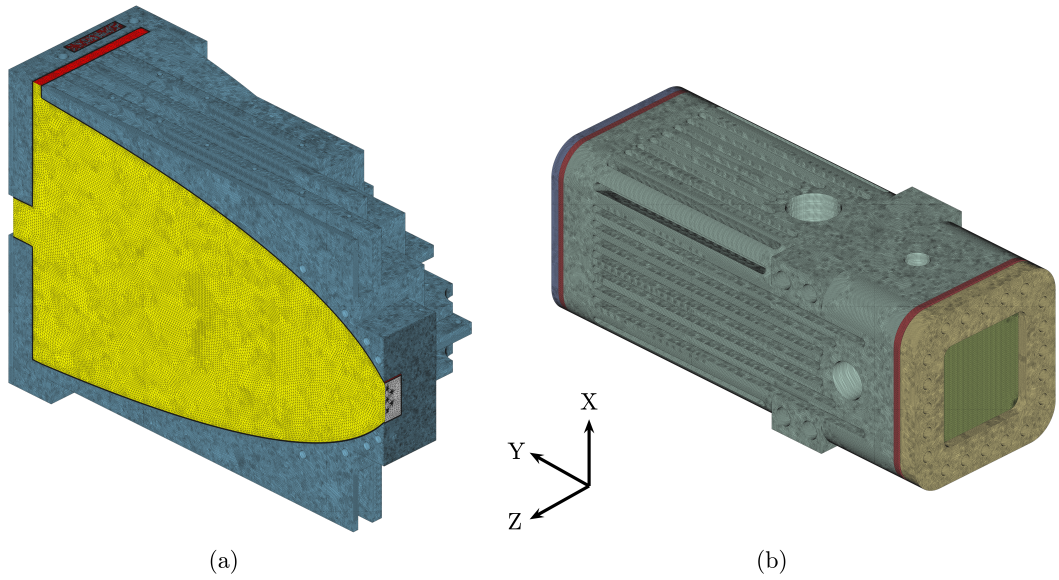


Figure 5.23: *a mesh representative of that used for the solid domain analysis (a) compound parabolic concentrator solid domain, in blue, showing integration with fluid domain, in yellow, grey, and red (b) coupon coolant air assembly with the plenum in blue, the gaskets in red, the window in green, and the window bracket in beige*

to a considerable amount of light incident on the front face of the CPC on either side of the exit aperture. The effect of the corners on the interior of the CPC shows an apparent 'funnelling' effect of the reflected rays in to the corners of the VCSEL bracket plate. These values were imported in to Workbench[25] and scaled by the estimated absorbance coefficients to determine the final boundary conditions of the heat flux on the respective faces.

5.7.2 Meshes

For the CPC-VCSEL bracket, the fluid mesh was taken from the previous analysis using the mesh settings consistent with the results in Figure 5.19. The refinements and inflation layer were kept the same. The solid mesh was defined using body sizing with local face refinement for the cooling channels. The mesh was consistent across the fluid-solid interface to reduce interpolation errors. The mesh used for the mechanical analysis is found in Figure 5.23 (a), which shows how it fits around the fluid domain. The mesh of the plenum is presented in Figure 5.23 (b). A similar approach to refining the body sizing, with targeted refinement on cooling channel faces and component interfaces, was implemented.

[25] Ansys®Academic Research Workbench, Release 21.2

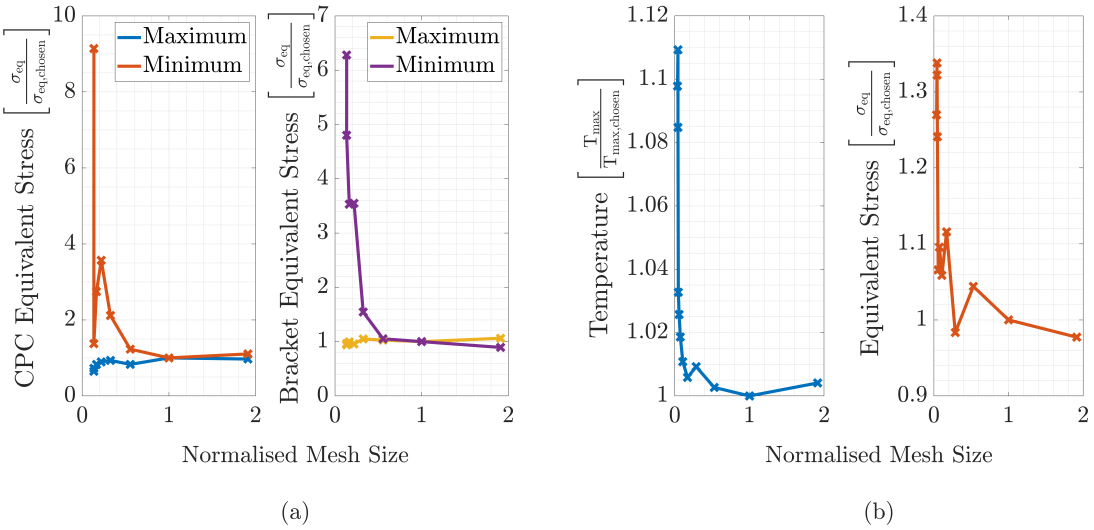


Figure 5.24: *tracked values versus mesh size for (a) CPC solid (b) plenum assembly*

A mesh-independence study was conducted and is presented in Figure 5.24, where (a) corresponds to the CPC-VCSEL bracket assembly, and (b) is the plenum assembly. The maximum temperature and von Mises stress values converge with the decreasing body size for both assemblies. Face refinement was conducted on several surfaces for the CPC-VCSEL bracket assembly; however, these results are not presented. The sharp angle formed by the exit aperture and the front face of the CPC created a thin region in which a numerical singularity was formed [9]. This caused the local stress values to diverge to infinity as the artefacts of the solution process were unresolved. The results presented average out over local node values to remove the effect of this singularity.

5.7.3 Results and Discussion

Thermal fields are presented in Figures 5.25 and 5.26. The maximum temperatures for the coupon coolant air and energy supply assemblies are within the operating limits [58, 62, 109]. The temperatures in the coupon coolant air supply are lower than those reported in the low-order model. This is due to the reduced temperature in the coupons' mounting region. The temperature decreases from maximum in the centre to roughly 525 °C in this area. The maximum gasket temperature is below the 900 °C operating maximum [65] at 725 °C. The Inconel 718 bolts are below the maximum allowed temperature at 580 °C [109]. The peak temperature for the coupon energy supply is 182 °C, below the creep threshold of 200 °C

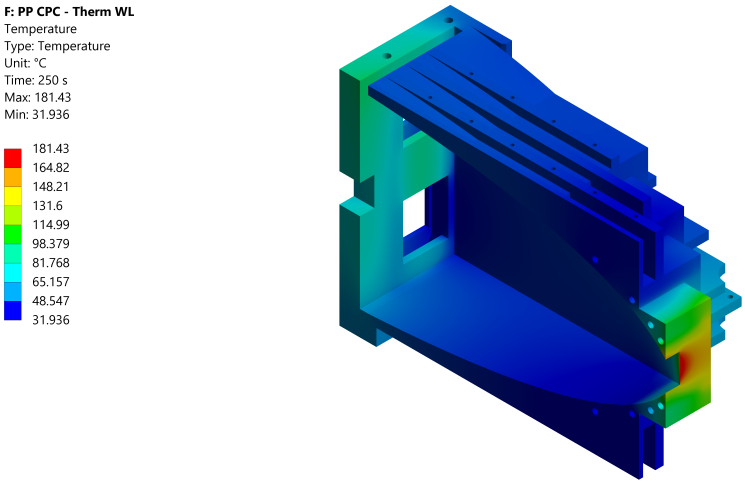


Figure 5.25: *thermal field for the VCSEL bracket and CPC assembly*

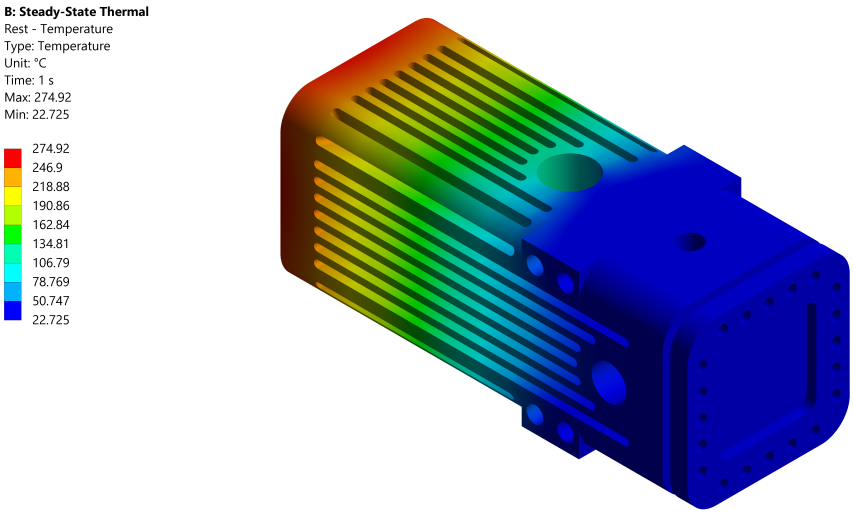


Figure 5.26: *thermal field of the plenum*

for 6061-T6. The hottest region is on the side of the exit aperture where the reflected flux was greatest. This is also the section of the outlet that is farther from the cooling channels. A maximum wall temperature of 119 °C occurs in both C1 channels. It is below the boiling point of 130 °C of water at 2.7 bar, actual [58]. This is considered safe from boiling as the cooling system did not drop below this pressure.

The maximum temperatures and stresses for the critical components are presented in Table 5.7. Maximum stresses tend to occur at sharp edges generated by CAD where manufacturing capabilities require a fillet [1], generating numerical singularities with applied loading [9]. Local stresses near these features were sampled and averaged over a radius of

0.1 mm to attenuate the effect of the singularity.

It was not enough to understand the stresses in the components, as the nature of the cyclic testing profile for the coupon will result in cyclic thermal loading on the broader rig. To evaluate whether the rig would survive testing, the lifespan of each component was estimated through stress-life data provided by various sources. The analysis assumed that simple cyclic monotonic loading was representative of the stresses experienced in the components during testing. Creep damage was neglected due to low temperatures. The number of cycles to failure was estimated using experimental results for constant-amplitude loading at representative temperatures.

Component	VCSEL Bracket & CPC	Plenum	Bolt	Gasket	Sapphire Window
T_{max}	182 °C	275 °C	575 °C	715 °C	34 °C
σ_{max}	90.13 MPa	153 MPa	289 MPa	84 MPa	16 MPa
N_f	1.2E6	4.0E5	1E8	-	-
Cite	[132]	[62]	[109]		

Table 5.7: *number of cycles to failure in Effusion Lifespan and Stress Addition components as estimated through finite element analysis and S-N data for simple monotonic cyclic loading with a magnitude of* σ_{max}

The estimate of the number of cycles to the fatigue limit for the steel component at 300 °C is well above the required minimum of 10000 cycles. The factor of safety is approximately 4. Data for the gasket and sapphire window were not available; however, both maximum stresses are substantially below the yield and rupture stresses, respectively.

The final investigation was in to the deformation of the plenum in response to the thermal and mechanical loads imposed by the coupon. The deflection of the component in the x- and z- directions was taken and normalised about the centre-line of the plenum. Integrating about the bolt-hole centre lines and averaging yields a mean displacement of 2.6 E-4 m. It is 0.32% of the original width of 61 mm. The small displacement of the mounting ring is considered negligible compared to the initial dimensions. It was concluded that the rigid boundary condition of the coupon mounting is a reasonable approximation.

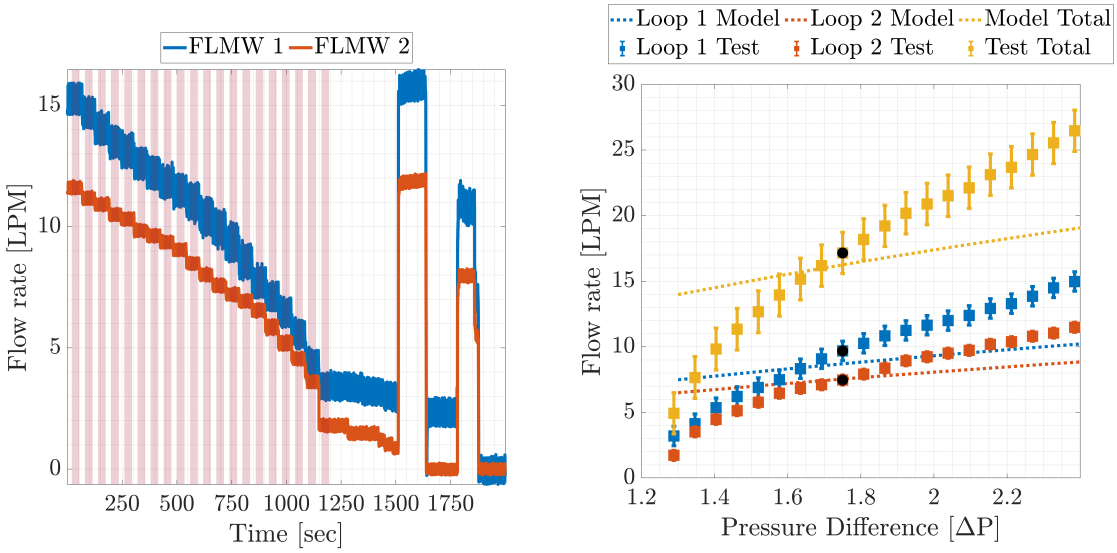
ELSA Commissioning and Component Troubleshooting

The following chapter presents investigations conducted to confirm the performance of major Effusion Lifespan and Stress Addition (ELSA) sub-systems. The primary motivation for assessing baseline performance was to validate the modelling introduced in the previous chapter. It was also essential to ensure that there was minimal risk of damage to ELSA or the rest of the facility due to overheating. The results confirm that ELSA performs in accordance with the design predictions and is safe to operate.

6.1 Water Cooling System

The performance of the water cooling system is essential for the operation of the ELSA. Components are required to be protected from thermal loading during all testing campaigns, and vertical-cavity surface-emitting lasers (VCSELs) require no less than 60 LPM of water for their own cooling. The supply of cooling water is governed by the pump head settings and the cooling channel and supply line configuration. As the latter is fixed, the flow rates through the auxiliary supplies were investigated for a range of pump heads. A range of set points from 24 m to 1 m was evaluated, with the pressure decreasing with each step.

There was considerable fluctuation in the measurements reported by the mass flow meters. The flow varied periodically with a peak-to-peak period of 5.27 sec. This was most likely caused by oscillations in the flow conditions due to a combination of VCSEL requirements and pump adjustments to meet and maintain the set point. A time average was taken over 35 seconds at each pump head to average out the oscillations. These sample periods are coloured pale red in Figure 6.1 (a), with averaged values reported as points in Figure 6.1 (b). The final indicated sample window corresponds to a pump head of 5 m. The measured



(a) (b)

Figure 6.1: *(a) raw data for the water cooling system tests, with red shades identifying the sampling windows to average-out oscillations in flow measurement (b) comparison of the true network to the low order network model*

flow rate was observed to not decrease in step with subsequent decreases in the pump head, suggesting that the flow meter has a lower limit. The results were confirmed with a visual assessment of the flow meters, which showed that the transfer magnet did not respond to less than 4 LPM of cooling water flow. Therefore, no averaging below this threshold was performed nor reported.

The lack of response in the transfer magnet was then investigated using two step-changes from 0% to 100% and back to 0% of the maximum pump head, identified in Figure 6.1 (a). This was done to establish a minimum measurement that would reliably alarm the control system in the event that the cooling water stopped flowing. For the first shut-off, FLMW 2 reported 0 LPM, while FLMW 1 reported 2.25 LPM, and both reported 0 LPM for the second drop. The 2.25 LPM value was rounded to 3 LPM for the control system alarm threshold.

The model, introduced in Section 5.6, shows reasonable agreement with the experimental results. Pump head settings below 9 m and above 21 m display some divergence due to the assumption of Reynolds-independent loss coefficients used in modelling. Between these two heads, the model provides a reasonable approximation of the network characteristics. The black circle denotes the selected pump head setting of 13 m, corresponding to a Loop 1

flow of 9.7 LPM and a Loop 2 flow of 7.5 LPM. This puts the total demand for ELSA at 17.2 LPM, below the maximum of 60 LPM. The estimated HTC values for this pressure differential are effectively identical to those derived in Table 5.5. Flow measurements confirm that ELSA is able to obtain the required cooling to protect all components and leave enough cooling water for the VCSEL arrays.

6.2 Reflecting Surfaces

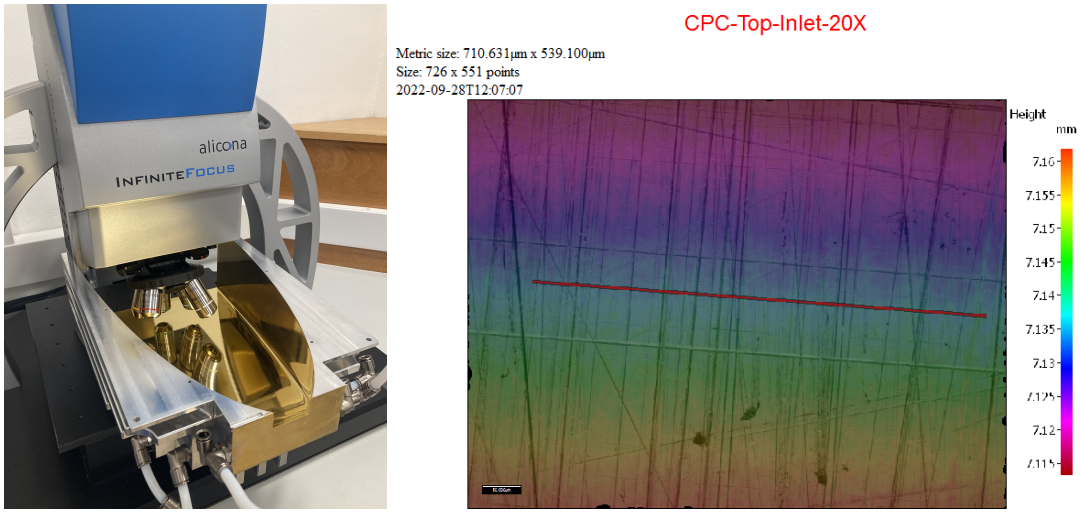
The total power transmitted through the compound parabolic concentrator (CPC) and the magnitude of the maximum flux are functions of the reflective capabilities of the mirrored surfaces [64] and the shape of the CPC [29, 41, 71, 96]. An understanding of both was required to confirm the performance of the CPC for later modelling. The former was determined through experimental correlations that correlated the reflectance of a gold-plated surface with the roughness of the surface [64]. The latter is more challenging and was inferred through a comparison of experimentally observed temperatures and finite element analysis (FEA) thermal fields.

6.2.1 Surface Finish

The surface finish of the polished and gold-plated reflecting surfaces was assessed using an Alicona[1] G4 InfiniteFocus system with 10x and 20x magnification. The size of the CPC limits a comprehensive measurement of the entire surface, so a sampling approach was used. Accurate surface roughness measurements were made more difficult because of the curvature of the CPC surfaces. The assumption was made that the sampling of the surface represents the mean roughness. The roughness statistics for three paths at the sampling location were obtained and averaged. For each of the two CPC halves, the roughness was measured at both the inlet and the outlet ends. One location was sampled from the VCSEL bracket.

Figure 6.2 shows the measurement set-up and the example path taken from the top of the CPC. The colour gradient in Figure 6.2 (b) represents the distance from the optical receiver to the measurement area. It captures the macro-curvature of the parabolic reflecting surface. It represents an effective misalignment of the surface with the instrument surface on which the component rests. Each path was selected to sample perpendicularly to this

[1] Alicona Imaging GmbH (2022). *G4 InfiniteFocus - Spec Sheet* https://www.alicona.com/en



(a) (b)

Figure 6.2: *(a) Alicona measurement set-up for one half of the compound parabolic concentrator, showing the approximate location of a sample taken at the exit aperture and the visual quality of the reflecting surfaces. (b) Alicona data with a sampling path shown in red and the vertical gradient identifying the curvature present on the reflecting surface*

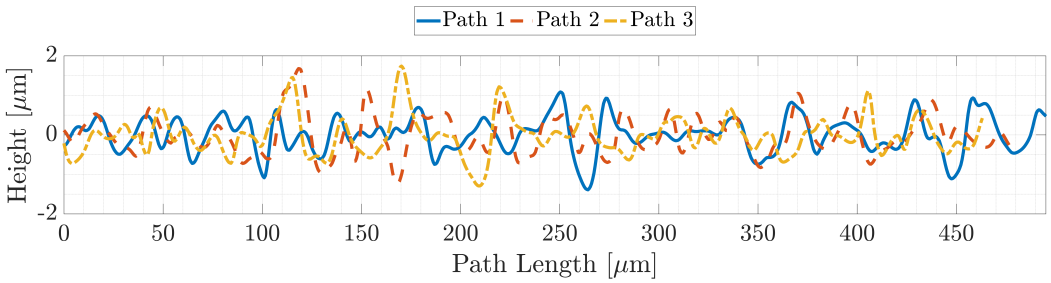


Figure 6.3: *roughness data sampled at three paths for the compound parabolic concentrator*

gradient to minimise the effect of the CPC geometry. Example paths 1-3 are provided in Figure 6.3. The variation in roughness at the inlet of the CPC is consistent for all paths.

The mean roughness values for each path are presented in Table 6.1. The surface finish of the CPC was estimated to be between 221 nm and 360 nm, with a global average of 281 nm. Using Jacksons' experimental correlation [64], this corresponds to a surface efficiency, ρ, of 0.95, while the roughness of the VCSEL bracket corresponds to a ρ of 0.92. The surface efficiencies are aligned with the realistic case used in the design boundary conditions in Section 5.7.

Location	Path 1 [μm]	Path 2 [μm]	Path 3 [μm]	Mean [μm]
CPC-B Inlet	0.294	0.270	0.263	0.276
CPC-B Outlet	0.248	0.199	0.215	0.221
CPC-T Inlet	0.346	0.390	0.345	0.360
CPC-T Outlet	0.296	0.282	0.227	0.268
VCSEL Bracket	0.470	0.712	0.424	0.535

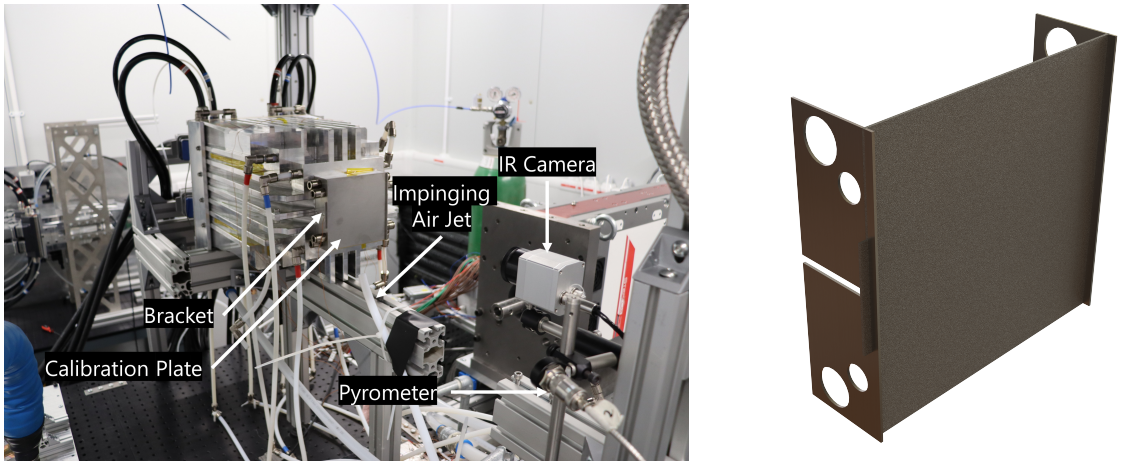
Table 6.1: *surface roughness values for major reflecting surfaces*

6.2.2 Pulse Testing

Deviations from the computer model in the machined geometry of the CPC will alter the total transmitted power and the distribution at the CPC exit aperture [29, 41, 71, 96]. A complete and direct measurement of the machined CPC geometry for comparison was not possible, as there was no equipment to do so. Direct measurement of IR light at the exit aperture was also not feasible, as available IR cameras [84, 85] are only receptive to light between 8 and 14 μm, above the 980 nm that the VCSELs emit. Additionally, the power supplied risked damaging any camera placed in the exit aperture. In lieu of these, a series of IR pulses were applied to a test sample, and the results were compared to both FEA and a 1D transient model. This combination approach allows the determination of both the CPC outlet distribution and optical properties of an Inconel 625 test piece, as explained below. The results indicate that the CPC distribution is captured by the ray tracing results. Data also suggest that conditioning is required for the test plate, as the coefficients of absorbance and emissivity of the coupon vary over time. This is consistent with a study of other nickel-based super-alloys [3].

6.2.2.1 set-up and Method

Figure 6.4 presents the experimental set-up with the calibration plate attached to the outlet of the CPC and the geometry of the 110 mm x 110 mm calibration plate. The calibration plate was laser cut from a 1.0 mm thick sheet of cold-rolled Inconel 625. It was mounted through slots in plates affixed to both sides of the CPC to minimise the contact area for



(a) (b)

Figure 6.4: *alternate calibration run testing set-up showing (a) calibration plate installed on ELSA with associated cooling connections (b) calibration plate*

conduction and the mechanical restraints on the plate. An Optris[2] PI 640i IR camera with a 15-degree lens was used to collect IR images of the rear face. Two CTratio 2M pyrometers were used to measure the maximum temperatures in the centre of the test piece for the front, or CPC-facing, and rear faces of the calibration plate.

Four calibration plates were cut to identical dimensions. They are designated ACR-1, ACR-2, ACR-3, and ACR-4, where ACR stands for Alternate Calibration Run, as this was the second such test performed for this CPC. The original test did not produce usable data as the wrong material, CR4 steel, was delivered instead of Inconel 625. ACR-1 and ACR-2 were polished to remove oxidised and deposited material on the surface. ACR-3 and ACR-4 were grit blasted using Saftigrit Brown from Guyson[3] to create a rougher surface relative to polishing. Each of the ACR specimens was analysed using the Alicona, following the same procedure as outlined above for the reflecting surfaces of the VCSEL bracket.

Following surface roughness measurements, each plate was subjected to 12 different pulses for a variety of VCSEL power levels and durations, as presented in Table 6.2. 200 SLPM of 100 psi dry lab air was supplied through a nozzle to the centre of the rear surface for 45 seconds after the VCSEL power was switched off. This returned the calibration plate to an ambient temperature of 22 °C. ACR-1 and ACR-3 were pulse-tested immediately after polishing and grit blasting, respectively. ACR-2 and ACR-4 were first cycled using the 4-D

[2]Optris ltd. (2020) www.optris.com/en
[3]Guyson Corporation (2020). https://www.guyson.com

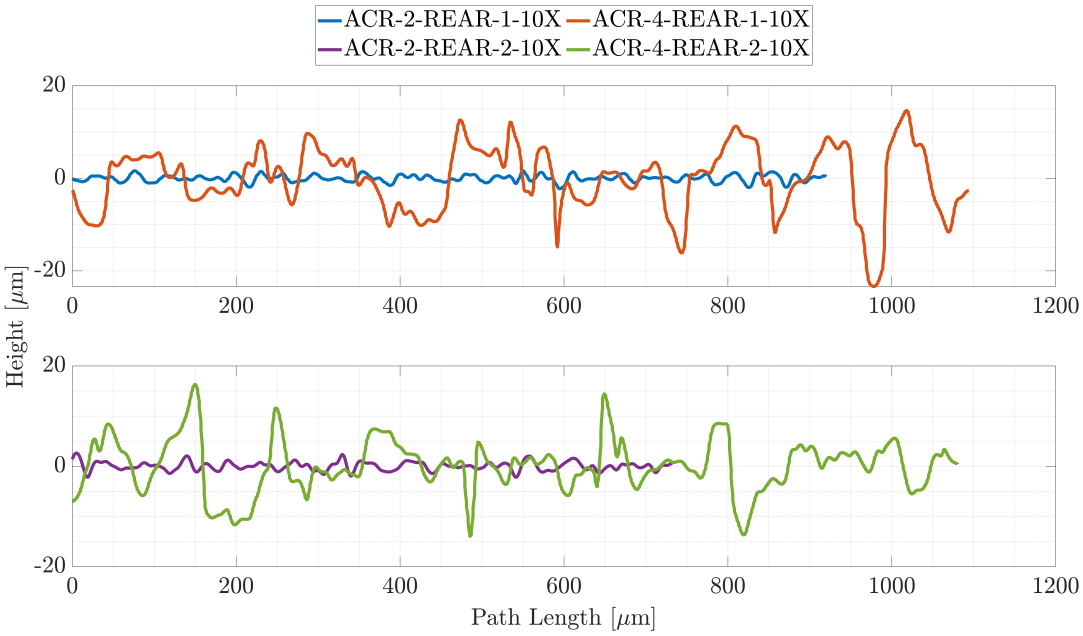


Figure 6.5: *comparison of roughness with different surface finishes for alternate calibration run-2 and alternate calibration run-4*

profile until both the absorbance and the emissivity of the calibration plate were constant with time. The former condition was met when the pyrometer measurements were constant. The latter was met when equation (6.1) produced a cycle-independent value.

$$\epsilon_{\mathrm{p}} = \left(\frac{\mathrm{T_{ir}}}{\mathrm{T_p}}\right)^4 \tag{6.1}$$

For which ϵ_{p} is the emissivity of the plate. $\mathrm{T_p}$ is considered the actual maximum temperature of the surface, as the ratio pyrometer was emissivity-independent [83], and $\mathrm{T_{ir}}$ is the averaged maximum temperature of 5 pixels in the location of the rear pyrometer measurement. The internal emissivity of the IR camera, ϵ_{ir}, was taken as unity.

Test\Time	1 sec	2 sec	4 sec
A	90 $\frac{\mathrm{W}}{\mathrm{cell}}$	50 $\frac{\mathrm{W}}{\mathrm{cell}}$	30 $\frac{\mathrm{W}}{\mathrm{cell}}$
B	110 $\frac{\mathrm{W}}{\mathrm{cell}}$	70 $\frac{\mathrm{W}}{\mathrm{cell}}$	40 $\frac{\mathrm{W}}{\mathrm{cell}}$
C	130 $\frac{\mathrm{W}}{\mathrm{cell}}$	90 $\frac{\mathrm{W}}{\mathrm{cell}}$	50 $\frac{\mathrm{W}}{\mathrm{cell}}$
D	150 $\frac{\mathrm{W}}{\mathrm{cell}}$	110 $\frac{\mathrm{W}}{\mathrm{cell}}$	60 $\frac{\mathrm{W}}{\mathrm{cell}}$

Table 6.2: *alternate calibration run pulse testing duration and corresponding vertical-cavity surface-emitting laser power settings*

6.2.2.2 Results and Discussion

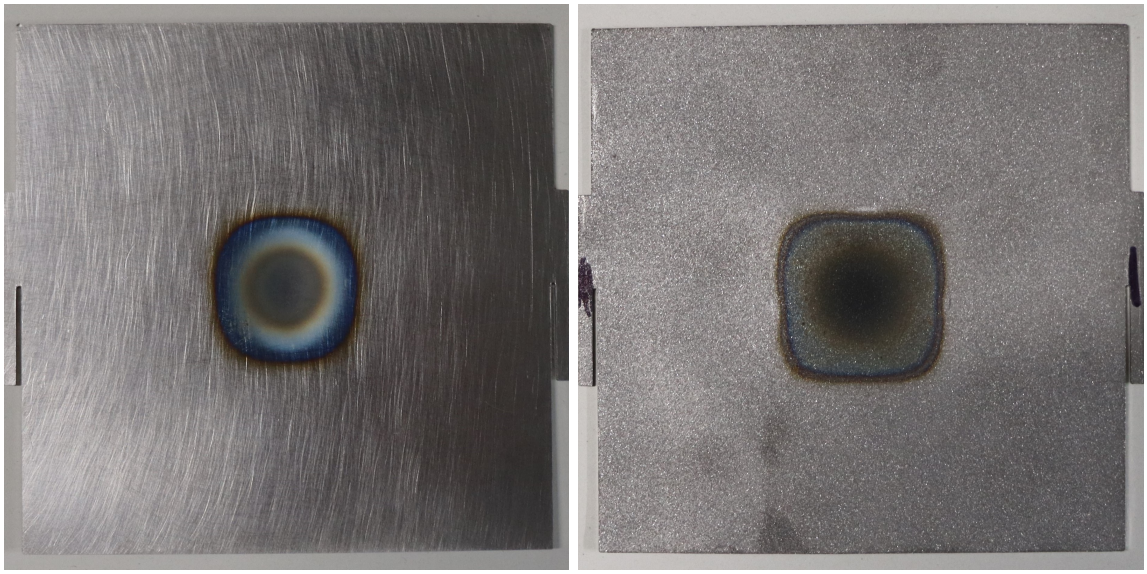
Data comparing the roughness of two locations on the rear surfaces of ACR-2 and ACR-4 are presented in Figure 6.5. A visual comparison can be found in Figure 6.6, in which the initial condition of each plate was consistent with the peripheral regions. A summary of the roughness for all plates is presented in Table 6.3.

Location	Path 1 [μm]	Path 2 [μm]	Path 3 [μm]	Mean [μm]
ACR-1 Front	0.709	0.830	0.620	0.720
ACR-1 Rear	0.676	0.805	0.667	0.716
ACR-2 Front	0.719	0.707	0.715	0.713
ACR-2 Rear	0.665	0.783	0.624	0.691
ACR-3 Front	4.157	3.998	4.779	4.311
ACR-3 Rear	3.584	4.204	4.166	3.985
ACR-4 Front	3.660	4.904	3.732	4.098
ACR-4 Rear	3.942	5.204	4.780	4.642

Table 6.3: *average surface roughness for each alternate calibration run plate*

ACR-2 and ACR-4 following test campaigns are presented in Figure 6.6. It is clear that the surface undergoes significant change at elevated temperatures. The hottest portion of the centre is grey-black. This is attributed to the formation of molybdenum and niobium precipitates with small amounts of carbon and other trace elements [108]. The centred rings of various colours radiating outward correlate with the decreasing temperature at increased distances from the centre. The plate displayed plastic mechanical behaviour during the early cycles. Figure 6.7 presents the visible bowing away from the CPC outlet exhibited by the ACR-2 specimen. This was driven by the large thermal stresses caused by sudden heating and expansion, resulting in fixed distortion. Plastic deformation increased the plate-CPC spacing from 1 mm to 5-6 mm for the four test pieces.

The maximum pulse temperatures for both the pyrometers and the rear IR camera for the ACR-4 plate are presented in Figure 6.8 (a). The early pyrometer one readings are anomalous. A spike occurs for surfaces experiencing a thermal ramp rate above an arbitrary



(a) (b)

Figure 6.6: *post-testing plates showing visual change for (a) alternate calibration run-2 (b) alternate calibration run-4*

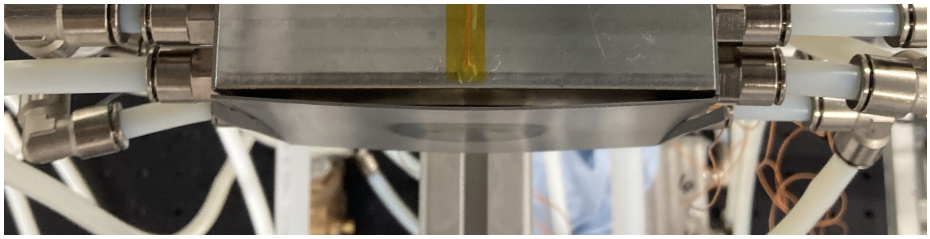


Figure 6.7: *plastic deformation of the calibration plate following testing*

threshold. This persists for around 50-200 ms before the reading assumes the 'correct' value. This phenomenon is independent of the method of heating, suggesting that it is due to interference within the pyrometer when power is first supplied. This was not observed in pyrometer 2, which experienced a lower ramp rate on the rear face of the plate. Pyrometer 2 measured a high temperature in the initial pulses, which decreased to a minimum at pulse 10. A progressive increase followed a steady value at 30 pulses. The IR camera temperatures were extracted from recordings taken of each pulse using the Optris PIX-Connect software. The plot shows an increase in the measured temperature with time at high temperatures. Figure 6.8 (b) presents the calculated emissivity of the materials' rear face. This was achieved by equating the energy received by the pyrometer with the IR camera.

It is clear that Inconel 625 requires conditioning at high temperatures to achieve a time-independent emissivity, since this condition was met after 140 pulses or 560 seconds.

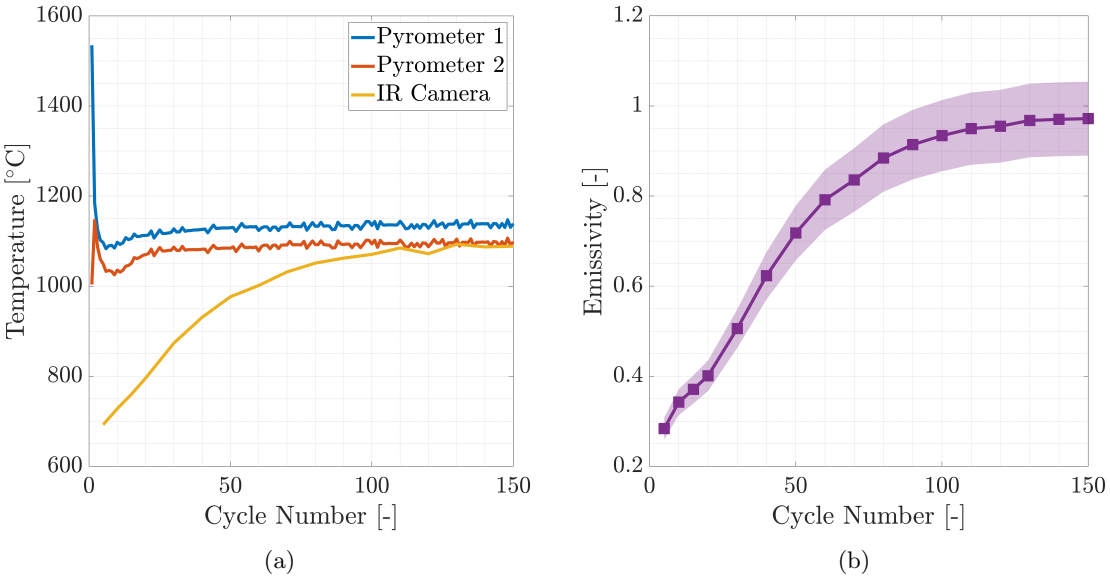


Figure 6.8: *(a) measured temperatures from cyclic testing for alternate calibration run-4 (b) corresponding surface emissivity as calculated through equation (6.1)*

This was consistent for both ACR-2 and ACR-4. It was concluded that this is independent of the surface finish and not a factor of the plate deflection, as this reaches a steady value after ten cycles. Chemical changes must exist within the material at high temperatures, which is responsible for this phenomenon. The formation of oxides is probably supported by the change in colour presented in Figure 6.6.

The temperature-dependent emissivities of ACR-2, ACR-3, and ACR-4 are presented in Figure 6.9. The emissivities of ACR-1 are not included, as the data set for each pulse is not complete. There is a clear linear relationship between the increase in metal temperature and emissivity of the ACR-2 and ACR-4 plates. This contrasts to ACR-3, in which the unconditioned plate displays an inverse relationship between emissivity and metal temperature. The difference between ACR-3 and ACR-4 supports the need to conditioning the test pieces before taking IR measurements of the surface, as the correlation between these two points is unknown over time.

The emissivity of the test piece is also a function of the surface roughness. An increase in the mean surface roughness of 523% increases the emissivity by 29%. The coefficients for the linear fit to ACR-2 and ACR-4, which satisfy equation $\epsilon = \mathrm{mT} + \mathrm{b}$, are provided in Table 6.4. Coupon-specific coefficients were determined by sampling a linear interpolation between the coefficients provided and the specific coupon roughness.

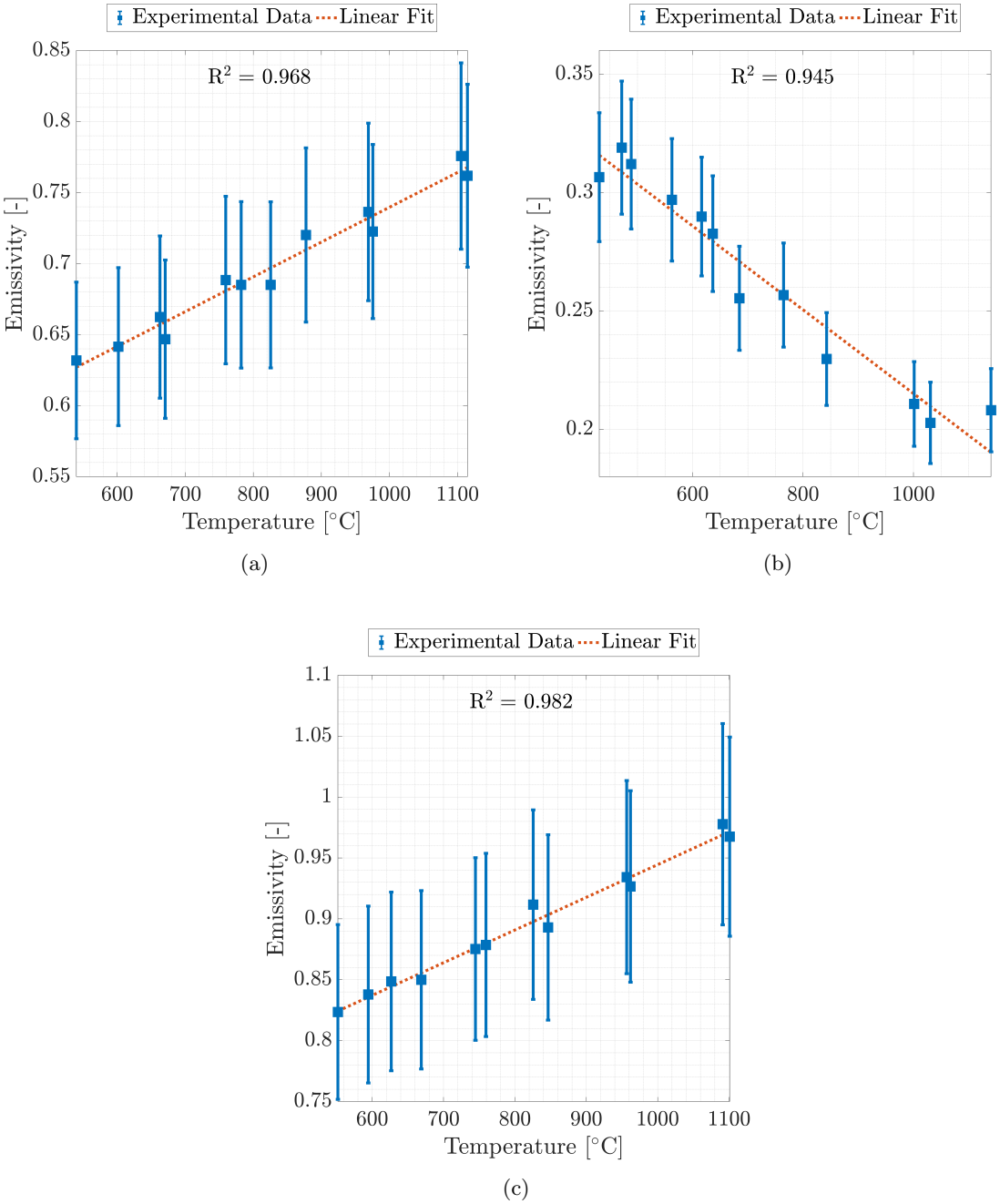


Figure 6.9: *calculated emissivity versus pyrometer (true) temperature for (a) alternate calibration run-2 (b) alternate calibration run-3 (c) alternate calibration run-4*

Mean Roughness [μm]	m [$\frac{1}{°C}$]	b [−]
0.702	2.45 E-4	0.495
4.370	2.68 E-4	0.676

Table 6.4: *linear fit coefficients for the emissivity of conditioned plates at each plate roughness*

6.2.3 Pulse Testing Finite Element Analysis

A comparison between the experimental results and the transient modelling was required to estimate the absorbance of the target plate and the CPC distribution. The former was achieved by sampling the maximum temperature, taken from experiments, for a series of absorbance values in FEA. The latter was achieved through the comparison of the thermal distributions at the end of the experimental and modelled pulses. The approach assumes that the thermal field is identical if the boundary conditions are identical.

6.2.3.1 FEA Domain and Boundary Conditions

A 110 mm x 110 mm x 1 mm thick plate was modelled in Mechanical[4]. It matched the dimensions of the pulse test plate in the absence of attachment slots, which were considered irrelevant to the thermal model. The material properties for Inconel 625 were taken from [108].

A transient thermal formulation was used under a range of conditions to match those in Table 6.2. The solution was broken in to two steps: a heating step for 1, 2, or 4 seconds, followed by a 1-second hold period in which no energy was supplied to the plate. The hold period allowed some propagation of thermal energy and ensured that the unheated side of the plate achieved its maximum temperature. This enabled a direct comparison with the observed experimental temperatures, as these were extracted when the plate reached a maximum temperature. A flux boundary condition on the heated face was applied using a CPC distribution, as described below. This flux boundary condition was scaled to the appropriate laser powers in Table 6.2 and scaled again by 0.25, 0.50, 0.75, and 1.00 to model a range of absorbance coefficients. The remaining sides of the calibration plate were modelled

[4] Ansys®Academic Research Mechanical, Release 21.2

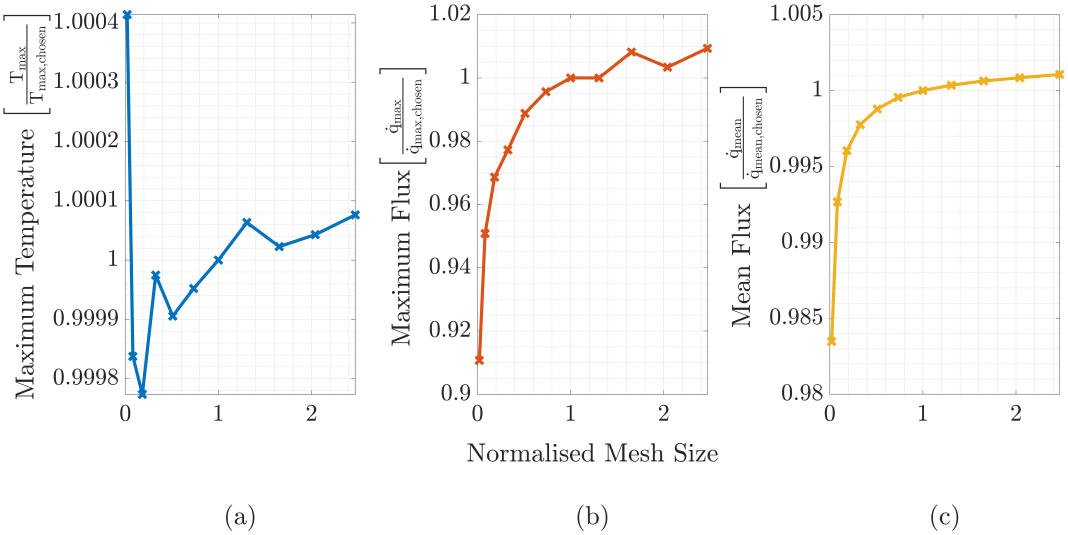


Figure 6.10: *alternate calibration run transient-thermal mesh-independence results for tracked values of (a) temperature (b) maximum heat flux (c) mean heat flux*

as perfectly insulated, as natural convection and conductive heat flow to the mounting were considered to have a negligible effect during the short-duration pulse.

A mesh study was performed by increasing the number of elements for the case of a 2-second pulse at 110 $\frac{W}{cell}$ and an absorbance of 1.00. The results of the mesh study are presented in Figure 6.10. The maximum temperature shows little dependence on the number of elements across the range studied, while both heat fluxes converge well.

6.2.3.2 Target Spacing

The deformation of the target plate during testing, altering the CPC-plate spacing from 1.0 mm to 5.0 mm, resulted in a different heat flux profile than that introduced in Chapter 5. It has previously been observed that the inclination of rays in the outlet aperture may approach 89 degrees [96]; therefore, increasing the plate spacing will radically alter the flux profile on the plate. A study was conducted using a LightTools[5] set-up similar to that in Chapter 5. The target plate spacing was set at 0.1 mm, 1.0 mm, 2.0 mm, 3.0 mm, 5.0 mm and 10.0 mm. The results for each spacing are presented in Figure 6.11. The results are scaled by the maximum flux value for the entire set. The evolution of the distribution with an increased spacing clearly shows the effect of surface inclination on the incoming rays.

[5]Synopsis inc. (2022) *LightTools(64) 2022.03 SR1* https://www.synopsis.com

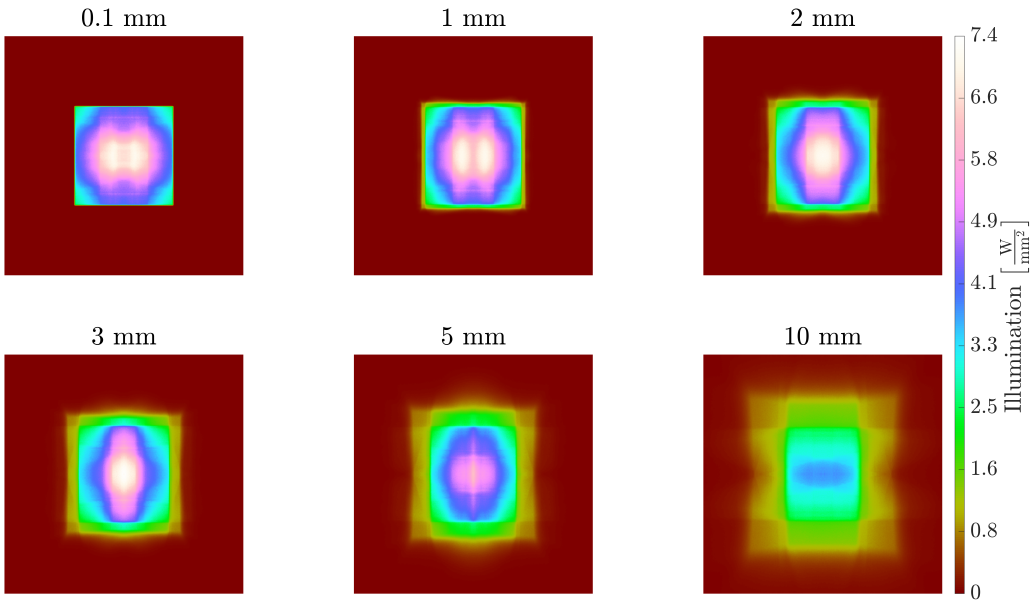


Figure 6.11: *illumination at various CPC-target spacings*

Increasing the spacing focusses the rays until 3 mm, beyond which the rays begin to diverge. The peak flux is roughly 4% greater due to this focussing effect for the 3.0 mm spacing compared to the 1.0 mm spacing. The distribution at 5 mm was used as the boundary condition for the FEA of the plate.

6.2.3.3 1D Model

The absorbance was also estimated using a 1D transient heat equation for a 1 mm thick Inconel 625 domain. The material properties were taken from [108]. A MATLAB[6] script solved for the thermal distribution at each time step using the following matrix:

$$\begin{bmatrix} T_1 \\ T_2 \\ \vdots \\ T_{n-1} \\ T_n \end{bmatrix}_{t+\delta t} = \begin{bmatrix} \frac{2\tau\delta z\dot{q}_{max}}{k} \\ 0 \\ \vdots \\ 0 \\ 0 \end{bmatrix} + \begin{bmatrix} 1-2\tau & 2\tau & 0 & \dots & 0 \\ \tau & 1-2\tau & \tau & \ddots & \vdots \\ 0 & \ddots & \ddots & \ddots & 0 \\ \vdots & \ddots & \tau & 1-2\tau & \tau \\ 0 & \dots & 0 & 2\tau & 1-2\tau \end{bmatrix} \begin{bmatrix} T_1 \\ T_2 \\ \vdots \\ T_{n-1} \\ T_n \end{bmatrix}_t \tag{6.2}$$

Where there is n number of nodes through the thickness of the plate, with spacing δz. τ

[6]The MathWorks, Inc (2021). *MATLAB version: 9.10 (R2021a)* https://www.mathworks.com

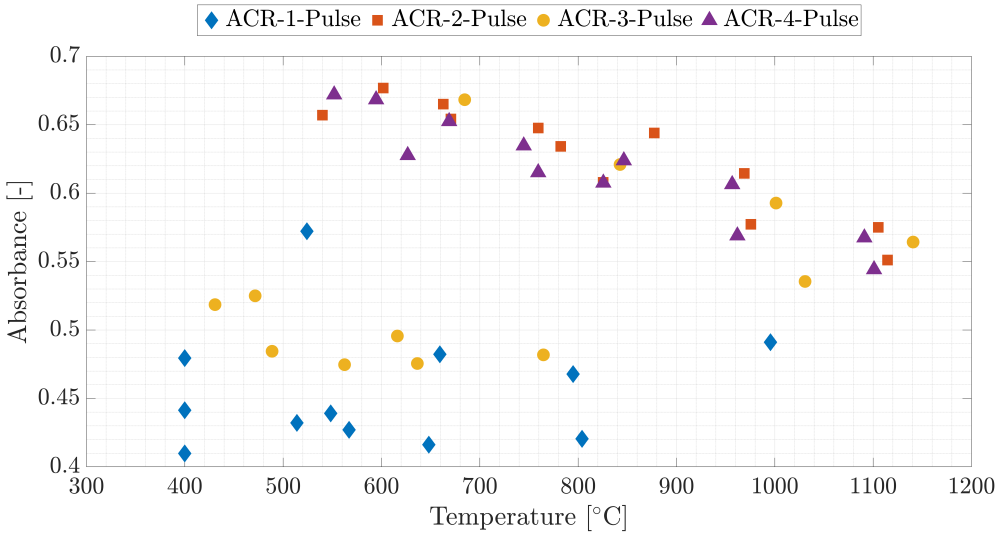


Figure 6.12: *inconel 625 absorbance versus temperature from alternate calibration run testing*

is the transient constant of the system, defined as

$$\tau = \frac{\mathrm{k}}{\rho \mathrm{C_p}} \frac{\delta \mathrm{t}}{\delta \mathrm{z}^2} \tag{6.3}$$

δt is the time interval. $\dot{\mathrm{q}}_{\mathrm{max}}$ is defined as the maximum flux value for the LightTools distribution, scaled by the absorbance coefficient.

6.2.3.4 Results and Discussion

The maximum temperatures for each cycle were extracted and directly compared with the maximum pyrometer data. The absorbance coefficient for each pulse was taken as a linear interpolation of the FEA data using the pyrometer value as the sampling point. These are reported in Figure 6.12. It is clear that there was a dependence on both conditioning and temperature. ACR-1 and ACR-3 exhibit a relatively lower absorbance than their conditioned counterparts. This is attributed to the combination of thermally accelerated oxidation and precipitate formation with cycling. Both ACR-2 and ACR-4 exhibit similar absorbance of the IR radiation despite different surface finishes. Both exhibit a fractional absorbance that decreases with increasing temperature. It ranges from a maximum of 0.675 at 550 °C to a minimum of 0.52 at 1150 °C.

The comparison between the 1D model and the experimental data is shown in Figure 6.13.

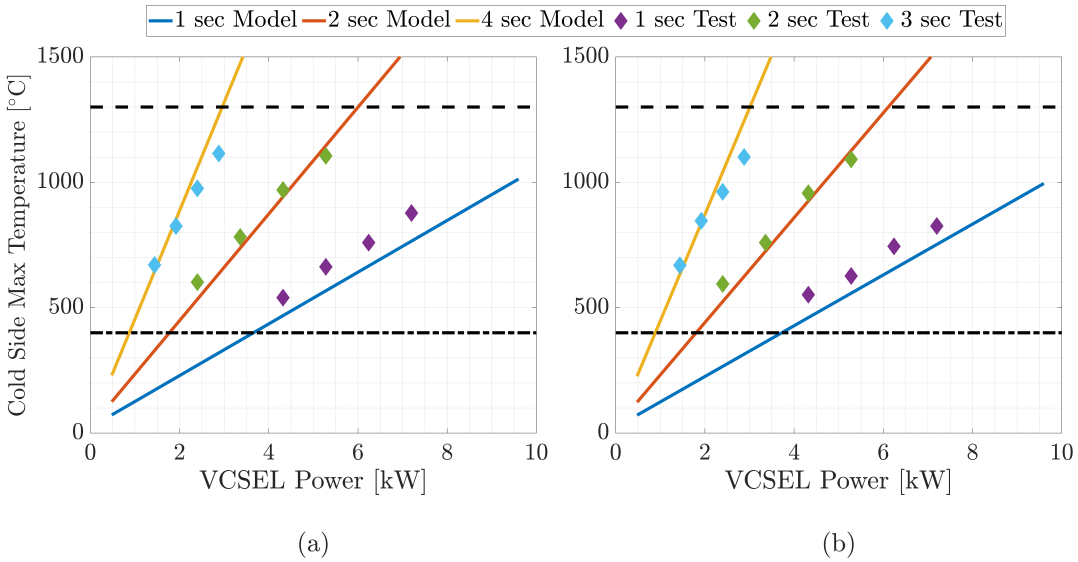


Figure 6.13: *comparison of maximum temperatures of low-order transient model and alternate calibration run testing for (a) alternate calibration run-2 (b) alternate calibration run-4*

Both experimental data sets display a robust linear relationship with increasing power. The 1D model was calibrated by scaling the absorbance of the plate until the root mean square difference between the experimental results and the model was minimised. For ACR-2, this occurs at a value of 0.58. For ACR-4, this occurs at a value of 0.57. The low-order model agrees well with the FEA of the calibration plate. The median value for the absorbance of the FEA is taken to be 0.62. This represents a per cent difference of 6.4% for ACR-2 and 8.1% for ACR-4, attributed to the minor contribution of conduction perpendicular to the plate normal in the FEA that was omitted from the 1D modelling. This results in a more significant absorbance coefficient in the FEA as the peak temperature was relatively lower because of this loss. Both results confirm that the absorbance and reflectance values used for the modelling in Chapter 5 are representative of an Inconel 625 target plate.

The relative thermal distributions achieved at the end of each pulse are presented in Figure 6.14. The top row is the distribution at the time step with the maximum temperature of FEA. The middle row is the distribution of ACR-2. The bottom row shows the distributions from ACR-4. IR image data were corrected for using the emissivity values in Figure 6.9. There is reasonable alignment in the central region of each plate. The slightly elliptical red and yellow regions exhibit a general overlap in shape; however, the peripheral region was much more square for the experimental cases. This is attributed to the deformation of the

plate and the slight influence of the curvature on both the absorbance of the surface and the intensity of the illumination at varying distances from the CPC outlet. It is also possible that the CPC may also have imperfect reflecting surfaces.

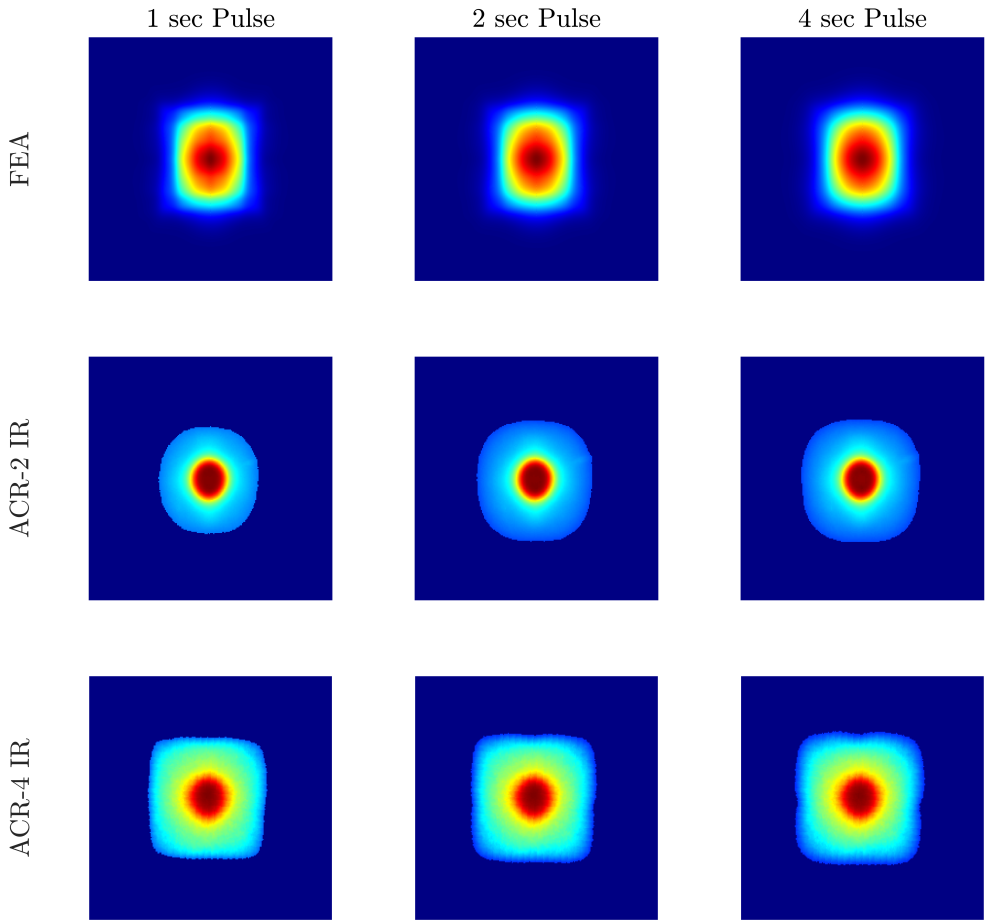
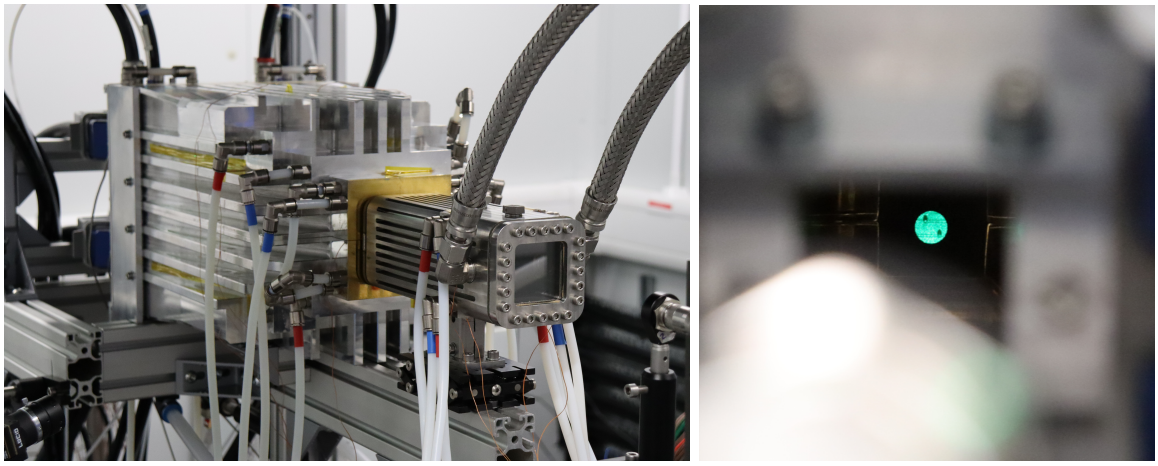


Figure 6.14: *comparison of thermal distributions achieved through finite element analysis and experiments*

ACR-2 has a thermal peak close to the centre, while ACR-4 is much more dispersed. This is thought to be attributable to the differences in conditioning with varying distances from the centre. The highest temperature was experienced in the centre of both plates, and chemical processes were accelerated in this region. This meant that the centre was conditioned faster and to a greater extent than the peripheral region. This results in a relatively lower emissivity in these regions. The thermal conductivity of the material used for modelling may under-approximate the true conductivity. This leads to a tighter



(a) (b)

Figure 6.15: *(a) full experimental set-up of the Effusion Lifespan and Stress Addition with the plenum and all coolant and supply lines installed (b) representative positioning of the measurement region pyrometer 1, over the centre of the coupon*

distribution about the centre as the dispersion during the short test is reduced. Although there are some differences in the outlet distribution, it was concluded that the predictive modelling performed in Chapter 5 was reasonable. Further supporting evidence for the CPC distribution is also provided in the work described in Sections 6.5 and 6.6.

6.3 Hold Testing

Following the baseline test of the CPC, the thermal response of the coupon coolant air supply was evaluated. This was done to ensure that all constituent components remained below respective melting temperatures and that the measured temperatures were in line with the FEA results introduced in Chapter 5. Two tests were run: the first involved an extended hold to determine the quasi-steady thermal distribution in the plenum after 70 minutes. It consisted of 50 minutes of VCSEL supply with water cooling and 20 minutes of only water cooling after the VCSELs were turned off. The second test consisted of 15-minute cycles with 10 minutes of VSCEL power with water cooling followed by 5 minutes of water cooling after the VCSELs were switched off. The latter matched the cycle profile used for the TMF testing and was used to determine the number of cycles required to reach a quasi-steady-state.

A solid coupon without an internal cavity was constructed from steel and affixed to the

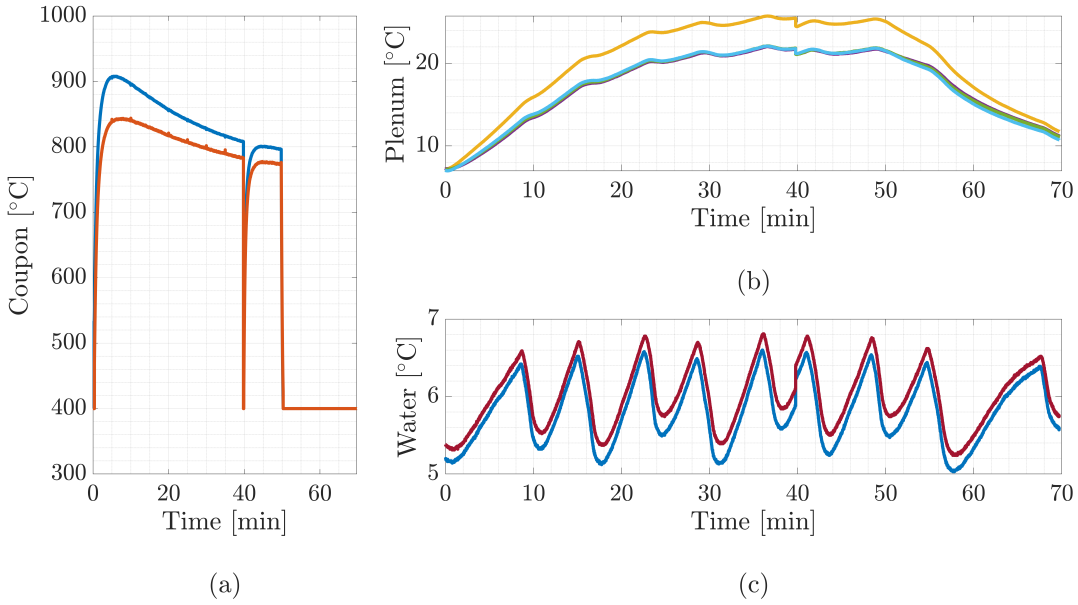


Figure 6.16: *long-hold test temperatures in (a) coupon pyrometer readings (b) plenum thermocouples (c) water cooling loop return flow*

end of the plenum. Both the coupon cooling air supply and the water cooling fittings were connected to the plenum; however, the 100 psi air supply was not used for the coupon coolant or the exhaust management system due to the lack of internal geometry. The experimental set-up is presented in Figure 6.15. 1.344 kW of VCSEL power was supplied to the test section at a spacing of 1.5 mm ± 0.5 mm.

Figure 6.16 presents the relevant data from the long-hold test. A control system issue resulted in an interlock failure at 40 minutes; however, this was corrected and testing was resumed before the plenum temperatures dropped significantly. The system reached a quasi-steady-state after roughly 37 minutes of heating. The plenum cooled off quickly after the VCSEL shut-down, returning to 11-12 degrees in 20 minutes. It was observed that the coupon remains too hot to touch after this time due to the low thermal conduction of the gasket material [65]. The maximum temperature of 25 °C was achieved for the thermocouples placed 1 cm from the coolant channels. This is a 15 °C decrease from the FEA presented in Figure 5.26, suggesting that the overall temperature in the plenum is below the predictions. This was expected for the lower coupon temperature achieved during testing. The cycling testing data are presented in Figure 6.17. After three cycles, the thermal profile of the plenum is independent of the cycle number. The reduction in peak temperature values was expected due to the addition of a cooling phase.

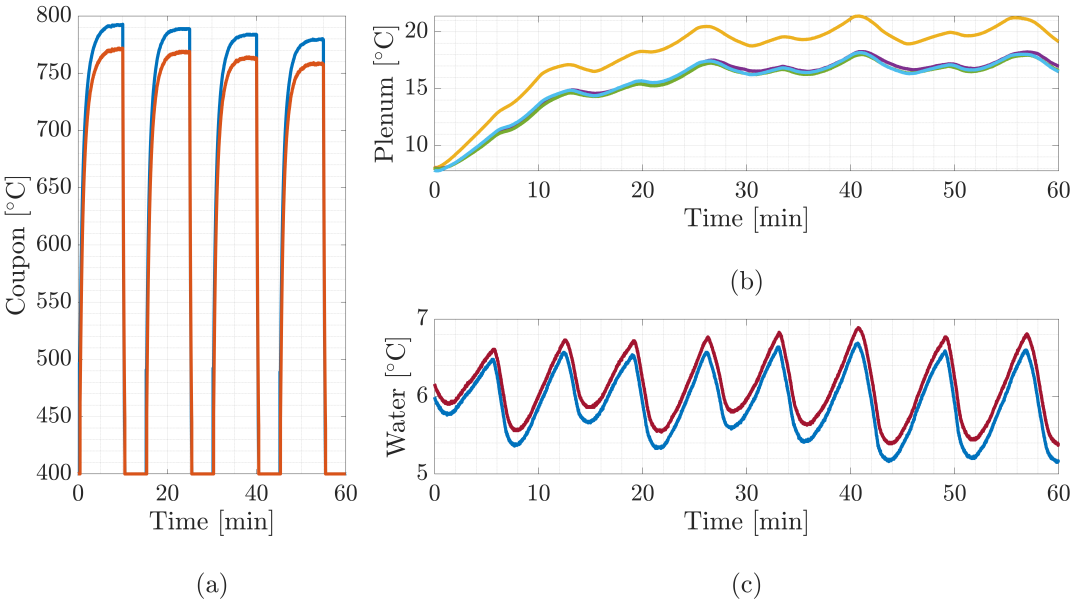
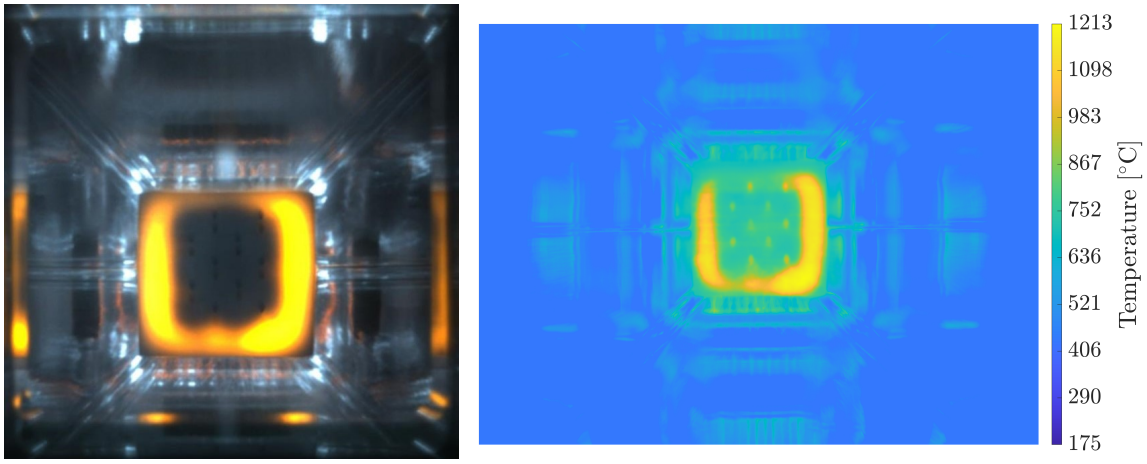


Figure 6.17: *cyclic-hold test temperatures in (a) coupon pyrometer readings (b) plenum thermocouples (c) water cooling loop return flow*

The temperature of the supplied coolant water varies with a long periodicity of approximately 5 minutes. It oscillates about a mean of 6 °C. This mean is consistent with the chiller settings. This was initially thought to be a function of the oscillating flow rate; however, the periodicity does not match. These relatively small oscillations are believed to be an artefact of the chiller control program. As seen in Figures 6.16 and 6.17, the oscillations in the inlet temperature of the coolant loop are aligned with the thermal oscillations observed in the plenum. The magnitude of oscillations in the plenum is considered to have a negligible effect on the coupon during testing due to the long conduction pathway through the plenum, coupled with the low thermal diffusivity of the steel and gasket [62, 65]. The water cooling system functions as intended to keep the plenum at or below the design temperatures while demonstrating a negligible effect on the coupon temperature. A visual inspection of the plenum assembly followed both tests, but no signs of wear were detected.

6.4 IN625-C-I1

The first DWEC coupon, IN625-C-I1, was tested to establish a baseline for the coupon geometry, following the assessment of ELSA sub-components. This was done to ensure that the coupon performance was in line with the design requirements introduced in Chapter 3.



(a) (b)

Figure 6.18: *imaging of IN625-C-I1 in (a) visible spectrum (b) emissivity-corrected infrared spectrum*

The experimental set-up was identical to Figure 6.15, with the substitution of the coupon in Figure 3.13. 1.920 kW of power and 100 SLPM of 22.9 °C coolant air were supplied to the coupon. The ratio of exhaust management to coupon flow was 5. VCSEL power and coolant air were provided for a total of 600 seconds. IR images of the hot-wall were taken following four cycles, which were implemented to achieve proper conditioning of the coupon. Two identical cycles were run for comparison due to the size restriction of the viewing port in the VCSEL bracket. For the first, the pyrometer was mounted to record the true temperature of the hot surface. For the second, the pyrometer was replaced with the IR camera. The cold side pyrometer data was compared and found to be equivalent, supporting the assumption that the thermal field was constant between both cycles and that the results may, therefore, be equated.

A maximum pyrometer temperature of 742 °C in the centre of the hot side with a thermal difference of 200 °C was established. Figure 6.18 presents the images of the digital and IR cameras. The emissivity coefficients were interpolated using this roughness from the values in Table 6.4 for the post-processing of the IR image. The mean surface roughness for the coupon is 0.78 μm, sampled at a hot-wall location using Alicona procedures identical to those outlined previously. The corrected IR image data correspond to the pyrometer reading of 742 °C in the central region, which supports the method of interpolating Table 6.4 for cold-rolled results to the 3D-printed coupon.

The most important result of this test is the ring of high-temperature material around

the central region. This is attributed to the lack of pedestals and impingement holes, which resulted in a significant conduction pathway between the centre and the cool mounting. With increased thermal resistance, the coupon can not conduct enough energy to adequately remove excess heat. Of particular concern was that an increase in temperature would risk crossing the solidus temperature in the outer region of the ring, since the maximum at this location is 1214 °C. Several attempts were made to minimise this. The position of the coupon was altered in all directions and both the VCSEL and the coolant air supplies were altered without a meaningful effect.

6.5 Addressing Coupon Overheating

Cycling the existing coupon design without mitigating the overheating region would not produce representative results. Uneven temperatures and the associated un-representative stress field were to be avoided; therefore, a redesign of the coupon was required. Modification of the existing design was preferable due to time and budget constraints. Altering the internal cavity was not possible following the brazing of the slot plugs. Additional film holes were not thought to impact internal cooling sufficiently. It was hypothesised that the addition of impingement holes around the central region would increase local cooling and remove excess heat due to the high stagnation Nusselt numbers present [21]. There were concerns about the number of film holes and their interactions. Increasing the number of holes for the same mass flow rate decreases the impingement jet velocity as the total cross-sectional area increases. A high density of impingement holes may also act unfavourably as the disk of accelerating fluid leaving the impingement site may interact with neighbouring jets. Various conjugate domains were developed and assessed in Fluent[7].

6.5.1 Domain and Boundary Conditions

A total of 6 domains, presented in Figure 6.19, were investigated. Existing holes are coloured red, and new holes are coloured green. V0 through V3 represent the initial attempt to add new insertion holes at a spacing identical to the central region. V4 is the extreme case of a large number of film holes at high density. V5 is the final case investigated with targeted spacing, as informed by the five previous solutions.

[7] Ansys®Academic Research Fluent, Release 21.2

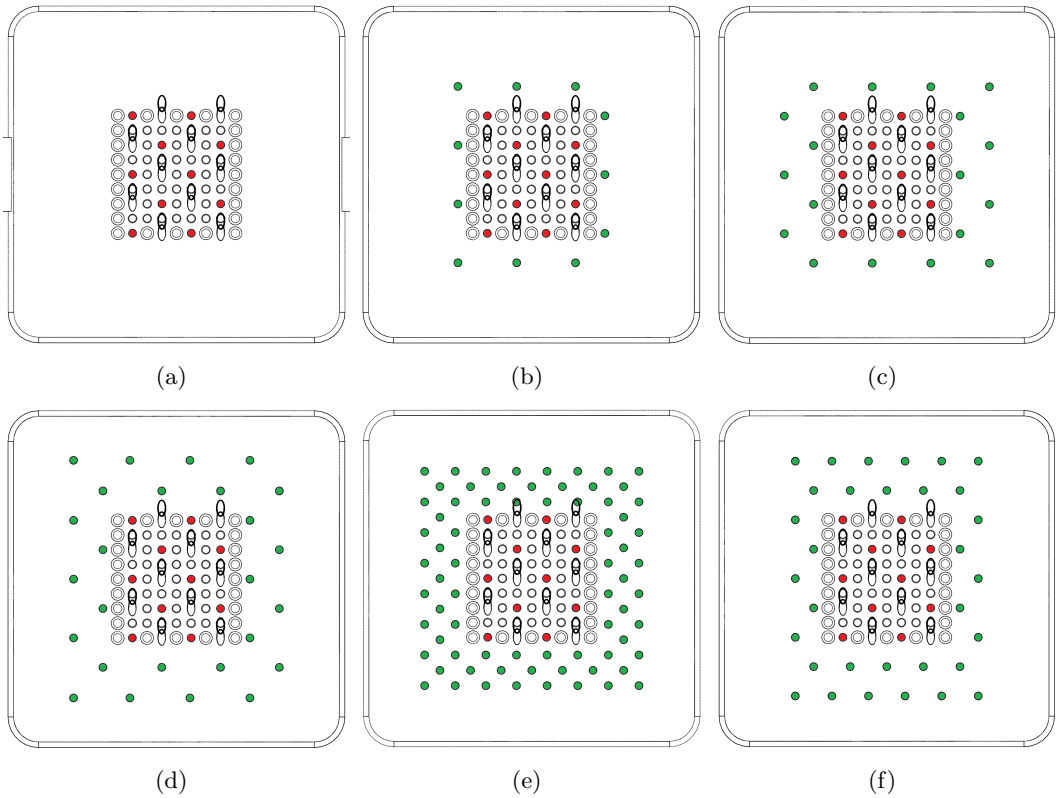


Figure 6.19: *impingement hole configurations of (a) V0 (b) V1 (c) V2 (d) V3 (e) V4 (f) V5, showing existing impingement holes in red and proposed holes in green.*

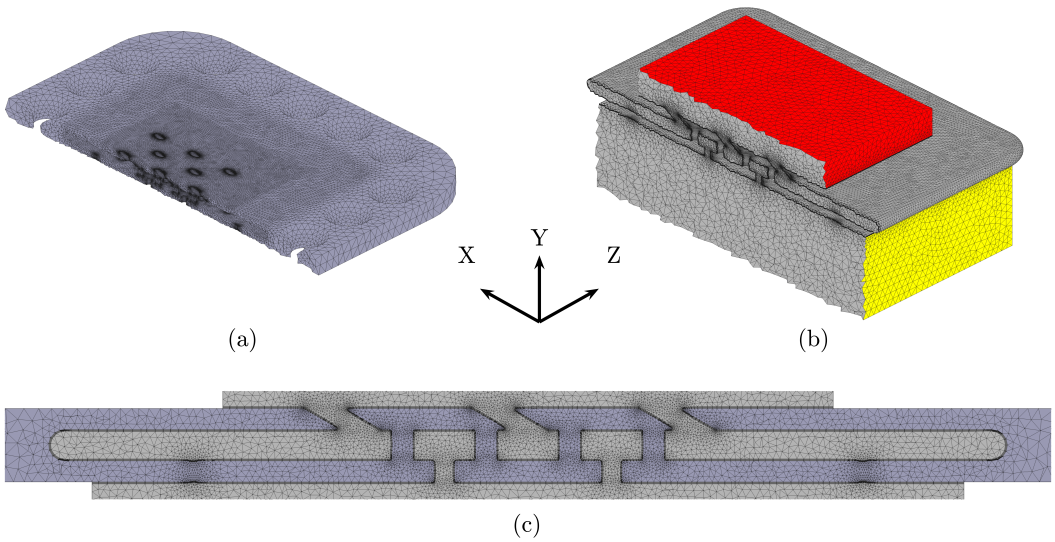


Figure 6.20: *components of the conjugate mesh showing (a) solid domain (b) fluid domain (c) integration of solid and fluid domains with refinements around fillets*

The solid domain, shown in Figure 6.20 (a), was taken directly from the CAD file. The fluid domain, shown in 6.20 (b), was constructed in SpaceClaim[8] by extracting the internal volume and adding additional volume to the interior and exterior of the solid domain. Shared topology was implemented through DesignModeler[9]. The material properties for air at 27 °C were used: $C_p = 1006\frac{J}{kgK}$, $k = 0.0242\frac{W}{m°C}$, $\mu = 1.7894E-5\frac{kg}{ms}$, with the density governed by the ideal gas law. The material properties for Inconel 625 were taken from [108].

The fluid inlet underneath Figure 6.20 (b) was set to 27 °C with a mass flow rate condition of 2 $\frac{g}{sec}$. The four adjacent sides were set as symmetry planes to prevent friction losses at a fluid-fluid interface. The five surfaces of the fluid domain that did not touch the coupon were set as an outlet with a gauge pressure of 0 bar and a back-flow temperature of 27 °C. Each of the fluid-solid interfaces was automatically coupled. The coupon hot-wall exterior face has coupling disabled to allow for the VCSEL supply. This was assumed to have minimal impact on convection because the film jets were predicted to detach immediately. This was specified using a boundary flux, obtained by scaling the distribution in Figure 5.22 by 0.12, accounting for the VCSEL power at 20% capacity and an estimated absorbance of 0.6. Boundary conditions were constant across each of the designs, so the impact on absolute temperatures and gradients may be compared.

6.5.2 Mesh and Models

The mesh was constructed using a tetrahedral method with an inflation layer on the fluid-solid interfaces. Body sizing was used for the fluid domain, with refined face sizing on each of the walls. Local refinements were made to capture the curvature of the fillets. An inflation layer with a total thickness of 0.12 mm was used. Twenty layers were used at a growth rate of 1.2 to ensure that the y+ values remained below unity for the high-velocity flow. The mesh used for the V5 solution is shown in Figure 6.20. The solid domain sizing was constrained using the fluid wall sizing through Shared Topology, while a growth factor factor of 1.2 ensured there were sufficient nodes through the wall thickness. A mesh refinement study was performed on the V0 geometry. The results are presented in Figure 6.21. The minimum boundary mass flow rate, the average HTC area, and the mass-average solid temperature were tracked and converged well after two refinement steps. Further refinement

[8] Ansys®Academic Research SpaceClaim, Release 21.2
[9] Ansys®Academic Research DesignModeler, Release 21.2

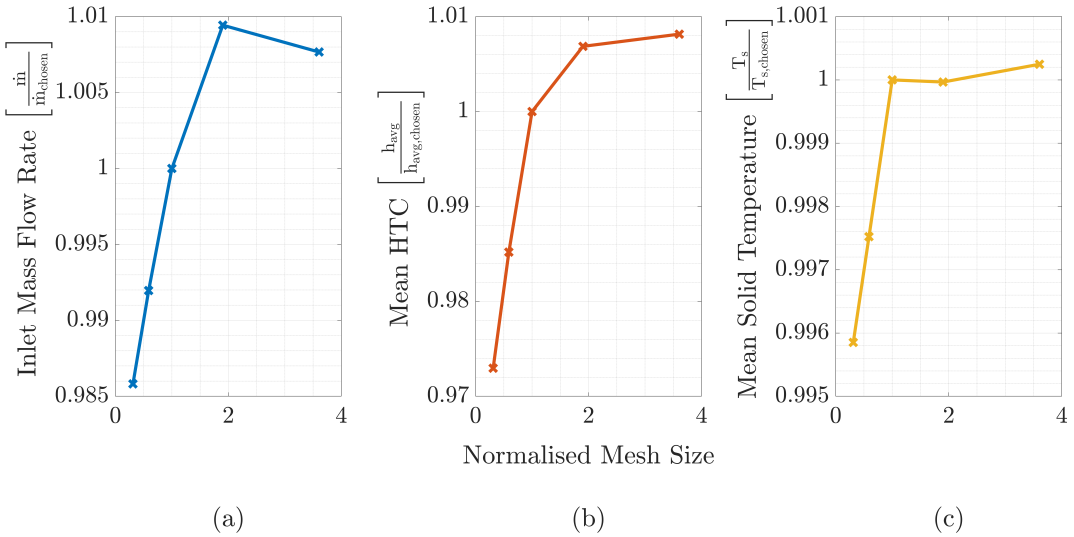


Figure 6.21: *mesh-independence results for the conjugate model showing (a) total mass flow rate (b) area-average convective HTC (c) mass-average solid temperature*

shows an impact of 1% on these values.

The k-ϵ standard and realisable, and k-ω standard and SST models were considered and investigated for the refined mesh. Both of the k-ω models proved unstable. The standard formulation produced a singularity in the solution, and the SST did not converge at a reasonable level. Both of the k-ϵ models converged. The realisable provides the most realistic thermal gradient as compared to the experimental results. Thermal and compressibility effects were enabled due to the presence of large heat fluxes and high Mach numbers [8]. The iterations were run until the standard residual conditions, mass balance, and energy balance were met. The latter two are defined as a $< 1\%$ and $< 3\%$ imbalance, respectively.

6.5.3 Results and Discussion

The hot-side results for each case are presented in Figure 6.22. The V0 case shows good agreement with the thermal distribution as the maximum temperature was over-estimated, but the central region, at 719 °C, was near to the 742 °C measured in the tests. This overestimation may be caused by manufacturing defects that are not modelled in the geometry of the conjugate solution. A comparison of holes is shown in Figure 6.26. The 3D-printed holes are slightly smaller than the 1.2 mm specifications. This is thought to reduce local coolant flow in the physical coupon, decreasing effective cooling in this region.

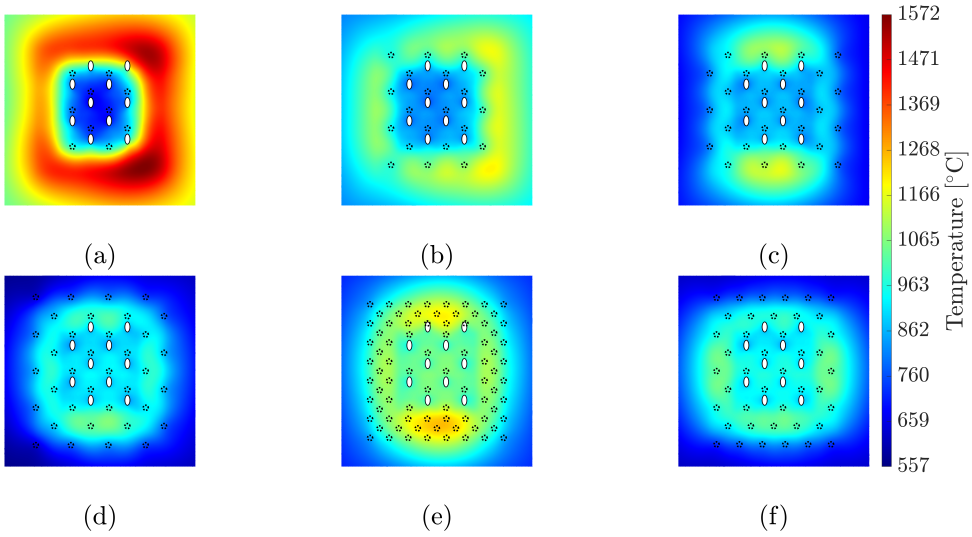


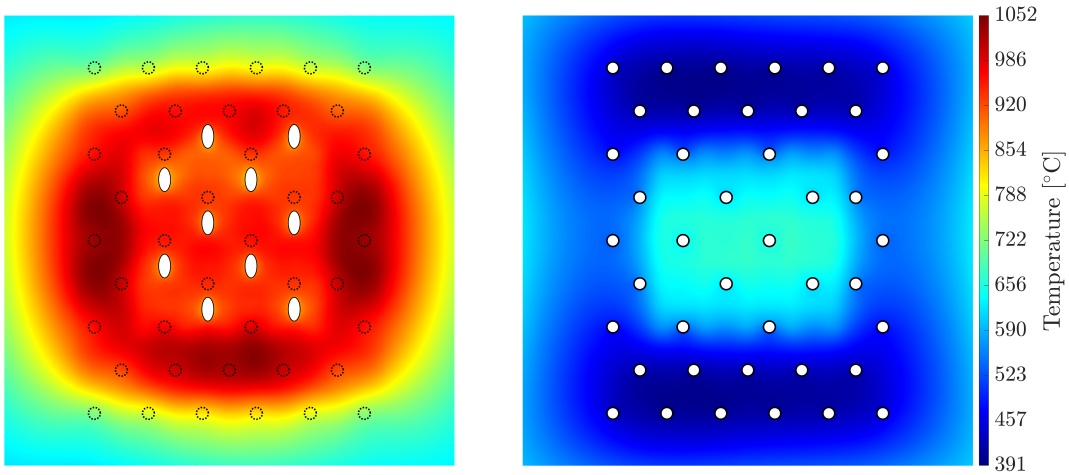
Figure 6.22: *hot side thermal distributions for (a) V0 (b) V1 (c) V2 (d) V3 (e) V4 (f) V5*

This disagreement was considered beneficial for this assessment, as the cooling effects of each design would be more pronounced in experiments where the holes were larger.

Design Number	T_{max} [°C]	T_{pyro1} [°C]	T_{pyro2} [°C]	ΔT_{centre} [°C]	R_{over} [–]
V0	1571	719	614	105	1.86
V1	1198	837	559	278	1.33
V2	1165	885	599	285	1.24
V3	1066	937	645	292	1.11
V4	1257	1067	758	309	1.14
V5	1052	967	671	296	1.07

Table 6.5: *relevant temperature values for coupon redesign variants*

The relevant thermal results are presented in Table 6.5. Increasing the number of impingement holes for identical heating and cooling parameters results in increased temperatures in the centre. This appears to have a comparatively minimal effect on the cold side. An increase in thermal gradients was observed through the coupon. It was clear from the results that successive variations offer a better reduction in over-temperature, defined as R_{over}. The exception is V4, which has a high density of impingement holes. The excessive flow area reduces the effectiveness of the jet. V5 was selected due to the small R_{over} value of 1.07. Figure 6.23 shows the thermal distribution of the hot- and cold-faces. The cold-face has a



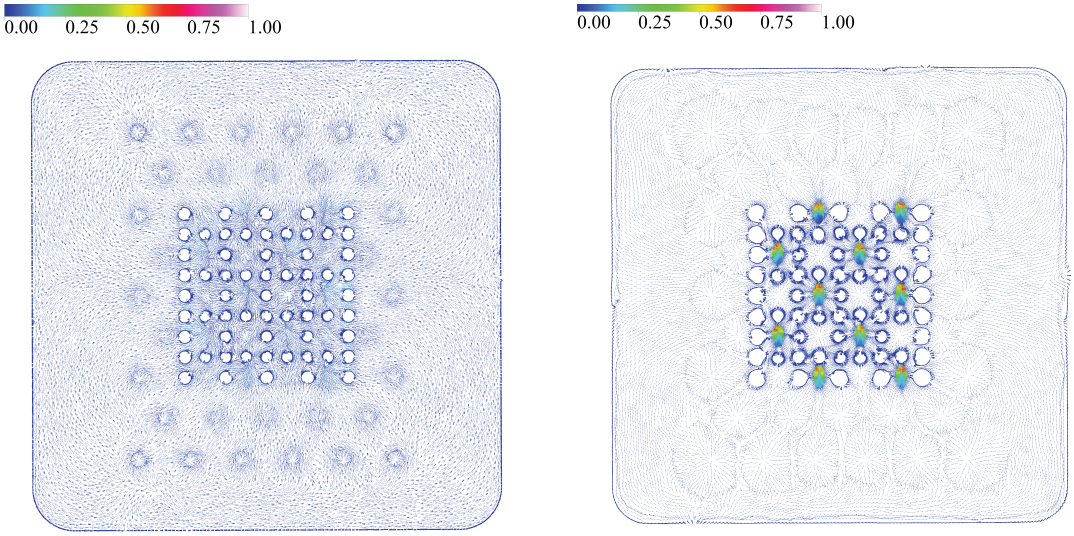
(a) (b)

Figure 6.23: *thermal distributions for the V5 design (a) hot side (b) cold side*

maximum in the centre, where the pedestals conduct comparatively large amounts of energy because of the short conduction pathway and large net cross-sectional area.

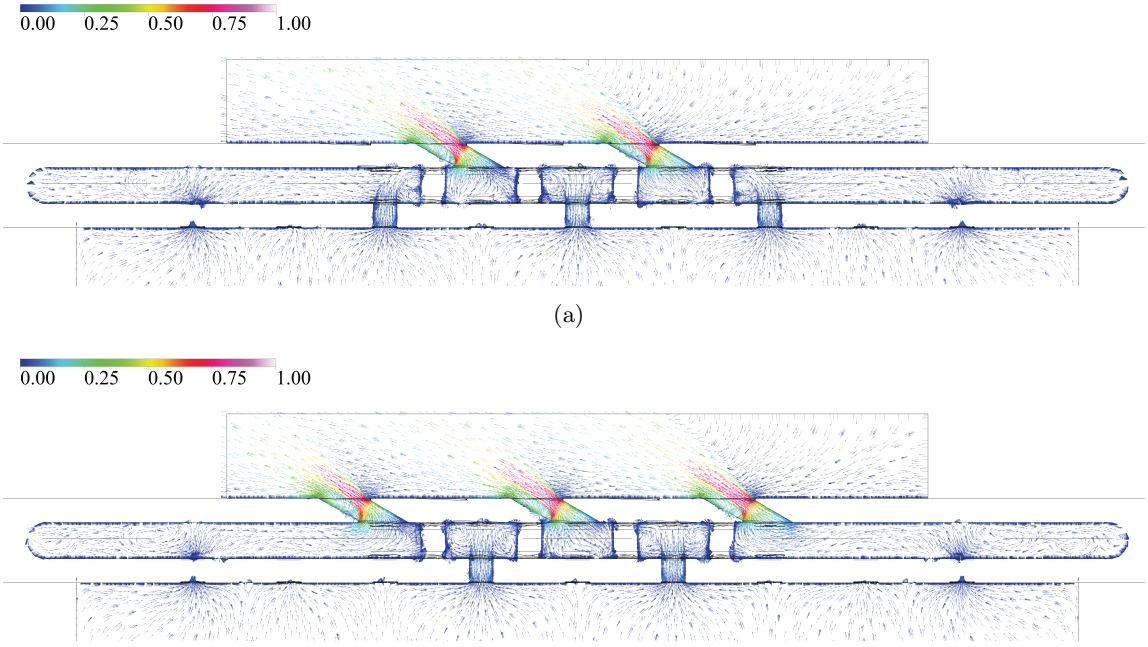
Figures 6.24 and 6.25 provide flow vectors for several sampling locations within the coupon for the V5 design. Vectors are normalised by the maximum flow velocity in the domain, which is reported in the legend. Figure 6.24 shows a slice at the pedestal mid-height and adjacent to the interior of the hot-wall. The mid-height slice of the pedestal provides an understanding of the migration of coolant air in the cavity due to the presence of the uncoupled walls. The vast majority of the impingement jet flow migrates directly towards the centre to be exhausted out of the film holes. Some circulate with relatively low velocity away from the impingement holes. Due to the extent of the impingement holes in the stream-wise direction, this peripheral flow migrates from the stream-wise to span-wise sides. This appears to exhibit pseudo-symmetry in agreement with the pseudo-symmetry of film and central impingement hole locations. The adjacent hot-wall slice allows for a comparison of the flow that accelerates away from the impingement region. The additional exterior impingement holes display locally asymmetric flow. This suggests that some may be modelled as jets in cross-flow. The central impingement holes display apparent uniformity in their shape. This indicates that the impingement behaviour in the centre emulates the infinite flat plate case without cross-flow.

Figure 6.25 shows a slice along the x-y plane for the case of 2 or 3 rows of film holes. For



(a) (b)

Figure 6.24: *flow vector field sampled for an x-z plane (a) pedestal mid-height (b) hot-wall adjacent*



(a)

(b)

Figure 6.25: *flow vector field sampled for an x-y plane (a) 2 rows of film holes (b) 3 rows of film holes*

the 2-hole case, the impingement holes between the outer row of pedestals exhibit a strong deflection due to the presence of high cross-flow from the impingement holes from the left or right. They shift towards the nearest film hole and strike the neighbouring pedestal fillet. This behaviour was not seen with the 3-row case, as the flow from the new impingement holes encounters a film hole first. In both cases, the central film hole exhibits the highest relative mass flow rate and velocity. The impingement holes, in this case, behave in line with previous results [31, 76]. The results indicate immediate separation of the flow. This confirms assumptions made in the decoupling of domains on the exterior wall.

Due to the theorised effectiveness of the configuration, additional impingement holes in the V5 configuration were spark-eroded in to the cold-wall of the remaining coupons. An example of the IN625-C-I2 component is provided in Figure 6.26. It is clear that the shape is slightly different between the holes formed by different manufacturing techniques. This trend is consistent with all remaining coupons.

6.6 IN625-C-I2

To confirm the efficacy of the modelled geometry, IN625-C-I2 was tested using a range of power and coolant flow rates to establish an engine-representative T_{max} and ΔT. The results confirm that the conjugate model introduced in Section 6.5 accurately captured the thermal phenomena in the coupon and coolant air domains. Subsequently, the coupon was cycled to investigate the effect of further conditioning of the heated surface. The coupon experienced rapid failure as a result of repeated thermo-mechanical loading.

6.6.1 Thermal Distribution

An identical approach to the C-I1 coupon was applied to C-I2 for confirmation of the redesign. The surface roughness was measured at 0.76 μm. The coupon was bolted to the plenum and no leaks were detected. Conditioning was performed using four 600-second cycles. 2.880 kW of VCSEL power and 94.1 SLPM of 27.2 °C air were supplied. The maximum pyrometer temperature of 982 °C with a thermal difference of 185 °C was achieved. The ratio of air flow from the VCSEL bracket to coupon air flow was 5. Thermal results are presented in Figure 6.27. The corrected IR image data match the pyrometer reading in the same location. The measured thermal distribution aligns well with the prediction of V5 in Figure 6.23. The

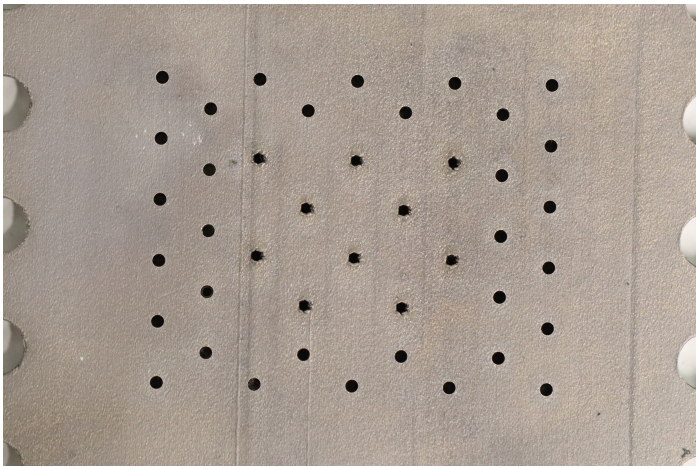
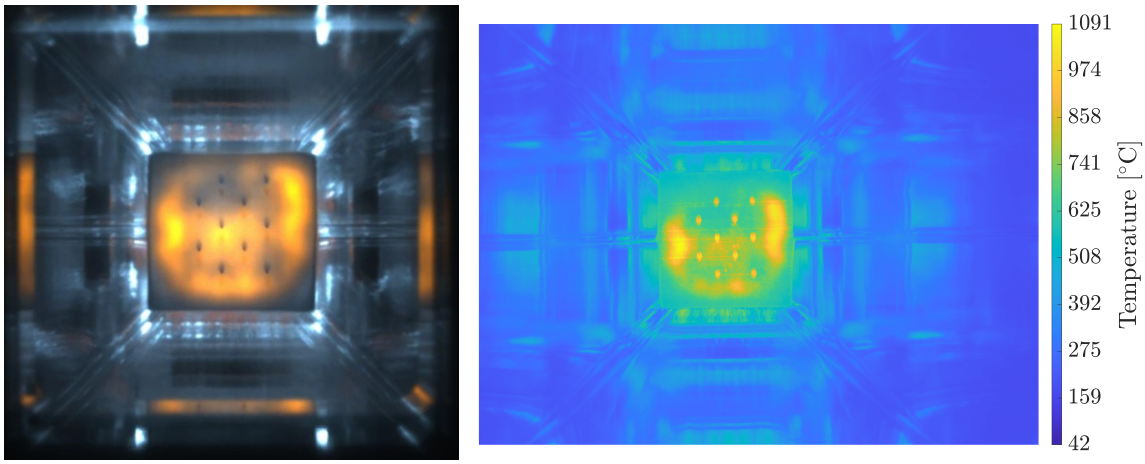


Figure 6.26: *cold-wall of IN625-C-I2 post-machining showing the difference in 3D-printed and machined impingement hole profiles.*



(a) (b)

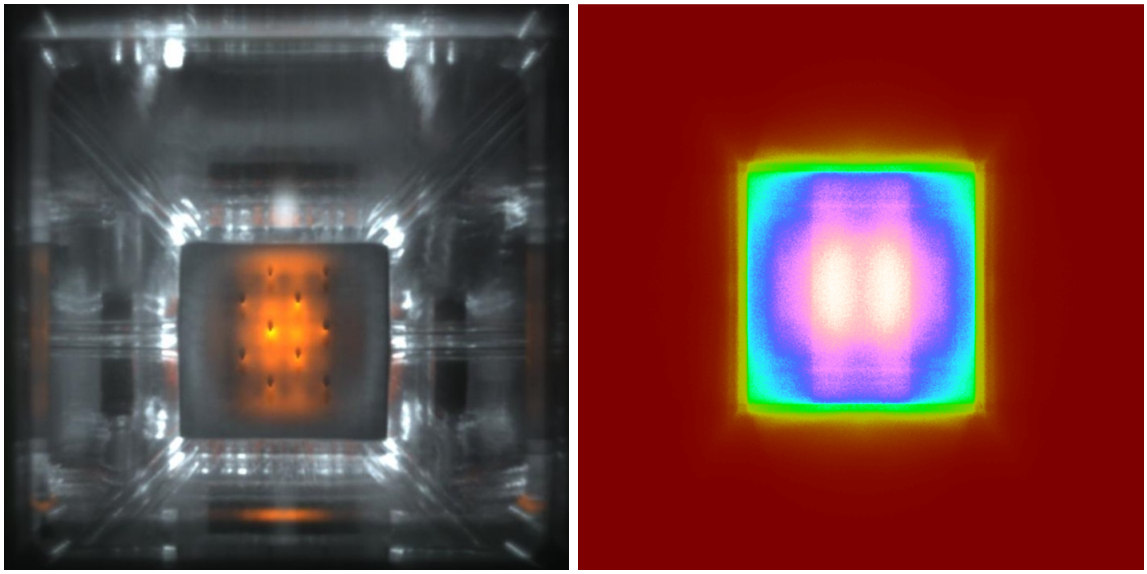
Figure 6.27: *imaging of IN625-C-I2 in (a) visible spectrum (b) emissivity-corrected infrared spectrum*

measured R_{over} for this case is 1.09, which was considered adequate to progress.

6.6.2 Initial Failure

The IN625-C-I2 coupon used a 4-D pulse profile with the flux supply scaled to ensure the maximum temperature was near 975-1000 °C. 4-second pulses were supplied in the absence of any coolant air, followed by 1 second of rest and 40 seconds of 200 SLPM coolant air to bring the coupon back to lab temperature.

The pyrometer initially over-reported the temperature before stabilising at the correct value within 200 ms. The maximum coupon temperature started at roughly 900 °C and increased over 10 cycles with the same power setting. The power settings were increased



(a) (b)

Figure 6.28: *(a) IN625-C-I2 glowing hot following vertical-cavity surface-emitting laser pulse (b) ray tracing illuminance distribution*

twice throughout; however, the measured thermal drift was not explained by the input of the cycle. The explanation of this through an increase in absorbance was also considered unsatisfactory. Pulse testing suggests that the absorbance normalises within 30 cycles. This drift is thought to be indicative of accumulations of dislocations, which increase the conductive pathways between the hot-wall and the pedestals. This requires confirmation by CT imaging. This was not feasible due to time and budget constraints.

Figure 6.28 presents a digital camera image from cycle 80. It shows the instant the VCSEL was shut off. The glowing material is proportional to the thermal distribution in Figures 6.18 and 6.27. The thermal distribution at all times during the pulse is considered proportional to the illuminance at each point due to the short pulse and low thermal conductivity [108]. The digital image is presented alongside the illuminance distribution for a 1 mm target spacing from the modelling. It offers a qualitative comparison of the exit flux. The two large central lobes are clearly visible. High-flux regions extending in stream-wise directions match the thermal distribution, which shows a rectangular area at high temperatures. This results in local maxima near the boundaries of the CPC exit aperture, outside where the pedestals provide conduction away from the hot surface.

Cyclic testing was aborted on cycle 220 due to the rapid formation of cracks presented in Figure 6.29. Cracks from thermal cycling visible at room temperature suggest an

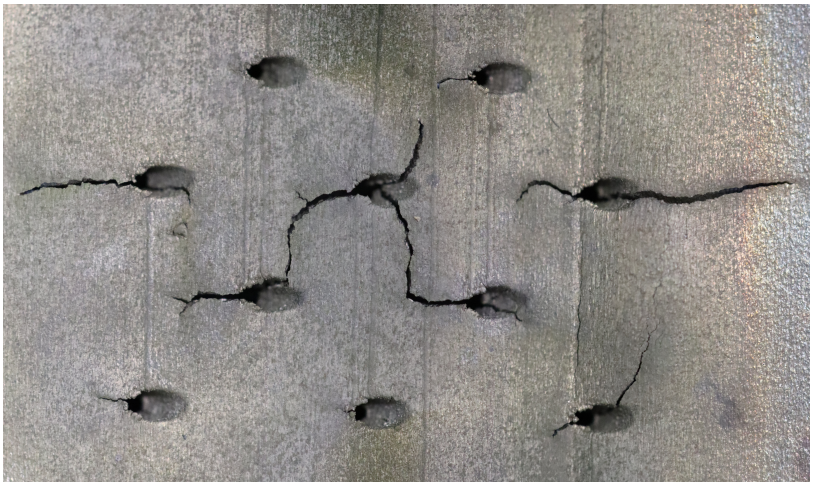


Figure 6.29: *IN625-C-I2 post cycling exhibiting large cracks originating from the central film holes, where the local temperature was greatest*

accumulation of compressive plastic strain at high temperatures. The test section experiences a large tensile force during cooling, which causes failure. These cracks were observed to close as the coupon was heated. Growth was not observed because of the rapid nature of their formation. They originate from the highly inclined film holes on each of the stream-wise sides where the stresses were predicted to be greatest [31, 101, 103]. In addition, they are the largest and most connected along the centre line. This correlates with the high-temperature region in Figure 6.28

6.7 Summary

The performance of the water cooling loop was recorded and compared with the network flow model used in Chapter 5. It confirmed that the system will not draw more than 60 PM of cooling water and that the estimates of the HTC values were reasonable. Hold testing adds further validation to prior modelling as measured values for the plenum temperature in the presence of a high-temperature coupon align with FEA results. The temperatures were well below the design tolerances, and no rapid failure was observed outside the coupon. Undulations in cooling water flow rates and temperatures were observed in both tests; however, these were shown to have a negligible impact on the coupon temperature.

The performance of the CPC was assessed in two ways: thermal distribution results measured during the pulse testing show agreement in the central region and disagree with the remainder of the thermal field when compared to FEA. This was attributed to the plastic

deformation of the calibration plate due to thermal stresses and the resulting misalignment. The distribution at the CPC outlet and the deformation hypothesis were supported by the IN625-C-I2 tests. A direct measurement of the thermal field was possible using images captured during the IN625-C-I2 tests. Qualitatively, it shows alignment with the ray tracing. The regions that glow brightest were those that receive the most VCSEL energy for the short pulse. In-plane conduction was considered negligible due to the short pulse length. This was supported by the results of the pulse testing. The confirmation of the CPC flux was vital for subsequent modelling.

Pulse testing was performed to categorise the behaviour of the material. The necessity of conditioning an Inconel 625 sample was shown, as both the absorbance and emissivity changed with time. Time-independent temperature-emissivity values were taken after conditioning. These were observed to follow a strong linear relationship. Coefficients from a linear fit were extracted. The interpolation of these coefficients to the surface roughness of a new sample was supported by the alignment between the emissivity-independent pyrometer and the IR image data. The absorbance of the test piece appears to be independent of the surface finish and aligns well when comparing the FEA-derived results to those of a 1D transient thermal model.

IR imaging of the initial coupon was possible following the acquisition of emissivity data. The thermal field shows regions of over-temperature away from the pedestals where there was a lack of conduction to remove heat. A re-configuring of the VCSELs was considered and abandoned due to a lack of performance. A new impingement hole arrangement was proposed and evaluated to reduce this over-temperature with agreement between computational and experimental results. A significant component of the redesign was the establishment of a conjugate model to assess the coolant flow and coupled coolant-coupon thermal fields. This was recycled for use in later analysis.

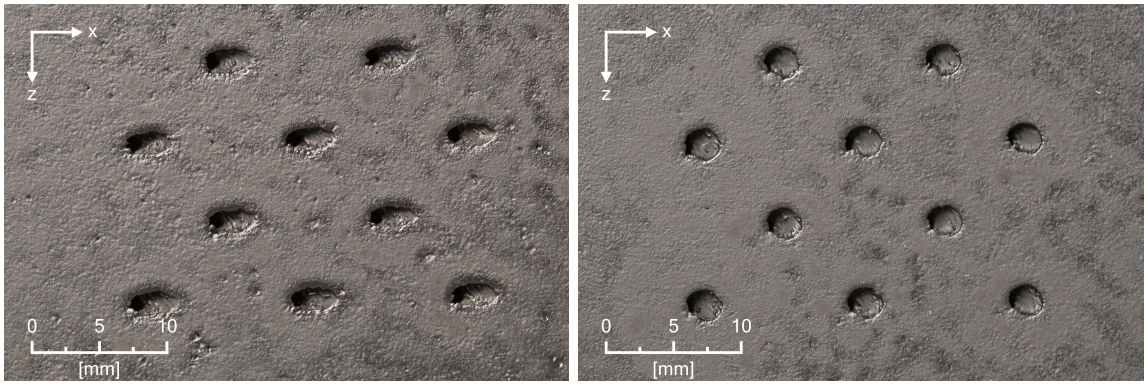
Accidental failure occurred in IN625-C-T2. Cracks originated from the highly-inclined film hole wedges and remain open at room temperature. The failure of the test piece occurred on shut-down, most likely due to high tensile stresses caused by the accumulation of compressive plastic strain. It offers the first experimental suggestion that the stress data derived and analysed computationally by Skamniotis [100, 101, 102, 103, 105] applies to the actual case.

Testing of DWEC Coupons

The previous chapter successfully confirmed the satisfactory operation of the Effusion Lifespan and Stress Addition (ELSA) sub-components and the coupon. This chapter lays out the methodology used and the results of thermo-mechanical fatigue (TMF) testing of double-wall effusion-cooled (DWEC) coupons. Preliminary tests were performed to establish an understanding of how ELSA supply settings affect the thermal field. This understanding was then used to perform cyclic testing on seven coupons of various geometric, material, and thermal configurations. The results continue to support the prior stress and failure analysis [100, 101, 102, 103, 105], with the majority coupons showing crack growth from the film hole wedge (FHW), while suggesting that failure through buckling of the hot-wall is life-limiting for extreme thermal cases.

7.1 Thermal Distribution Testing

Due to the slight variations in the surface finishes and transient absorbance of Inconel 625, the TMF testing profiles had to be established through a series of educated guesses. Constant tweaks were performed manually through the alteration of control program input files to ensure that the temperatures were near-constant as testing progressed. The greatest challenge was the initial cycles when little was known about how the specific coupon would react to incident infrared light provided by the vertical-cavity surface-emitting lasers (VCSELs). A series of tests were performed to establish a relation between the maximum pyrometer temperature, T_{max}, and thermal gradient normal to the plate, ΔT_{normal}, is then used to inform these initial control settings. These values were selected based on their proven impact in dictating the number of cycles to failure [105].



(a) (b)

Figure 7.1: *Aremco 840-CM applied to the surface of (a) IN625-C-T1 (b) IN625-E-T1*

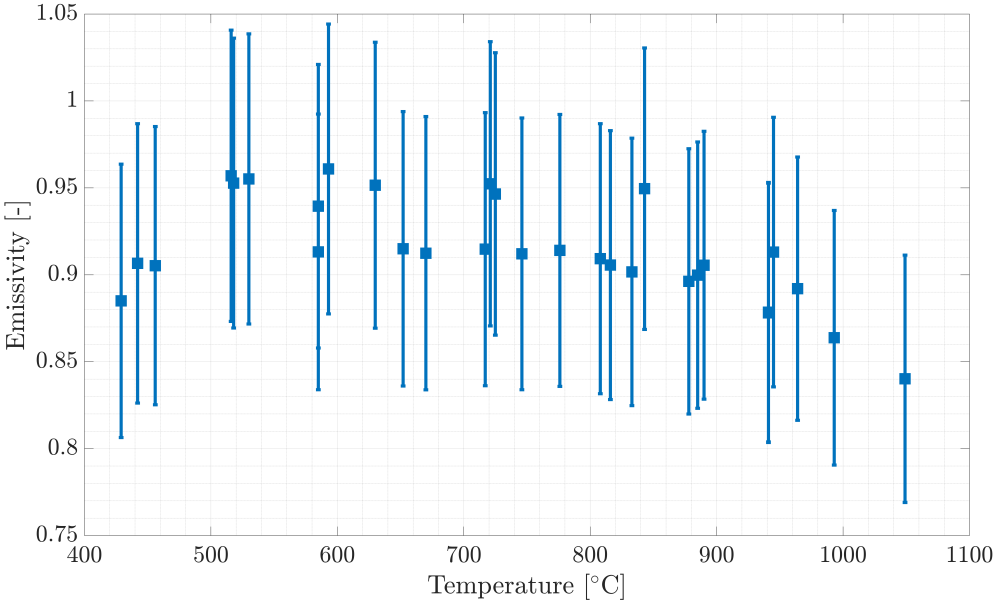
7.1.1 Experimental Method

Both coupon designs, circular and elliptical holes, were investigated. These were bolted to the plenum and leak tested before a range of VCSEL power settings and coolant air flow rates were administered until a quasi-steady thermal field was established. The VCSEL power was set to 6 $\frac{\mathrm{W}}{\mathrm{cell}}$ and step by 6 $\frac{\mathrm{W}}{\mathrm{cell}}$ to a maximum of 90 $\frac{\mathrm{W}}{\mathrm{cell}}$. The coolant flow rates are: 1 $\frac{\mathrm{g}}{\mathrm{sec}}$, 2 $\frac{\mathrm{g}}{\mathrm{sec}}$, 3 $\frac{\mathrm{g}}{\mathrm{sec}}$, and 4 $\frac{\mathrm{g}}{\mathrm{sec}}$. The cycles consisted of four 5-minute holds to ensure that the highest $\mathrm{T_{max}}$ was obtained at the end of the test. Later cycles omitted the lowest flow rates due to $\mathrm{T_{max}}$ exceeding 1000 °C.

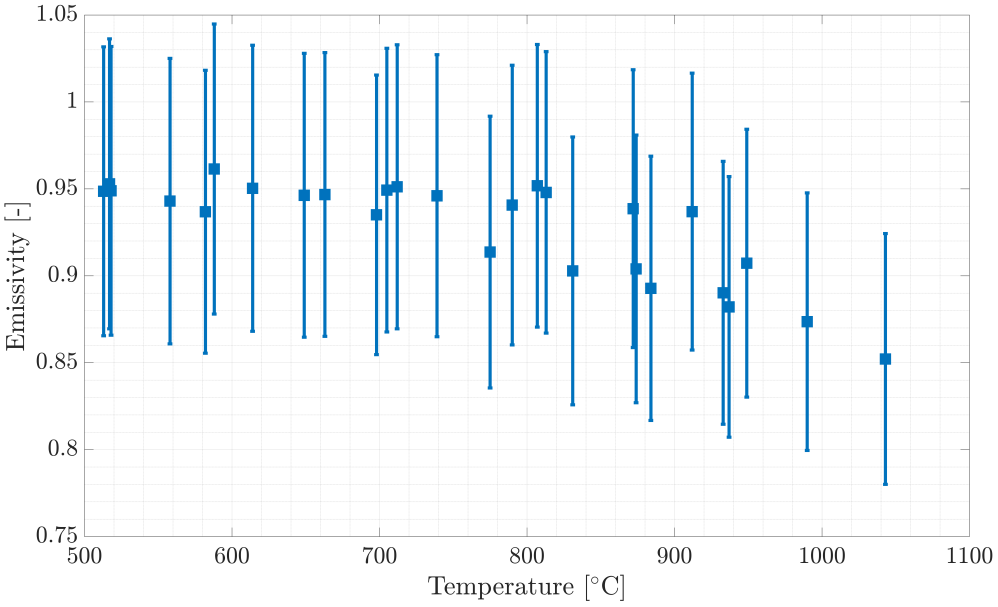
Commissioning tests established both the need for component conditioning and the risk of fatigue failure in the DWEC system during short pulses. It was decided to remove the need for conditioning and minimise the risk of premature failure. A high-emissivity coating was applied to the exterior of the coupons' hot-wall. Figure 7.5 shows how Aremcos' 840-CM [51, 52, 53, 54, 55, 56, 57] was used due to its availability and service temperature of 1093 °C. It was sprayed on and cured in the oven prior to testing.

7.1.2 Results and Discussion

$\mathrm{T_{max}}$ was calculated using the pyrometer one temperature, although the commissioning tests indicated that the true maximum exists outside the pyrometer measurement area. $\Delta\mathrm{T_{normal}}$ was calculated using the difference in pyrometers 1 and 2. IR images were taken at the end of each hold when the thermal field was quasi-steady. To ensure that the emissivity values were correct, average emissivities were calculated using Equation (6.1).

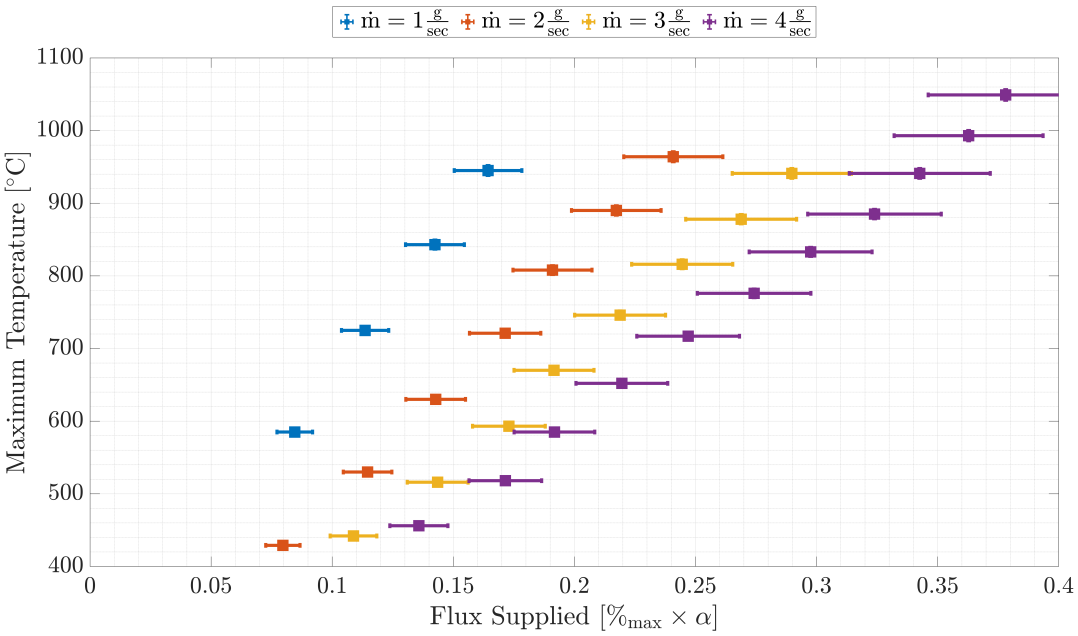


(a)

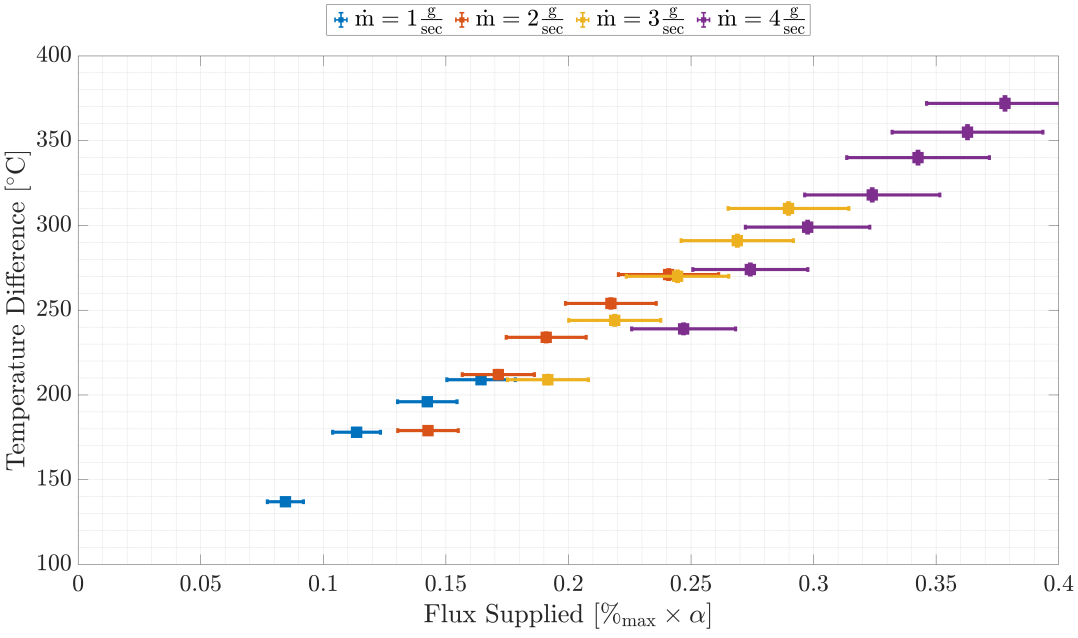


(b)

Figure 7.2: *emissivity versus temperature for (a) IN625-C-T1 (b) IN625-E-T1*

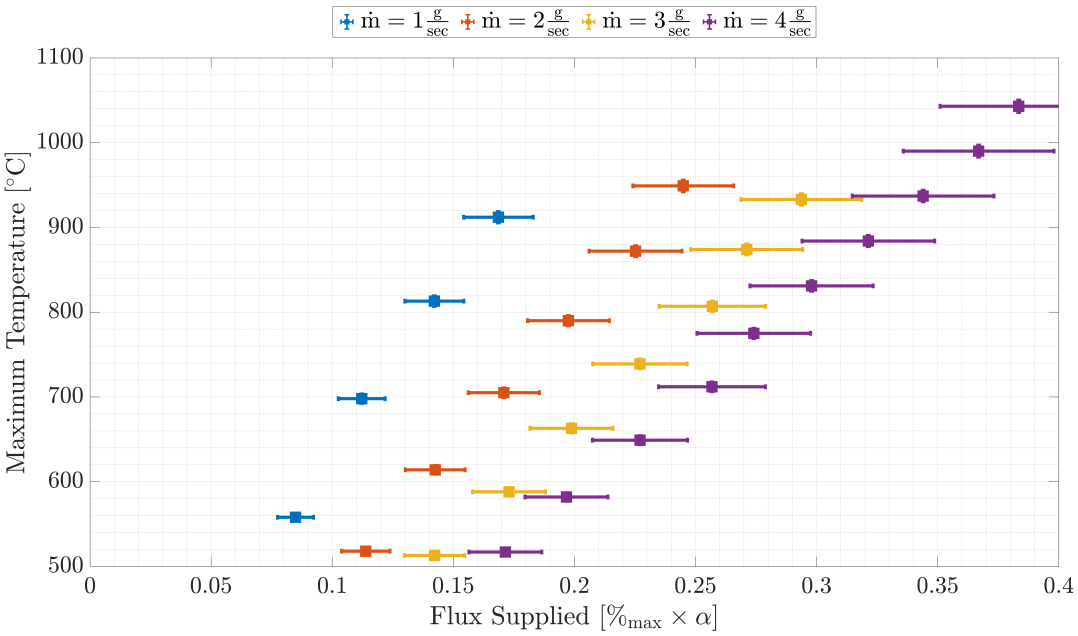


(a)

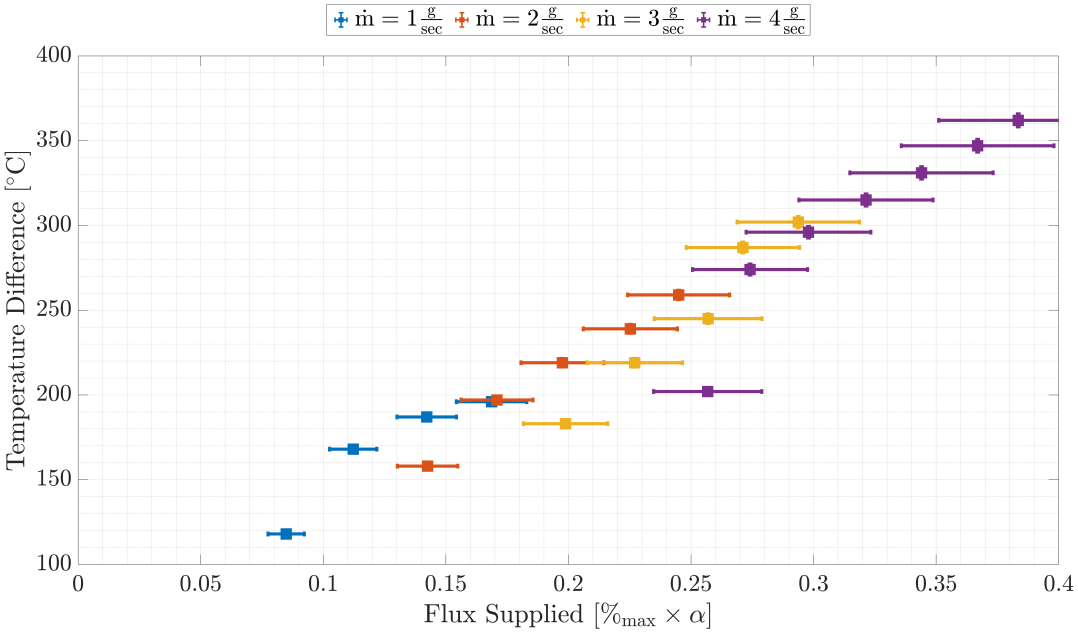


(b)

Figure 7.3: *effect of vertical-cavity surface-emitting laser power and coolant flow rate for IN625-C-T1 (a)* T_{max} *(b)* ΔT_{normal}

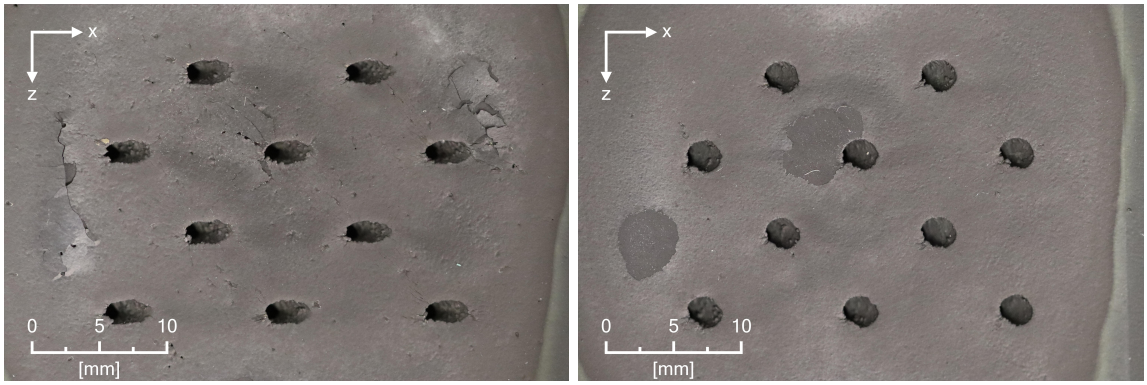


(a)



(b)

Figure 7.4: *effect of vertical-cavity surface-emitting laser power and coolant flow rate for IN625-E-T1 (a)* T_{max} *(b)* ΔT_{normal}



(a) (b)

Figure 7.5: *distress of Aremco 840-CM coating following testing for (a) IN625-C-T1 (b) IN625-E-T1*

Emissivity values for both coupons are presented in Figure 7.2. There is an apparent decrease in the average spectral emissivity for the range of temperatures investigated for both coupons. These values were used to scale the x-axis of the thermal data presented in Figures 7.3 and 7.4.

The maximum temperatures for both hole designs exhibit a strong linear variation in proportion to the scaled VCSEL power supplied. The slope decreases with increasing flow rate, indicating a clear dependence on the increased convection. The thermal gradient normal to the plate also exhibits a strong linear dependence on the scaled VCSEL power at high power settings. At low power settings, the convective cooling and conduction through the plenum dominate the thermal field. This causes a sharp decline in ΔT_{normal}. The increase rate of ΔT_{normal} is significantly less than T_{max} for the same increase in the VCSEL power. This effect is most pronounced at low coolant flow rates where T_{max} increases by 460 °C with an increase in ΔT_{normal} of only 70 °C.

Figure 7.5 presents the effects of the test on the Aremco 840-CM coating. The remaining coupons were thought to be coated to ensure that reliable absorbance and emissivity values may be used; however, the distress pictured altered the plan. The flaking of the material was driven by the mismatch in thermal expansion, rendering the paint brittle. The flaked regions exhibited anomalous IR measurements, with a sharp decrease in measured temperature. This was corrected for when extracting the temperatures for the emissivity values.

7.2 Thermo-Mechanical Fatigue Testing

With confirmation of ELSAs' satisfactory performance and an understanding of appropriate control settings, TMF testing of the DWEC coupons was performed. The coupons exhibited failure from the FHW, with two high-temperature coupons experiencing buckling failure on the hot-wall. The results show a clear dependence on the maximum temperature, a departure from the thermal gradient used in previous work [36, 101, 102, 103].

7.2.1 Experimental Method

Seven coupons were tested: 6 were constructed of 3D-printed Inconel 625, and 1 was constructed of single-crystal cast CMSX-4. 2 target temperatures and two thermal gradients were selected for the 6 Inconel 625 coupons. These are presented in Table 7.1. They were chosen to provide a range of engine-representative cases aligned with prior work [101].

Test Section	T_{max} [°C]	T_{min} [°C]	ΔT_{normal} [°C]
IN625-C-T2	900	700	200
IN625-C-T3	1100	900	200
IN625-C-T4	900	550	350
IN625-E-T2	900	700	200
IN625-E-T3	1100	900	200
IN625-E-T4	900	550	350
CMSX-4-T1	900	700	200

Table 7.1: *coupon target temperatures for the quasi-steady region of thermo-mechanical fatigue cycling*

The total cycle length of each cycle was 900 seconds. 600 seconds of constant VCSEL power was followed by 300 seconds of maximum-flow rate cooling air. A 5-second delay between the start of the cycle and the VCSEL power-on was implemented. This ensured enough time for the operator to abort the cycle should the mass flow controllers fail to initialise. Failure to initialise was estimated to occur for 1 in every 1000 cycles and caused melting in one of the coupons. Taking in to account this 5-second offset, the actual test profile was as follows:

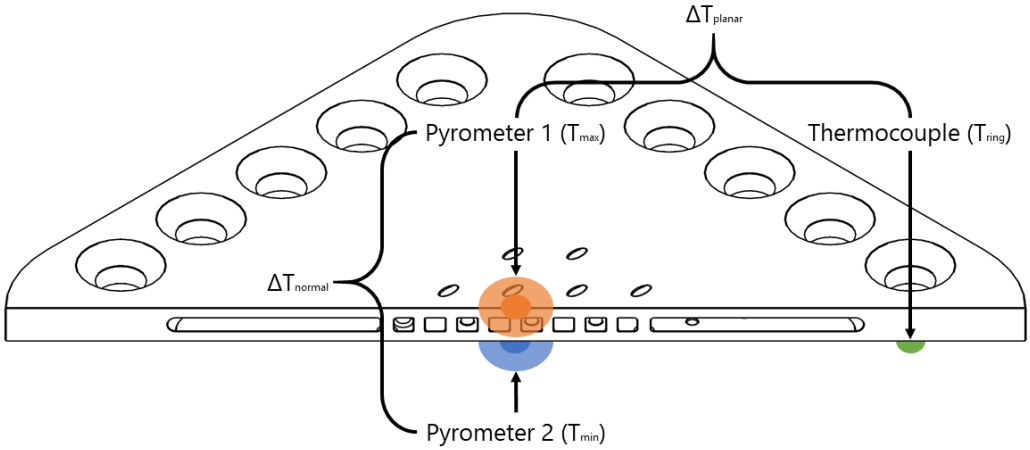


Figure 7.6: *pyrometer and thermocouple measurement locations with thermal gradient definitions*

1. 0 - 5 sec: VCSEL power off, Alicat mass flow rate set to cycle target
2. 5 - 605 sec: VCSEL power and Alicat mass flow rate set to cycle target
3. 605 - 900 sec: VCSEL power off, Alicat mass flow rate set to a maximum of 200 SLPM

295 seconds of maximum coolant air followed by 5 seconds of reduced flow ensured the coupon was returned to near-initial temperatures. As the pyrometers do not measure below 400 °C, the data from the IR camera was used to confirm this for the IN625-C-T2 coupon.

The appropriate VCSEL power and coolant flow rates were first estimated using the data in Figures 7.3 and 7.4. The emissivity was estimated using surface roughness data, and the equivalency with the absorbance was used for the steady-state thermal field. The true VCSEL power setting was then calculated using:

$$\dot{q}_{\text{VCSEL,true}} = \dot{q}_{\text{VCSEL,scale}} \left(\frac{1}{\epsilon_{\text{coupon}}} \right) \tag{7.1}$$

The target VCSEL power and coolant flow rates were adjusted throughout the testing to ensure that T_{max} and ΔT_{normal} remain as consistent as possible.

A thermal profile of the centre of each coupon wall was obtained using pyrometers, which allowed the calculation of T_{max} and ΔT_{normal}. In tests designated IN625-C-XX, the mounting temperature was not tracked as it was assumed to be irrelevant. This assumption was disregarded for subsequent tests, and a type K thermocouple was placed between the coupon and the hot gasket to enable the calculation of ΔT_{planar}. Figure 7.6 shows the

approximate locations of these measurements. Imaging of the exterior of the hot surface was obtained using a Canon EOS 850D [25] with a Canon EF 100 mm f/2.8L Macro Lens [24]. Imaging of the external surface was performed every ten cycles as increased capture rates increased the time requirements beyond what was available due to facility sharing. The coupons were cycled beyond the initial crack detection to collect growth data.

7.2.2 Results

VCSEL set points and the measured coolant air mass flow rate, as well as the temperature, are presented. Among these are the thermal results, T_{max} and ΔT_{normal}, for each coupon. For those with a type K thermocouple, ΔT_{planar} is presented. Each cycle is normalised by the target temperatures, and transient cycle data is shown as an overlay of each cycle. Three images are provided for each cycle. The first offers a reference to the condition of the coupon after manufacture. The second is the frame following the cycle in which the first crack was detected. The third is the state of the coupon at the conclusion of cycling. For crack detection images, a single crack is highlighted; however, more cracks were present.

Most coupons were tested over several days at a rate of 4 cycles per hour plus time for imaging. Gradual increases in the temperature of the coolant air were observed throughout each day. They were attributed to increases in exterior air temperature due to the sun, with sharp drops indicating the start of a new day. The change in the temperature of the coolant air in all tests was on the order of 1% and is considered negligible.

All coupons exhibited thermal overshoot for the initial cycles. It was suggested that this is the combination of transient infrared absorbance and some annealing of the 3D-printed material. A darkening of the surfaces is also apparent, as oxidation and some localised melting are thought to accumulate.

Inconel 625 coupons for both the T2 and T4 profiles exhibit similar trends. The coupons were printed on their sides, with passes in the x-direction building up in the z-direction. This created overlapping regions of notched material on the leading edges, the FHWs, of each hole. These act as nucleation sites for crack growth, which occurs in ten cycles. Following a further 10-cycle delay, the cracks continue to propagate. They carve curved paths, linking neighbouring film holes on the stream-wise ends. However, elliptical holes do not have the same overhang. These cracks do not grow from the FHW but instead from all around,

radiating perpendicular to the film hole fillet.

For the T3 profiles, both T_{max} and ΔT_{normal} were observed to increase on the order of 4% between cycles 10 and 20. This was consistent regardless of hole shape and continued until catastrophic failure was observed in Cycles 29 and 27, resulting in a sharp increase in T_{max} for circular and elliptical hole coupons, respectively. A large crack between the downstream film holes formed immediately during these start-up cycles. For IN625-C-T3, this was accompanied by a loud crack, akin to dropping a piece of crockery. This noise was not observed for IN625-E-T3. Inspection of the coupons after removal from the plenum revealed an elevated surface topology in the central test region. Due to increasing ΔT_{normal} during testing, it is hypothesised that buckling failure occurred due to thermal expansion in the centre. It is thought that the bowing-out resulted in a disconnection between some or all of the pedestals and the outer wall, reducing conduction.

For the T4 profiles, the normal gradient falls short of the target, averaging 89.5% across all cycles. No further increase was possible due to the Alicat flow limit. A negative thermal gradient was also observed during the initial cool-down due to the significant contribution of impinging jets to the hot-wall following the VCSEL shut-down. Furthermore, ΔT_{planar} was still transient as the VCSELs were shut off. The relative magnitude of the planar gradient is of the order of 40% less than the T2 profile. During cycle 80, the coolant supply controller failed to initialise and the outer surface was recorded at more than 1500 ° C before the emergency shut-down was activated. The small ridges on the right side of the elliptical coupon show the extent of the damage.

The CMSX-4 coupon required only 78% of the VCSEL power and 51% of the coolant flow rate at identical coolant temperatures, compared to IN625-C-T2. The mean normalised cycle for the planar gradient was 3.80, which is considered reasonable due to the comparable thermal conductivity of CMSX-4 [2] and Inconel 625 [108]. The images in Figure 7.20 show that the casting of the coupon removes the large overhanging regions of the film holes and reduces the size of the largest notches by an estimated 50%. The shape of the film holes is also considerably more uniform and roughly 15% smaller than the Inconel 625 coupons. The general shape of the cracks is similar to that observed in IN625-C-T2 and IN625-C-T4; however, the width of the crack after 200 cycles is approximately 20% the width of comparable Inconel 625 cracks.

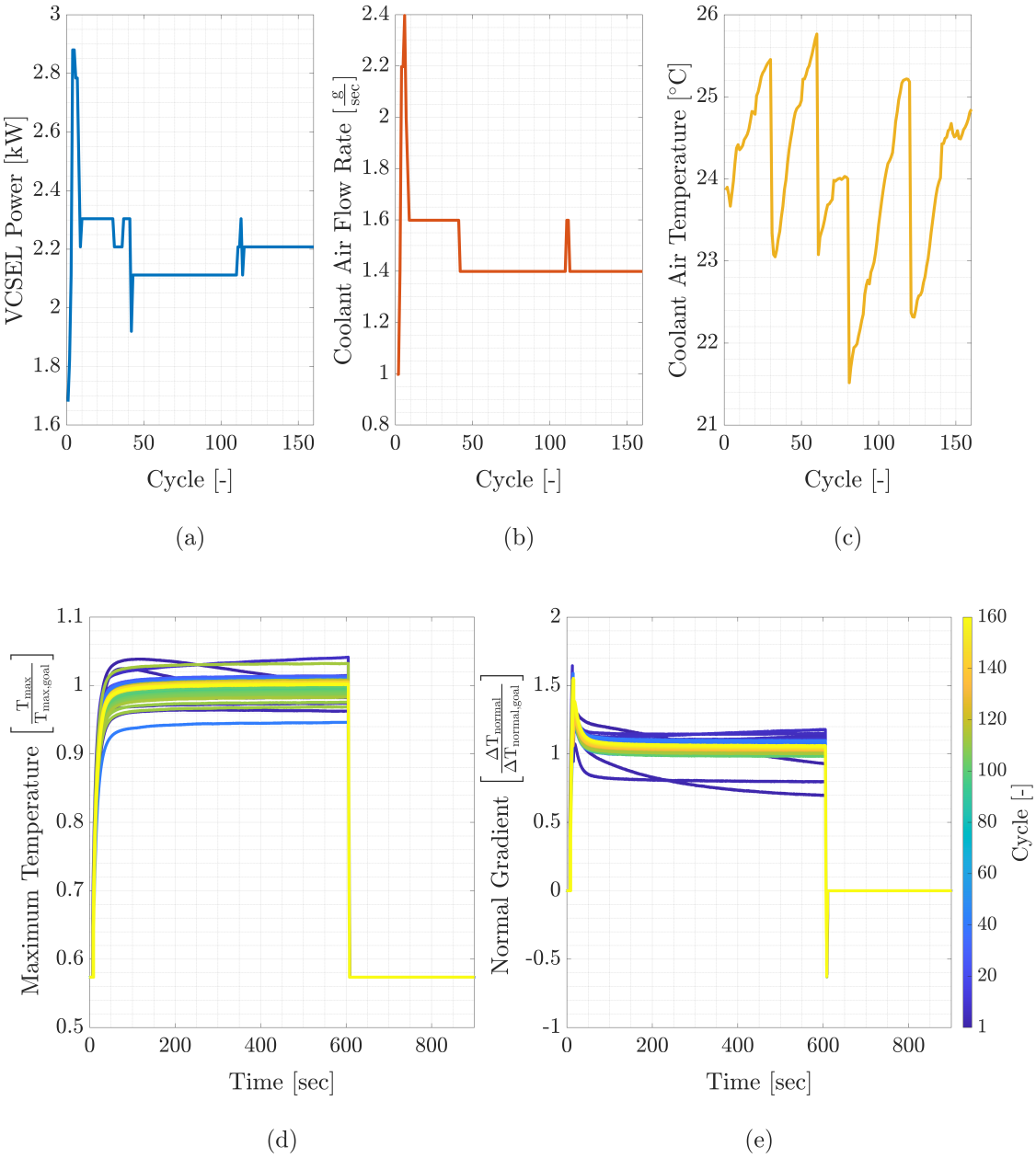


Figure 7.7: *IN625-C-T2 testing profiles of (a) vertical-cavity surface-emitting laser power (b) coolant flow rate (c) coolant temperature (d)* $\mathrm{T_{max}}$ *(e)* $\Delta\mathrm{T_{normal}}$

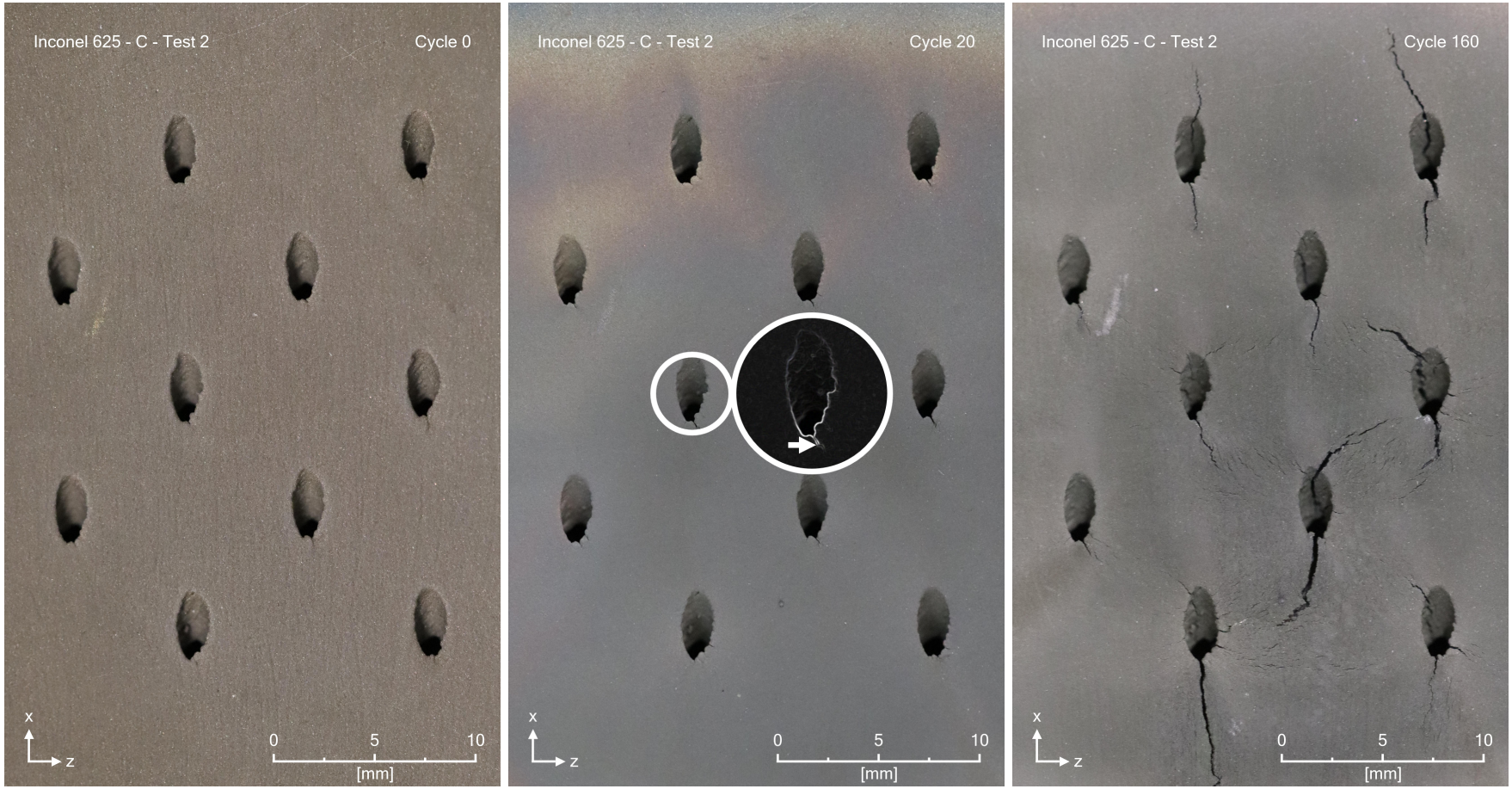


Figure 7.8: *progression of cycling fatigue on the exterior surface of IN625-C-T2*

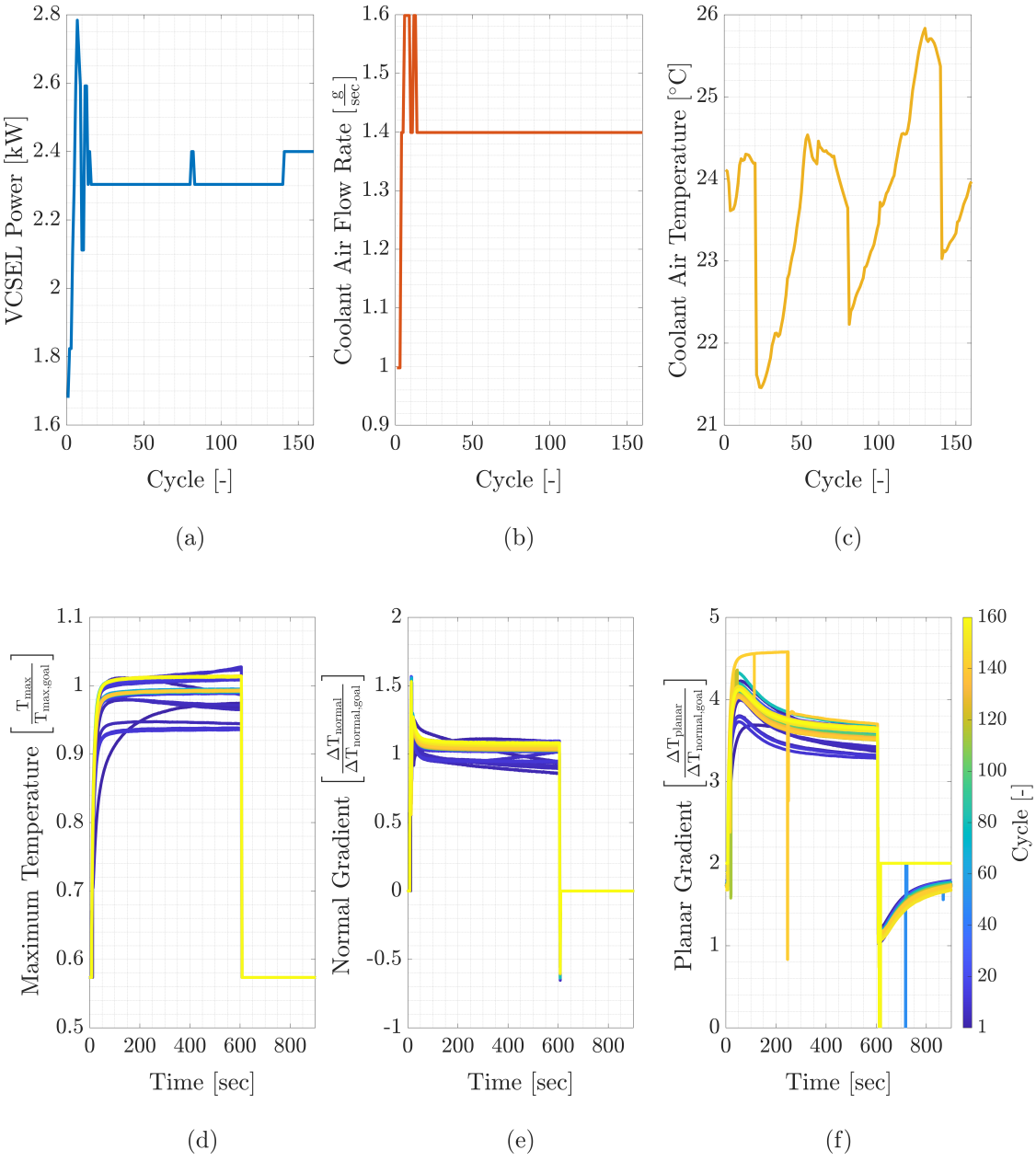


Figure 7.9: *IN625-E-T2 testing profiles of (a) vertical-cavity surface-emitting laser power (b) coolant flow rate (c) coolant temperature (d)* $\mathrm{T_{max}}$ *(e)* $\Delta\mathrm{T_{normal}}$ *(f)* $\Delta\mathrm{T_{planar}}$

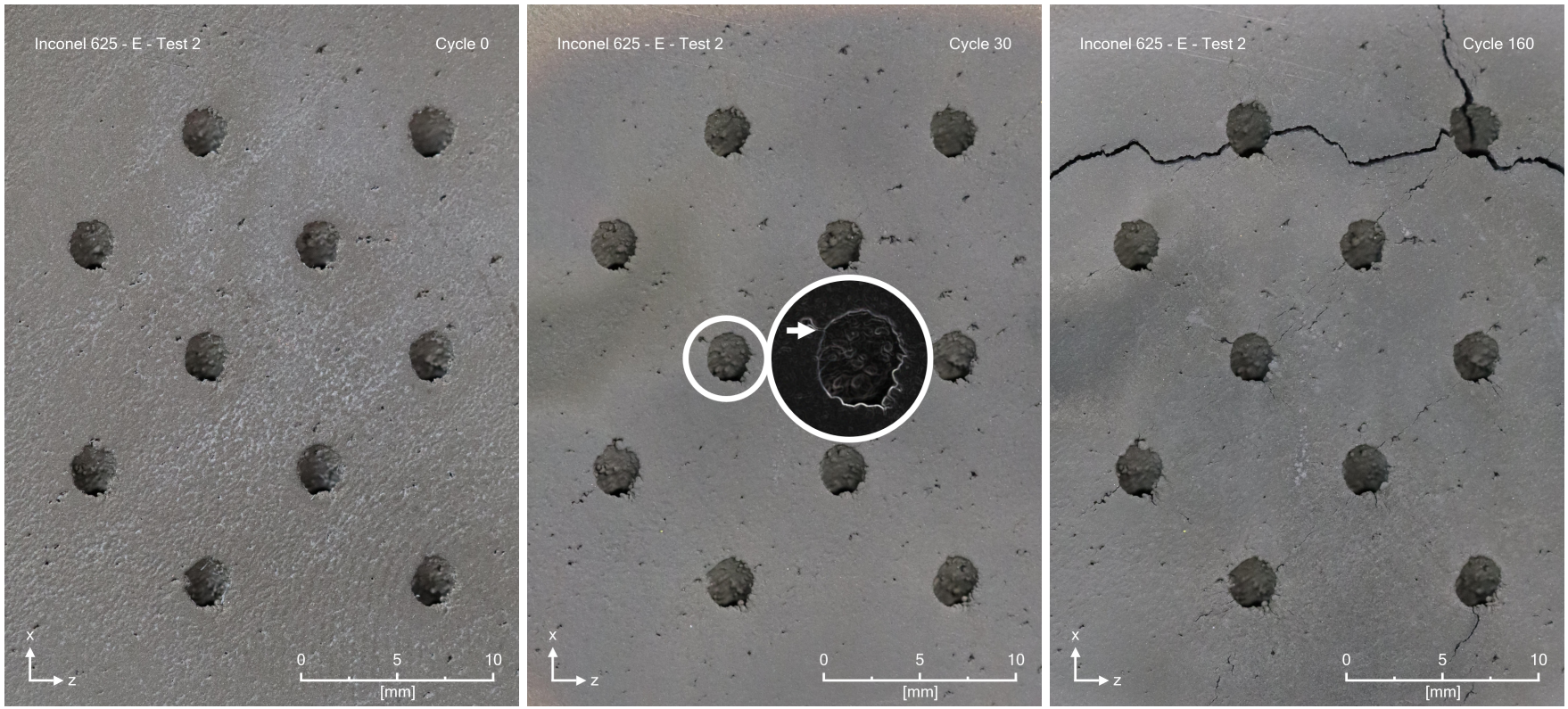


Figure 7.10: *progression of cycling fatigue on the exterior surface of IN625-E-T2*

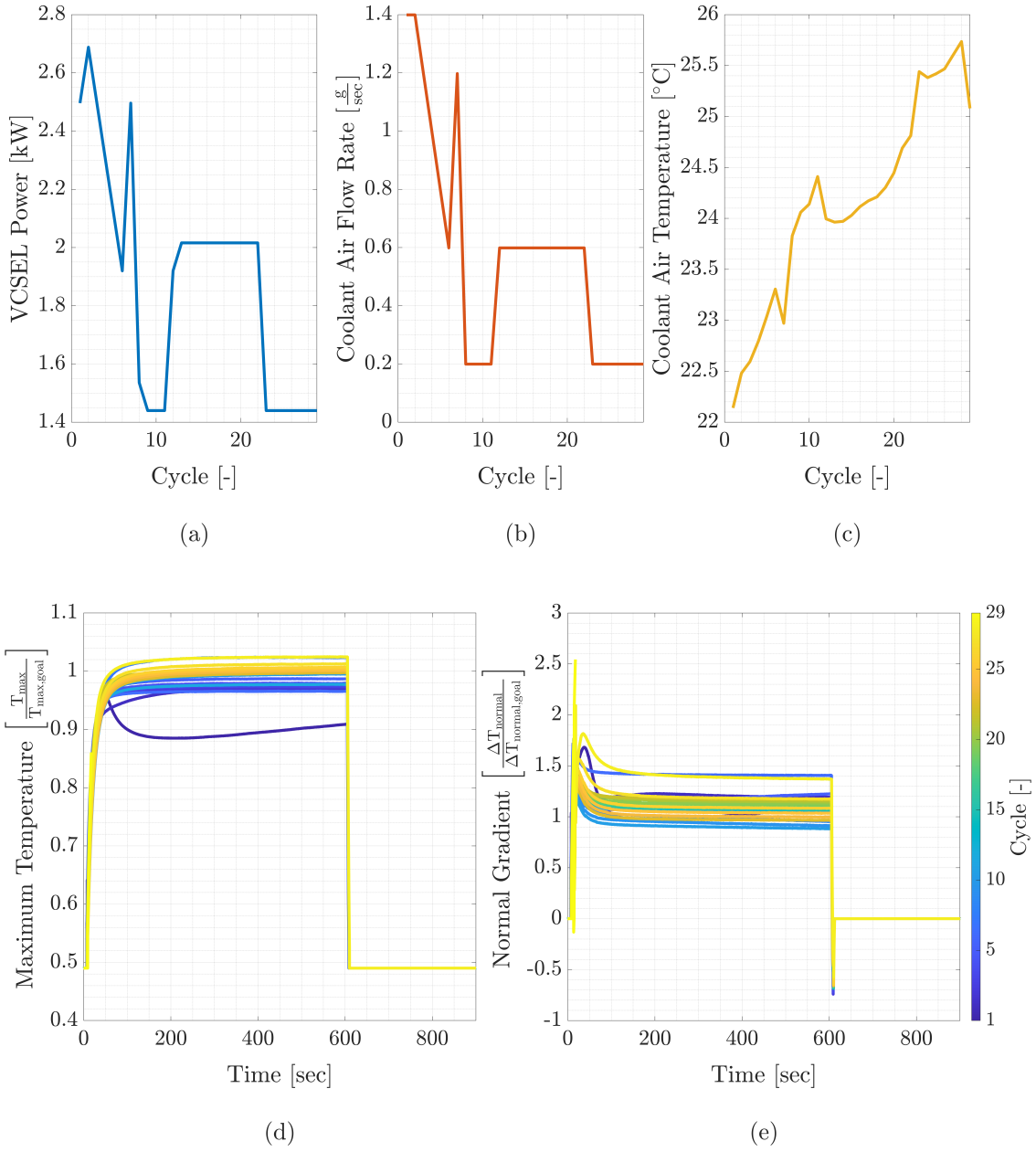


Figure 7.11: *IN625-C-T3 testing profiles of (a) (a) vertical-cavity surface-emitting laser power (b) coolant flow rate (c) coolant temperature (d)* $\mathrm{T_{max}}$ *(e)* $\Delta\mathrm{T_{normal}}$

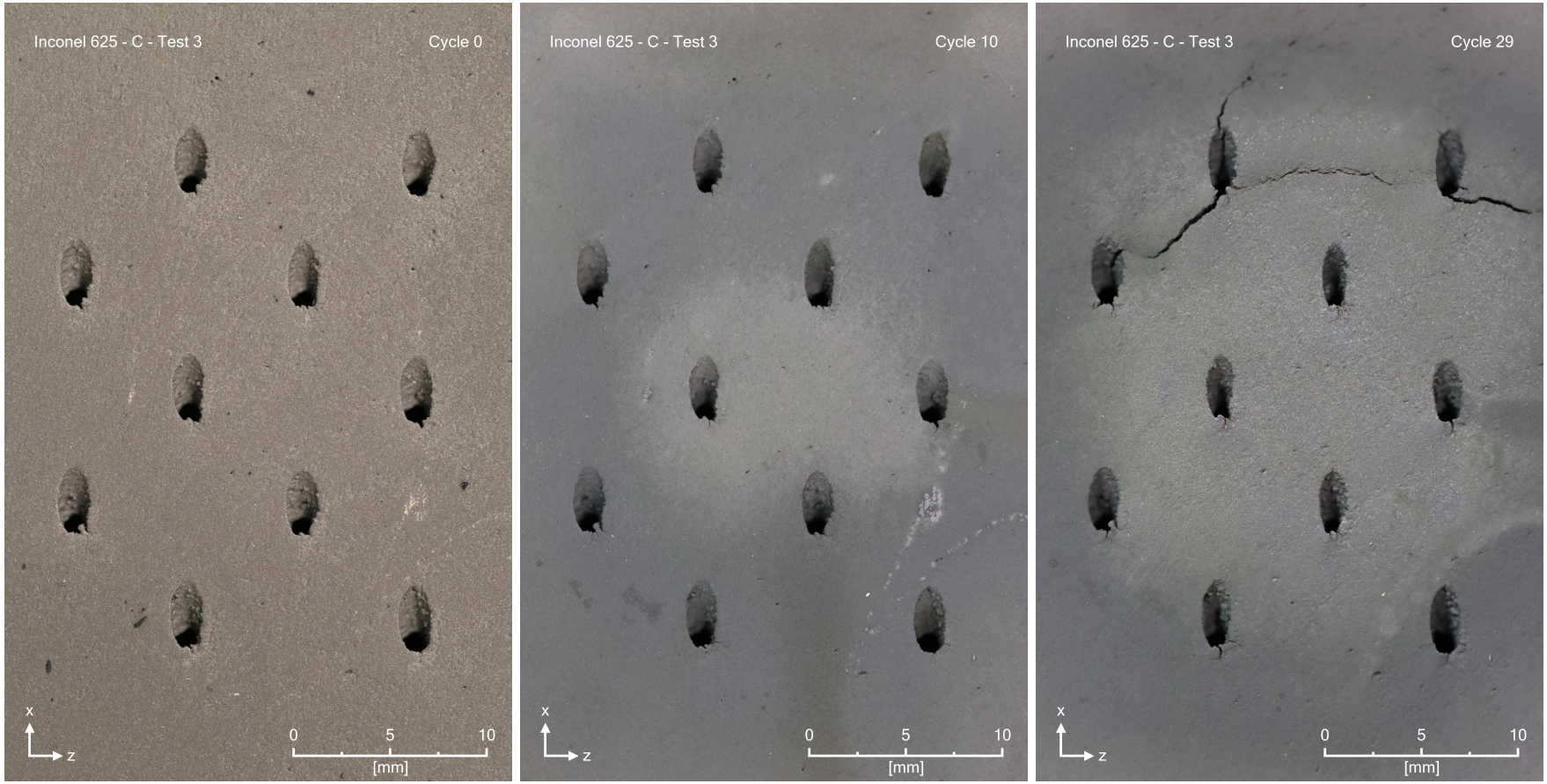


Figure 7.12: *progression of cycling fatigue on the exterior surface of IN625-C-T3*

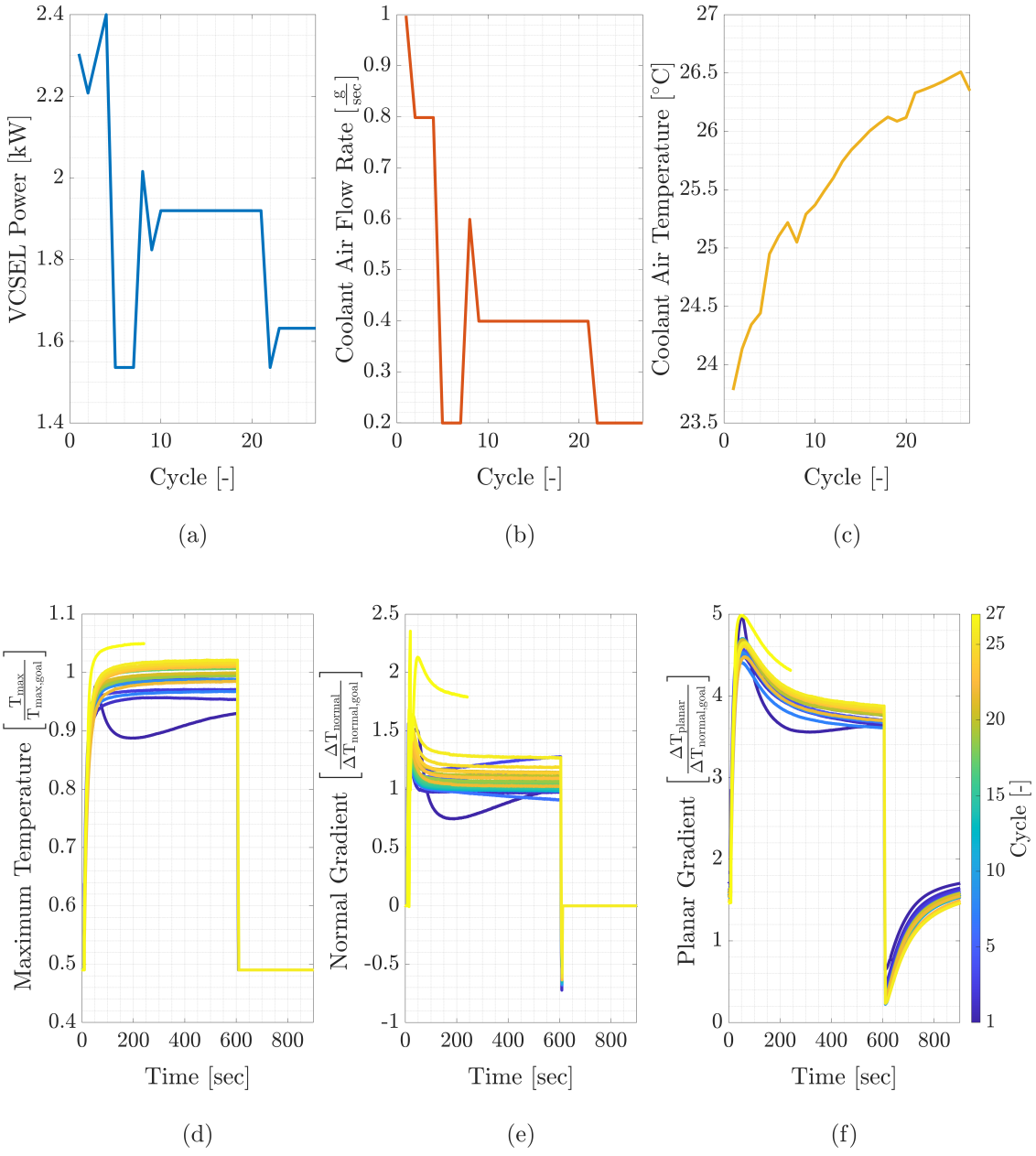


Figure 7.13: *IN625-E-T3 testing profiles of (a) vertical-cavity surface-emitting laser power (b) coolant flow rate (c) coolant temperature (d)* T_{max} *(e)* ΔT_{normal} *(f)* ΔT_{planar}

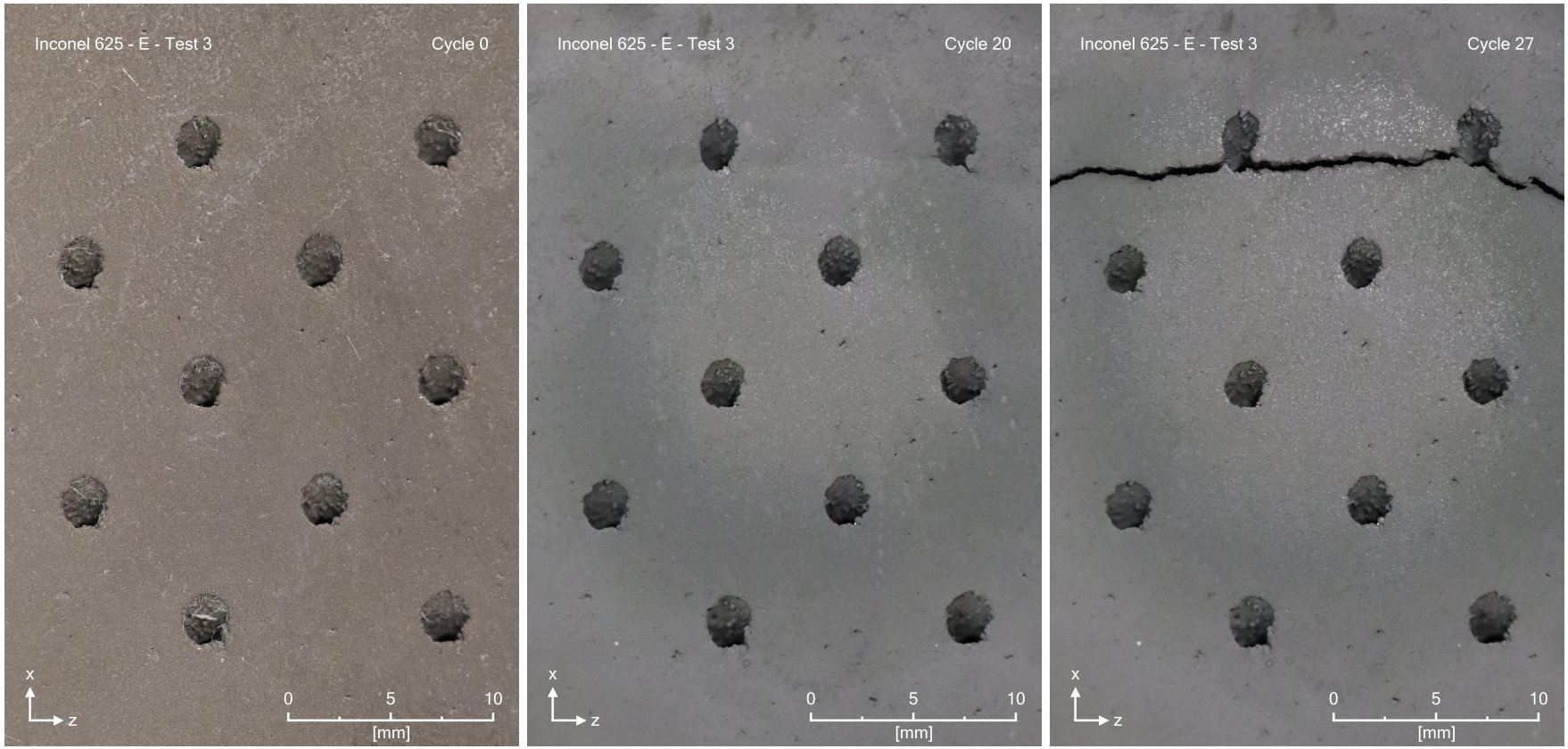


Figure 7.14: *progression of cycling fatigue on the exterior surface of IN625-E-T3*

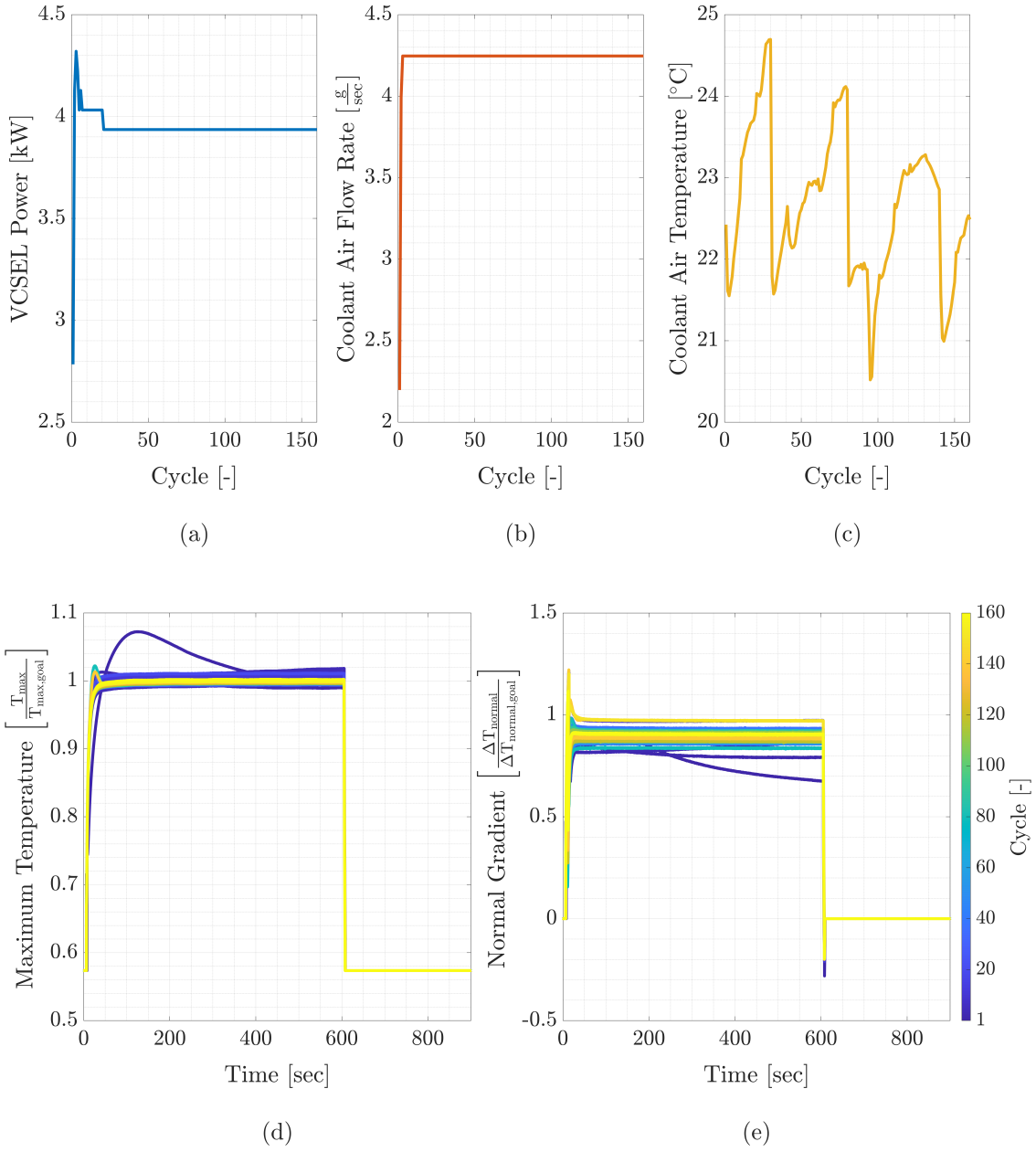


Figure 7.15: *IN625-C-T4 testing profiles of (a) vertical-cavity surface-emitting laser power (b) coolant flow rate (c) coolant temperature (d)* $\mathrm{T_{max}}$ *(e)* $\Delta\mathrm{T_{normal}}$

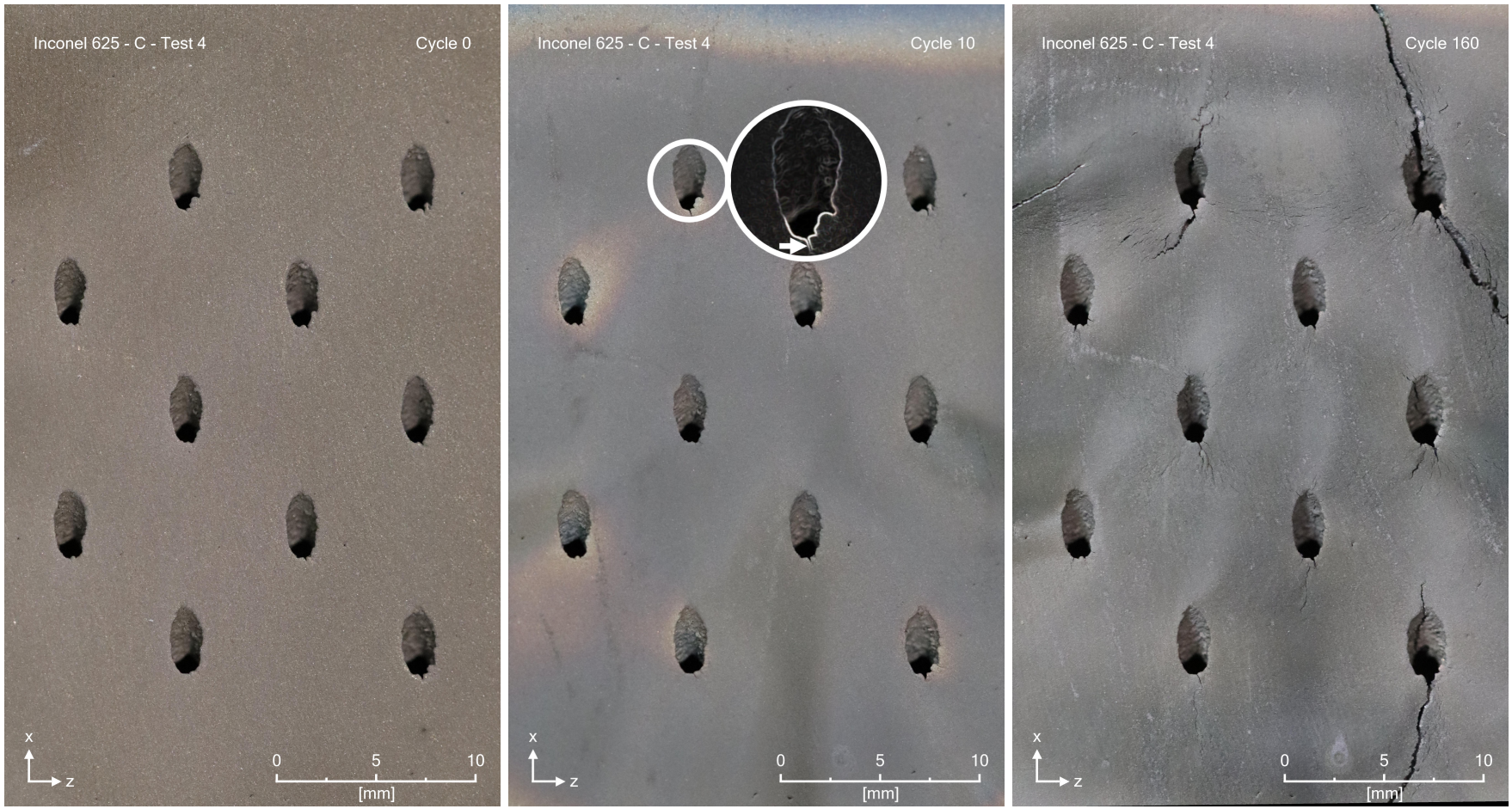


Figure 7.16: *progression of cycling fatigue on the exterior surface of IN625-C-T4*

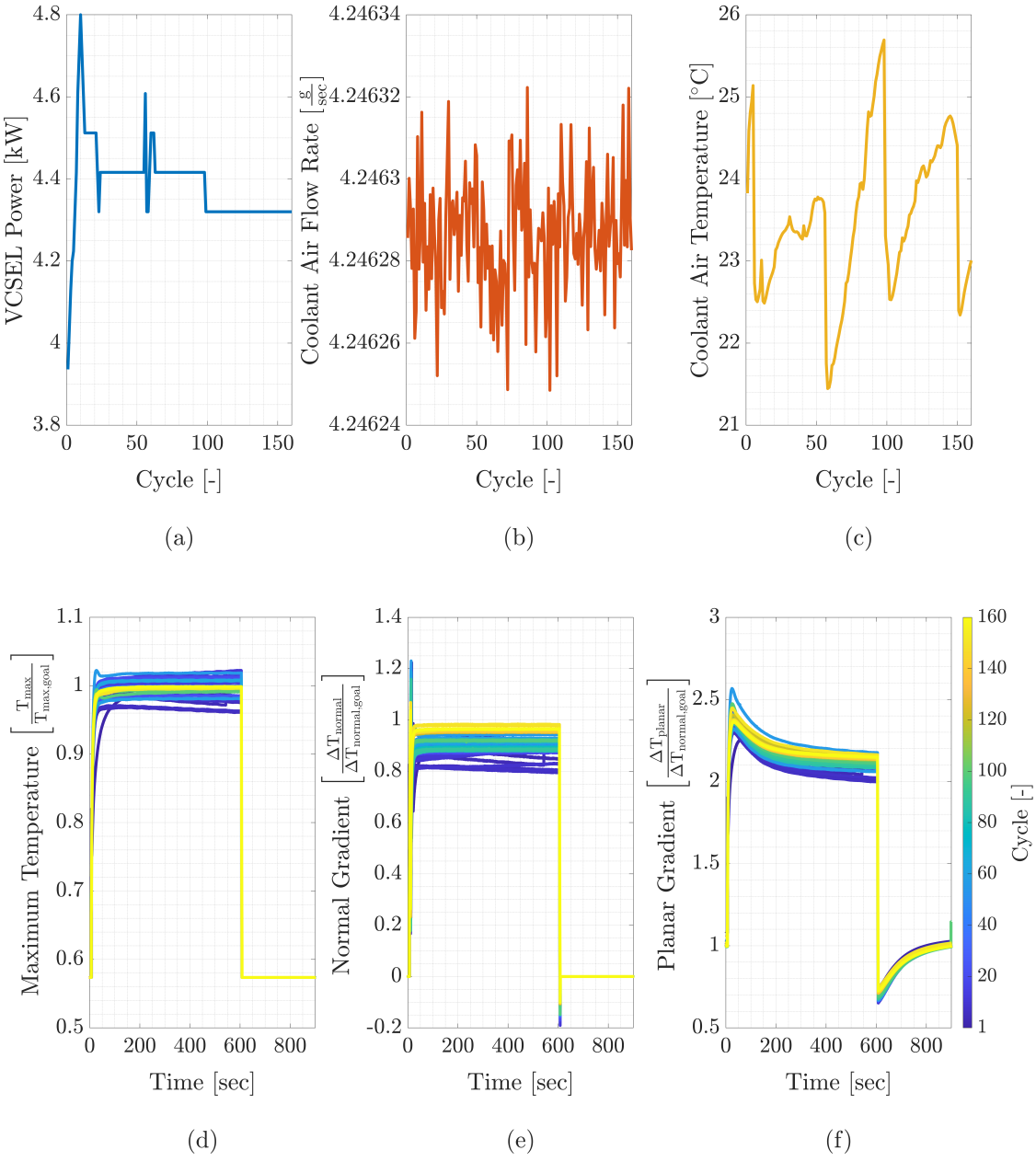


Figure 7.17: *IN625-E-T4 testing profiles of (a) vertical-cavity surface-emitting laser power (b) coolant flow rate (c) coolant temperature (d)* T_{max} *(e)* ΔT_{normal} *(f)* ΔT_{planar}

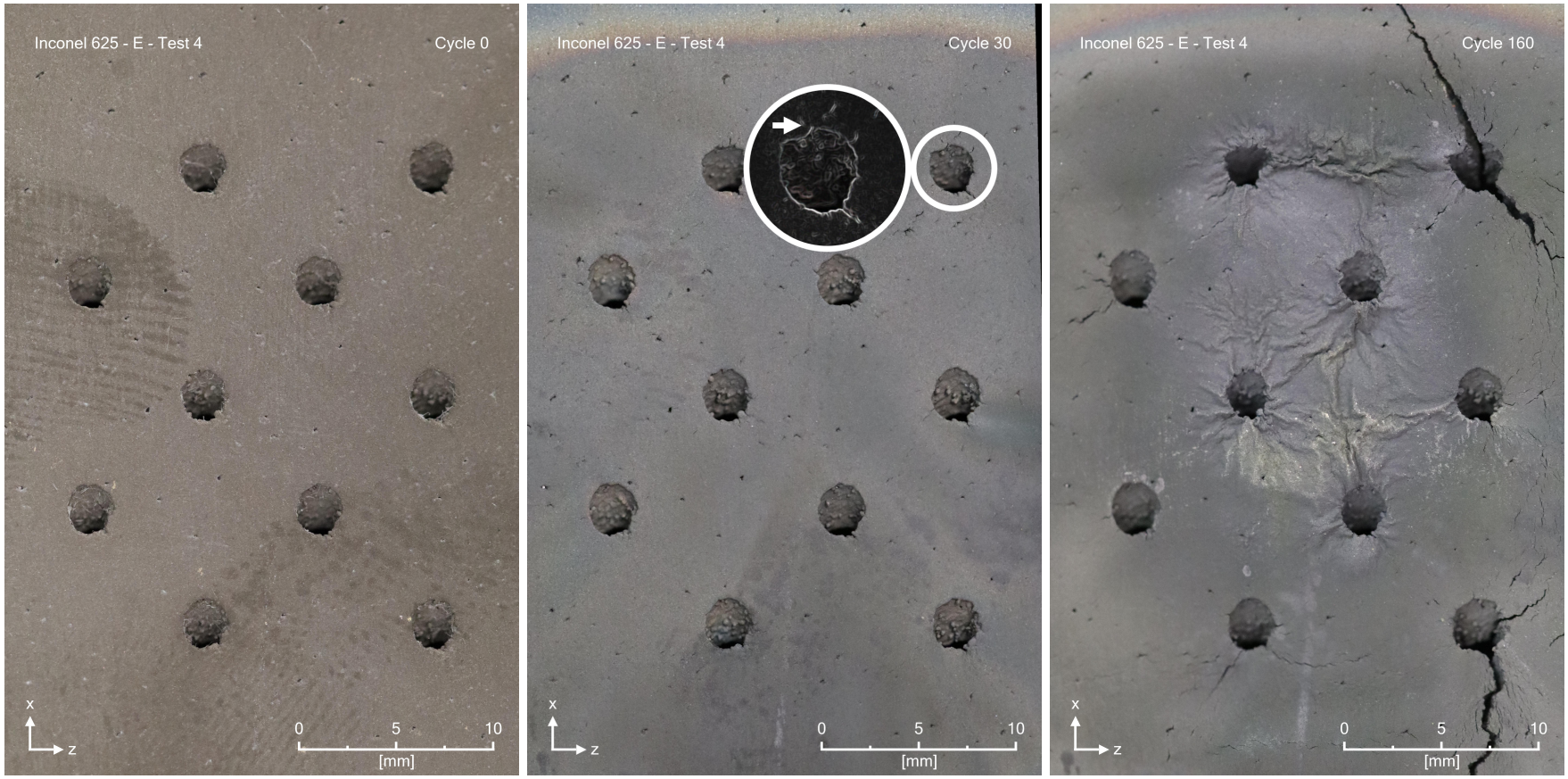


Figure 7.18: *progression of cycling fatigue on the exterior surface of IN625-E-T4*

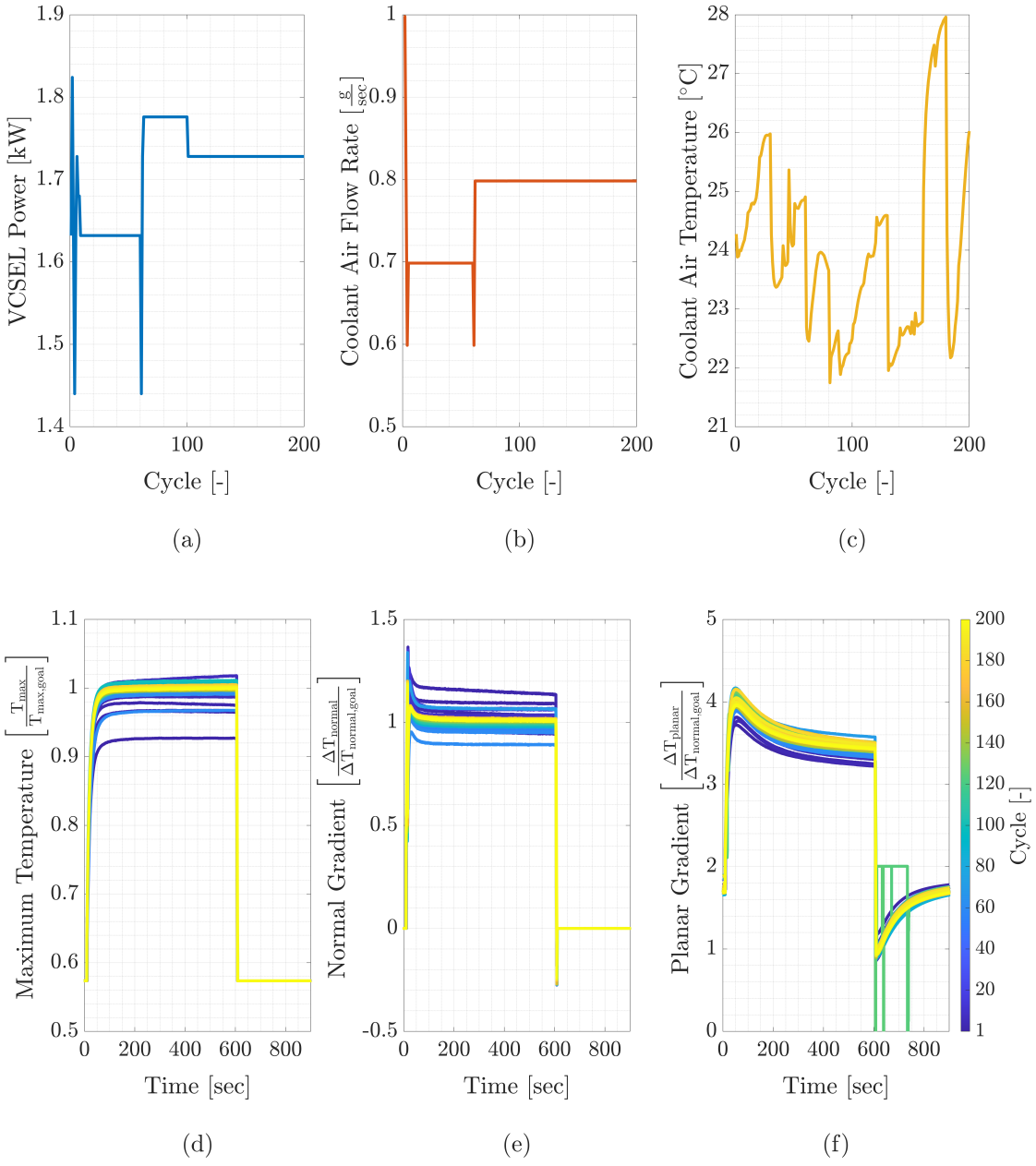


Figure 7.19: *CMSX-4-T1 testing profiles of (a) vertical-cavity surface-emitting laser power (b) coolant flow rate (c) coolant temperature (d)* $\mathrm{T_{max}}$ *(e)* $\Delta\mathrm{T_{normal}}$ *(f)* $\Delta\mathrm{T_{planar}}$

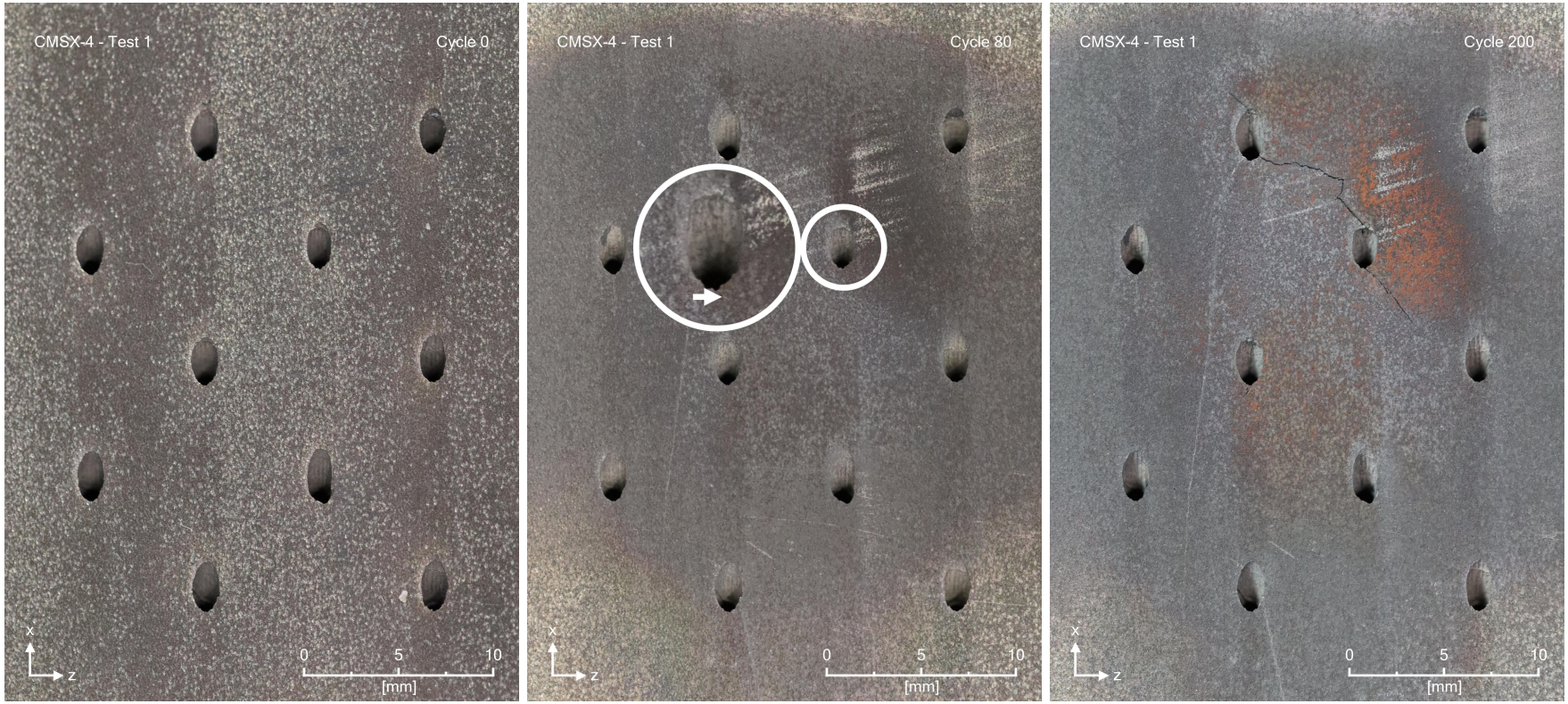


Figure 7.20: *progression of cycling fatigue on the exterior surface of CMSX-4-T1*

7.3 Summary

The crack initiation from the sharp wedge upstream of the film holes is aligned with the predictions and modelling by Skamniotis [101], which concludes that the region of maximum stress and near-maximum temperature exists in this general region. Variations in exact location are a function of anisotropic properties of both 3D-printed Inconel 625, which may be influenced by the direction of printing, and the single-crystal nature of CMSX-4, as shown by [104, 106]. Imaging of internal surfaces and features was not possible due to the enclosed geometry; however, no increase in T_{max} suggests that the pedestals remain connected as conduction remains nearly constant. This contrasts with the results of the T3 test, where there is a marked increase in T_{max} following apparent buckling failure and the separation of the hot-wall of the pedestal. Images of the rear surfaces of every coupon were captured after cycling. There is no detectable damage to the outer surface of the cold-wall.

The use of fatigue crack initiation as a method was used despite pre-existing imperfections around the film holes due to the additive manufacturing process. This was used due to a lack of literature on the energy required to propagate a crack in 3D-printed Inconel 625. Furthermore, the CMSX-4 coupon, of which actual blades are cast and machined, did not exhibit the same degree of imperfections.

A comparison of Inconel T2-T4 profiles indicated that, in the coarse sampling of surface images, there is relatively little dependence on ΔT_{normal}. The number of cycles to crack detection and failure mode appeared to adhere to ΔT_{planar}. When comparing E-T2 to E-T4, the true ΔT_{planar} are equivalent. Although T_{ring} was not measured for C-T2 and C-T4, the similarity of the geometry for both coupons leads to the assumption that ΔT_{planar} are effectively identical between both coupon variants. The results of the T3 testing show that if ΔT_{planar} exceeds some upper limit, buckling failure and potential de-lamination of the pedestals and wall are possible for this mechanically constrained case.

The use of elliptical film holes showed promise over traditional circular holes for both aerothermal and thermo-mechanical performance. A 6% reduction in flow rate and an increase of 5.7% in VCSEL power was needed to obtain equivalent T_{max} and ΔT_{normal} in E-T2, compared to C-T2. For the T4 cycles, 11.1% more VCSEL power was required to achieve similar thermal profiles. Mechanical performance was assessed using both the

Test Section	Pre-Testing [g]	Post-Testing [g]	Difference [g]
IN625-C-T2	189.32	189.32	0
IN625-C-T3	183.69	183.38	-0.31
IN625-C-T4	185.23	185.22	-0.01
IN625-E-T2	185.02	185.01	-0.01
IN625-E-T3	186.21	186.21	0
IN625-E-T4	184.93	184.93	0
CMSX-4-T1	184.18	183.18	0

Table 7.2: *coupon masses before and after testing, accurate to ± 0.03 g*

number of cycles to crack initiation and the relative size of cracks after 160 cycles. Elliptical holes offer an increase of 50% and 200% for the T2 and T4 tests, respectively. The centres of elliptical hole coupons also have shorter, more narrow cracks after 160 cycles for the T2 tests. The cracks are roughly 50% the total length and width after nearly 27 hours of heating. The melting of the T4 tests renders that comparison void. The exception to this is the crack present in the trailing edge holes for the T2, which is thought to be due to the proximity of the film hole and the edge of the test region, resulting in a higher stress state.

Visual inspection of the coupons and testing data further support the use of cast single-crystal CMSX-4 over 3D-printed, highly polycrystalline Inconel 625 as the material of choice. The overhanging regions and notches in the Inconel 625 components provide ideal conditions for crack development, and the cross-granular cracks propagate at a much higher rate. Furthermore, the reduction in coolant flow rate by 49% required to maintain an equivalent thermal distribution indicates superior aerothermal performance. The exact factors influencing this are unknown, as the material properties are relatively similar.

The weights of the components are provided in Table 7.2. During the course of the testing, there was no significant weight change for most coupons, except IN625-C-T3, which showed a loud crack during failure. The release of material was hypothesised to have occurred, although 0.31 g of material is considered negligible. The lack of material released as cracks form indicates a minimal risk of FOD in later stages of the engine as the components accumulate wear.

Computational Analysis of Experimental Conditions

The complex geometry of the double-wall effusion-cooled (DWEC) system and the harsh thermal loading conditions achieved during the tests limited the feasibility of direct stress and strain measurements on critical features. In lieu of these measurements, a numerical approach was taken to estimate the number of cycles to crack initiation, N_f. A fictitious elastic stress state was extracted from a transient simulation and tuned to the mean coupon testing conditions. Then three Neuber-type methods were applied with creep modelling to estimate the strain range and N_f. The results show adherence to the trends observed during the tests, with a clear dependence on T_{max}. Additionally, a crystal-plasticity approach implemented by Skamniotis [104] is shown to provide a reasonable approximation of the life of a CMSX-4 coupon.

8.1 Finite Element Analysis

Thermo-elastic finite element analysis (FEA) was performed in Mechanical[1] for each of the Inconel 625 T2 and T4 coupons and the CMSX-4 coupon. Modelling of the buckling failure of the T3 coupons was omitted. The failure point, P_f, was defined as a point along the span-wise centre-line of the film hole on the furthest extent of the fillet between the exterior of the hot-wall and the film hole. The temperature and uni-axial components for a complete cycle at P_f are the focus of this section.

8.1.1 Domains and Boundary Conditions

The domain is presented in Figure 8.1. It represents the entire coupon composed of 3 components: the mounting ring, the central test section, and a unit block. Shared topology

[1] Ansys®Academic Research Mechanical, Release 23.1

Test Section	$\dot{q}_{VCSEL}$ [kW]	$\dot{m}_c$ [$\frac{g}{sec}$]	T_c [°C]	T_{max} [°C]	ΔT_{normal} [°C]	ΔT_{planar} [°C]
IN625-C-T2	2.192	1.51	24.0	898	208	–
IN625-C-T4	3.944	4.22	22.6	898	313	–
IN625-E-T2	2.317	1.42	23.7	893	209	727
IN625-E-T4	4.383	4.29	23.5	896	322	751
CMSX-4-T1	1.708	0.77	24.0	898	200	702

Table 8.1: *total test average values for the quasi-steady hold region during fatigue testing*

was applied through DesignModeler[2]. The material properties for Inconel 625 were taken from [108]. The material properties for CMSX-4 were taken from Table 3 in Appendix II, which represents the crystallographic direction $< 001 >$. The complete crystallographic orientation in the final test specimens is unknown as a result of a lack of control during manufacture. For this reason, this analysis assumed elastic isotropy throughout the domain. The Youngs' Modulus, thermal expansion, and specific heat capacity were all modelled as dependent on temperature.

The average values of the test conditions are presented in Table 8.1. The vertical-cavity surface-emitting laser (VCSEL) target distribution provided in Figure 5.22 was applied to the exterior surface of the coupon and scaled by both the fractional power setting reported in Table 8.1 and an absorbance coefficient. This ensured the thermal distribution throughout simulations matched experiments. The fluid-solid interfaces were modelled using imported HTCs from a user-defined function (UDF) in Fluent[3], defined using:

$$h = \frac{\dot{q}_{wall}}{A_{wall}\left(T_{wall} - T_{c,i}\right)} \tag{8.1}$$

The heat transfer coefficient (HTC) fields were extracted from the conjugate domain established in Chapter 6. The coolant mass flow rates and temperatures were copied from Table 8.1. The VCSEL power was scaled until the correct T_{max} was obtained. A perturbation study was performed on the area-average of the total field, and values were shown to change

[2]Ansys®Academic Research DesignModeler, Release 23.1
[3]Ansys®Academic Research Fluent, Release 23.1

by less than 15% from an average wall temperature of 27 °C to an average wall temperature of 1358 °C. A constant field was considered a reasonable approximation and was extracted at the correct T_{max}. This was done to ensure the best fit during the quasi-steady hold of each cycle. The simulation applied these for 600 seconds before applying the 4.3 $\frac{g}{sec}$ HTCs for the remaining 300 seconds.

	IN625-C-T2	IN625-E-T2	IN625-C-T4	IN625-E-T4	CMSX-4-T1
α	0.438	0.429	0.398	0.391	0.447

Table 8.2: *absorbance coefficients used in finite element analysis of transient cycling*

A final calibration of the model was performed by scaling the magnitude of the VCSEL and HTC fields in a steady-state formulation. For all cycles, a scaling of 1.05 of the HTCs ensured a correct thermal gradient. The absorbance coefficients are presented in Table 8.2. Then these scaling values were applied to the transient boundary conditions outlined above. An attempt was made to model the conductive losses through the plenum using a convective boundary condition on the bolt holes, marked in green in Figure 8.1 (a). A value of 1300 $\frac{W}{m^{2\circ}C}$ and a fluid temperature equal to the coolant temperature were shown to be approximate T_{ring} within 5%. The initial temperature was set to the mean coolant temperature in Table 8.1.

The global mechanical domain featured an imported body temperature for each of the three components and rigid mounting on the bolt holes for the entire cycle. Following the global mechanical solution, a unit block was extracted following the sub-modelling procedure [9]. Body temperature was applied to the domain, and the solid-solid interfaces feature a cut-boundary deformation constraint for the entire cycle. In this analysis, the effect of fluid pressure and gravity was neglected.

8.1.2 Mesh and Formulation

An example of the mesh utilised is provided in Figure 8.1, which shows the various stages of refinement to obtain the final assembly. The global domain in (a) was assigned a body size for the mounting ring and a refined size for both the centre region and the unit block in

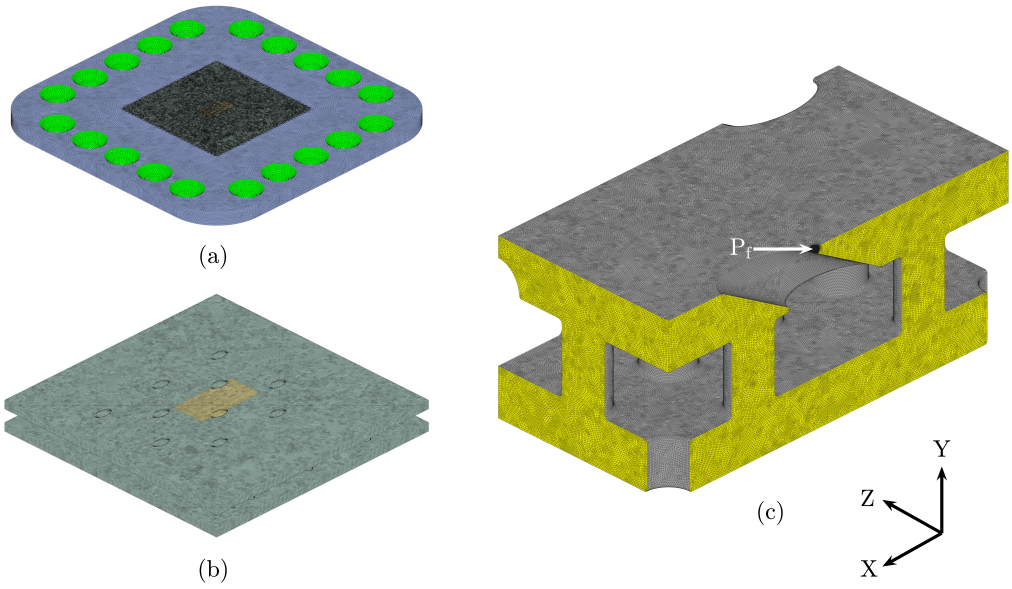
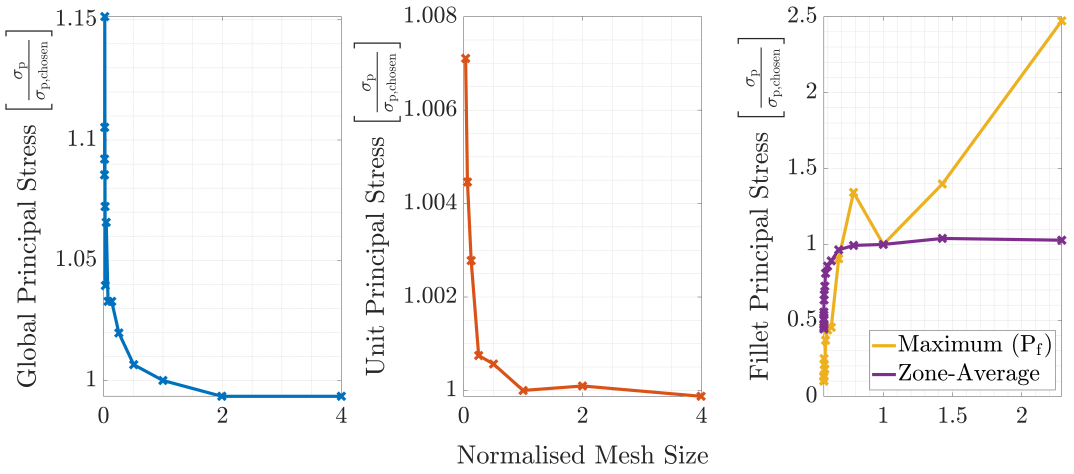


Figure 8.1: *(a) global modelling utilised (b) close up of central region featuring mesh refinement (c) sub-modelling unit domain*

(b). A mesh-independence study with a steady formulation in this domain was performed. The results are presented in Figure 8.2 (a). An additional mesh study was performed on the unit block by first reducing the global mesh size. Minimal change was noted in Figure 8.2 (b). The shift from the global to the unit domains allowed an increase in the mesh density around P_f. The body size for a sphere of influence was defined and reduced. The results are presented in Figure 8.2 (c). The apparent convergence and then substantial divergence of the maximum equivalent stress value at this point indicates a singularity [9]. It is thought that this may be related to the imported boundary condition and the location of the mesh nodes that affect the interpolation of the displacements. To remove the singularity from this study and the results, a small region was redefined around P_f, in which the mean stress values were extracted. Figure 8.2 (c) shows that this results in adequate mesh-independence as it is a more robust formulation.

The nature of the modelled cycles necessitates a transient thermal solution to capture the full effects of the evolving thermal field over the course of testing; however, utilising a transient structural solver was unnecessary. A dimensional analysis [112] was conducted to relate the propagation of thermal energy and elastic waves. The propagation of elastic



(a) (b) (c)

Figure 8.2: *mesh-independence results for (a) global mesh refinement (b) unit body refinement (c) fillet refinement*

waves is associated with the speed of sound in a material, estimated using:

$$v_s = \left(\frac{E}{\rho}\right)^{\frac{1}{2}} \tag{8.2}$$

The time for recovery from elastic stress states is then estimated as:

$$t_{ew} \approx l\left(\frac{\rho}{E}\right)^{\frac{1}{2}} \tag{8.3}$$

The magnitude of thermal propagation in the material due to conduction is governed by the Fourier conduction equation:

$$\rho C_p \frac{\delta\theta}{\delta t} = k\frac{\delta}{\delta x}\left(\frac{\delta\theta}{\delta x}\right) \tag{8.4}$$

The characteristic time for thermal propagation is therefore:

$$t_{hc} \approx \frac{\rho C_p}{k} l^2 \tag{8.5}$$

Tan [112] states that if $t_{ew} << t_{hc}$, the problem may be fully decoupled. In the extreme case, the mechanical solution at each time step solved by the transient solver may be modelled as quasi-steady. Solving Equations (8.3) and (8.5) for Inconel 625 and CMSX-4 at

900 °C with coupon dimensions of 85 mm x 85 mm yields the following:

	Inconel 625	CMSX-4
t_{ew}	2.9 E-5 sec	3.6 E-5 sec
t_{hc}	3.3 E+3 sec	3.1 E+3 sec

Table 8.3: *characteristic time values for the coupon geometry and selected materials*

As shown in Table 8.3, the characteristic time of the thermal response is on the order of 10^8 compared to the elastic case. This is considered sufficient to fully decouple the thermal and mechanical domains and employ a steady-state structural solver at each transient thermal step. The complete structural solution was then linearly interpolated for P_f.

8.1.3 Results and Discussion

Figures 8.3-8.5 present relevant thermal values for each of the types of cycles investigated. The elliptical hole coupons are presented due to the availability of ΔT_{planar} from the experimental data. The comparable plots for the circular holes adhere to T_{max} and ΔT_{normal} in the same manner. FEA data are presented alongside the mean cycle values, calculated by averaging the temperatures in Figures 7.9, 7.17, and 7.19 at each time step.

The simulations of the Inconel 625 coupons show reasonable adherence to the thermal fields. For both simulated cycle types. T_{max} is within 1% of the mean values of the cycles and ΔT_{normal} is within 3% for the T2 profile and 5% for the T4 profile. There is some discrepancy with ΔT_{planar} as it appears to settle on a value greater than the mean toward the end of the heating phase. However, it remains within 3% of the mean cycle values. For both cycles, T_{max} is under-predicted by the solver during the heating phase. This is thought to be the result of a mismatch in thermal diffusivity between the available data [108] and the 3D-printed coupon. The pyrometers were unable to measure below 400 °C, and as such, there appears to be significant disagreement between the two, although this is fictitious. The overshoot in ΔT_{normal} in both heat-up and shut-down was captured by the FEA results. The magnitude of the overshoot on heat-up is over-predicted by the FEA yet converged to the correct value quickly. The overshoot in ΔT_{planar} during start-up is captured. Despite the failure to perfectly converge to the temperature towards the end of the heating cycle,

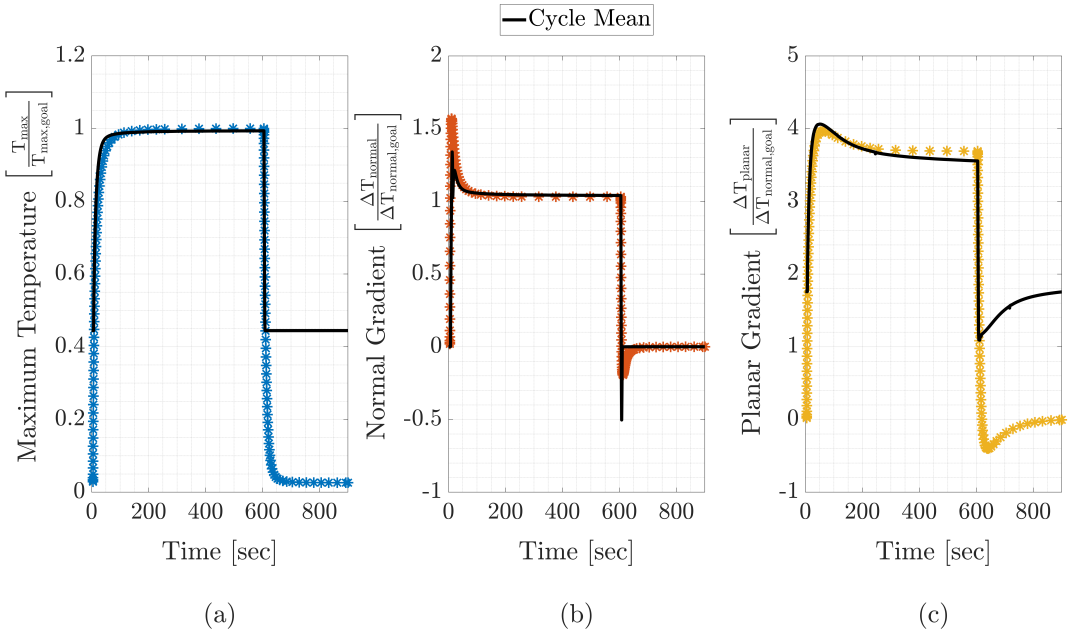


Figure 8.3: *comparison of finite element analysis to testing data for IN625-E-T2 (a)* T_{max} *(b)* ΔT_{normal} *(c)* ΔT_{planar}

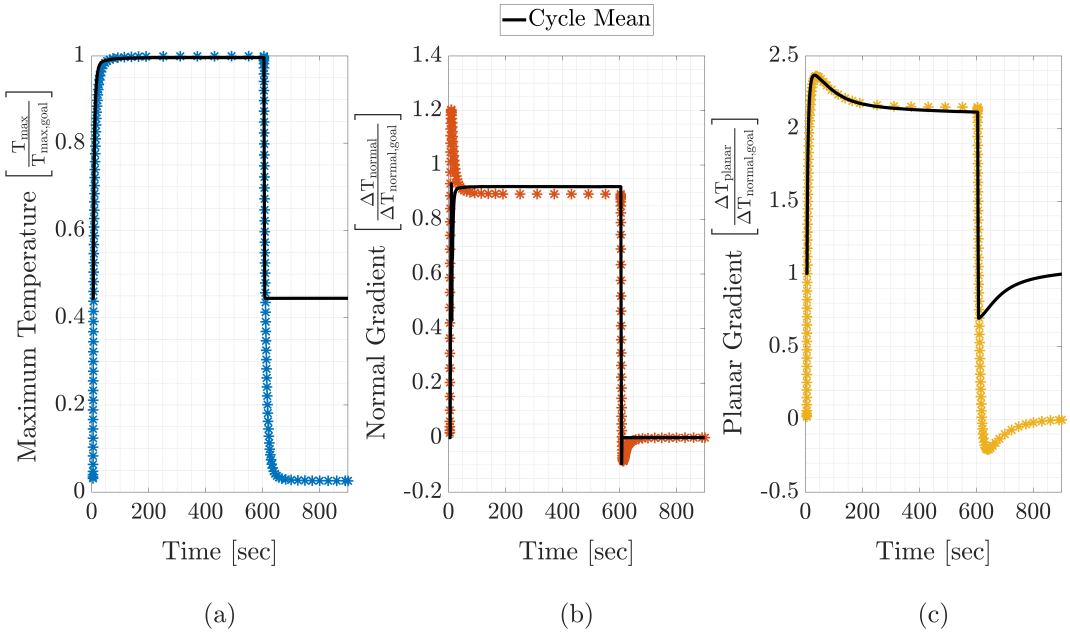


Figure 8.4: *comparison of finite element analysis to testing data for IN625-E-T4 (a)* T_{max} *(b)* ΔT_{normal} *(c)* ΔT_{planar}

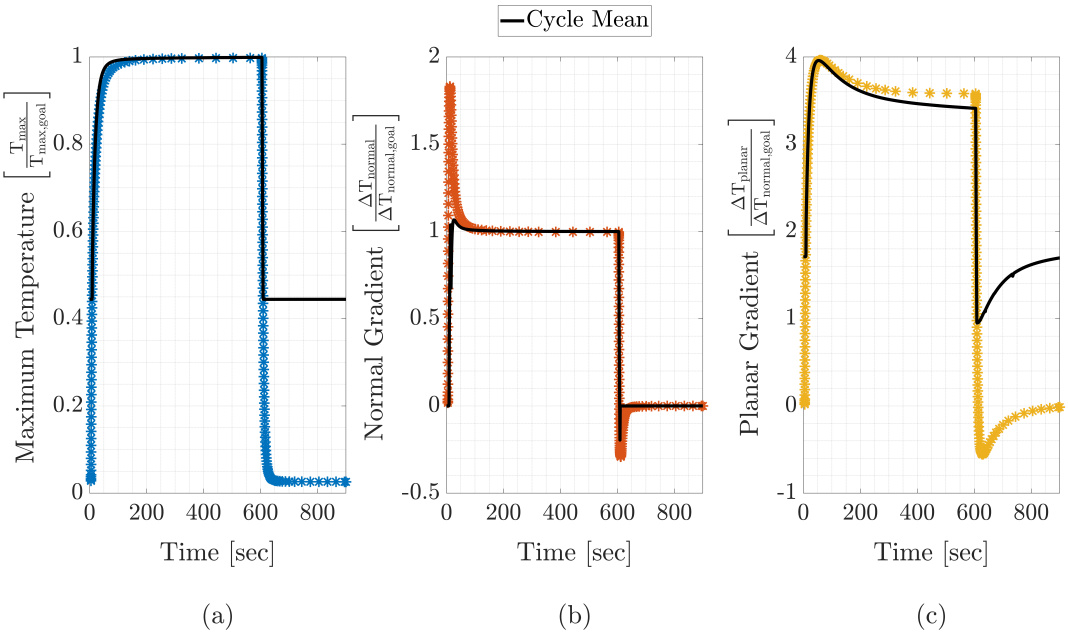


Figure 8.5: *comparison of finite element analysis to testing data for CMSX-4-T1 (a)* T_{max} *(b)* ΔT_{normal} *(c)* ΔT_{planar}

the convective boundary condition to approximate the conductive losses through the plenum is considered reasonable for this application. A 3% change far from P_f is estimated to have negligible effects.

The values for the CMSX-4 simulation follow trends similar to those observed for Inconel 625. The agreement between the mean experimental results and FEA is of the order of 1% for both T_{max} and ΔT_{normal} during the quasi-steady region. ΔT_{planar} is over-predicted by 6%, yet this is considered to have negligible effect at P_f. The overshoot for ΔT_{normal} is more pronounced, briefly exceeding the target by 80% before settling back to the appropriate value. These overshoots in ΔT_{normal} are not reflected in the Cauchy stress state, which more closely resembles the profile of T_{max}.

The components of the stress state are reported in Figure 8.6 (a). These were extracted from P_f and filled in using a linear interpolation between the solution time steps. Each stress component shows a profile similar to T_{max}, which indicates a localised dependence on the maximum temperature to determine the stress state. This was expected for the constrained coupon, as the effect of heating to T_{max} was shown to have a significant contribution to the final stress state in Chapter 4. The maximum principal stresses were calculated at each time step using the Cauchy stress tensor. CMSX-4 values are presented in Figure 8.6 (b). The maximum and median principal stresses are shown to have a small magnitude relative to

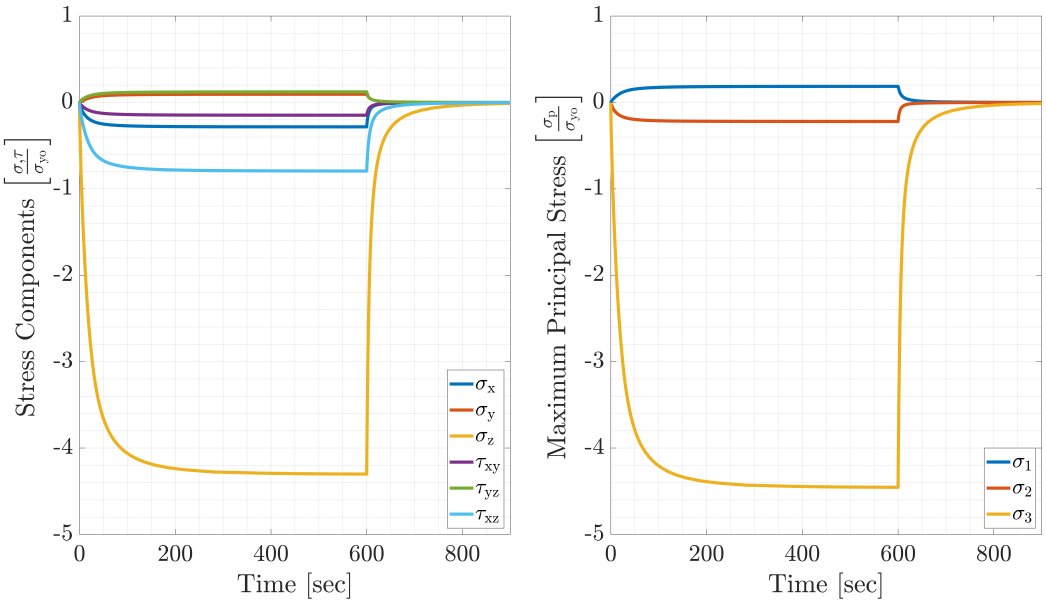


Figure 8.6: *(a) Cauchy component stresses in the unit coordinate system over the modelled cycle (b) maximum principal stresses for the aforementioned Cauchy stress state*

both the minimum principal stress and the room-temperature yield stress, to which the plot was normalised. For later modelling purposes, the maximum absolute value of the stress state was used. As the minimum principal stress was roughly 21 times the subsequent largest principal stress by magnitude, this value was used to model a uni-axial stress state for strain range and lifespan estimation. The most significant component stress, σ_z, confirms that the stress state is effectively parallel to the principal direction of the cast coupon, with minimal variation during heating. As such, values for CMSX-4 in the $< 001 >$ direction were used.

8.2 Elastic-Plastic Modelling

The fictitious elastic stress state of all modelled cycles exhibited a similar behaviour with respect to the orientation and relative magnitude of the principal stresses. The minimum principal stress has the largest magnitude and the constant relative magnitudes of the Cauchy stress tensor indicated the direction of this stress was unchanging. As such, the use of a 1D model was implemented to determine the total strain range and estimate the number of cycles to failure.

8.2.1 Strain Range Estimation

The strain range was estimated using a MATLAB[4] script, which implements an approach utilised by Skamniotis [101]. The script utilises the incremental stress state at each time step to determine the incremental strain. If the stress state at the current time step was elastic, an elastic strain was calculated using:

$$\Delta\epsilon_{\mathrm{e}} = \frac{\Delta\sigma}{\mathrm{E}} \tag{8.6}$$

If the new stress state exceeds the yield stress, the plastic strain increment was estimated using a Neuber [78], Molski-Glinka [73], and constant strain [101] approach. The Neuber method, which stipulates that the complementary strain energy density is conserved, follows:

$$\begin{aligned} \mathrm{E_n} &= \frac{1}{\mathrm{E}}\left(\delta\sigma_{\mathrm{fe,i}}^2 + 2|\delta\sigma_{\mathrm{fe,i}}\sigma_{\mathrm{fe,i-1}}|\right) \\ \delta\epsilon_{\mathrm{p,n}} &= \begin{cases} \text{heat}: & -\frac{\mathrm{E_n} - |\delta\sigma_{\mathrm{tr,i}}\epsilon_{\mathrm{p,i-1}}|}{|\sigma_{\mathrm{tr,i-1}}| + |\delta\sigma_{\mathrm{tr,i}}|} \\ \text{cool}: & -\frac{\mathrm{E_n}}{|\sigma_{\mathrm{tr,i}}| + \frac{|\delta\sigma_{\mathrm{tr,i}}|}{2}} \end{cases} \end{aligned} \tag{8.7}$$

The Molski-Glinka method stipulates that only the strain energy density is conserved. Thus the plastic strain was governed by:

$$\begin{aligned} \mathrm{E_g} &= \frac{1}{\mathrm{E}}\left(\frac{\delta\sigma_{\mathrm{fe,i}}^2}{2} + |\delta\sigma_{\mathrm{fe,i}}\sigma_{\mathrm{fe,i-1}}|\right) \\ \delta\epsilon_{\mathrm{p,g}} &= \begin{cases} \text{heat}: & -\frac{\mathrm{E_g}}{|\sigma_{\mathrm{tr,i-1}}| + \frac{|\delta\sigma_{\mathrm{tr,i}}|}{2}} \\ \text{cool}: & -\frac{\mathrm{E_g}}{|\sigma_{\mathrm{tr,i}}| + \frac{|\delta\sigma_{\mathrm{tr,i}}|}{2}} \end{cases} \end{aligned} \tag{8.8}$$

Where fe denotes the fictitious elastic result of FEA and tr represents the true stress state, limited to the yield stress at the given increment temperature. i and $\mathrm{i}-1$ denote current and previous time steps, respectively. For the constant strain case, the plastic strain is equal to the elastic strain calculated in Equation (8.6). An elastic follow-up factor [28, 101] is implemented for both Neuber-type methods to account for the fact that the creep-plastic location was surrounded by an elastic volume.

Creep strain was also taken in to account using an identical model from [101]. The stress

[4]The MathWorks, inc (2023), *MATLAB version: 23.1 (R2023a)*, https://www.mathworks.com

relation due to creep was calculated by adapting uni-axial creep data for Inconel 625 [82] and CMSX-4 [101]. The stress relaxation over a short duration was modelled by adapting steady-state testing results according to:

$$\delta\sigma_{\mathrm{cr}} = \mathrm{sgn}\,(\sigma)\,\frac{\mathrm{E}}{\mathrm{Z}}\dot{\epsilon}_{\mathrm{o}}\delta\mathrm{t}\left|\frac{\sigma}{\sigma_{\mathrm{o}}}\right|^{\mathrm{n}}\exp\,(\mathrm{x}) \tag{8.9}$$

Where E is the Youngs' Modulus, Z is the elastic follow-up factor [28], $\dot{\epsilon}_{\mathrm{o}}$is the reference strain rate, σ_{o} is the creep reference stress, n is the creep exponent, and x is defined as:

$$\mathrm{x} = -\frac{\mathrm{q}}{\mathrm{R}}\left(\frac{1}{\mathrm{T}} - \frac{1}{\mathrm{T}_{\mathrm{ref}}}\right) \tag{8.10}$$

For which Q and R represent the activation energy and the gas constant, respectively. T is the temperature at which the creep occurred and $\mathrm{T}_{\mathrm{ref}}$ is the creep reference temperature. Material-specific values are presented in Appendix II. Temperature-dependent yield stresses and Youngs' Moduli were taken from [108] and Table 3 in Appendix II.

Skamniotis [104] proposed an alternative model to estimate $\mathrm{N_f}$. It relates the plastic strain range to the fatigue life. The plastic strain range is defined as:

$$\Delta\epsilon_{\mathrm{p}} = \Delta\epsilon - \frac{\Delta\sigma}{\mathrm{E}} \tag{8.11}$$

Where $\Delta\epsilon$ is the total strain range, $\Delta\sigma$ is the total stress range, and E is the Youngs' Modulus evaluated at the mean cycle temperature. The plastic strain range is then used to define:

$$\tilde{\gamma}_{\mathrm{c}} = 2\Delta\epsilon_{\mathrm{p}}\frac{1}{\mathrm{SFn}} \tag{8.12}$$

Where SF and n are material constants for CMSX-4. SF is the Schmidt factor and n is the number of active slip systems. For CMSX-4, the SF is 0.4082, and n is 8. This represents the octahedral slip system active in the $< 001 >$ direction. The fatigue life is then found by evaluating:

$$\mathrm{N_f} = \mathrm{f_1 e}^{\mathrm{f_2}\tilde{\gamma}_{\mathrm{c}}} \tag{8.13}$$

Where $\mathrm{f_1}$ and $\mathrm{f_2}$ are constants for a best-fit curve to the experimental data. For CMSX-4 in the $< 001 >$ direction, they are defined as 132,400 and -3874, respectively [104]. Equations

(8.11)-(8.13) were applied to the total strain ranges presented in Table 8.4 to provide alternate estimates.

8.2.2 Results

The modelled hysteresis curves are presented in Figures 8.7 - 8.8. Subscripts are used to identify which cycle was labelled, with points 0-5 marked for clear identification. These are defined below:

0. The initial stress and strain state before cycling
1. The limit of purely elastic deformation during the first heat-up
2. When T_{max} obtains 97% of the maximum value, corresponding to the end of heating
3. VCSEL shut-down, and the start of the cooling component of the cycle
4. The limit of purely elastic deformation during the first cool-down
5. The end of the cycle

Stress values are normalised by the temperature-dependent yield stress. The hysteresis curves are coloured corresponding to the fillet temperature, T_f, normalised to the cycle minimum and maximum. Normalised curves obey expected distributions, with the overall shape adhering to the expected box-like shape from the example provided in Figure 2.6. A region of stress relaxation and creep strain accumulation during the thermal dwell is found between points 2 and 3.

The strain range data from the hysteresis curves is summarised and presented in Table 8.4 for each of the coupons and plastic models, as predicted by the Scholz-Manson-Coffin relationship [95]. The strain range is defined as the difference in strain between points 5 and 3. Due to a lack of availability in the literature, the CMSX-4 equations were applied to the Inconel 625 coupons.

Table 8.5 presents the prediction of the lifespan using the crystal plasticity approach [104], in combination with the Neuber-type methods.

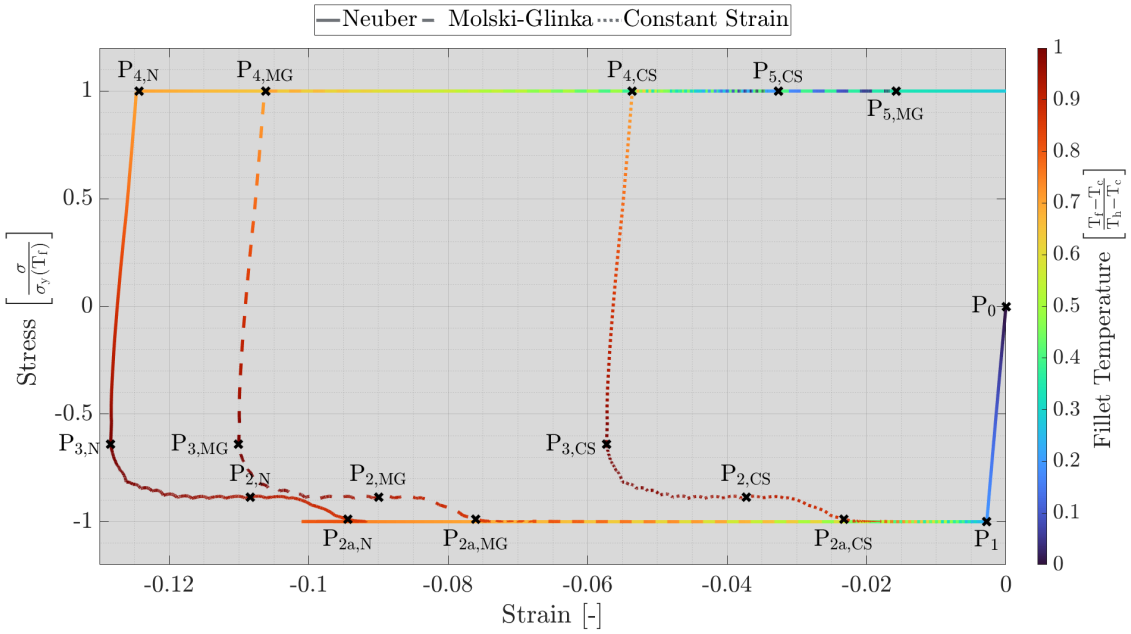


Figure 8.7: *IN625-C-T2 hysteresis curves for various plastic formulations*

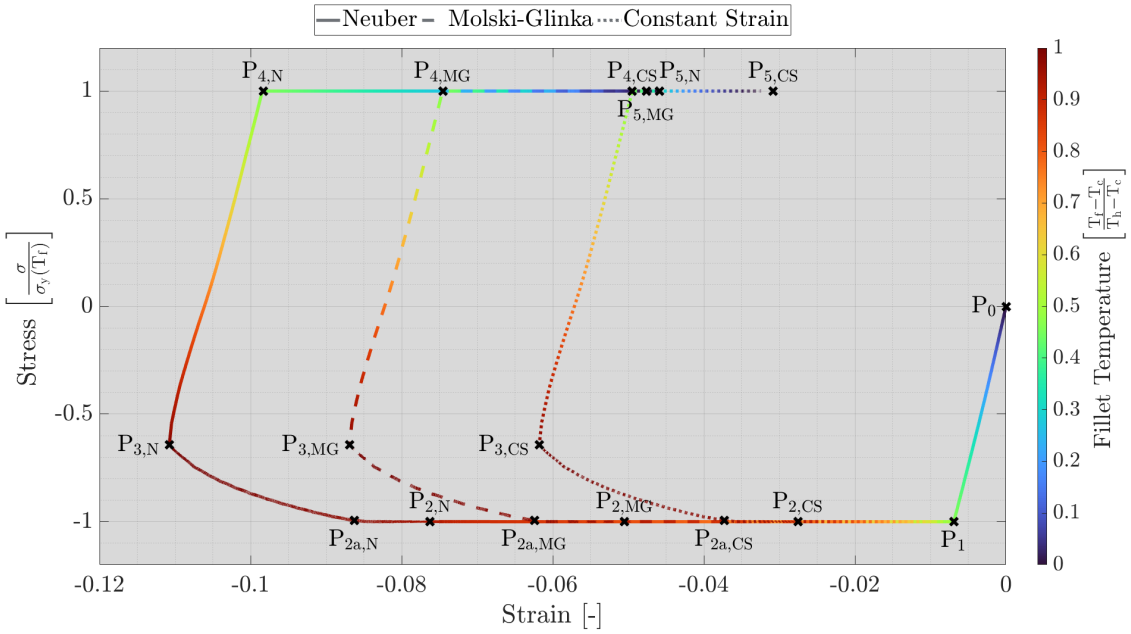


Figure 8.8: *CMSX-4-T1 hysteresis curves for various plastic formulations*

Test Section	Testing	Neuber		Molski-Glinka		Constant Strain	
	N_f	$\Delta\epsilon$	N_f	$\Delta\epsilon$	N_f	$\Delta\epsilon$	N_f
IN625-C-T2	20	0.180	-	0.094	1	0.025	195
IN625-C-T4	10	0.193	-	0.099	1	0.025	182
IN625-E-T2	30	0.114	-	0.060	5	0.020	548
IN625-E-T4	30	0.121	-	0.064	4	0.021	469
CMSX-4-T1	80	0.065	4	0.039	23	0.031	65

Table 8.4: *strain range and number of cycles to crack initiation as predicted by Neuber-type methods and the Scholz-Manson-Coffin relationship [95]*

Neuber		Molski-Glinka		Constant Strain	
$\Delta\epsilon_p$	N_f	$\Delta\epsilon_p$	N_f	$\Delta\epsilon_p$	N_f
0.050	0	0.023	2	0.015	114

Table 8.5: *strain range and number of cycles to crack initiation as predicted by Neuber-type methods and the Skamniotis relation [104] for CMSX-4*

8.3 Discussion

Estimates of the life span for DWEC components are in mild agreement with the experimental results. For the Scholz-Manson-Coffin relation, the Neuber method offers the most conservative measure of the lifespan of the plastic models investigated, followed by the Molski-Glinka and Constant Strain approaches. In line with the observed tests, the strain range and N_f estimates for the T2 and T4 tests are very similar. There is a 7-20% drop in predicted cycles to crack initiation from T2 to T4, model dependent. The elliptical holes display a reduced strain range and increased life span, ranging from 157-400%, depending on the model. The reality is that the true strain range, assuming that the Scholz-Manson-Coffin equation was correctly applied, should fall between those estimated through the Molski-Glinka and Constant Strain approaches. For the CMSX-4 component, all three methods appear to err on the conservative side. The constant strain approach is, at best, under-predicting N_f by 8.6%. This is most likely due to the high sensitivity of N_f for ultra-low-cycle fatigue.

It is commonly observed that strain range and life span estimates for ultra-low-cycle

fatigue display increased sensitivity to modelled conditions. The strain ranges and N_f estimates presented in Table 8.4 offer conservative predictions of the CMSX-4 coupon with available FEA stresses. The observed N_f of 71-80 cycles is best matched by the Skamniotis relation [104] in Equation (8.13). For both, the Neuber method is shown to dramatically under-predict the number of cycles to crack initiation as the strain range estimation was conservative. The Molski-Glinka and constant strain methods straddle the observed result.

The results for the Inconel 625 coupons are only approximate due to the lack of available literature. Despite this, the strain ranges show agreement with the experimental results. For both T2 and T4 profiles, the circular holes display a similar strain range. The largest discrepancy of 7.2% is observed for the Neuber method. The strain range is effectively identical for the constant strain approach. A similar trend is observed with the elliptical holes in the T2 and T4 profiles. The results align with the previously concluded dependence on T_{max} and ΔT_{planar} for the determination of N_f. When circular holes are compared with elliptical ones, an increased strain range is estimated for the circular holes. This is in line with the reduced life span of the circular holes brought on by greater stress concentrations present.

The lack of availability in the literature restricts the plastic strain and creep models from modelling a transient-independent case. Neuber-type methods do not account for the rate of load. Creep modelling [28, 101] was adapted from steady 1D tests and was not modified to account for stress ramping. In an attempt to minimise error, the FEA results were interpolated onto a fine temporal resolution, such that the stresses at each time step may be assumed to be steady. δt was adjusted until the strain range was constant with further refinement. This step minimised the spike marked as P_{2a}. This small strain overshoot and correction is thought to be due to the lack of transience in utilised models and the simple linear summation of various strain terms failing to capture complex interactions in this region. In addition, the available creep models were calibrated by tensile testing. A compressive model is required to appropriately model the phenomena in the DWEC system.

Broader material features that influence the domain were also investigated. The elastic follow-up factor was altered to assess whether this influences this result. All coupons were found to be insensitive to Z in the range of Z = [1,100]. Additionally, the crystallographic directions will affect the results. The principal direction continued to be of primary impor-

tance and was measured in the CMSX-4 coupon following casting. The orientation of the secondary directions was not determined. The local variation in crystal growth was also not determined. A combination of these effects results in considerable uncertainty about the actual material properties in the direction parallel to the maximum principal stresses used in the modelling. With an an-isotropic factor of 2.85 [99], the stress state may change by up to 185%, which will have a profound impact on the estimation of life.

8.3.1 Perturbation Analysis

Following the numerical study, a perturbation analysis was performed to investigate the sensitivities to various boundary conditions and solution inputs. The total uncertainty, U_{tot}, of the total strain range was estimated through a root-sum-square-method [113]:

$$U_{tot} = \sqrt{\sum_{i}^{N} (U_i)^2} \tag{8.14}$$

The individual per cent, U_i, was established using [113]:

$$U_i = \left(\frac{\delta \Delta\epsilon}{\delta \chi_i}\right) \frac{\Delta \chi_i}{\Delta \epsilon} \tag{8.15}$$

Where $\frac{\delta \Delta\epsilon}{\delta \chi_i}$ is the partial derivative of $\Delta\epsilon$ relative to the true value, $\Delta\chi$ is the magnitude of the uncertainty and $\Delta\epsilon$ is the most likely measured value.

Stresses in the coupon were generated through thermal loading, and the boundary conditions of the FEA thermal solution were altered for this analysis. A complete transient solution was obtained using a configuration identical to that in Section 8.1. The total strain range for each change in boundary condition was estimated using the two Neuber and constant strain models. The results are presented in Table 8.6. The performance of error analysis was computationally expensive, requiring several weeks to run various cases with alteration of the boundary conditions at the given mesh size and in various Workbench[5] modules. For this reason, it was considered impractical to carry out this investigation for all coupons. The results of the Inconel 625 coupons were considered secondary and were omitted from this analysis.

It is clear that a considerable percentage of errors are present. This aligns with the

[5] Ansys®Academic Research Workbench, Release 23.1

Value	Neuber		Molski-Glinka		Constant Strain	
	$\frac{\delta\Delta\epsilon}{\delta\chi_i}$	U_i	$\frac{\delta\Delta\epsilon}{\delta\chi_i}$	U_i	$\frac{\delta\Delta\epsilon}{\delta\chi_i}$	U_i
h_{loss}	2.90 E-4	0.446	1.50 E-4	0.385	6.00 E-5	0.194
$T_{c,in}$	1.24 E-3	0.561	5.54 E-4	0.419	1.98 E-4	0.188
h_{cool}	4.02 E-3	0.499	2.02 E-3	0.418	8.93 E-4	0.232
$\dot{q}_{VCSEL}$	4.27 E+0	0.617	2.12 E+0	0.510	9.79 E-1	0.297
	U_{tot}:	107%	U_{tot}:	87.1%	U_{tot}:	46.4%

Table 8.6: *uncertainty calculations for the CMSX-4 coupon under T2 conditions*

previous understanding of the sensitivity of plastic strain modelling and life span estimation in ultra-low-cycle regimes, with the two Neuber-type methods exhibiting the most significant sensitivity. The conductive loss model contributes the least, with the exception of the constant strain model, in which the coolant temperature has the second-greatest effect. The VCSEL power supply has the greatest contribution in all cases. This aligns with the low-order model and the experimental results, which indicate a dependence on T_{max} for the stress field along with the properties of the material.

Conclusion

Numerous studies have investigated the aerothermal benefits [30, 76, 79, 80, 126] of a double-wall effusion-cooled (DWEC) system, and there is a growing wealth of literature dedicated to modelling the thermo-mechanical performance [31, 36, 37, 76, 100, 101, 102, 103, 104, 105, 106]. Modelling complex material phenomena is challenging, as identifying the correct thermal and mechanical loading for computational domains remains challenging. The absence of available literature requires approximations in loading and transience. In addition, lifespan estimates are sensitive to stress states, which, in turn, are sensitive to changes in boundary conditions. Complex materials add further difficulty, as the orientation of an anisotropic crystal structure at critical locations, such as film holes, is unknown. Usually, only the primary direction is controlled, and the secondary direction is left to arbitrarily orient itself. Together, these results form the basis for the need to experimentally evaluate the double-wall effusion-cooled geometry under engine-representative conditions.

To start, a coupon design for TMF testing was studied and presented. It offers a stress field with a maximum compressive stress around the film holes, yet exaggerated in magnitude compared to a theoretical blade [31, 36, 37, 76, 100, 101, 102, 103, 104, 105, 106]. The design outperformed others proposed due to the simplicity, stress field, compatibility with the proposed VCSEL power supply, and the ability for pyrometer measurements. A region of high tensile stress was observed in the exterior pedestal fillets due to the removal of pedestals in the peripheral region. An optimisation study was conducted to reduce these over-stresses, which were decreased by 41% with localised scaling, without impacting the global stress state. The study indicates that local stresses in the blade may be addressed through this local scaling approach. During commissioning, a further redesign study was presented, showing that additional impingement cooling may supplement pedestal conduction in the peripheral regions. The coupon overheat of 46% was reduced to less than 9% using this technique.

An analytical model was developed to allow the study of the influence of constraints,

geometry, and thermal loading on the final stress state. The thermal boundaries modelled a lossless case, analogous to that presented by Elmukashfi [36], and a loss case, modelling a decreased temperature towards the mounting due to conduction through the plenum. The assumptions in the analytical model were confirmed by FEA of the coupon geometry. The results indicate a 3% discrepancy for the 2D case and a 4% discrepancy for the 3D case, where the model over-predicted the mean stresses in the disconnected region. This was attributed to a lower mean temperature due to 3D conduction not captured in the 2D model. A study was conducted using the validated model to assess the adherence to the results of the coupon design and the relative contribution of various thermal phenomena. The results indicate that the analytical model under-predicts the nominal stress distribution in the hot-wall and fails to capture a small moment contribution present in the cold-wall; however, the maximum nominal stress value is within 3.2% of the FEA result. A comparison of the relative effects of both the loss and step thermal phenomena indicates that the global step in temperature from the initial temperature affects the magnitude of the stress field 57 times more than the loss term. While the initial definition of ΔT is defined by the difference in temperature through the hot-wall, the model indicates that there is a dependence on the difference between the initial and maximum temperatures to determine the stress state.

A test rig, the Effusion Lifespan and Stress Addition (ELSA), was developed to integrate within the existing Oxford Laser Heating Facility (OLAHF) [63, 64] architecture present at the Oxford Thermofluids Institute. A flexible design technique for a compound parabolic concentrator (CPC) was presented in which the location of the focal point was unconstrained and a custom inlet and outlet size was possible for a variable acceptance angle. A study showed a sharp decrease in optical efficiency between a 12.5- and 30-degree acceptance angle, correlated to an increased distance between the focal point and exit aperture. The study also showed that the use of four 2.4 kW vertical-cavity surface-emitting lasers (VCSELs) with a reflecting surface on the VCSEL bracket exhibited an optical efficiency greater than that defined by Cooper [29] for a square aperture. This feature increased the optical efficiency by an average of 98.4% across all variants studied. A truncated CPC with a 15-degree acceptance angle was chosen due to its maximum flux of 7.4 $\frac{\mathrm{W}}{\mathrm{mm}^2}$, and centrally focused flux. An exhaust management system was included in the design of the VCSEL bracket. The positive pressure variant is shown to prevent hot coupon exhaust from contacting the

VCSEL arrays, instead forcing it out through a slot in the VCSEL bracket. A low-order flow network model was developed to investigate the cooling water capabilities that protect the components of ELSA and OLAHF. An estimated 18 LPM is achievable at a 1.75 bar pump head. At 6 °C, this is adequate to cool ELSA without diverting more than 60 LPM away from the VCSEL cooling system [87]. Finally, a finite element analysis (FEA) was performed to fine-tune the location of the cooling channels and identify the maximum temperatures and stresses in the components. All components are within the respective creep limits and the maximum temperature of 119 °C is predicted in the C1 channels. This is considered acceptable as it is below the 130 °C boiling point of water at 2.7 bar [58], which the network model predicts for the cooling channel. The maximum stresses were used to estimate the number of cycles until the failure of critical components, which is estimated to be 10000 cycles. This was done using established S-N curves at the maximum stresses extracted from each component for a simplified constant amplitude loading.

Then, rig commissioning was performed to validate the prior modelling of ELSA components. The water cooling loops are shown to demand a combined maximum of 26.2 LPM at the maximum pump head setting, and a pump head of 1.75 was used for testing. There is some discrepancy between the network model and the experimental results; however, these are thought to be due to the Reynolds-independent formulation for the loss coefficients in the model. The surface roughnesses of the gold-plated CPC and VCSEL bracket reflecting surfaces were measured to be 0.281 μm and 0.535 μm, providing a surface reluctance of 0.95 and 0.92, respectively. A series of pulses were applied to a 1 mm thick sheet for a range of durations and power settings to determine the emissivity and absorption of Inconel 625. The results show a clear dependence on conditioning, as the emissivity of the surface increases by almost 300% due to the oxidation and formation of precipitates on the outer surface as the component accrues time at elevated temperatures. Unconditioned samples display a decreasing emissivity with increasing temperature, and conditioned samples exhibit the opposite relation. The coefficients for the linear fits of the conditioned samples were linearly interpolated for coupon surface roughness values. The results align with the actual temperatures measured by ratio pyrometers, validating the method and indicating that the manufacturing process has a negligible bearing on the emissivities. FEA results of the pulses were compared with the experimental data to estimate a mean absorbance of

0.598, which is independent of the surface finish but dependent on the conditioning. This agrees with a 1D transient model with a best fit of 0.58 and 0.57 for ACR-2 and ACR-4, respectively. The absorption coefficients of the Inconel 625 coupons are found to be 31% lower, indicating that the manufacturing process has an impact on absorption. The CPC distribution was qualitatively compared with the FE results as there was no possibility for direct measurement. There exists a general agreement in the centre of the CPC outlet; however, the periphery in experiments decreases in temperature at a lower rate than FEA. The observed deformation of the pulse test specimens was offered as an explanation for the discrepancies. Qualitative confirmation of outlet distribution was found through IN625-C-I2 testing, which is closely aligned with the LightTools results. Finally, rig temperatures were investigated using hold and long-cycle tests. The measured plenum temperatures remain below 30 °C for all tests, indicating that the modelling over-predicts the actual case in line with the exaggerated boundary conditions used in FEA. Undulations in coolant flow rate and temperature have negligible impact on measured coupon temperatures.

Following a successful set of commissioning tests, Inconel 625 coupons with circular and elliptical holes were tested in various ELSA control settings to establish an understanding of the required settings and limits for future tests. More than 1000 °C was recorded at less than 50% power and a maximum thermal difference of 365 °C was observed with 4 $\frac{g}{sec}$ of coolant airflow. Both T_{max} and ΔT_{normal} show a strong dependence on the VCSEL power. The remaining Inconel 625 and CMSX-4 coupons were then cycled over selected thermal fields. All components exhibited crack formation after a series of 15-minute cycles. The results show a clear benefit of single-crystal CMSX-4, as it survived eight times longer than its Inconel 625 counterpart. The results further support those derived in the analytical model: T_{max} was the dominant factor in determining failure. T2 and T4 tests, controlled for hole shape, show negligible variation in crack formation at near-identical T_{max} but differing gradients. The opposite is true when comparing T2 and T4 with both T3 tests. The latter suffered early failure through the apparent fracture, inferred from the bowing-out of the hot-wall and a sharp increase in T_{max}. Cracks in circular holes appear at the sharp-film hole wedge adjacent to the exterior of the hot-wall for the T2 and T4 profiles, in line with predictive modelling [101, 103, 104, 105, 106] of peak stress locations and crack initiation. Finally, elliptical holes outperform their circular counterparts. Elliptical holes were observed

to survive triple the number of cycles in both the T2 and T4 test profiles. An increase in VCSEL power and a decrease in coolant flow were required in the elliptical hole coupons to achieve the same temperatures as those with circular holes, indicating an increase in convective efficiency.

Lastly, the T2 and T4 tests were evaluated using a conjugate numerical model. A transient conjugate thermal solution feeds in to two static structural solutions, using a sub-modelling procedure to allow local mesh refinement around critical features [9]. The elastic stress state and temperature were extracted from the final solution at critical locations near the film hole wedge. Two Neuber-type methods and a constant strain approach were used to estimate the total strain range and life span using a modified Manson-Coffin relation [95]. The results indicate that a 1D model was a reasonable approximation of the stress state at the film hole wedge due to the relative magnitude of the principal stresses. The Scholz-Manson-Coffin equation offered a conservative estimate for the life span in the ultra-low-cycle regime for the CMSX-4 piece for all elasto-plastic models. N_f was ignored for the Inconel 625 components as no model was available for use. An estimate of life span from Skamniotis [104] utilises a crystal plasticity approach to correlate the plastic strain range with the active slip planes. This formulation was combined with the Molski-Glinka and constant strain approaches. The two methods estimate 2 and 114 cycles to crack initiation, respectively, straddling the observed result of 80.

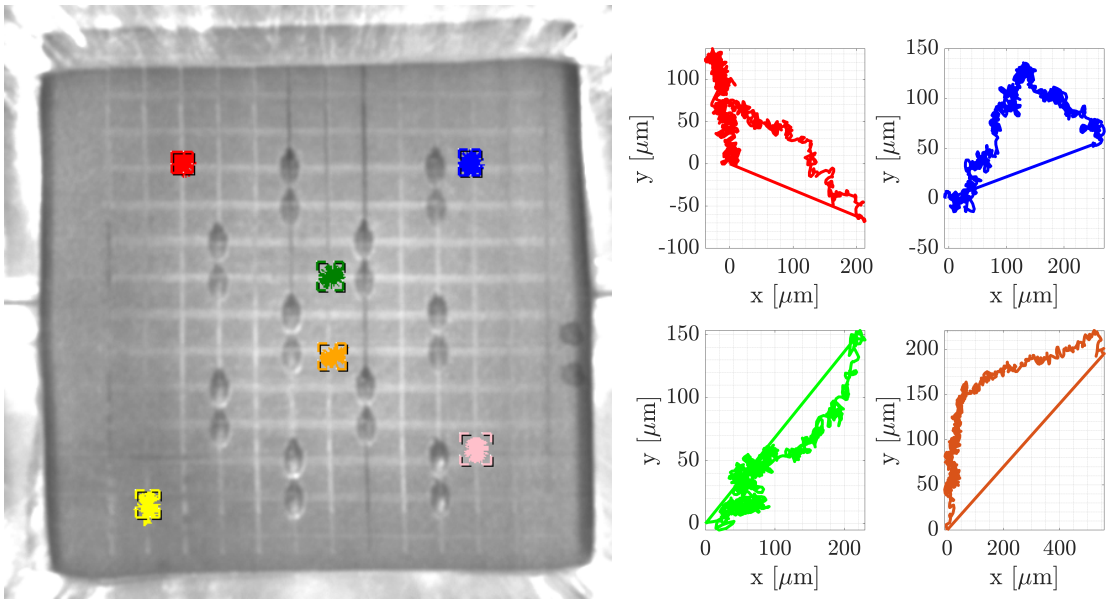
9.1 Future Work

The coupons and rig resign were the first generations of an assembly that showed considerable promise. Suggestions for future work are laid out below.

ELSA

1. The importance of alignment between the CPC and the target is shown by the spacing study in Figure 6.11. Furthermore, the eventual modelling may be inaccurate if the x- and z-locations were shifted. The design and construction of an assembly to adjust the spacing and alignment should be undertaken to increase the precision of the set-up.

2. An initial attempt was made to optimise the spatial activation of VCSEL to achieve



(a) (b)

Figure 9.1: *motion amplification locations and displacements during hold testing*

the desired CPC outlet profile. The results indicated that a thorough understanding of the location of VCSEL at the CPC input will allow future designs to tailor outlet profiles with a greater degree of precision.

3. Manual control and cycle-by-cycle update of control settings increase variation in testing profiles. The development and application of a control program to automatically scale inputs to maintain testing conditions during cycles will benefit future work.

4. A clear drawback of the current mounting assembly is the quasi-rigid constraint imposed on the coupon due to the plenum. In pursuit of engine-specific conditions, alternative mounting configurations should be investigated to ensure less restricted deformation while maintaining a seal for the cool air.

Measurements and Modelling

1. Acoustic emission detection is used extensively in failure analysis. Integrating this in to existing ELSA/OLAHF infrastructure is possible. This would enable the development of an acoustic database, which may assist in accurate crack detection. Motion amplification should also be investigated to compare the displacement fields of the experiment with FEA. The results of the IN625-C-I3 sample are presented in Figure

9.1. The method was not refined in this work, as various filters for the acquisition camera should be investigated.

2. Radiance measurements of the calibration plates were challenging to perform. Removing the need to use correlations to correct the IR data would benefit the determination of the CPC profile. A proposed solution is the use of a grid through which the pyrometer measures the emissivity-independent temperatures.

3. The external cracks are presented in this work and do not prove the absence of internal cracks. Strategic sectioning of coupons and detection methods during cycling, such as CT, should be used. An area of particular interest is the FHW on the internal side of the hot-wall.

4. The disagreement between the 2D model and the 3D geometry is attributed to the corner regions, where L_2 does not capture the full length of the section. Work should be done to quantify this discrepancy through an effective length or another such metric.

Coupon

1. The elliptical hole shows promise in its reduction in coolant requirements and 200% increase in service life over traditional circular holes. The internal geometry should be varied and re-scaled to assess the performance of the highly constrained coupon.

2. The results of the low-order model indicate that the effect of reducing the thickness of the cold-wall differs from Skamniotis [102]. The next series of coupons could investigate this.

3. The results suggest that ΔT_{planar} is the key parameter in determining failure in the highly-constrained coupon. The risk of buckling in engine-representative conditions may prove to be an issue with specific DWEC geometries and should be considered.

4. Finally, CMSX-4 should be used extensively. The casting processes will continue to improve and the 3D-printed Inconel 625 does not provide adequate fatigue resistance to gather meaningful results for this set-up. Due to the significant change in Youngs' Modulus in CMSX-4, the orientation of the secondary direction local to the film hole wedge should be measured.

References

[1] 3D-Hubs. *CNC Machining: The Manufacturing and Design Guide*. URL: https://www.hubs.com/get/cnc-machining-guide/.

[2] Abas, R. A., Hayashi, M., and Seetharaman, S. "Thermal diffusivity measurements of CMSX-4 alloy by the laser-flash method". In: *International Journal of Thermophysics* 28 (1 Feb. 2007), pp. 109–122. ISSN: 0195928X. DOI: 10.1007/s10765-007-0163-5.

[3] Alaruri, S., Bianchini, L., and Brewington, A. "Effective spectral emissivity measurements of superalloys and YSZ thermal barrier coating at high temperatures using a 1.6 m single wavelength pyrometer". In: *Optics and Lasers in Engineering* 30 (1 1998), pp. 77–91. ISSN: 0143-8166. DOI: 10.1016/S0143-8166(97)00108-5. URL: https://www.sciencedirect.com/science/article/pii/S0143816697001085.

[4] Albion. *PN20 Bronze Swing Check Valve*. URL: https://www.albionvalvesuk.com/wp-content/uploads/2022/05/ART-384-rev1.pdf.

[5] Alicat-Scientific. *Technical Data for MC-Series Mass Flow Controllers*. Aug. 2020. URL: https://www.alicat.com/wp-content/documents/specifications/DOC-SPECS-MC-HIGH.pdf?_gl=1*cfud94*_gcl_au*MjEwNDgzNjcyMy4xNjk2OTQ2ODU2.

[6] Amaral, S. et al. "Design and optimization of the internal cooling channels of a HP turbine blade: part I - methodology". In: ASME, June 2008, pp. 967–976. ISBN: 978-0-7918-4314-7. DOI: 10.1115/GT2008-51077. URL: https://asmedigitalcollection.asme.org/GT/proceedings-pdf/GT2008/43147/967/2687584/967%5C_1.pdf.

[7] Andrews, G., Gupta, M., and Mkpadi, M. "Full coverage discrete hole film cooling: cooling effectiveness". In: *International Journal of Turbo and Jet Engines* 2 (3 Jan. 1985), pp. 199–212. ISSN: 2191-0332. DOI: 10.1515/TJJ.1985.2.3.199.

[8] ANSYS. *Ansys Fluent User's Guide*. 2021.

[9] ANSYS. *Mechanical User's Guide*. 2023.

[10] Arvanitis, S. T., Symco, Y. B., and Tadros, R. N. "Multiaxial life prediction system for turbine components". In: *Journal of Engineering for Gas Turbines and Power* 109 (1 1987), pp. 107–114. ISSN: 0742-4795. DOI: 10.1115/1.3239997. URL: https://asmedigitalcollection.asme.org/gasturbinespower/article-pdf/109/1/107/5495029/107%5C_1.pdf.

[11] Aust, J. and Pons, D. "Taxonomy of gas turbine blade defects". In: *Aerospace* 6 (5 May 2019). ISSN: 22264310. DOI: 10.3390/AEROSPACE6050058.

[12] Basquin, O. H. "The exponential law of endurance tests". In: 1910, pp. 625–630.

[13] Boley, C. D. et al. "Metal powder absorptivity: modeling and experiment". In: *Applied Optics* 55 (23 Aug. 2016), p. 6496. ISSN: 0003-6935. DOI: 10.1364/ao.55.006496.

[14] Bours, R. *Modern Design Considerations for Pressure Relief Systems*. 2016. URL: https://fluidhandlingpro.com/modern-design-considerations-for-pressure-relief-systems/#:~:text=When%5C%20sizing%5C%20the%5C%20relief%5C%20system,risk%5C%20of%5C%20loss%5C%20of%5C%20containment..

[15] Brkic, D. and Praks, P. "An efficient iterative method for looped pipe network hydraulics free of flow-corrections". In: *Fluids* 4 (2 June 2019). ISSN: 23115521. DOI: 10.3390/fluids4020073.

[16] BSI. *BS EN ISO 204-2018 - TC–[2023-11-10–11-51-28 AM]*. 2018.

[17] BSI. *BS EN ISO 4126-1-2013+A2-2019 - TC–[2022-04-28–12-01-02 PM]*. 2019.

[18] BSI. *BS EN ISO 4126-7-2013+A1-2016–[2022-04-27–03-48-56 PM]*. July 2013.

[19] BSI. *BS ISO 4126-10-2010–[2022-04-27–04-35-42 PM]*. Oct. 2010.

[20] Budynas, R. G. (G., Nisbett, J. K., and Shigley, J. E. *Shigley's Mechanical Engineering Design*. 9th ed. McGraw-Hill, 2011. ISBN: 0073529281.

[21] Bullough, C. K. et al. "The characterization of the single crystal superalloy CMSX-4 for industrial gas turbine blading applications". In: 1998, pp. 861–878. ISBN: 3-89336-228-2. URL: https://www.researchgate.net/publication/259778979.

[22] Burgreen, D. "Structural growth induced by thermal cycling". In: *Journal of Basic Engineering* 90 (4 Dec. 1968), pp. 469–475. ISSN: 0021-9223. DOI: 10.1115/1.3605168. URL: https://asmedigitalcollection.asme.org/fluidsengineering/article-pdf/90/4/469/5764809/469%5C_1.pdf.

[23] Burgreen, D. "The thermal ratchet mechanism". In: *Journal of Basic Engineering* 90 (3 Sept. 1968), pp. 319–324. ISSN: 0021-9223. DOI: 10.1115/1.3605098. URL: https://asmedigitalcollection.asme.org/fluidsengineering/article-pdf/90/3/319/5764231/319%5C_1.pdf.

[24] Canon. *Canon EF 100mm f/2.8L Macro IS USM Specifications*. URL: https://www.canon.co.uk/lenses/ef-100mm-f-2-8l-macro-is-usm-lens/specification.html.

[25] Canon. *Canon EOS 850D Specifications*. URL: https://www.canon.co.uk/cameras/eos-850d/specifications/.

[26] Carter, T. J. "Common failures in gas turbine blades". In: *Engineering Failure Analysis* 12 (2 Apr. 2005), pp. 237–247. ISSN: 13506307. DOI: 10.1016/j.engfailanal.2004.07.004.

[27] Cengel, Y. A. and Cimbala, J. M. *Fluid Mechanics, Fundamentals and Applications*. 1st ed. McGraw-Hill, 2006. ISBN: 9780072472363.

[28] Chen, H. and Ponter, A. R. "A simplified creep-reverse plasticity solution method for bodies subjected to cyclic loading". In: *European Journal of Mechanics, A/Solids* 23 (4 July 2004), pp. 561–577. ISSN: 09977538. DOI: 10.1016/j.euromechsol.2004.04.003.

[29] Cooper, T. et al. "Performance of compound parabolic concentrators with polygonal apertures". In: *Solar Energy* 95 (Sept. 2013), pp. 308–318. ISSN: 0038092X. DOI: 10.1016/j.solener.2013.06.023.

[30] Courtis, M. and Ireland, P. "Influence of porosity on double-walled effusion-cooled systems for gas turbine blades". In: American Society of Mechanical Engineers, June 2022. ISBN: 978-0-7918-8603-8. DOI: 10.1115/GT2022-80377.

[31] Courtis, M. et al. "Coupled aerothermal-mechanical analysis in single crystal double wall transpiration cooled gas turbine blades with a large film hole density". In: *Applied Thermal Engineering* 219 (Jan. 2023). ISSN: 13594311. DOI: 10.1016/j.applthermaleng.2022.119329.

[32] Cumpsty, N. *Jet Propulsion*. 2nd ed. Cambridge University Press, Aug. 2013. ISBN: 9780521541442.

[33] Cunha, F. J. “Heat Transfer Analysis”. In: 1st ed. US Department of Energy, 2006, pp. 391–411. URL: https://netl.doe.gov/carbon-management/turbines/handbook.

[34] Cunha, F. J., Dahmer, M. T., and Chyu, M. K. “Thermal-mechanical life prediction system for anisotropic turbine components”. In: *Journal of Turbomachinery* 128 (2 Apr. 2006), pp. 240–250. ISSN: 0889504X. DOI: 10.1115/1.2137740.

[35] Dye, D. et al. “Welding of single crystal superalloy CMSX-4: experiments and modelling”. In: *Superalloys* (2004), pp. 485–491. DOI: 10.7449/2004/Superalloys_2004_485_491.

[36] Elmukashfi, E. et al. “Analysis of the thermomechanical stresses in double-wall effusion cooled systems”. In: *Journal of Turbomachinery* 142 (5 May 2020). ISSN: 15288900. DOI: 10.1115/1.4046268.

[37] Elstrop, S. “Turbine Cooling Research Double-Skin Systems”. In: (2014).

[38] Festo. *Push-In Fittings NPQH*. Apr. 2022. URL: https://www.festo.com/media/pim/898/D15000100122898.PDF.

[39] Frasier, D. J. et al. *Process and Alloy Optimization for CMSX-4 Superalloy Single Crystal Aerofoils*. 1984.

[40] Fullagar, K. P. L. et al. “Aero engine test experience with CMSX-4 ® alloy single crystal turbine blades”. In: *Journal of Engineering for Gas Turbines and Power* 118 (Apr. 1996), pp. 380–388. ISSN: 0742-4795. DOI: 10.1115/1.2816600. URL: https://asmedigitalcollection.asme.org/gasturbinespower/article-pdf/118/2/380/5732455/380%5C_1.pdf.

[41] Ghamrawi, A. et al. “Comparative study on photovoltaic and thermal solar energy concentrators”. In: 2013. ISBN: 9780989130530. URL: https://api.semanticscholar.org/CorpusID:55602917.

[42] Gillespie, D. R. H. “Intricate Internal Cooling Systems for Gas Turbine Blading”. In: (2006).

[43] Goldstein, R. J. and Behbahani, A. I. “Impingement of a circular jet with and without cross flow”. In: *International Journal of Heat and Mass Transfer* 25 (9 1982), pp. 1377–1382. ISSN: 0017-9310. DOI: 10.1016/0017-9310(82)90131-4. URL: https://www.sciencedirect.com/science/article/pii/0017931082901314.

[44] Greuner, H. et al. "Design, performance and construction of a 2 MW ion beam test facility for plasma facing components". In: *Fusion Engineering and Design* 75-79 (SUPPL. Nov. 2005), pp. 345–350. ISSN: 09203796. DOI: 10.1016/j.fusengdes.2005.06.021.

[45] Greuner, H. et al. "High heat flux facility GLADIS:. Operational characteristics and results of W7-X pre-series target tests". In: *Journal of Nuclear Materials* 367-370 B (SPEC. ISS. Aug. 2007), pp. 1444–1448. ISSN: 00223115. DOI: 10.1016/j.jnucmat.2007.04.004.

[46] Grundfos. *Data Booklet - In-Line Circulator Pumps*. 2023. URL: https://product-selection.grundfos.com/uk/products/tp-tpe/tpe3-i?tab=documentation.

[47] Han, J.-C. "Recent studies in turbine blade cooling". In: *The International Journal of Rotating Machinery* 10 (6 Nov. 2004), pp. 443–457. ISSN: 1023-621X. DOI: 10.1080/10236210490503978.

[48] Hancock, D. et al. "Testing advanced divertor concepts for fusion power plants using a small high heat flux facility". 2018.

[49] Health, G. B., Executive., S., and Britain), S. O. (*Safety of pressure systems : pressure systems safety regulations 2000. Approved code of practice and guidance on regulation*. 2014.

[50] Holland, M. J. and Thake, T. F. "Rotor blade cooling in high pressure turbines". In: *Journal of Aircraft* 17 (6 1980), pp. 412–418. ISSN: 00218669. DOI: 10.2514/3.44668.

[51] Honnerova, P. and Martan, J. *Technical Note - Aremco Products 840 CM High-Emissivity Paint at 300 C*. 2015.

[52] Honnerova, P. and Martan, J. *Technical Note - Aremco Products 840 CM High-Emissivity Paint at 400 C*. 2015.

[53] Honnerova, P. and Martan, J. *Technical Note - Aremco Products 840 CM High-Emissivity Paint at 500 C*. 2015.

[54] Honnerova, P. and Martan, J. *Technical Note - Aremco Products 840 CM High-Emissivity Paint at 600 C*. 2015.

[55] Honnerova, P. and Martan, J. *Technical Note - Aremco Products 840 CM High-Emissivity Paint at 700 C*. 2015.

[56] Honnerova, P. and Martan, J. *Technical Note - Aremco Products 840 CM High-Emissivity Paint at 800 C*. 2015.

[57] Honnerova, P. and Martan, J. *Technical Note - Aremco Products 840 CM High-Emissivity Paint at 900 C*. 2015.

[58] Howatson, A. M. et al. *Engineering Tables and Data*. 1st ed. Springer Dordrecht, 1972. ISBN: 978-94-010-9314-9. DOI: 10.1007/978-94-010-9314-9.

[59] Huber, A. M. and Viskantay, R. "Effect of jet-jet spacing on convective heat transfer to confined, impinging arrays of axisymmetric air jets". In: *International Journal of Heat and Mass Transfer* 37 (18 1994), pp. 2859–2869. ISSN: 0017-9310. DOI: 10.1016/0017-9310(94)90340-9. URL: https://www.sciencedirect.com/science/article/pii/0017931094903409.

[60] IATA. *Resolution on the Industry's Commitment to Reach Net Zero Carbon Emissions by 2050*. 2019. URL: https://www.iata.org/contentassets/d13875e9ed784f75bac90f000760e998/iata-agm-resolution-on-net-zero-carbon-emissions.pdf.

[61] Institute, N. D. *High-Temperature High-Strength Nickel Base Alloys*. 1995.

[62] Iron, A. and Institute, S. *High-Temperature Characteristics of Stainless Steels*. 1998. URL: https://nickelinstitute.org/media/1699/high_temperaturecharacteristicsofstainlesssteel_9004_.pdf.

[63] Jackson, Z. "Charactising the behaviour of supercritical carbon dioxide at high heat fluxes". In: (2023).

[64] Jackson, Z. et al. "The Oxford Laser Heating Facility: A new experimental facility for investigating components at high-heat fluxes". Oct. 2023.

[65] Klinger. *Klinger Milam PSS*. 2019. URL: https://www.klinger.co.uk/storage/app/media/Product%5C%20Specifications/Jointing%5C%20materials/Milam%5C%20PSS.pdf.

[66] Kolagar, A. M. et al. "Failure analysis of gas turbine first stage blade made of nickel-based superalloy". In: *Case Studies in Engineering Failure Analysis* 8 (Apr. 2017), pp. 61–68. ISSN: 22132902. DOI: 10.1016/j.csefa.2017.04.002.

[67] Krewinkel, R. "A review of gas turbine effusion cooling studies". In: *International Journal of Heat and Mass Transfer* 66 (2013), pp. 706–722. ISSN: 00179310. DOI: 10.1016/j.ijheatmasstransfer.2013.07.071.

[68] Kukla, C. et al. "Joining of thermoplastic tapes with metal alloys utilizing novel laser sources and enhanced process control in a tape placement process". In: vol. 66. Elsevier B.V., 2017, pp. 85–90. DOI: 10.1016/j.procir.2017.03.307.

[69] Li, Q. et al. "100 kW electron-beam high heat flux test facility for testing EAST and CFETR divertor components". In: *Fusion Engineering and Design* 183 (Oct. 2022). ISSN: 09203796. DOI: 10.1016/j.fusengdes.2022.113276.

[70] Melis, M. E. and Gladden, H. J. "A unique high heat flux facility for testing hypersonic engine components". In: American Institute of Aeronautics and Astronautics Inc, AIAA, 1990. DOI: 10.2514/6.1990-5228.

[71] Metcalf, I., Chen, G., and Cooper, T. A. "Toward a best-form CPC-like nonimaging optical concentrator". In: *Optics Express* 30 (25 Dec. 2022), p. 44556. ISSN: 10944087. DOI: 10.1364/oe.476189.

[72] Michels, D., Hadeler, J., and Lienhard, J. H. "High-heat-flux resistance heaters from VPS and HVOF thermal spraying". In: *Experimental Heat Transfer* 11 (4 1998), pp. 341–359. ISSN: 15210480. DOI: 10.1080/08916159808946570.

[73] Molski, K. and Glinka, G. "A method of elastic-plastic stress and strain calculation at a notch root". In: *Materials Science and Engineering* 50 (1981), pp. 93–100.

[74] Moustapha, H. et al. *Axial and Radial Turbines*. 1st ed. Vol. 1. Concepts NREC, 2003. ISBN: 9780933283121. URL: https://books.google.co.uk/books?id=fJFVAAAACAAJ.

[75] Murguran, S. *Engineering Thermodynamics*. Vol. 1. Alpha Science International, Feb. 2014. ISBN: 9781842658437.

[76] Murray, A. V. "Advanced Gas Turbine Cooling: Double-Wall Turbine Cooling Technologies in Turbine NGV/Blade Applications". In: (2019).

[77] Nabic. *Safety Relief Valve*. URL: https://www.nabicvalves.com/product/safety-relief-valves/fig-542-safety-relief-valve/.

[78] Neuber, H. "Theory of stress concentration for shear-strained prismatical bodies with arbitrary nonlinear stress-strain law". In: *Journal of Applied Mechanics* 28 (4 1961), pp. 544–550. DOI: doi.org/10.1115/1.3641780. URL: http://asmedigitalcollection.asme.org/appliedmechanics/article-pdf/28/4/544/5444285/544_1.pdf.

[79] Ngetich, G. C. "Study of Double-Wall Effusion Cooling Scheme for Gas Turbine Blade Applications". In: (2019).

[80] Noort, M. V. D., Murray, A. V., and Ireland, P. T. "Low order heat and mass flow network modelling for quasi-transpiration cooling systems". In: June 2022. DOI: 10.1115/GT2022-81780. URL: https://asmedigitalcollection.asme.org/GT/proceedings-pdf/GT2022/86045/V06BT15A012/6935783/v06bt15a012-gt2022-81780.pdf.

[81] Öchsner, A. *Classical Beam Theories of Structural Mechanics*. Springer International Publishing, 2021. ISBN: 9783030760359. DOI: 10.1007/978-3-030-76035-9.

[82] Oliveira, M. M. D. et al. "Mechanical behavior of inconel 625 at elevated temperatures". In: *Metals* 9 (3 Mar. 2019). ISSN: 20754701. DOI: 10.3390/met9030301.

[83] Optris. *CTratio 2M Technical Data*. 2021.

[84] Optris. *Infrared Cameras Brochure*. 2019.

[85] Optris. *Optris PI 640i Technical Data*. 2019.

[86] Padture, N. P., Gell, M., and Jordan, E. H. "Thermal barrier coatings for gas-turbine engine applications". In: *Science* 296 (5566 2002), pp. 280–284. DOI: 10.1126/science.1068609. URL: https://www.science.org/doi/pdf/10.1126/science.1068609.

[87] Philips-Photonics. *Application Note: Cooling Water Requirements of VCSEL Laser Modules*. Feb. 2018.

[88] Philips-Photonics. *Application Note: Intensity Patterns of PPM412 Type VCSEL Laser Modules*. Sept. 2017.

[89] Philips-Photonics. *High Power Infrared Sources for Industrial Heating*. 2018.

[90] Prokůpek, J. et al. "HELCZA—High heat flux test facility for testing ITER EU first wall components". In: *Fusion Engineering and Design* 124 (Nov. 2017), pp. 187–190. ISSN: 09203796. DOI: 10.1016/j.fusengdes.2017.03.059.

[91] Pruijmboom, A. et al. "VCSEL arrays expanding the range of high-power laser systems and applications". In: Laser Institute of America, Oct. 2018, pp. 1–8. ISBN: 978-1-940168-05-0. DOI: 10.2351/1.5063168.

[92] Ritchie, H. *Climate Change and Flying: What Share of Global CO2 Emissions Come from Aviation?* Oct. 2020. URL: https://ourworldindata.org/co2-emissions-from-aviation#:~:text=Aviation%5C%20accounts%5C%20for%5C%20around%5C%202.5,impacts%5C%20on%5C%20climate%5C%20into%5C%20account.%5C&text=Flying%5C%20is%5C%20a%5C%20highly%5C%20controversial,personal%5C%20and%5C%20collective%5C%20carbon%5C%20emissions..

[93] Rolls-Royce. *The Jet Engine*. Rolls-Royce plc, 1996. ISBN: 0902121235.

[94] San, J. Y. and Shiao, W. Z. "Effects of jet plate size and plate spacing on the stagnation Nusselt number for a confined circular air jet impinging on a flat surface". In: *International Journal of Heat and Mass Transfer* 49 (19-20 Sept. 2006), pp. 3477–3486. ISSN: 00179310. DOI: 10.1016/j.ijheatmasstransfer.2006.02.055.

[95] Scholz, A. et al. "Modeling of mechanical properties of alloy CMSX-4". In: *Materials Science and Engineering: A* 510-511 (C June 2009), pp. 278–283. ISSN: 09215093. DOI: 10.1016/j.msea.2008.04.103.

[96] Schwartz, N. "Laser-Based High Heat Flux Testing for Power Exhaust in Fusion Devices". In: (2020).

[97] Sellers, J. P. "Gaseous film cooling with multiple injection stations". In: *AIAA Journal* 1 (9 1963), pp. 2154–2156. ISSN: 00011452. DOI: 10.2514/3.2014.

[98] Shi, D. et al. "Accelerated LCF-creep experimental methodology for durability life evaluation of turbine blade". In: *Fatigue and Fracture of Engineering Materials and Structures* 41 (5 May 2018), pp. 1196–1207. ISSN: 14602695. DOI: 10.1111/ffe.12763.

[99] Siebörger, D., Knake, H., and Glatzel, U. "Temperature dependence of the elastic moduli of the nickel-base superalloy CMSX-4 and its isolated phases". In: *Materials Science and Engineering* 298 (1 2001), pp. 26–33. ISSN: 0921-5093. DOI: 10.1016/S0921-5093(00)01318-6. URL: https://www.sciencedirect.com/science/article/pii/S0921509300013186.

[100] Skamniotis, C. and Cocks, A. C. "2D and 3D thermoelastic phenomena in double wall transpiration cooling systems for gas turbine blades and hypersonic flight". In: *Aerospace Science and Technology* 113 (June 2021). ISSN: 12709638. DOI: 10.1016/j.ast.2021.106610.

[101] Skamniotis, C. and Cocks, A. C. "Creep-plasticity-fatigue calculations in the design of porous double layers for new transpiration cooling systems". In: *International Journal of Fatigue* 151 (Oct. 2021). ISSN: 01421123. DOI: 10.1016/j.ijfatigue.2021.106304.

[102] Skamniotis, C. and Cocks, A. C. "Minimising stresses in double wall transpiration cooled components for high temperature applications". In: *International Journal of Mechanical Sciences* 189 (Jan. 2021). ISSN: 00207403. DOI: 10.1016/j.ijmecsci.2020.105983.

[103] Skamniotis, C., Courtis, M., and Cocks, A. C. "Multiscale analysis of thermomechanical stresses in double wall transpiration cooling systems for gas turbine blades". In: *International Journal of Mechanical Sciences* 207 (Oct. 2021). ISSN: 00207403. DOI: 10.1016/j.ijmecsci.2021.106657.

[104] Skamniotis, C., Grilli, N., and Cocks, A. "Crystal plasticity finite element modelling of nickel superalloys under severe thermomechanical load cycles, application to transpiration cooled turbine blades".

[105] Skamniotis, C., Grilli, N., and Cocks, A. C. "Crystal plasticity analysis of fatigue-creep behavior at cooling holes in single crystal Nickel based gas turbine blade components". In: *International Journal of Plasticity* 166 (July 2023). ISSN: 07496419. DOI: 10.1016/j.ijplas.2023.103589.

[106] Skamniotis, C. et al. "Fuel savings through hotter jet engines and transpiration cooling: a turbine blade design guide".

[107] Soares, C. *Gas Turbines: A Handbook of Air, Land and Sea Applications*. Elsevier Science and Technology, Oct. 2014. ISBN: 9780124104617.

[108] Special-Metals. *Inconel ® alloy 625 Material Data*. 2007.

[109] Special-Metals. *Inconel ® alloy 718 Material Data*. 2007.

[110] Swagelok. *Gaugeable Tube Fittings and Adapter Fittings*. 2022. URL: https://www.swagelok.com/downloads/webcatalogs/en/ms-01-140.pdf.

[111] Swagelok. *Hose and Flexible Tubing*. 2022. URL: https://www.swagelok.com/downloads/webcatalogs/en/ms-01-180.pdf.

[112] Tan, Q.-M. *Dimensional Analysis: With Case Studies in Mechanics*. 1st ed. Springer, 2011. ISBN: 978-3-642-19234-0. DOI: 10.1007/978-3-642-19234-0.

[113] Taylor, J. R. *An Introduction to Error Analysis, The Study of Uncertainties in Physical Measurements*. 2nd ed. University Science Books, 1997. ISBN: 0-935702-75-X.

[114] Thulin, R. D., Howe, D. C., and Singer, I. D. *Energy Efficient Engine, High-Pressure Turbine Detailed Design Report*. Jan. 1982. URL: https://ntrs.nasa.gov/search.jsp?R=19840020719.

[115] Timoshenko, S. and Goodier, J. N. *Theory of Elasticity*. 2nd ed. McGraw-Hill Book Company, 1951.

[116] UQG-Optics. *Data Sheet: Barium Fluoride Window*. URL: https://www.uqgoptics.com/catalogue/optical-windows/ir-windows-uv-crystals/barium-fluoride-baf2-windows/.

[117] UQG-Optics. *Data Sheet: Calcium Fluoride Window*. URL: https://www.uqgoptics.com/catalogue/optical-windows/ir-windows-uv-crystals/calcium-fluoride-caf2-windows-plates/.

[118] UQG-Optics. *Data Sheet: Cold Mirrors*. 2019. URL: https://www.uqgoptics.com/materials/cold-mirrors/.

[119] UQG-Optics. *Data Sheet: Germanium Uncoated Window*. URL: https://www.uqgoptics.com/catalogue/optical-windows/ir-windows-uv-crystals/germanium-ge-windows-uncoated-ar-ar-ar-dlc-coated/.

[120] UQG-Optics. *Data Sheet: IR Fused Quartz Window*. URL: https://www.uqgoptics.com/catalogue/optical-windows/ir-windows-uv-crystals/ir-fused-quartz-windows-plates/.

[121] UQG-Optics. *Data Sheet: Magnesium Fluoride Window*. URL: https://www.uqgoptics.com/catalogue/optical-windows/ir-windows-uv-crystals/magnesium-fluoride-mgf2-windows/.

[122] UQG-Optics. *Data Sheet: Sapphire Window*. URL: https://www.uqgoptics.com/catalogue/optical-windows/sapphire/sapphire-windows-plates-cut-to-c-axis/.

[123] UQG-Optics. *Data Sheet: Silicon Window*. URL: https://www.uqgoptics.com/catalogue/optical-windows/ir-windows-uv-crystals/silicon-si-windows-uncoated-ar-coated/.

[124] UQG-Optics. *Data Sheet: Zinc Selenide Window*. URL: https://www.uqgoptics.com/catalogue/optical-windows/ir-windows-uv-crystals/zinc-selenide-znse-windows/.

[125] UQG-Optics. *Data Sheet: Zinc Sulphide Window*. URL: https://www.uqgoptics.com/catalogue/optical-windows/ir-windows-uv-crystals/zinc-sulphide-zns-windows/.

[126] Wambersie, A. "High Porosity Cooling Features for Turbine Blade Applications". In: (2023).

[127] Weiler, T. et al. "Optical modelling of VCSEL-assisted thermoplastic tape placement". In: June 2016.

[128] Weiler, T. et al. "Tailored irradiation by VCSEL for controlled thermal states in thermoplastic tape placement". In: SPIE-Intl Soc Optical Eng, Feb. 2018, p. 15. ISBN: 9781510615311. DOI: 10.1117/12.2291015.

[129] Weiler, T. et al. "Transient thermal analysis of laser-assisted thermoplastic tape placement at high process speeds by use of analytical solutions". In: *Journal of Thermoplastic Composite Materials* 31 (3 Mar. 2018), pp. 311–338. ISSN: 15307980. DOI: 10.1177/0892705717697780.

[130] Winston, R., Minano, J. C., and Benitez, P. *Nonimaging Optics*. 1st ed. Academic Press, 2005. ISBN: 9780127597515.

[131] Xu, L. et al. "Evolution of Rolls-Royce air-cooled turbine blades and feature analysis". In: vol. 99. Elsevier Ltd, 2015, pp. 1482–1491. DOI: 10.1016/j.proeng.2014.12.689.

[132] Zakaria, K. A., Abdullah, S., and Ghazali, M. J. "Elevated temperature fatigue life investigation of aluminium alloy based on the predicted S-N curve". In: *Jurnal Teknologi (Sciences and Engineering)* 63 (1 July 2013), pp. 75–79. ISSN: 01279696. DOI: 10.11113/jt.v63.1345.

Appendix I: Derivation of DWEC Coupon Equations

This appendix complements the derivation presented in Chapter 4. It serves to illustrate why certain terms were considered negligible. It references equations derived in the free body diagrams and the constraint considerations of Chapter 4.

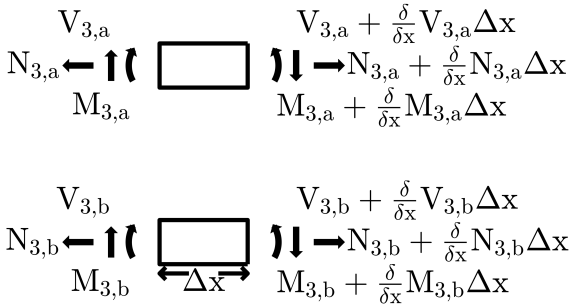


Figure 1: Zone 3 differential free body diagram

Zone 3 Differential Relations

Figure 1 features an infinitesimally small vertical slice of the zone 3 DWEC domain, of width Δx, shown in Figure 4.1. Applying static equilibrium to this sub-domain:

$$\Sigma F_x = N_{3,a} + \frac{\delta}{\delta x} N_{3,a} \Delta x - N_{3,a} + N_{3,b} + \frac{\delta}{\delta x} N_{3,b} \Delta x - N_{3,b} = 0 \tag{1}$$

$$\Sigma F_y = V_{3,a} - V_{3,a} + \frac{\delta}{\delta x} V_{3,a} \Delta x + V_{3,b} - V_{3,b} + \frac{\delta}{\delta x} V_{3,b} \Delta x = 0 \tag{2}$$

The sum of the moments about the rightmost side of the inner skin, at point P, is taken as:

$$\begin{aligned} \Sigma M_{P_{3,b}} =& M_{3,a} + \frac{\delta}{\delta x} M_{3,a} \Delta x - M_{3,a} + M_{3,b} + \frac{\delta}{\delta x} M_{3,b} \Delta x - M_{3,b} - V_{3,a} \Delta x - V_{3,b} \Delta x \\ &+ \left(H + \frac{t_a}{2} + \frac{t_b}{2} \right) N_{3,a} - \left(H + \frac{t_a}{2} + \frac{t_b}{2} \right) \left(N_{3,a} + \frac{\delta}{\delta x} N_{3,a} \Delta x \right) \end{aligned} \tag{3}$$

Simplifying the above equations to get the first three governing equations:

$$\frac{\delta}{\delta x} N_{3,a} + \frac{\delta}{\delta x} N_{3,b} = 0 \tag{4}$$

$$\frac{\delta}{\delta \mathrm{x}} \mathrm{V}_{3,\mathrm{a}} + \frac{\delta}{\delta \mathrm{x}} \mathrm{V}_{3,\mathrm{b}} = 0 \tag{5}$$

$$\frac{\delta}{\delta \mathrm{x}} \mathrm{M}_{3,\mathrm{a}} + \frac{\delta}{\delta \mathrm{x}} \mathrm{M}_{3,\mathrm{b}} - \mathrm{V}_{3,\mathrm{a}} - \mathrm{V}_{3,\mathrm{b}} - \left(\mathrm{H} + \frac{\mathrm{t_a}}{2} + \frac{\mathrm{t_b}}{2} \right) \frac{\delta}{\delta \mathrm{x}} \mathrm{N}_{3,\mathrm{a}} = 0 \tag{6}$$

Zone 3 Normal Forces

The zero-total curvature condition in zone 3 requires that the displacement of both walls must be equivalent for the same x-location:

$$\mathrm{u}_{\mathrm{x,a}} = \mathrm{u}_{\mathrm{x,b}} \tag{7}$$

Differentiation of the original x-displacement relation and substitution using the strain-displacement relation yields:

$$\frac{\delta}{\delta \mathrm{x}} \mathrm{u}_{\mathrm{x,a}} = \frac{\delta}{\delta \mathrm{x}} \mathrm{u}_{\mathrm{x,b}} \quad \text{and} \quad \epsilon_{\mathrm{a}} = \epsilon_{\mathrm{b}} \tag{8}$$

This allows for the derivation of equation (4.18). Substituting the components in to equation (4.18), and taking the derivative:

$$\frac{\delta}{\delta \mathrm{x}} \left(\frac{1}{\mathrm{Et_a}} \mathrm{N}_{3,\mathrm{a}} \right) + \frac{\delta}{\delta \mathrm{x}} \left(\alpha \mathrm{T}_{3,\mathrm{a}}(\mathrm{x}, \mathrm{y}) \right) = \frac{\delta}{\delta \mathrm{x}} \left(\frac{1}{\mathrm{Et_b}} \mathrm{N}_{3,\mathrm{b}} \right) + \frac{\delta}{\delta \mathrm{x}} \left(\alpha \mathrm{T}_{3,\mathrm{b}}(\mathrm{x}, \mathrm{y}) \right) \tag{9}$$

Across all three thermal cases, the thermal field of both centre lines is constant. Therefore, their derivative terms are reduced to zero. Combining equations (4) and (9) and factoring out the derivative:

$$\left(1 + \frac{\mathrm{t_b}}{\mathrm{t_a}} \right) \frac{\delta}{\delta \mathrm{x}} \mathrm{N}_{3,\mathrm{a}} = 0 \tag{10}$$

Due to the nature of $\mathrm{t_a}$ and $\mathrm{t_b}$ of being non-zero, the only solution to this equation that satisfies all conditions is that:

$$\frac{\delta}{\delta \mathrm{x}} \mathrm{N}_{3,\mathrm{a}} = 0 \quad \text{and} \quad \frac{\delta}{\delta \mathrm{x}} \mathrm{N}_{3,\mathrm{b}} = 0 \tag{11}$$

Which requires the normal forces in zone 3 to be constant within each wall.

Zone 3 Shear Forces and Moments

A similar approach is taken with equations (6) and (4.23). Taking the derivative of equation (6) and applying the conclusion in equation (11):

$$\frac{\delta}{\delta \mathrm{x}}\left(\frac{12}{\mathrm{E}\mathrm{t}_{\mathrm{a}}^{3}}\mathrm{M}_{3,\mathrm{a}}\right)-\frac{\delta}{\delta \mathrm{x}}\left(\alpha\frac{\mathrm{T}_{\mathrm{h}}-\mathrm{T}_{\mathrm{c}}}{\mathrm{t}_{\mathrm{a}}}\right)=0 \tag{12}$$

As the thermal field is constant across all three cases:

$$\frac{1}{\mathrm{t}_{\mathrm{a}}^{3}}\frac{\delta}{\delta \mathrm{x}}\mathrm{M}_{3,\mathrm{a}}=0 \tag{13}$$

For which the only solution is:

$$\frac{\delta}{\delta \mathrm{x}}\mathrm{M}_{3,\mathrm{a}}=0 \tag{14}$$

Therefore, the moment carried by the outer skin in zone 3 must be constant within each skin. Substituting the values in to equation (6):

$$0+0-\mathrm{V}_{3,\mathrm{a}}-\mathrm{V}_{3,\mathrm{b}}-\left(\mathrm{H}+\frac{\mathrm{t}_{\mathrm{a}}}{2}+\frac{\mathrm{t}_{\mathrm{b}}}{2}\right)0=0 \tag{15}$$

Thus, it is concluded that no net shear force is carried by zone 3. This is supported by FEA which shows $\mathrm{V}_{3,\mathrm{a}}=\mathrm{V}_{3,\mathrm{b}}=0$; however, the conclusion from the equation above is:

$$\mathrm{V}_{3,\mathrm{a}}+\mathrm{V}_{3,\mathrm{b}}=0 \tag{16}$$

It is of note that this is coherent with the condition applied at the symmetry plane, which dictates that the net shear force at $\mathrm{x}=\mathrm{x}_3$ must be zero. In addition, the moments in zone 2 are taken to be zero, as there is no thermal curvature and no applied moment across the boundary at $\mathrm{x}=\mathrm{x}_2$. The conclusions above require that all of the net shear forces in each domain must be zero to satisfy equilibrium; therefore, they are omitted in the derivation. The only moments that exist where there is a thermal gradient in the y-direction are in wall A of zone 3.

Appendix II: Selected Material Properties

The following appendix is a consolidation of various relevant material properties for CMSX-4 and Inconel 625. These were taken from multiple sources, and where there were discrepancies, mean values were calculated. Mechanical and thermal properties of Inconel 625 and Inconel 718 are omitted, as a full accounting can be found in [108, 109]. Tables 1 and 2 present the relative mass of the various constituent elements. Inconel 718 is included for the sake of emissivity comparison.

Source	Ni	Cr	Co	Mo	W	Ta	Al	Ti	Hf	Re
[61]	62	7	10	0.6	6	6	5.6	1	0.1	3
[99]	63.1	7.6	10.3	0.4	2	2	12.5	1.3	0.1	1
Mean	62.6	7.3	10.1	0.5	4	4	9.1	1.1	0.1	2

Table 1: *Chemical composition of CMSX-4 by per cent-mass*

Metal	Ni	Cr	Co	Mo	Al	Ti	Fe	Nb	C	Mn	Si	Trc
625 [108]	58	20	1	8	0.4	0.4	5	3.2	0.1	0.5	0.5	2.9
718 [109]	50	20	1	3	0.5	1	16.2	5	0.08	0.35	0.35	2.7

Table 2: *Chemical composition of Inconel by per cent-mass*

Table 3 provides a complete accounting of the mechanical and thermal properties used in simulations and analysis involving CMSX-4. The various moduli and Poissons' ratios were calculated by Dye [35] using the Sieborger relations [99]. There are a few gaps in the thermal conductivity relative to the rest of the data set. Sampling is performed through linear extrapolation between specified data points. The last two rows are separated as they denote the solidus and liquidus temperatures of CMSX-4 [61]. Although not used in this work, they are included for completeness.

Temp T [°C]	Density ρ $\left[\frac{\text{kg}}{\text{m}^3}\right]$ [35]	Youngs' Modulus E [GPa] [99]	Shear Modulus G [GPa] [99]	Poissons' Ratio ν [–] [99]	Yield Stress σ_y [MPa] [101]	Thermal Conductivity k $\left[\frac{\text{W}}{\text{m°C}}\right]$ [2]	Specific Heat C_p $\left[\frac{\text{J}}{\text{kg°C}}\right]$ [35]	Thermal Expansion α $\left[\frac{1}{\text{°C}}\right] * 10^{-6}$ [35]
20	8700	127.3	131.3	0.389	806.0	7.81	397	11.1
100	8665	125.0	128.7	0.391	809.0	-	415	11.8
200	8618	122.0	125.5	0.394	811.0	12.17	431	12.8
300	8572	118.0	121.9	0.395	821.0	-	445	13.7
400	8525	115.0	118.6	0.395	828.0	16.05	456	14.7
500	8479	111.0	114.3	0.395	837.0	-	466	15.6
600	8433	106.0	109.9	0.396	870.0	19.21	488	16.5
700	8387	101.0	107.1	0.398	958.0	-	532	17.4
800	8342	96.0	102.3	0.403	872.0	20.42	530	18.3
900	8296	90.2	99.0	0.410	664.0	20.64	540	19.2
1000	8251	82.7	93.7	0.420	452.0	18.85	550	20.1
1100	8206	75.1	88.3	0.430	279.0	18.92	560	21.0
1200	8161	67.6	82.9	0.440	120.7	20.23	570	21.8
1300	8116	60.1	77.5	0.450	40.2	-	580	22.7
1320	8107	58.6	76.4	0.452	20.4	24.78	580	19.5
1380	7754	54.0	73.2	0.458	20.4	24.07	675	18.6

Table 3: *Physical and thermal properties of CMSX-4,* $< 001 >$ *direction*

Temperature T [°C]	CMSX-4 Emissivity ϵ [−]	Inconel 718 Emissivity ϵ [−]
923	0.846	0.822
973	0.831	0.840
1023	0.819	0.851
1073	0.805	0.861
1123	0.794	0.872
1173	0.790	0.883
1223	0.790	0.895
1273	0.792	0.901

Table 4: *Relevant emissivity values for CMSX-4 and Inconel 718, taken from [3]*

The emissivity values for CMSX-4 and Inconel 718 are presented in Table 4. Emissivity values for solid Inconel 625 are not readily available in the literature. Due to the similarities in composition between both types of Inconel, as is evident in Table 2, the general emissivity trend and magnitudes were assumed to be similar to Inconel 718.

Material	Q $[\frac{\text{J}}{\text{mol}}]$	$\dot{\epsilon}_{\text{o}}$ $[\frac{1}{\text{sec}}]$	σ_{o} [MPa]	T_{ref} [°C]	n [−]
CMSX-4	4.0 E+5	2.78 E-4	800	830	10.00
Inconel 625	4.7 E+5	2.78 E-4	500	700	11.76

Table 5: Creep properties for selected materials, reproduced from [28, 101]

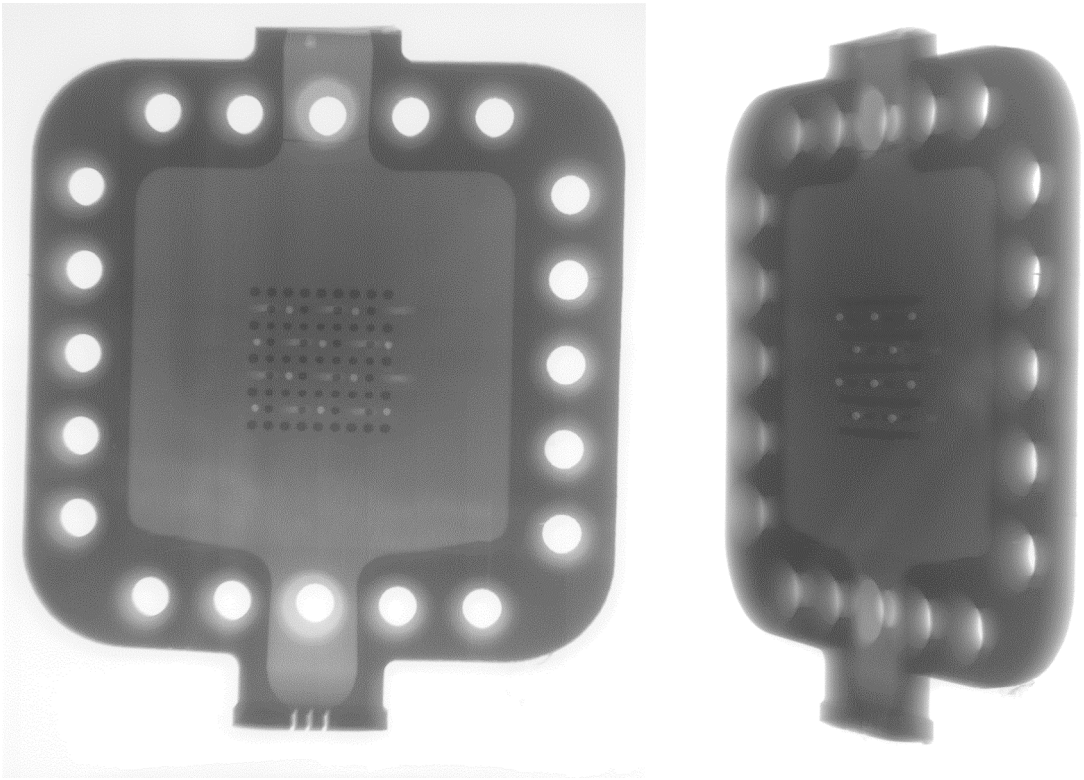
Material	Orientation	A_1	B_1	A_2	B_2	C
CMSX-4	$< 001 >$	202	-2.58	0.199	-0.04	3.01
CMSX-4	$< 111 >$	2.93	-1.16	2.13	-1.454	1.34

Table 6: *Manson-Coffin coefficients for relevant crystallographic directions, reproduced from [95]*

Appendix III: Manufacturing

Cast CMSX-4 Coupon

The CMSX-4 coupon was cast as a single-crystal and was provided by Mick Wickins at the University of Birmingham. Following casting, the specimen was extracted from the exterior and interior mould through high-frequency vibrations which powderise the ceramic material for easy removal, leaving the metal behind. The removal of excess metal was performed at the University of Oxfords' Begbroke Site, using a wire-eroder. This achieved the final shape and dimensions used in the testing.



(a) (b)

Figure 2: *X-ray imaging (a) normal to the coupon at 450 kV (b) normal to the film hole inclination at 450 kV*

X-ray imaging and bore-scope images were taken following extraction from the mould. Figure 2 presents two orientations of the coupon. Figure 3 presents a bore-scope image of the pedestals within the cavity as viewed through one of the side slots. It is clear from Figures

2 and 3 that the internal characteristics have been adequately resolved. The 10 film holes and 10 impingement holes were formed, along with each of the 61 pedestals. The increased diameter of the exterior pedestals can be clearly seen. There is some additional material in the lower corners of the coupon. This is most likely due to cracking of the mould during the casting process. This was a common occurrence as the coupon shape proved challenging to construct appropriately with the intricate geometry and small internal dimensions.

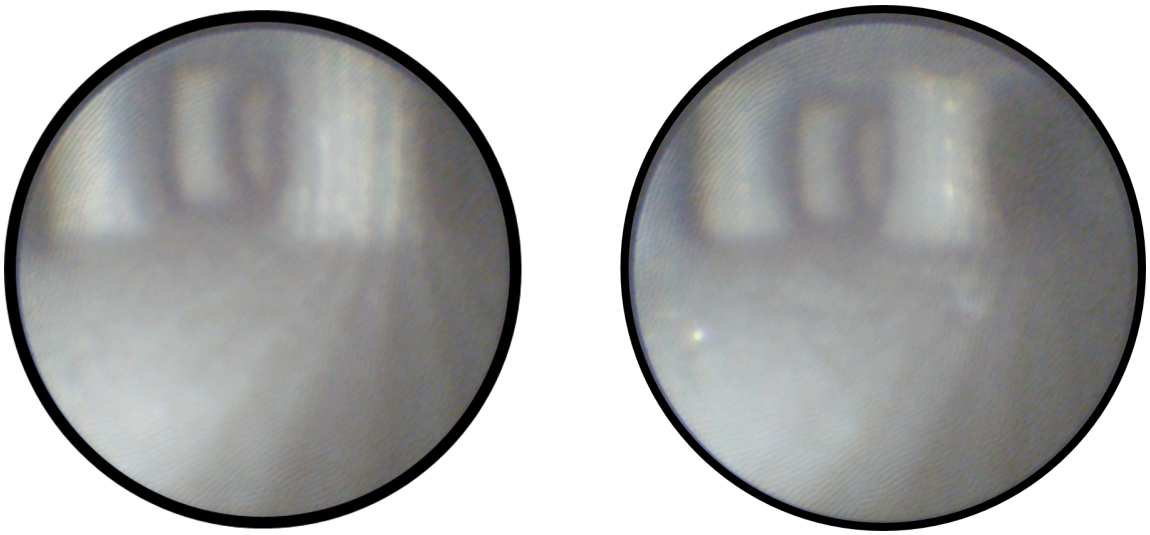


Figure 3: *Bore-scope images of internal features of the CMSX-4 cast coupon*

The bore-scope images were taken with an Endoscan Micro Flexible Endoscope[1] with a 1 mm diameter body. A 90-degree side-view prism with a 50-degree field of view was used. It is clear that the pedestals feature some minor filleting. It was not possible to discern whether this was due to the proper resolution of the 0.6 mm radius fillets during mould formation and casting or whether this was a by-product of the casting process. It has been commonly observed that the liquid CMSX-4 can fail to fill the entire mould for small features.

Additive Manufacture Inconel 625 Coupon

The Inconel 625 coupons were 3D-printed and provided by 3T[2]. Polishing of the exterior and braze surfaces is conducted following extraction from the printer. Figure 4 presents an example image of the internal features, as well as the appearance of the components at the

[1]Endoscan Ltd., https://www.endoscan.co.uk/microflexible
[2]3T Additive Manufacturing Ltd., https://www.3t-am.com

braze site. The 3D print quality of the slot was high and minimal polishing was required to obtain a sufficiently smooth surface for brazing. The plugs were ground to match the individual holes. As is apparent from Figure 4, the pedestals have formed properly from the printing.

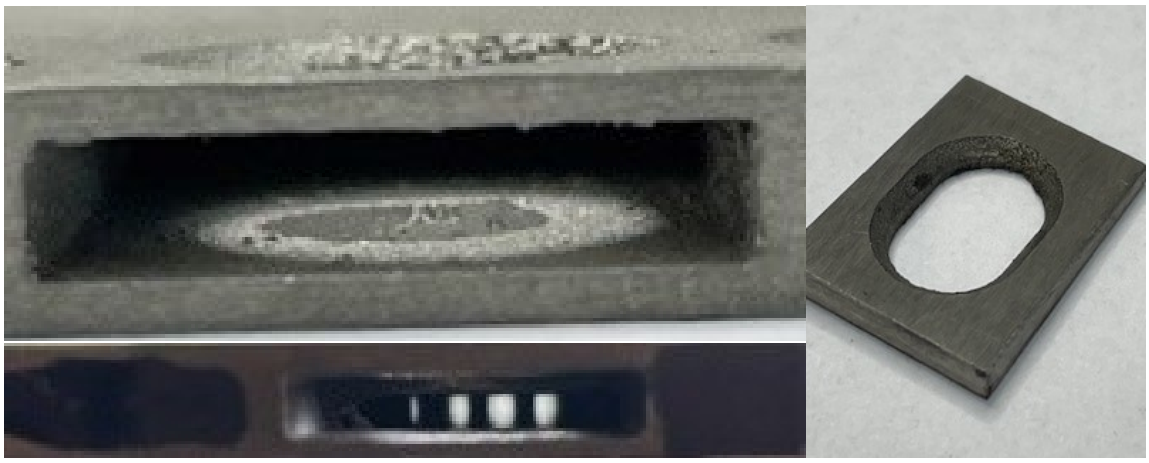


Figure 4: *Enhanced images of (top left) the prepared side-slot ahead of brazing (bottom left) the pedestals in the 3D-printed coupon (right) the polished plug ahead of brazing*

Figure 5 presents a comparison between the scans provided by 3T[2] and the original CAD file. The primary external features show good adherence to the requested dimensions. The scale of the colour bar is in mm. The mean deviation from the design size is 0.15 mm. No internal scans were possible for these components. The image in Figure 4 was the only one that confirmed the proper printing of the interior. This was assumed to be uniform across all printed components.

Braze Quality

The plugs were brazed in to the side slots by Kepston[3]. A steel braze was applied to the exterior of the plug before brazing was performed in a vacuum chamber to ensure correct bonding of the material. Before brazing, it was observed that the CMSX-4 side slot contained protrusions about 60-70% of the depth through the side wall, requiring additional grinding of the plugs to ensure adequate fit.

[2]3T Additive Manufacturing Ltd., https://www.3t-am.com
[3]Kepston Ltd., https://www.kepston.co.uk/furnace_brazing

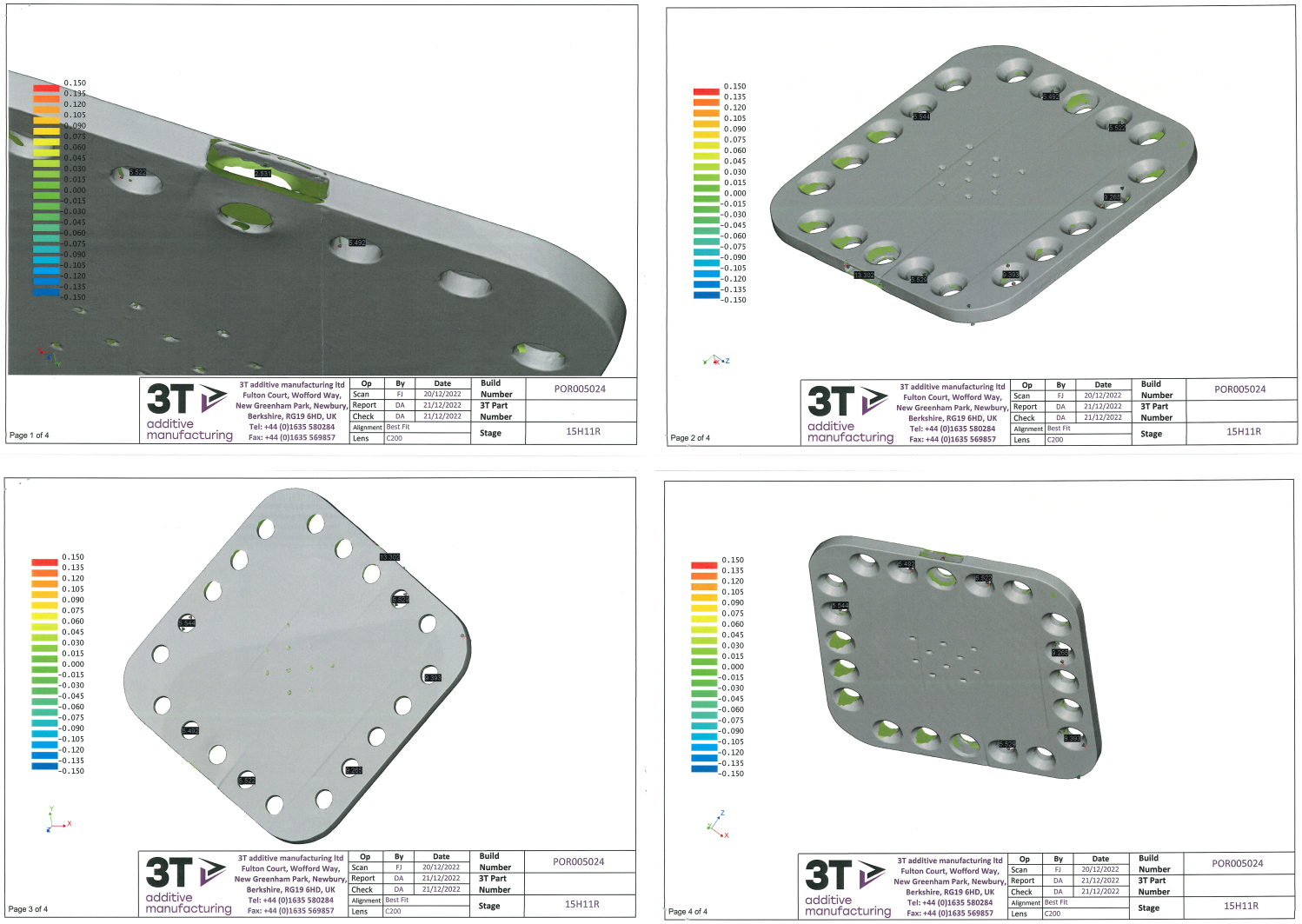
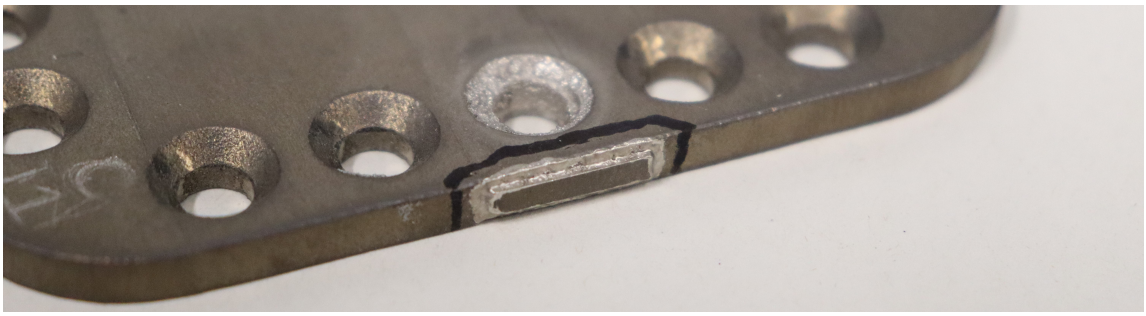


Figure 5: *Comparison of 3D-printed coupon to original CAD specifications*



(a)



(b)

Figure 6: *Representative images of braze quality for (a) CMSX-4 (b) Inconel 625*

The results of the brazing process are presented in Figure 6. Figure 6 (b) is considered representative of each of the Inconel components, as they are all visually identical. Due to the final shape of the plugs, with a slight inward draft along its length, the small clearance required to initiate capillary action was not met for the CMSX-4 component. Additional brazing material was added to the external surfaces to create a suitable seal. A similar approach was taken with the Inconel 625 coupons, although the 3D-printed surface appeared to be more conducive to brazing. Each component was leak-tested when initially placed on the plenum. No bubbles were observed in the spray-on leak detection medium during operation. Therefore, it was concluded that the braze operates as intended. A redesign of the coupon should utilise a non-drafted plug to ensure better the gap between the plug and the slot is minimised, enhancing capillary action.

Appendix IV: Strain Range MATLAB Script

```
function [NE,MG,KN,comp] = solvelastoplastic(elcycstr,ncycle)

% CMSX-4 Material Properties
[Es,sigyt] = loadsigyt;                         % [MPa] - Elastic Modulus, Yield Stress

% CMSX-4 Creep Modelling
Q = 400000;                                     % [J/mol] - Activation Energy
ero = 1/3600;                                   % [1/sec] - Strain Rate
so = 800;                                       % [MPa] - Reference Stress
Tr = 830;                                       % [degC] - Reference Temperature
n = 10;                                         % [-] - Exponent
R = 8.31;                                       % [J/molK] - Gas Constant

% CMSX-4 Recovery Factor
Zel = 4;                                        % [-] - Elastic Recovery;
Zpl = 1;                                        % [-] - Plastic Recovery;

% interpolate ANSYS values to discretised time steps
timeset = 0.01:0.01:elcycstr(end,1);            % [sec] - Reference

% [Time [sec], Temperature [C], Stress [Pa]]
elcycstr = [timeset',interp1(elcycstr(:,1),elcycstr(:,2),timeset)', ...
    interp1(elcycstr(:,1),elcycstr(:,3),timeset)'];

% build full cycle property matrix
comp = [0 27 0 0;zeros(size(elcycstr,1)*ncycle,4)];
comp(1,4) = interp1(sigyt(:,1),sigyt(:,2),comp(1,2));

for i = 1:ncycle

    comp(2+((i-1)*size(elcycstr,1)):1+(i*size(elcycstr,1)),1:3) = elcycstr;

end

% extract relevant data points
time = comp(:,1);                               % [sec]
temp = comp(:,2);                               % [C]
strs = comp(:,3);                               % [Pa]

% initialise solution
NE = [time zeros(length(time),5)];              % Neuber Method
MG = [time zeros(length(time),5)];              % Molski-Glinka Method
KN = [time zeros(length(time),5)];              % Kinematic Method

% solve for each model

for i = 1:3

    % initialise variables
    s_old = 0;
    s_new = 0;
    Sold = 0;
    Snew = 0;
    dep = 0;
    p_old = 0;
    e_new = 0;
    e_old = 0;
    ecr_old = 0;
    ecr_new = 0;
    ee = 0;
    de = 0;
    ep = 0;
    ecr = 0;
```

```
p_new = 0;
ds_creep = 0;
dp = 0;
ep_new = 0;
ep_old = 0;
ecr_old_Z0 = 0;
ecr_new_Z0 = 0;
dThigh_old = 0;

% solve at each time increment
for j = 2:length(time)

    % determine time step
    dt = time(j) - time(j-1);

    % determine temperature step
    dThigh_new = temp(j) - temp(j-1);
    Thalf = mean([temp(j) temp(j-1)]);

    %%%%%%%%%%%%%%%%%%%%%%%%%%%%%%%%%%%%%%%%%%%%%%%%%%%%%%%%%%%%%%%%%%%%%%%

    dS = (strs(j) - strs(j-1))/10^6;    %elastic stress increment

    E = interp1(Es(:,1),Es(:,2),Thalf,'linear','extrap');

    % define reference stress to calculate fictitious
    % elastic stress at unloading
    if  dThigh_new < 0 && dThigh_old == 0

        % represents the end of dwell
        Sold = s_old;
        ep_old = 0;

    elseif dThigh_new > 0 && dThigh_old ==0 && s_old > 0

        % represents the residual stress at room temperature
        % (or zero stress at first cycle)
        Sold = s_old;
        ep_old = 0;

        % increase plastic cooldown strain to account for Z>1 on heat-up
        % p_old = p_old + ecr_difference;

    end

    % use reference for elastic stress (useful for cyclic loading)
    Snew = Sold + dS;

    % assume initial elastic stress at end of increment
    s_new = dS + s_old;
    ds = dS;
    de = dS/E;
    e_new = e_old + de;

    %%%%%%%%%%%%%%%%%%%%%%%%%%%%%%%%%%%%%%%%%%%%%%%%%%%%%%%%%%%%%%%%%%%%%%%

    % yield stress at max temperature
    Sy_T = interp1(sigyt(:,1),sigyt(:,2),Thalf);

    if i == 1

        comp(j,4) = Sy_T;

    end

    if abs(s_new) > Sy_T

        Z = Zpl;
```

```
        % correct elastic stress
        s_new = sign(s_new)*Sy_T;

        % correct elastic parts
        ds = s_new - s_old;
        de = ds/E;
        e_new = e_old + de;

        if i == 1

            % elastoplastic strain for NEUBER (OK)
            En = (1/E)*(dS^2 + 2*abs(dS*Sold));

            if ds < 0

                dep = -(En - abs(ds*ep_old))/(abs(s_old) + abs(ds));

            else

                dep= -En/(abs(s_new) + abs(ds)/2);

            end

            if s_new > 0

                % change the direction of strain when unloading
                % i.e. residual stress (positive stress)
                dep = -dep;

            end

        elseif i == 2

            % elastoplastic strain for GLINKA (OK)
            Eg = (1/E)*(0.5*dS^2 + abs(dS*Sold));

            if ds < 0

                dep = -Eg/(abs(s_old) + 0.5*abs(ds));

            else

                dep = -Eg/(abs(s_new) + 0.5*abs(ds));

            end

            if s_new > 0

                % change the direction of strain when unloading
                % i.e. residual stress (positive stress)
                dep = -dep;

            end

        else

            % elastoplastic strain for kinematic
            % (same as the fictitious elastic)
            dep = dS/E;

        end

    else

        dep = ds/E; % no yielding
        Z = Zel;
```

```
        end

        ep_new = ep_old + dep;
        dp = dep - de;
        p_new = p_old + dp;

        %%%%%%%%%%%%%%%%%%%%%%%%%%%%%%%%%%%%%%%%%%%%%%%%%%%%%%%%%%%%%%%%%%%%%%%

        if j>2

            x = -(Q/R)*(1/(Thalf + 273) - 1/(Tr + 273));

            s_beg_dwell = 0.5*(s_old + s_new);
            %  s_beg_dwell = s_new;

            ds_creep = sign(s_beg_dwell)*(E/Z)*ero*dt*...
                ((abs(s_beg_dwell)/so)^n)*exp(x);

            ecr_new = ecr_old + ds_creep/(E/Z);
            ecr_new_Z0 = ecr_old_Z0 + ds_creep/E;
            ecr_difference = abs(ecr_new) - abs(ecr_new_Z0);

            e_new = e_new - ds_creep/E;
            s_new = s_new - ds_creep;

        end

        %%%%%%%%%%%%%%%%%%%%%%%%%%%%%%%%%%%%%%%%%%%%%%%%%%%%%%%%%%%%%%%%%%%%%%%

        s_old = s_new;
        e_old = e_new;
        Sold = Snew;
        p_old = p_new;
        ep_old = ep_new;
        ecr_old = ecr_new;
        dThigh_old = dThigh_new;
        ecr_old_Z0 = ecr_new_Z0;

        %%%%%%%%%%%%%%%%%%%%%%%%%%%%%%%%%%%%%%%%%%%%%%%%%%%%%%%%%%%%%%%%%%%%%%%

        % store solution data at each time step
        if i == 1                                % neuber energy

            NE(j,2:end) = [e_new,ecr_new,p_new,...
                e_new+ecr_new+p_new,s_new];

        elseif i == 2                            % molski-glinka energy

            MG(j,2:end) = [e_new,ecr_new,p_new,...
                e_new+ecr_new+p_new,s_new];

        elseif i == 3                            % kinematic equations

            KN(j,2:end) = [e_new,ecr_new,p_new,...
                e_new+ecr_new+p_new,s_new];

        end

    end

end

end
```